

WL-TR-97-1153

COMMUNICATION APPLICATIONS FOR  
DEFORMABLE MIRROR DEVICES



STEVEN C. GUSTAFSON      GORDON R. LITTLE  
TROY A. RHOADARMER      THERESA A. TUTHILL

UNIVERSITY OF DAYTON RESEARCH INSTITUTE  
300 COLLEGE PARK  
DAYTON OH 45469-0150

JUNE 1997

FINAL REPORT FOR 01/19/93-06/30/97

APPROVED FOR PUBLIC RELEASE; DISTRIBUTION IS UNLIMITED.

19980622 156

DTIC QUALITY INSPECTED 1

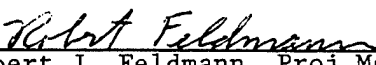
AVIONICS DIRECTORATE  
WRIGHT LABORATORY  
AIR FORCE MATERIEL COMMAND  
WRIGHT PATTERSON AFB OH 45433-7623

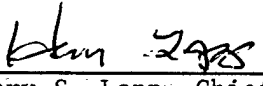
## NOTICE


USING GOVERNMENT DRAWINGS, SPECIFICATIONS, OR OTHER DATA INCLUDED IN THIS DOCUMENT FOR ANY PURPOSE OTHER THAN GOVERNMENT PROCUREMENT DOES NOT IN ANY WAY OBLIGATE THE US GOVERNMENT. THE FACT THAT THE GOVERNMENT FORMULATED OR SUPPLIED THE DRAWINGS, SPECIFICATIONS, OR OTHER DATA DOES NOT LICENSE THE HOLDER OR ANY OTHER PERSON OR CORPORATION; OR CONVEY ANY RIGHTS OR PERMISSION TO MANUFACTURE, USE, OR SELL ANY PATENTED INVENTION THAT MAY RELATE TO THEM.

THIS REPORT IS RELEASABLE TO THE NATIONAL TECHNICAL INFORMATION SERVICE (NTIS). AT NTIS, IT WILL BE AVAILABLE TO THE GENERAL PUBLIC, INCLUDING FOREIGN NATIONS.

THIS TECHNICAL REPORT HAS BEEN REVIEWED AND IS APPROVED FOR PUBLICATION.

  
Robert J. Feldmann, Proj Mgr  
EO Targeting Branch  
EO Sensor Technology Division

  
Henry S. Lapp, Chief  
EO Targeting Branch  
EO Sensor Technology Division

  
Richard D. Hunziker, Chief  
EO Sensor Technology Division  
Sensors Directorate

IF YOUR ADDRESS HAS CHANGED, IF YOU WISH TO BE REMOVED FROM OUR MAILING LIST, OR IF THE ADDRESSEE IS NO LONGER EMPLOYED BY YOUR ORGANIZATION PLEASE NOTIFY AFRL/SNJT WRIGHT-PATTERSON AFB OH 45433-7405 TO HELP MAINTAIN A CURRENT MAILING LIST.

Do not return copies of this report unless contractual obligations or notice on a specific document requires its return.

# REPORT DOCUMENTATION PAGE

Form Approved  
OMB No. 0704-0188

Public reporting burden for this collection of information is estimated to average 1 hour per response, including the time for reviewing instructions, searching existing data sources, gathering and maintaining the data needed, and completing and reviewing the collection of information. Send comments regarding this burden estimate or any other aspect of this collection of information, including suggestions for reducing this burden, to Washington Headquarters Services, Directorate for Information Operations and Reports, 1215 Jefferson Davis Highway, Suite 1204, Arlington, VA 22202-4302, and to the Office of Management and Budget, Paperwork Reduction Project (0704-0188), Washington, DC 20503.

1. AGENCY USE ONLY (Leave blank)		2. REPORT DATE 30 Jun 97	3. REPORT TYPE AND DATES COVERED Final 19 Jan 93-30 Jun 97	
4. TITLE AND SUBTITLE Communications Applications for Deformable Mirror Devices			5. FUNDING NUMBERS F33615-92-C-1120 PE 62204 PR 7662 TA 01 WU 64	
6. AUTHOR(S) Steven C. Gustafson, Gordon R. Little, Troy A. Rhoadarmer, and Theresa A. Tuthill				
7. PERFORMING ORGANIZATION NAME(S) AND ADDRESS(ES) University of Dayton, Research Institute 300 College Park Dayton, OH 45469-0150			8. PERFORMING ORGANIZATION REPORT NUMBER UDR-TR-97-105	
9. SPONSORING / MONITORING AGENCY NAME(S) AND ADDRESS(ES) Avionics Directorate, Wright Laboratory Air Force Materiel Command Wright-Patterson AFB, OH 45433-7623 POC: R. J. Feldmann 937-255-4174			10. SPONSORING / MONITORING AGENCY REPORT NUMBER WL-TR-97-1153	
11. SUPPLEMENTARY NOTES				
12a. DISTRIBUTION / AVAILABILITY STATEMENT Approved for public release distribution is unlimited			12b. DISTRIBUTION CODE	
13. ABSTRACT (Maximum 200 words)  This report reviews a technical effort that accomplished computer simulations and experimental demonstrations of piston-type micromirror arrays for laser beam steering, shaping, and aberration correction, especially simulations and demonstrations with possible relevance for communication applications. The effort successfully investigated the use of micromirror arrays for laser beam manipulations and illustrated both their potential advantages in terms of small size, high ruggedness, and low cost and their potential limitations in terms of small beam steering range and, in particular, low optical efficiency due to inactive inter-micromirror space, lack of tilt control, and diffraction into undesired orders. The report concludes that micromirror arrays could be useful in applications where high optical efficiency is not a priority; otherwise continuous mirrors with micro-mechanical actuation are likely to provide the best fine beam steering and beam shaping or aberration correction performance while retaining the potential advantages of small size, high ruggedness, and low cost.				
14. SUBJECT TERMS Deformable mirrors, optical MEMS, MICROMIRRORS			15. NUMBER OF PAGES 129	
			16. PRICE CODE	
17. SECURITY CLASSIFICATION OF REPORT Unclassified	18. SECURITY CLASSIFICATION OF THIS PAGE Unclassified	19. SECURITY CLASSIFICATION OF ABSTRACT Unclassified	20. LIMITATION OF ABSTRACT UL	

## *TABLE OF CONTENTS*

---

<u>Section</u>	<u>Page</u>
REPORT DOCUMENTATION PAGE.....	i
NOTICE.....	ii
TABLE OF CONTENTS.....	iii
LIST OF FIGURES.....	iv
ACKNOWLEDGEMENTS.....	ix
1. INTRODUCTION.....	1
1.1 Objective and Scope.....	1
1.2 History of the Technical Effort.....	6
1.3 Summary of Accomplishments.....	6
2. MICROMIRROR DESIGNS.....	8
2.1 Basic Micromirror Fabric tion Processes .....	8
2.2 Design and Characteristics of Initial TI Devices .....	10
2.3 Design of MUMPS Devices .....	14
3. MICROMIRROR SIMULATIONS .....	20
3.1 Initial Efforts .....	20
3.2 Far Field Beam Shaping .....	21
3.3 Far Field Beam Shaping in One Dimension .....	23
3.4 Far Field Beam Shaping in Two Dimensions .....	33
4. MICROMIRROR EXPERIMENTS .....	44
4.1 Experiments on Micromirror Characterization .....	44
4.2 Experiments on Micromirror Beam Steering and Shaping .....	51
5. CONCLUSION .....	57
6. REFERENCES .....	59
APPENDIX .....	65

## *LIST OF FIGURES*

<u>Figure</u>	<u>Page</u>
1.1 Schematic illustrating (without the required transition optics) how coherent distorted input light can be converted to coherent corrected output light using an array of micromirror elements, each of which can be individually pistoned (displaced in depth) [after Gustafson, et al., 1995]. .....	
1.2 (a) Subsystem for beam shaping, aberration control, optical control, optical interconnection, and active diffractive optics in general using a micromirror array (here labeled FBM, for flexure beam micromirror). (b) Example system for optical antenna aberration correction [after Gustafson, 1995]. .....	
1.3 General schematic for improving laser communications or laser radar performance using a micromirror array to implement active diffractive optics [after Gustafson, 1997]. .....	
2.1 Illustration of the MUMPS process for the fabrication of micromirrors [after Comtois, et al., 1995]. .....	
2.2 Illustration of a typical piston micromirror element [after Rhoadarmer, et al., 1994]. .....	
2.3 An initial TI piston micromirror device. (a) element detail. (b) 8 by 8 array, where each micromirror is 50 microns wide [after Florence, 1991]. .....	
2.4 Phase (a) and amplitude (b) versus control voltage for one element of the TI device shown in Figure 2.3 [after Florence, 1991]. .....	
2.5 (a) Complex plane plot of the single-micromirror data of Figure 2.4. (b) complex plane plot of vector combinations of this data for two micromirrors [after Rhoadarmer, et al., 1994]. .....	
2.6 (a) Square micromirror and (b) hexagonal micromirror fabricated using MUMPS: each micromirror is 50 microns wide and has flexure hinges two microns wide [after Comtois, 1996]. .....	

## *LIST OF FIGURES (continued)*

<u>Figure</u>	<u>Page</u>
2.7 (a) Detail of an array of hexagonal micromirrors, (b) a complete array of 127 micromirrors; each micromirror is 50 microns wide [after Comtois, 1996].` .....	
2.8 A 127-element hexagonal micromirror array with surrounding address lines [after Comtois. et al., 1996].....	
2.9 (a) An advanced array of 127 hexagonal micromirrors without etch holes and with a removable cover plate. all on a 1 cm square die; (b) detail of the cover plate that masks hinges and intermirror spaces [after Comtois, 1996]. .....	
3.1 (a) Far field irradiance showing diffraction orders due to an array of micromirrors with constant piston positions, (b) this irradiance for piston positions with a linear ramp, showing beam steering [after Rhoadarmer, 1994]. .....	
3.2 (a) Desired uniform beam shape. (b) beam shape obtained after adjusting micromirror piston positions to the correct phase [after Rhoadarmer. et al., 1994]. .....	
3.3 (a) Roughly uniform beam shape obtained using a backpropagation neural network. (b) histogram of rms error obtained for many neural network trials [after Rhoadarmer, 1994].....	
3.4 (a) Nearly uniform beam shape obtained using grid optimization. (b) histogram of rms error obtained for many trials [after Rhoadarmer 1994]. .....	
3.5 Diagram of simulated annealing optimization [after Rhoadarmer, 1994]. .....	
3.6 (a) Nearly uniform beam shape obtained using simulated annealing optimization. (b) histogram of rms error obtained for many trials [after Rhoadarmer, 1994]. .....	

## *LIST OF FIGURES (continued)*

<u>Figure</u>	<u>Page</u>
3.7 (a) Desired uniform beam shape. (b) improved simulated annealing result with rms error 0.029. (c) micromirror voltages that produce this result [after Rhoadarmer, 1994].	
3.8 (a) Desired parabolic beam shape with maximum. (b) simulated annealing result with rms error .0029. (c micromirror voltages that produce this result [after Rhoadarmer, 1994]. .....	
3.9 (a) Desired parabolic beam shape with minimum. (b) simulated annealing result with rms error 0.0031. (c) micromirror voltages that produce this result [after Rhoadarmer, 1994]. .....	
3.10 Beam shape obtained by adding zero-mean Gaussian noise of standard deviation (a) 10 degrees. (b) 20 degrees. and (c) 40 degrees to the phases that yield the near-uniform beam shape of Figure 3.7 [after Rhoadarmer, 1994]. .....	
3.11 Rms error relative to the desired uniform beam shape versus the standard deviation of added Gaussian phase noise [after Rhoadarmer, 1994]. .....	
3.12 Simulated annealing results for achieving a near-uniform beam shape in two dimensions. where the standard deviation of zero-mean Gaussian noise added to each micromirror is (a) degrees. (b) 5 degrees. and (c) 10 degrees [after Rhoadarmer, 1994]. .....	
3.13 (a) Plot proportional to the central portion of the far field irradiance reflected from an array of 127 hexagonal micromirrors for zero micromirror displacement. (b) similar plot for parabolic micromirror displacement [after Gustafson, et al., January 1996]. .....	
3.14 (a) Plot proportional to the far field irradiance reflected from the array of 127 hexagonal micromirrors with zero micromirror displacement. (b) central region of (a). (c) plot proportional to reflected far field irradiance with micromirror displacements optimized to yield as-constant-as-possible irradiance over a circular central region that includes only the central and first side lobes. (d) central region of (c) [after Gustafson, et al., January 1996]. .....	

## *LIST OF FIGURES (continued)*

<u>Figure</u>	<u>Page</u>
3.15 (a) Plot of the minimized quantity $I$ versus percent changes above the optimal phase values for the seven hexagonal rings of micromirrors, (b) as in (a) but for percent change below the optimal phase values [after Gustafson, et al., January 1996]. .....	
3.16 Normalized and radially averaged point spread functions for reflection from a hexagonal micromirror array for (a) solid line: a plane wave reflected from micromirrors with the same piston displacements, (b) dashed line; a quadratically aberrated wave reflected from these micromirrors, and (c) dash-dot line: micromirror piston displacements adjusted to compensate for the quadratic aberration. The peak intensities for (b) and (c) relative to (a) are -2.63 dB and -1.00 dB, respectively [after Roggemann, et al., 1997, used by permission]. .....	
4.1 Interferometric microscope system for micromirror characterization: the dash-dash line is the return reference beam, the dash-dot line is the return object beam, and the objects in the dotted box are perpendicular to the rest of the setup [after Rhoadarmer, et al., 1994]....	
4.2 Deflection in microns versus control voltage $V_a$ using the system of Figure 4.1 for 21 sample positions on an element of the micromirror array of Figure 2.3 [after Rhoadarmer, 1994]. .....	
4.3 Central cross sections of deflection versus control voltage for Figure 4.2. (a) perpendicular to addressing pad of Figure 2.3, (b) parallel to this pad [after Rhoadarmer, 1994]. .....	
4.4 (a) Deflection (one radian is 1.01 micron) versus control (or address) voltage at the center of one element of Figure 2.3 as the voltage is increased and decreased, (b) deflection (one lambda is 632 nm) versus control voltage at many positions: the solid curve is mean deflection [after Rhoadarmer, 1994]. .....	
4.5 Improved interference microscope system for micromirror characterization [after Michalick, et al., 1995]. .....	



## *LIST OF FIGURES (continued)*

<u>Figure</u>	<u>Page</u>
4.6 (a) Center deflection versus voltage for square and hexagonal micromirrors of the sort shown in Figure 2.6: the area A and spring constant k for each micromirror is indicated. (b) center deflection versus voltage for seven nominally identical hexagonal micromirrors [after Michalick. et al., 1995]. .....	
4.7 (a) Optical system design for micromirror array (or DMD) interfacing [after Gustafson. et al., August 1993], (b) experimental arrangement used to investigate micromirror array beam steering and shaping [after Gustafson. et al., October 1996]. .....	
4.8 Effects of bias voltage on the far-field intensity for a hexagonal array of 127 micromirrors as in Figure 2.8: the potential applied to each micromirror is (a) 0 volts. (b) 20 volts. and (c) 30 volts [after Gustafson. et al., October 1996]. .....	
4.9 Central maximum beam steering and shaping for a hexagonal array of 127 micromirrors as in Figure 2.8: (a) all micromirrors at 24 volts. (b) beam steering due to a stepped linear ramp pattern from 20 to 29.6 volts, where the pattern steps 0.8 volts between each of the 13 array rows. (c) beam shaping due to a quadratic hexagonal ring pattern from 20 to 27.2 volts, where the pattern follows $V(i) = 20 + (i-1)^2/5$ , $i = 1, 2, \dots, 7$ , for each of the seven array hexagonal rings with $i = 1$ at the center [after Gustafson. et al., October 1996].	
4.10 (a) Improved experimental system used to investigate micromirror array aberration correction. (b) radially averaged far field intensity versus distance from the central maximum using this system for an uncorrected (aberrated) and a corrected beam reflected from a hexagonal micromirror array as in Figure 2.8 [after Roggemann. et al., 1997, used by permission].	

## **ACKNOWLEDGEMENTS**

Since Texas Instruments was unable to deliver micromirror devices suitable for the breadboard demonstrations, the contributions of the Air Force Institute of Technology (AFIT) in designing and monitoring the fabrication of devices that proved to be eminently suitable was critical. In particular, the competence and enthusiasm of Dr. Victor Bright, Dr. Michael Roggemann, and Dr. Byron Welsh and their graduate students, especially Adrian Michalicek, John Comtois, Shawn Hick, and Peter Roberts, were essential to the success of the technical effort.

Troy Rhoadarmer, who completed his Master's Thesis through exceptionally intelligent and thorough contributions to the project, was a delight to work with both professionally and personally. Finally, Rick Shute and Bob Feldmann, the Air Force engineers most cognizant of the technical effort, were very helpful and also a pleasure to work with.

## **1. INTRODUCTION**

This section presents objective and scope, reviews the history of the technical effort, and summarizes accomplishments.

### **1.1 Objective and Scope**

The objective of the technical effort was to develop and demonstrate piston-type micromirror arrays for laser beam manipulations (including steering, shaping, and aberration correction) in laser communication applications.

Free-space laser communication is needed for exceptionally selective and high-bandwidth information transmission between stations that are in rapid relative motion, e.g., aircraft or satellite stations relative to each other or relative to ground stations. Such communication requires rapid laser beam steering and shaping and, typically, compensation for aberrations due to atmospheric turbulence.

Appropriate beam steering, shaping, and aberration correction may be implemented using lenses and mirrors that are mechanically adjusted in real time by electric motors or piezoelectric actuators. However, to reduce mechanical complexity and improve reliability, and thus realize savings in size, weight, and cost, macroscopic mechanical adjustments must be eliminated or at least restricted to coarse alignments.

Deformable mirrors that are key elements in adaptive optical systems [e.g., Tyson, 1991; Welsh and Gardner, 1989] may be used for beam steering, shaping, and aberration correction. These mirrors may be continuously deformable ("rubber") or they may be segmented, consisting of discrete elements whose depth and/or tilt can be varied in real time. Until recently, laser communications research [e.g., Begley, 1991] and adaptive optics research have not interacted significantly due to the large size, poor ruggedness, and high cost of the usual macro-mechanical deformable mirrors. This situation has changed, largely due to the recent availability of micro-mechanical deformable mirrors that can, in principle, avoid all of these limitations and which typically have a much

larger number of elements. Figure 1.1 shows, in schematic form and without the required transition optics, how coherent distorted input light can be transformed into corrected output light using an array of micromirror elements, each of which can be individually varied in depth (pistoned) over at least one half wavelength so that comprehensive phase modulation can be achieved.

If the segmented mirror elements are macroscopic, the depth (piston) and tilt of each element can be controlled independently at the expense of increased mechanical complexity and lack of ruggedness. However, if the mirror elements are microscopic (on the order of 100 microns wide or less), then the piston and effective tilt or phase and amplitude for each element is typically determined by a single control voltage, and independent control is not possible. Except for the lack of independent phase and amplitude control for each element, aspects of which have been discussed by several researchers [e.g., Cohen, 1992; Horner and Gianino, 1992], and for the lack of a 100% fill factor (i.e., the array has nonreflecting space between mirrors), micromirror array designs are extremely desirable for laser communications because of their small size, large number of elements, high degree of ruggedness, and potential low cost.

Figure 1.2(a) shows a general subsystem for beam shaping, aberration control, and, more generally, for implementing active diffractive optics. Here the use of a standard polarizing beam splitter and quarter wave plate permits nearly lossless transition to and from the reflective array. Active diffractive optical systems enabled by micromirror array technology could have wide spread and important applications, such as real-time aberration correction for high-resolution video systems. Figure 1.2(b) shows an example optical antenna system [Brown, 1991] that incorporates a micromirror array for aberration correction. Figure 1.3 shows a general schematic that incorporates a micromirror array to improve laser communication or laser radar performance.

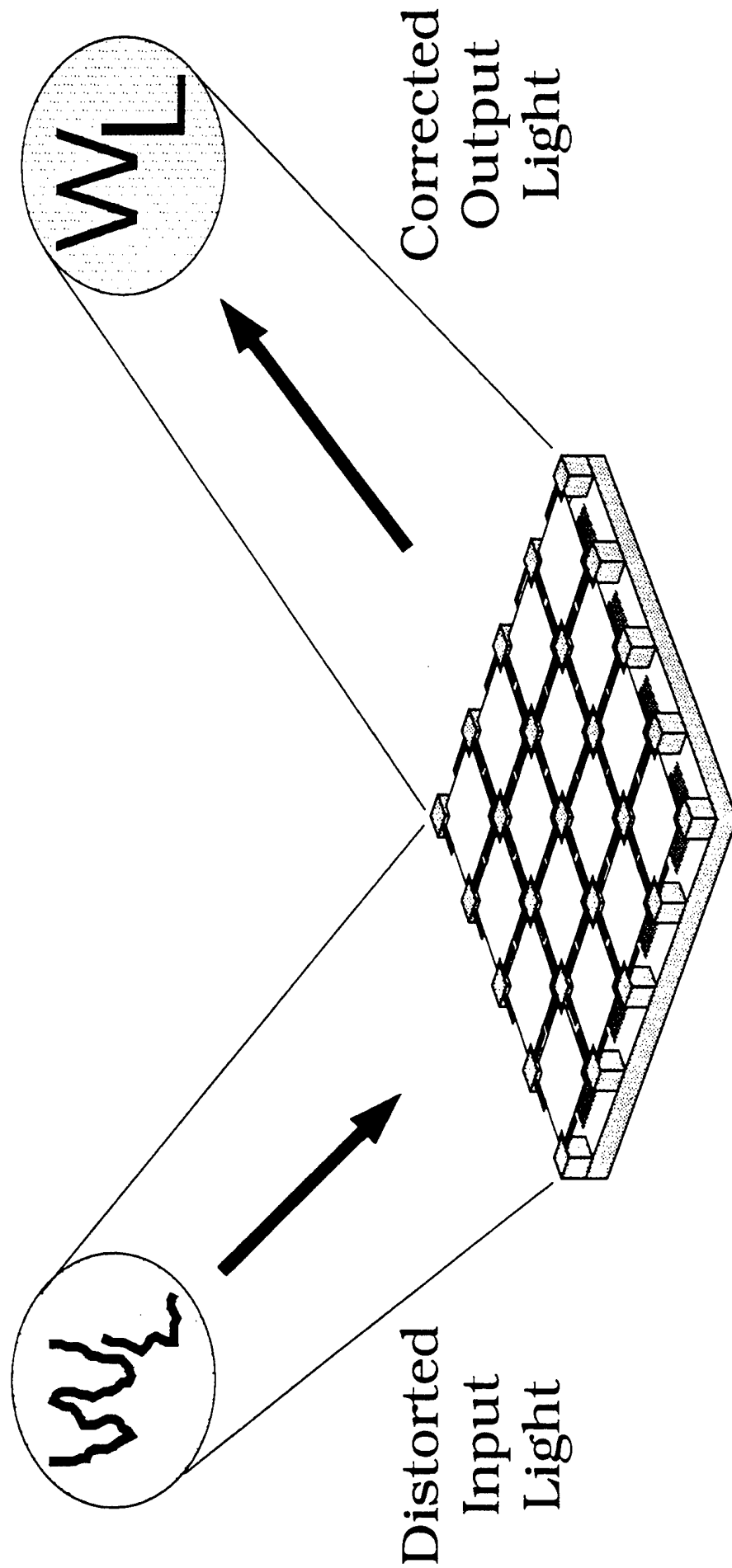


Figure 1.1. Schematic illustrating (without the required transition optics) how coherent distorted input light can be converted to coherent corrected output light using an array of micromirror elements, each of which can be individually pistoned (displaced in depth) [after Gustafson, et al., 1995].

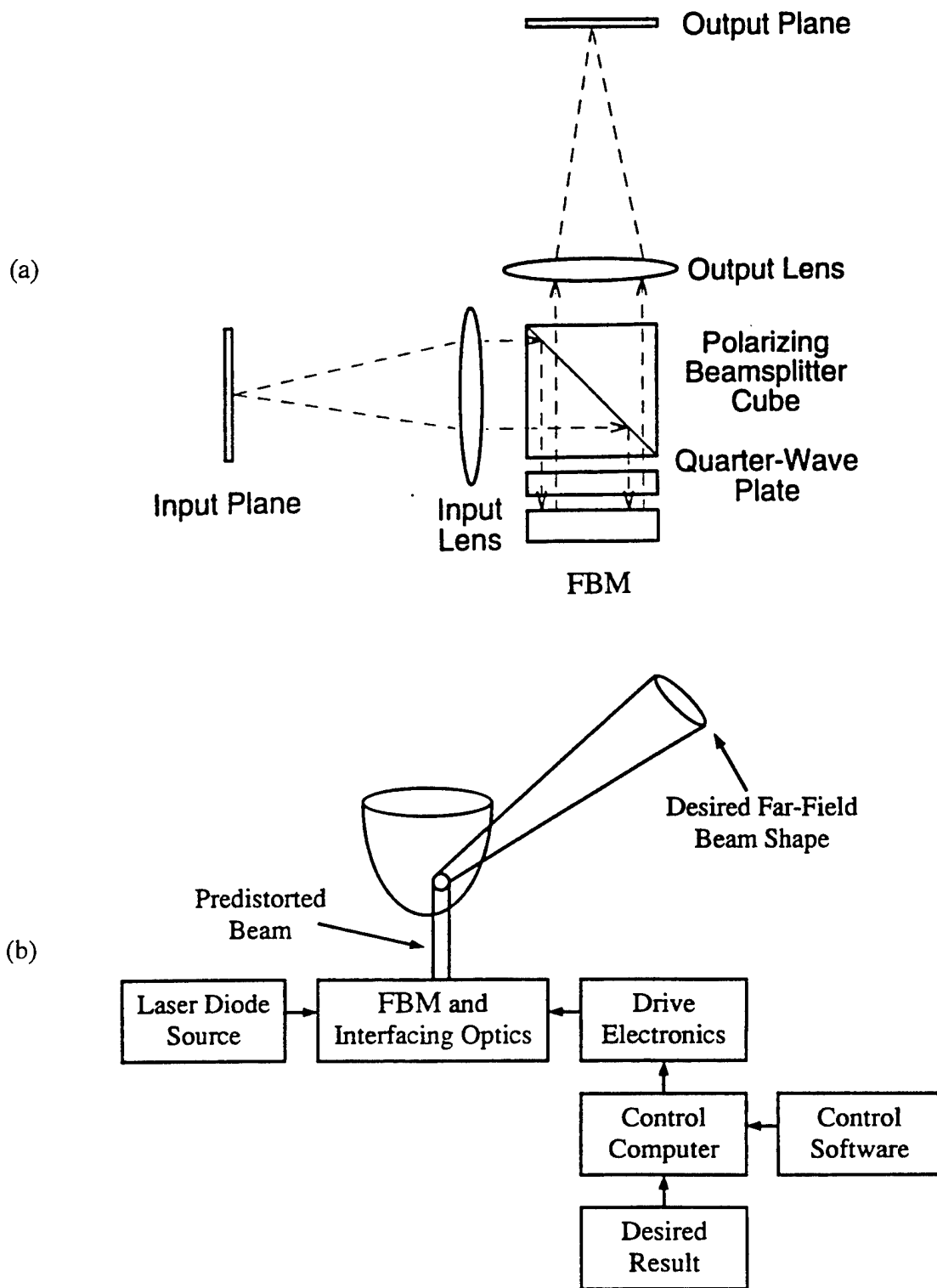
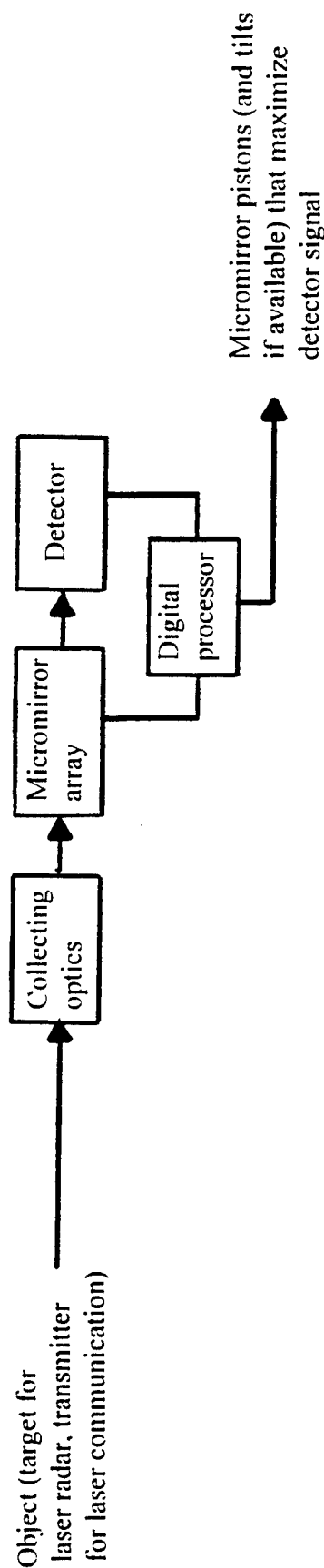


Figure 1.2. (a) Subsystem for beam shaping, aberration control, optical interconnection, and active diffractive optics in general using a micromirror array (here labeled FBM, for flexure beam micromirror), (b) Example system for optical antenna aberration correction [after Gustafson, 1995].



Detector	Micromirror Array	Digital Processor
<ul style="list-style-type: none"> <li>• Conventional point detector or</li> <li>• Advanced point detector E.g., optical parametric amplifier using periodically polled lithium niobate, erbium doped fiber amplifier, etc.</li> <li>• Wave front sensor array and one of the above</li> </ul>	<ul style="list-style-type: none"> <li>• Direct address small array E.g., 16 by 16 array of 30 micron square micromirrors with lenslet interfacing and binary or analog piston actuation</li> <li>• Indirect address large array E.g., 256 by 256 array of micromirrors with underlying CCD addressing electronics</li> </ul>	<ul style="list-style-type: none"> <li>• Inputs feedback from point detector (and wave front sensor if present) to optimize micromirror array pistons (and tilts if available)</li> <li>• Outputs micromirror pistons (and tilts if available) that maximize detector signal</li> </ul>

Figure 1.3. General schematic for improving laser communications or laser radar performance using a micromirror array to implement active diffractive optics [after Gustafson, 1997].

## **1.2 History of the Technical Effort**

The technical effort began 19 January 1993. The Preliminary Design Review was held on 4 August 1993, and the Critical Design Review was held on 18 July 1995. Written authorization to proceed with breadboard demonstrations was given on 26 July 1995, and these demonstrations were presented with increasing degrees of sophistication between October 1995 and December 1996.

Two key anticipated contributors to the technical effort (in accord with their attachments to the original proposal) were the Air Force Institute of Technology (AFIT) and Texas Instruments, Inc. (TI). The AFIT contribution was particularly significant in that (1) a majority of the technical effort was performed at The Adaptive Optics Laboratory operated by AFIT and located at Wright-Patterson AFB and in that (2) AFIT performed the layout design of many types of micromirror arrays, including the arrays used in the breadboard demonstrations, and monitored their fabrication by the DARPA-supported MUMPS (Multi-User MEMS (Micro-Electro-Mechanical System) Processing System) foundry. The TI contribution in terms of the provision of micromirror devices to the Government for use in the effort was critically hindered by business priorities that favored the development of tilting-type rather than piston-type devices. Thus, despite no-cost time extensions no devices suitable for use in the breadboard demonstrations were delivered by TI. However, the AFIT contribution ultimately compensated for this problem.

## **1.3 Summary of Accomplishments**

The technical effort successfully demonstrated the use of micromirror arrays for laser beam manipulations and illustrated (1) their advantages in terms of potential small size, high ruggedness, and low cost, and (2) their limitations in terms of small beam steering range and, in particular, low efficiency due to inactive inter-mirror space, lack of tilt control, and diffraction into undesired orders.



The effort directly resulted in six articles published in proceedings of professional meetings [Rhoadarmer, et al., April 1994; Rhoadarmer, et al., July 1994; Comtois, et al., October 1995; Gustafson, et al., January 1996, Gustafson, et al., October 1996; Gustafson, et al., March 1997] plus a Master of Science Thesis [Rhoadarmer, May 1994], and an Invention Disclosure [Gustafson, et al., June 1994]. The effort indirectly resulted in numerous additional publications, among the most significant of which is a paper that describes micromirror simulation and experimental work at AFIT [Roggemann, et al., 1997]. This paper includes comprehensive and well executed extensions of the effort reported here.

## **2. MICROMIRROR DESIGNS**

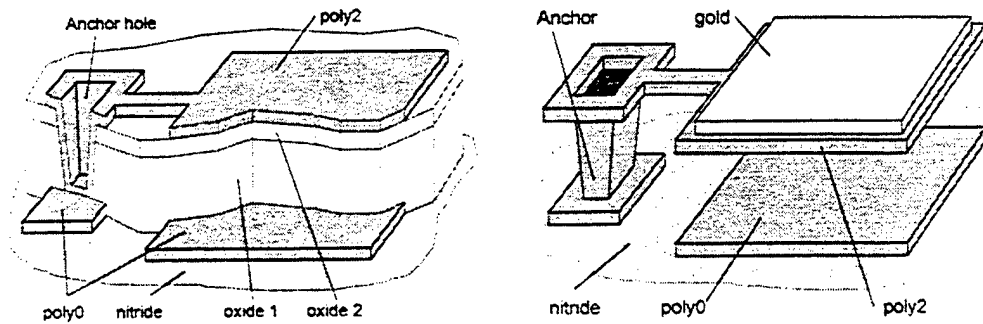
This section considers the design and fabrication of micromirror devices that may be appropriate for communications applications. In particular, design and fabrication efforts by TI and design efforts by the AFIT with fabrication by MUMPS are reviewed.

### **2.1 Basic Micromirror Fabrication Processes**

Figure 2.1(a) illustrates the MUMPS process, which involves the three-layer surface-micromachining of polysilicon. The lowest polysilicon layer (poly0) is non-releasable and is used for address electrodes and local wiring. The upper two polysilicon layers (poly1 and poly2) can be released to form mechanical devices; release is achieved by etching away the two layers of phosphosilicate glass (referred to as 'oxide' layers) that are deposited between the polysilicon layers. Gold may be deposited on top of the poly2 layer to form reflective surfaces, low resistance wiring, and bond pads.

The polysilicon and oxide layers are individually patterned, and unwanted material from each layer is removed by reactive ion etching before the next layer is added. The polysilicon layers are annealed at 1100°C to relieve stress and to diffuse phosphorus in from the surrounding oxide layers to make the polysilicon conductive. The polysilicon layers conform closely to the topology of the previously deposited and patterned layers, and this induced topology can have detrimental effects on the uniformity of the reflective surfaces and flexure hinges.

The polysilicon and oxide layers are built up over a silicon nitride layer which insulates them from a conductive n-doped silicon substrate. The layers are illustrated in Figure 2.1 for a simple device consisting of a metallized mirror with one flexure anchored to one support post. Note that this design does not use the poly1 layer, which would be located between the two oxide layers. The left portion of the Figure shows a cross-section of the device prior to metallization. After fabrication, the sacrificial oxide layers are etched away to release the mechanical polysilicon layers. The right portion of the



Material Layer	Thickness ( $\mu\text{m}$ )	Stress (MPa)	Resistivity ( $\Omega\text{-cm}$ )
poly0	0.52	19.7 compressive	$1.84 \times 10^{-3}$
poly1	2.0220	5.1 compressive	$2.58 \times 10^{-3}$
poly2	1.5650	5.1 compressive	$2.72 \times 10^{-3}$
metal (Cr/Au)	0.5540	$\sim 30$ tensile	$3.39 \times 10^{-6}$
silicon nitride	0.6213	19.2 compressive	-
oxide 1	2.0151	-	-
oxide 2	0.5230	-	-

Figure 2.1. Illustration of the MUMPS process for the fabrication of micromirrors [after Comtois, et al., 1995].

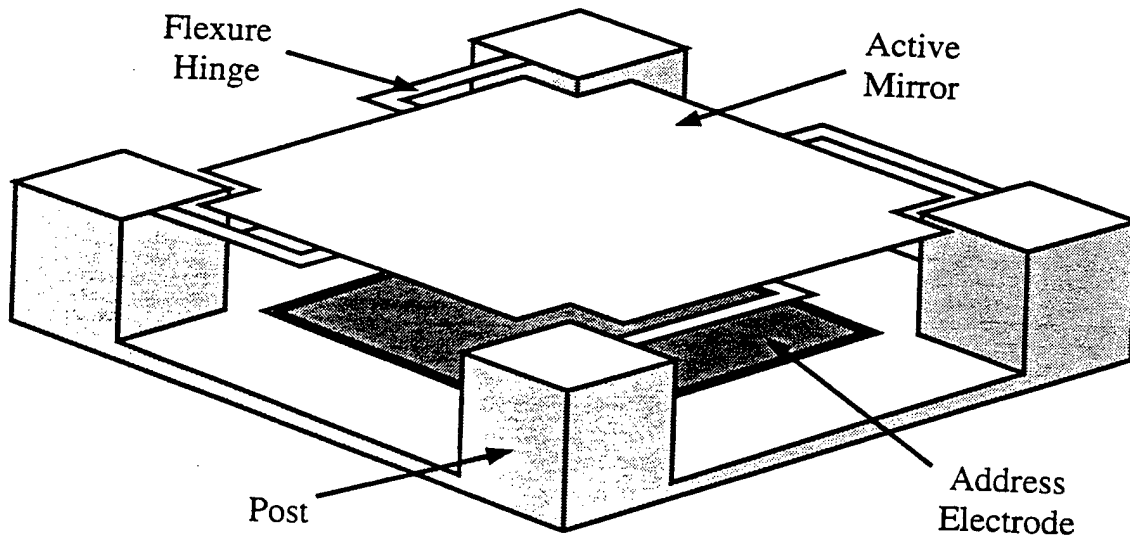


Figure 2.2. Illustration of a typical piston micromirror element [after Rhoadarmer, et al., 1994].

Figure shows the final structure after the sacrificial material has been removed. The bottom portion of the Figure lists typical layer properties.

Figure 2.2 illustrates a typical micromirror element for which flexure hinges permit mostly piston-like displacement. With fabrication using the MUMPS process the mirror is gold-coated polysilicon; with fabrication using the proprietary TI process the mirror is entirely metal (aluminum). Note that a conducting address electrode under the mirror enables the required electrostatic actuation.

## **2.2 Design and Characteristics of Initial TI Devices**

An initial TI device consisting of an 8 by 8 array of square micromirrors with 50 micron maximum extent is shown in Figure 2.3. It was used in some of the experiments described in Section 4; also, its characteristics were used in some of the simulations described in Section 3. Figure 2.4 shows phase and amplitude versus address voltage as measured by TI for a single element. Here the phase variation is due to piston displacement at a Helium-Neon laser 632 nm wavelength, and the amplitude variation is largely due to constructive and destructive interference between the reflective and nonreflective portions of the element (about 75% of the element is reflective). Figure 2.5(a) is a complex-plane plot of this phase and amplitude data: if the element was an ideal piston mirror the plot would be a circle of unit radius centered on the origin. Figure 2.5(b) is a complex plane plot of the vector combination of two elements; note that two (or more) elements form a "superpixel" that permits access to a large portion of the complex plane inside the origin-centered unit circle. Finally, below are some anticipated characteristics of a 256 by 256 array of square piston micromirrors that was to be fabricated using TI processes [e.g., Lin, 1994]:

- 256 x 256 phase-mostly pixels
- 37.5 x 37.5 micron pixel size
- 10 microsecond pixel response time

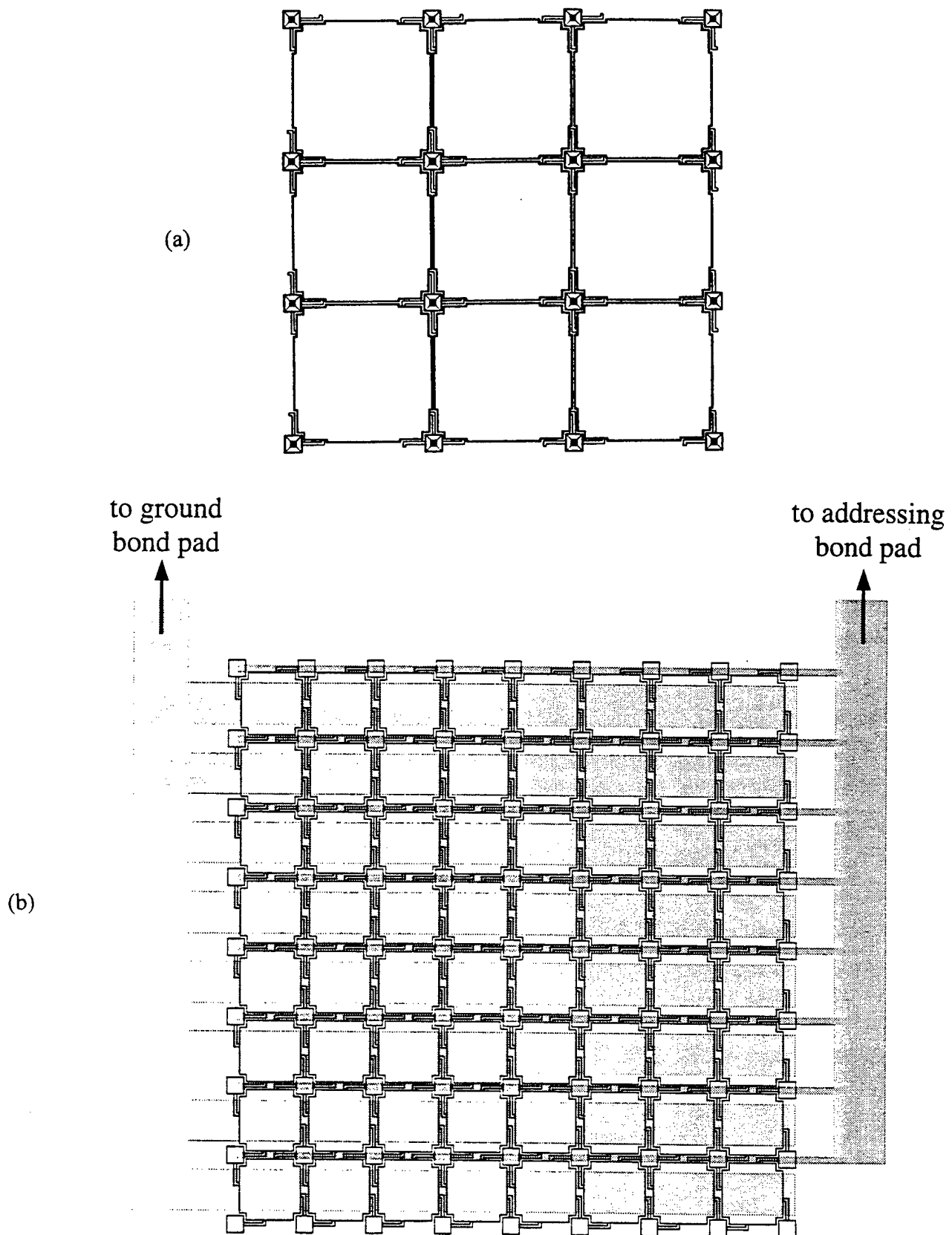


Figure 2.3. An initial TI piston micromirror device, (a) element detail, (b) 8 by 8 array, where each micromirror is 50 microns wide [after Florence, 1991].

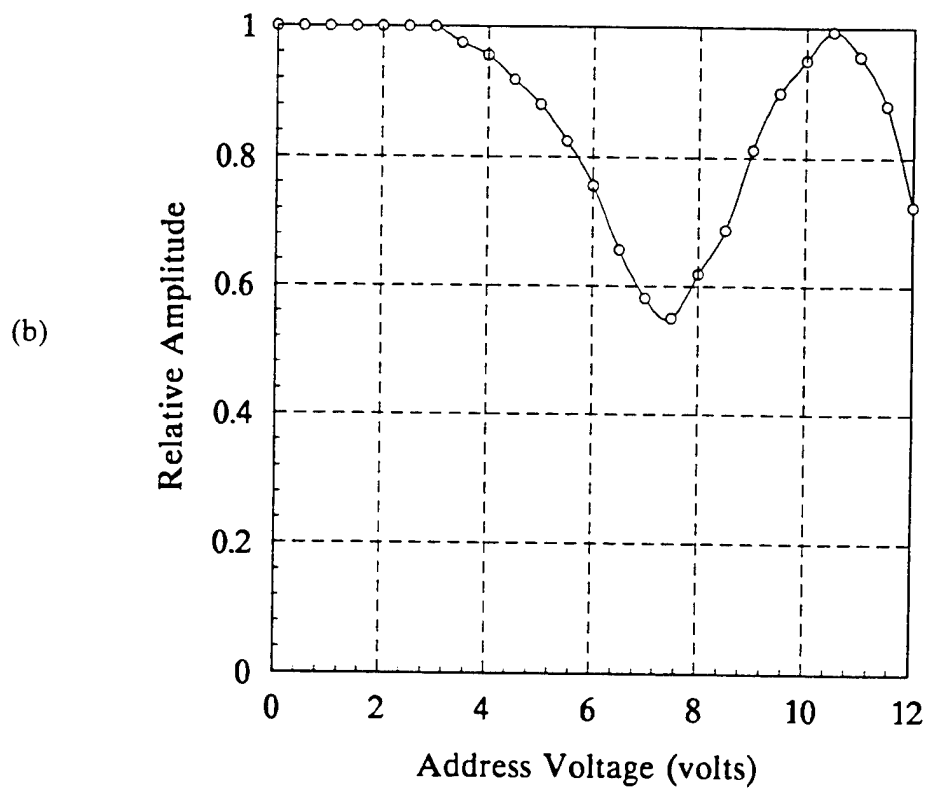
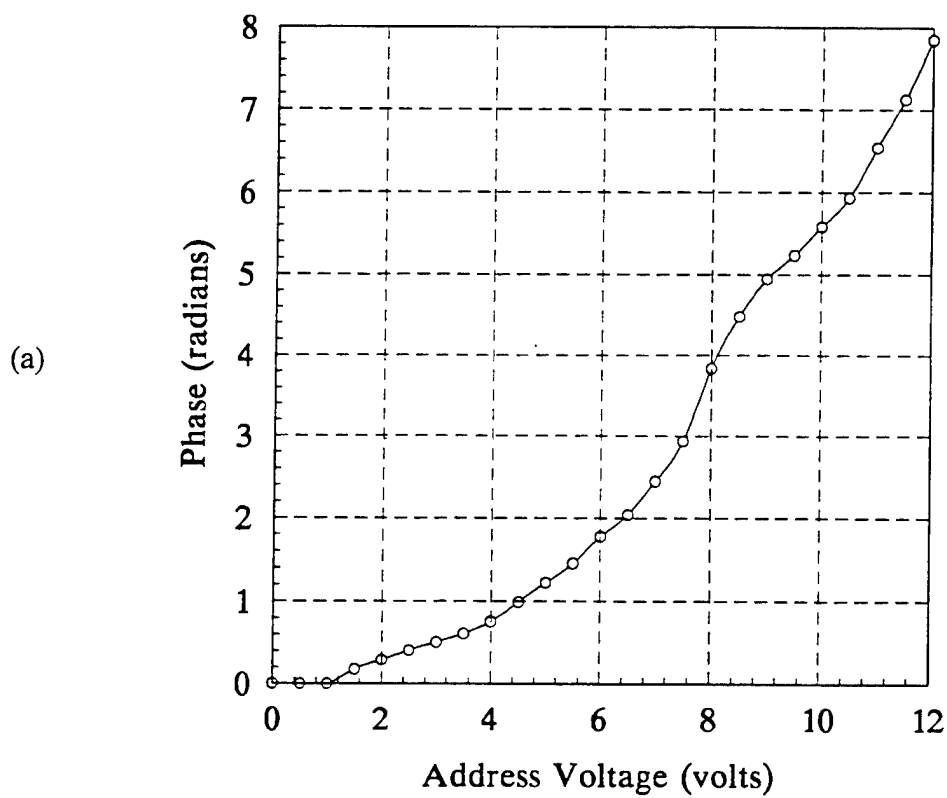


Figure 2.4. Phase (a) and amplitude (b) versus control voltage for one element of the TI device shown in Figure 2.3 [after Florence, 1991].

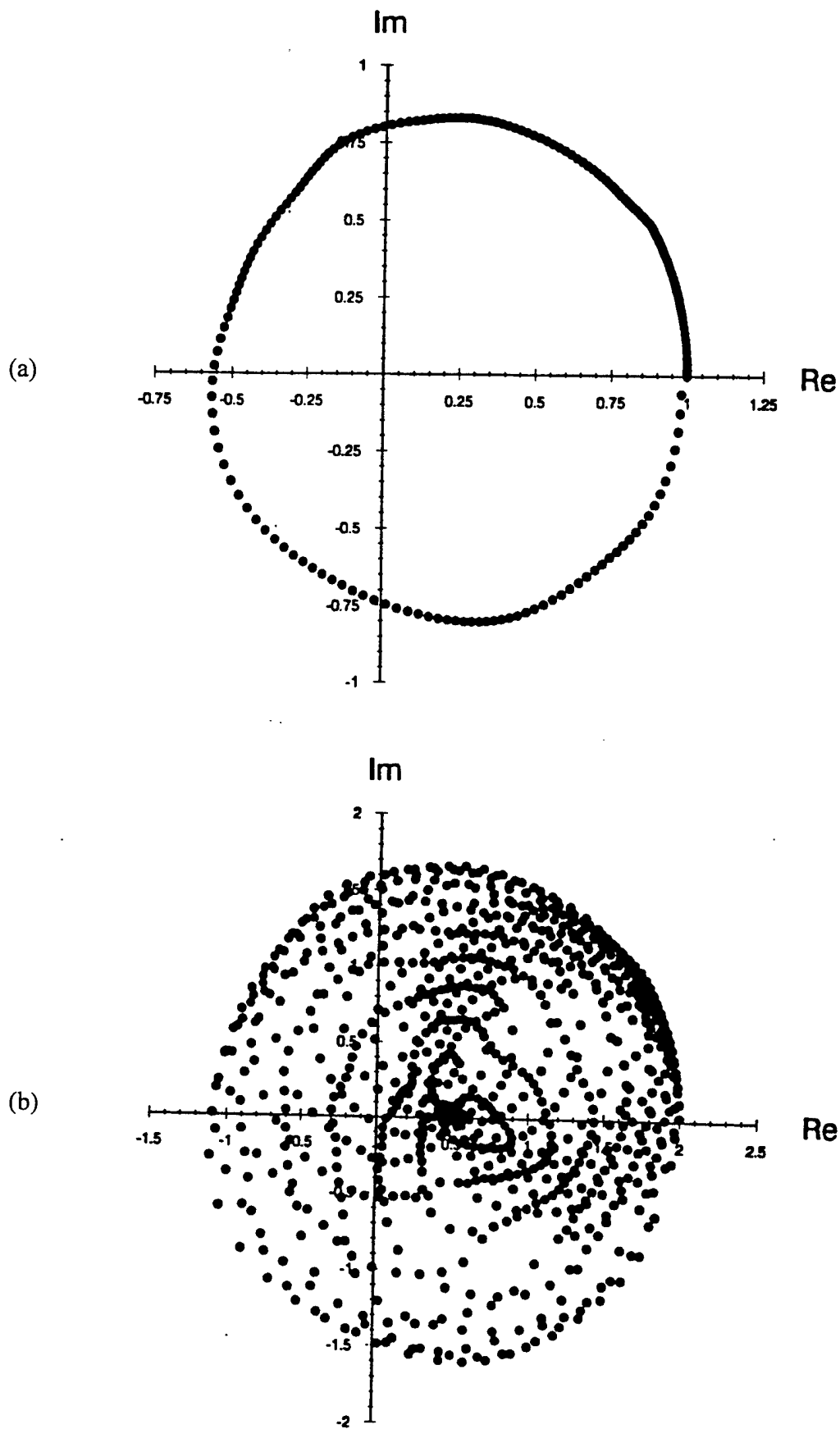


Figure 2.5. (a) Complex plane plot of the single-micromirror data of Figure 2.4, (b) complex plane plot of vector combinations of this data for two micromirrors [after Rhoadarmer, et al., 1994].

- 5 kHz device frame rate
- $2\pi$  radian or greater pixel phase range (at 632 nm)
- 7 bit pixel phase resolution
- 70% or greater optical efficiency (active reflective area)
- 2 to 14 volt random-access CMOS control

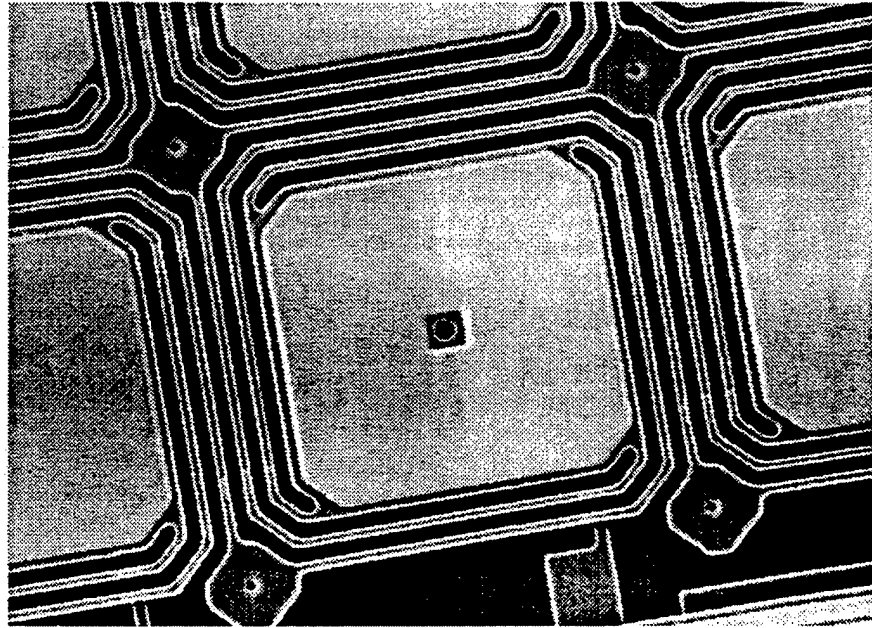
### 2.3 Design of MUMPS Devices

Figure 2.6(a) shows a square micromirror fabricated using MUMPS. Note that each flexure hinge extends around two sides of the micromirror; this long-hinge design permits the use of lower voltages to achieve a given piston displacement and can reduce stresses that adversely affect mirror flatness. A hexagonal micromirror also fabricated using MUMPS is shown in Figure 2.6(b); this design has three instead of four hinges to further reduce the voltage required to achieve a given displacement, and the hexagonal geometry can enable higher mirror packing density and thus reduce inactive inter-mirror space. The desirable characteristics of the hexagonal micromirror design have been detailed in an invention disclosure [Gustafson, et al., June 1994]. Both the square and hexagonal micromirrors are 50 microns wide and have two micron wide flexure hinges. Both also have a central etch hole that facilitates removal of the sacrificial oxide layer beneath the mirror, although this hole was later found to be unnecessary for micromirrors less than 100 microns wide.

Figure 2.7(a) shows details of an array of hexagonal micromirrors, and (b) shows a complete array of 127 micromirrors. Each micromirror in (b) is 50 microns wide, and the distance between adjacent micromirror centers is 75 microns. Figure 2.8 shows a complete array with surrounding significant portions of the address lines included. Finally, Figure 2.9(a) shows an advanced array of 127 hexagonal micromirrors, each 100 microns wide, that have no etch holes and that are arranged at an angle to the address lines to improve hinge width uniformity. This array can be covered by a plate with



(a)



(b)

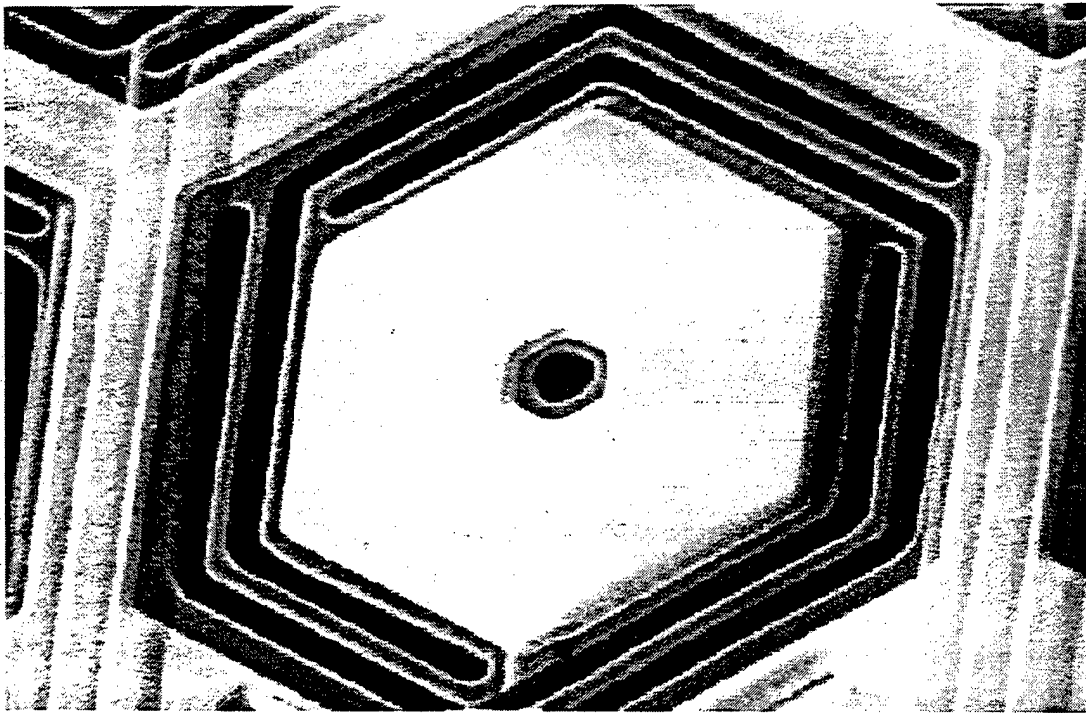


Figure 2.6. (a) Square micromirror and (b) hexagonal micromirror fabricated using MUMPS: each micromirror is 50 microns wide and has flexure hinges two microns wide [after Comtois, 1996].

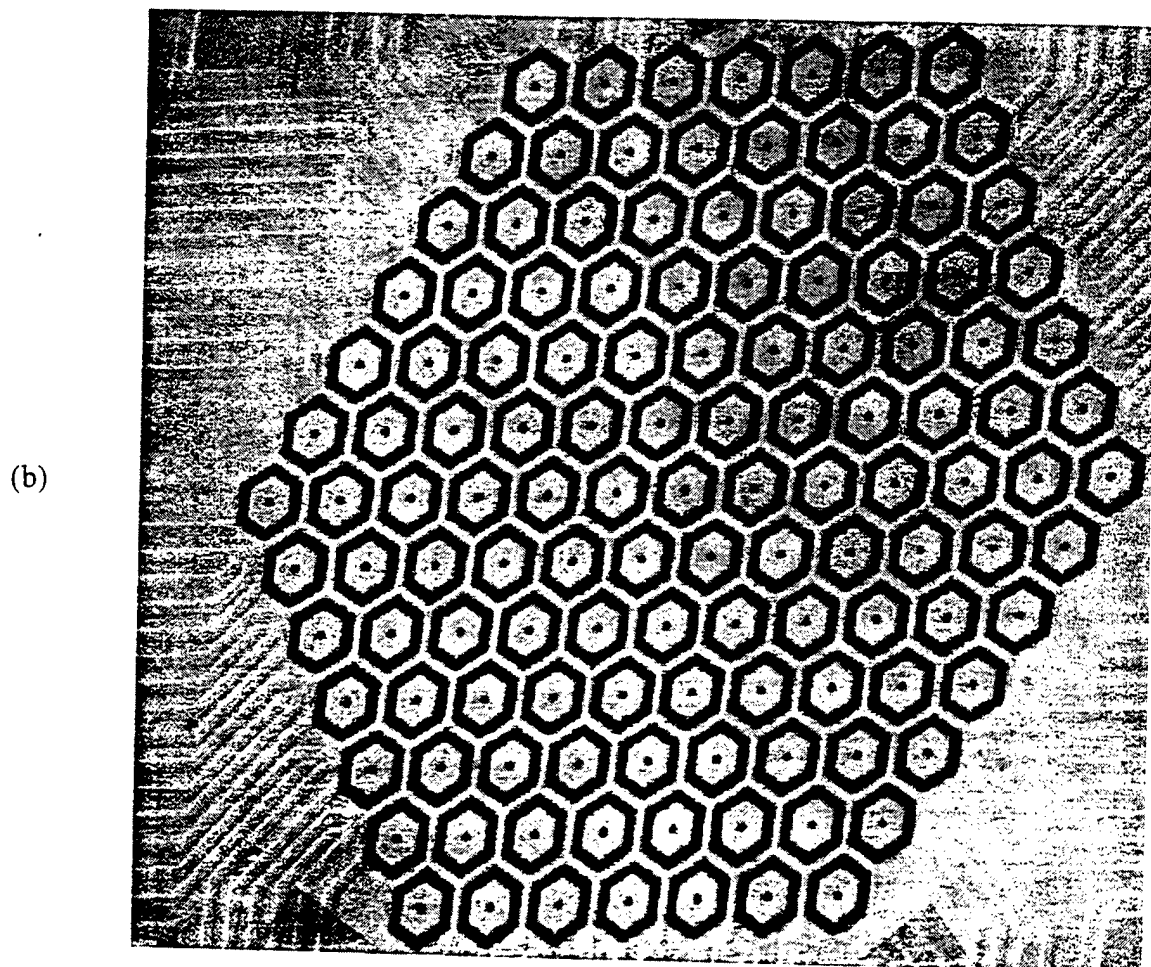
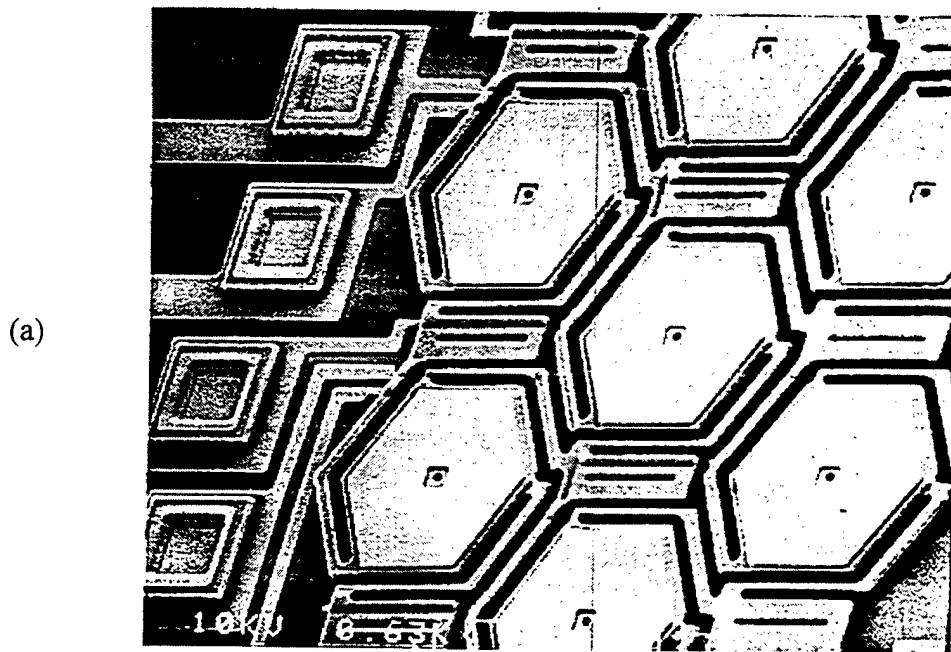


Figure 2.7. (a) Detail of an array of hexagonal micromirrors, (b) a complete array of 127 micromirrors; each micromirror is 50 microns wide [after Comtois, 1996].

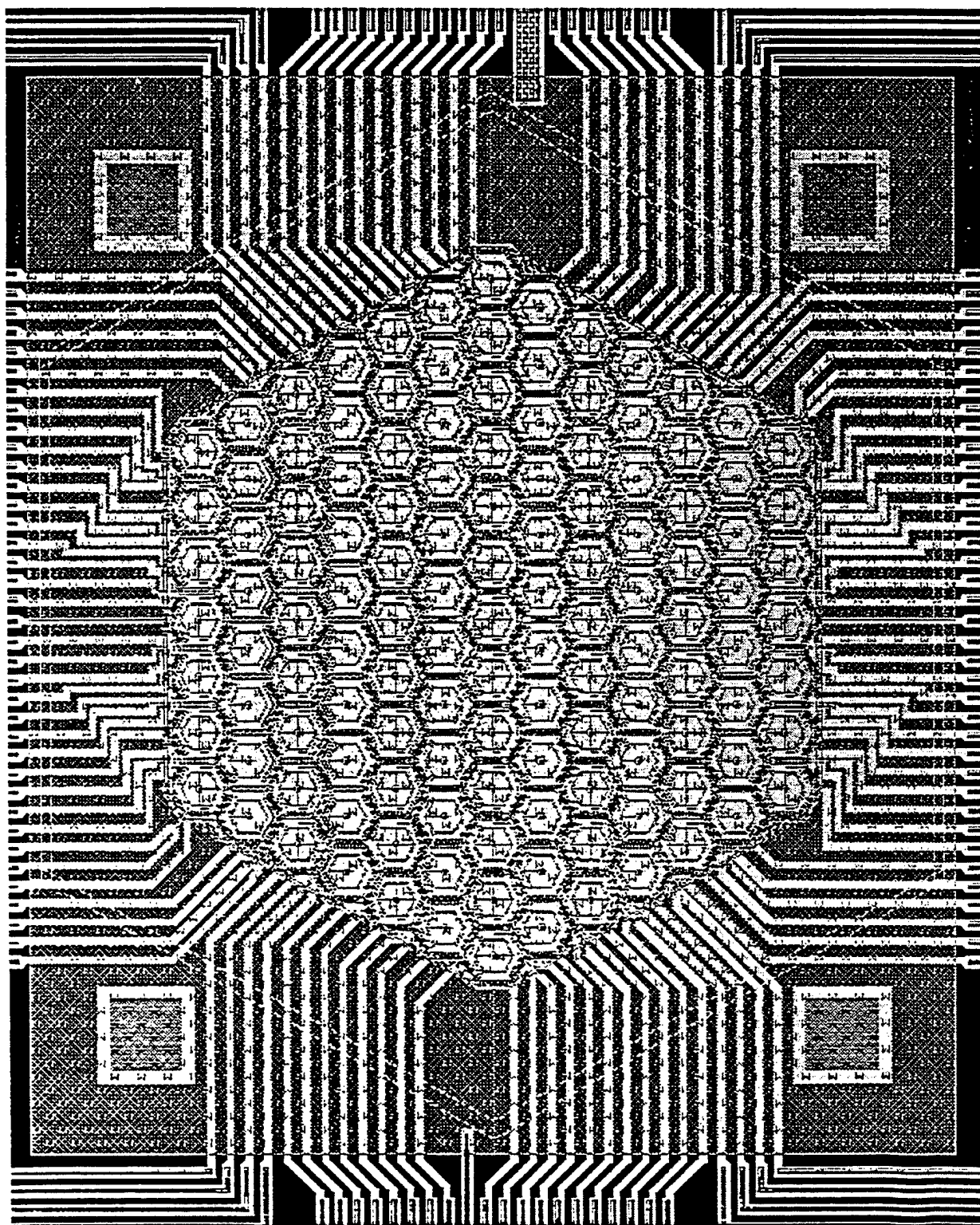


Figure 2.8. A 127-element hexagonal micromirror array with surrounding address lines  
[after Comtois, et al., 1996].

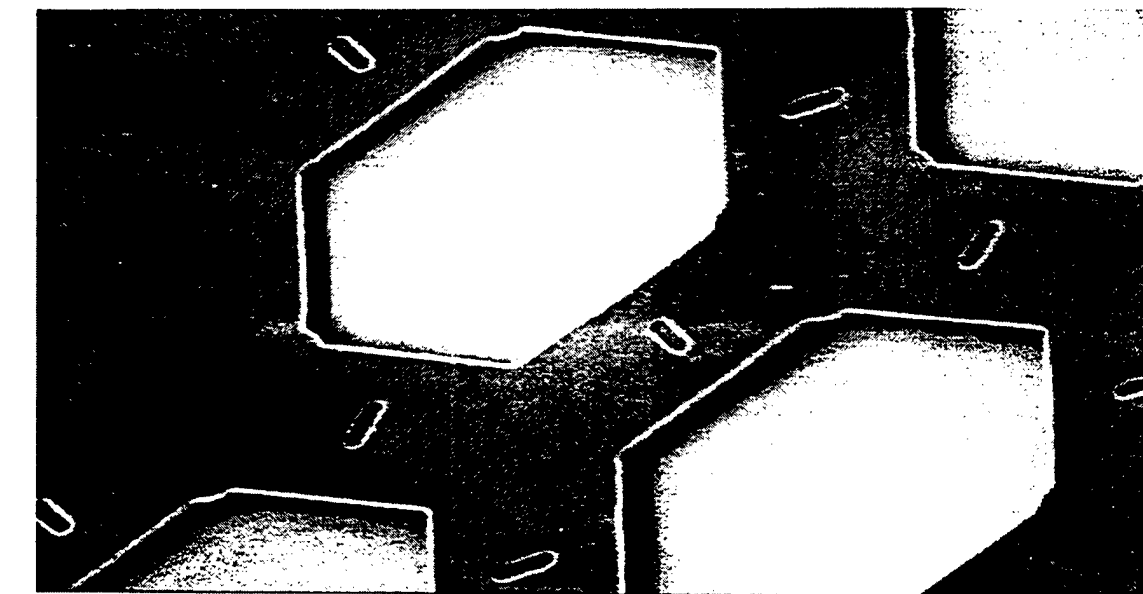
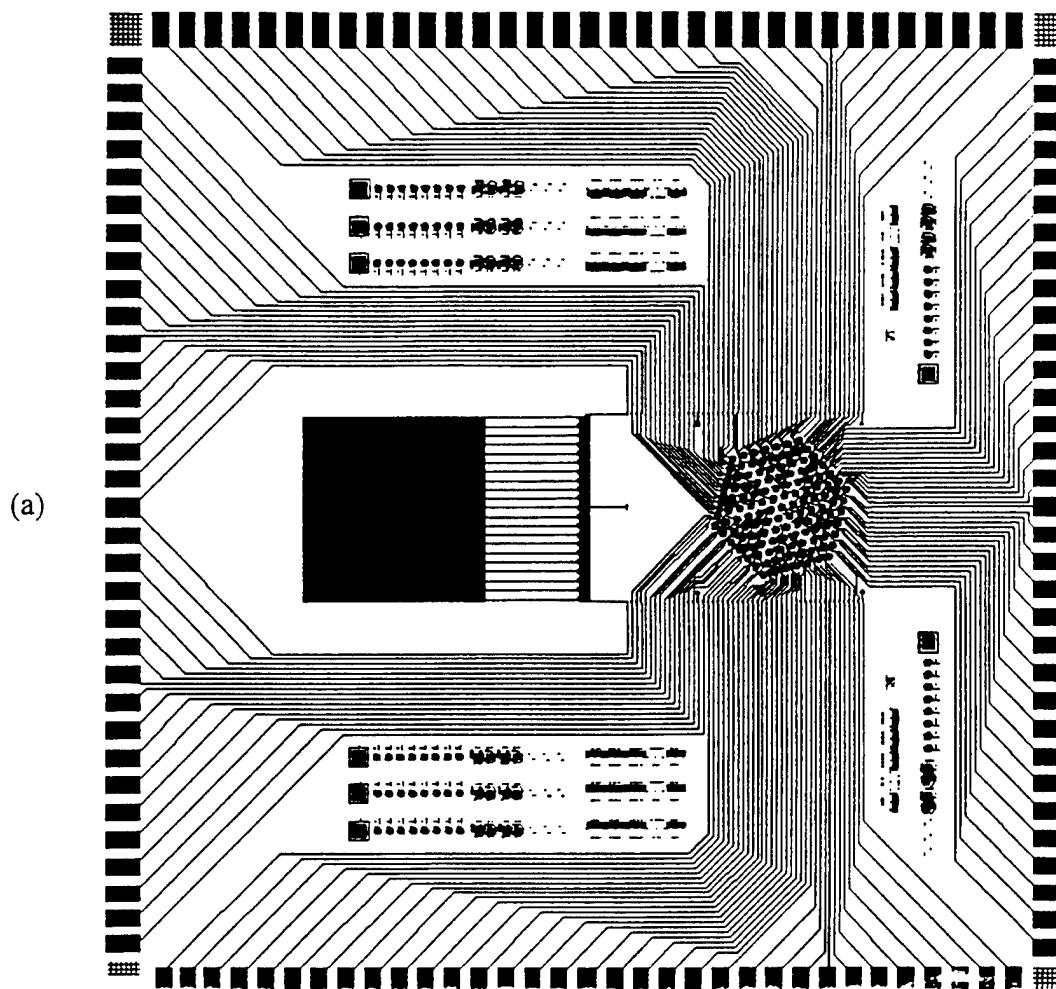


Figure 2.9. (a) An advanced array of 127 hexagonal micromirrors without etch holes and with a removable cover plate, all on a 1 cm square die; (b) detail of the cover plate that masks hinges and intermirror spaces [after Comtois, 1996].

hexagonal holes, shown in detail in Figure 2.9(b), so that the hinges and the inactive intermirror space are masked. In (a) the mask is the large dark square; it is rotated on long hinges until it rests on support posts in a plane parallel to and a few microns above the micromirrors.

### **3. MICROMIRROR SIMULATIONS**

This section considers micromirror simulations that may be appropriate for communications applications. In particular, determining the micromirror control voltages that produce desired laser beam steering and shaping functions are reviewed.

#### **3.1 Initial Efforts**

Initial efforts focused on developing techniques for determining the micromirror element voltages that yield desired beam shapes. In principle, for a sufficiently large number of elements, any well-behaved (e.g., devoid of discontinuity) far field beam shape (in both intensity and phase) may be produced for each diffraction order using coherent illumination [Rhoadarmer and Gustafson, 1992]. Also, given measured element phase and amplitude values versus voltage as in Figure 2.4 for a typical piston-type element, the far field beam shape may be readily found by Fourier transforming these values for any pattern of voltages applied to an array. However, the inverse problem, determining the address voltages that produce (as nearly as possible) a desired beam steering and shape, is extremely difficult because phase and amplitude cannot be controlled independently and their relationship to address voltage is nonlinear. A direct solution to the problem would require the simultaneous solution of as many nonlinear equations in as many unknowns as mirror elements. However, this solution is unfeasible because the number of mirror elements required for adequate beam steering and shaping may be 10,000 or more.

One solution to this problem, inspired in part by previous work [e.g., Sandler, et al., 1991; Suzuki, 1991], is as follows. First, neural network training data is generated by computing far field diffraction patterns for a large number of randomly selected address voltages. Next, a basis function neural network is trained on this data to produce interpolating or approximating surfaces, where diffraction pattern samples are inputs, address voltages are outputs, and there is a different surface for each output. Finally, the address voltages for any desired far field diffraction pattern (i.e., beam steering and shape) are obtained from the surfaces.

Here each basis function neural network interpolation and extrapolation surface is developed by specifying nonlinear functions relative to each set of inputs and forming a linear combination of these functions that generates the corresponding outputs. For extrapolation the nonlinear functions must decrease with distance (as is the case for Gaussian functions). Radial basis function interpolation and extrapolation is implemented by specifying radially symmetric basis functions centered on each set of inputs. Basis function techniques are the only computationally viable choice for interpolating or extrapolating large numbers of data points with scattered data input sets (as opposed to regularly spaced sets), since they are the only techniques for which linear (as opposed to nonlinear) simultaneous equation solving dominates the computation as the number of data points increases [e.g., Poggio and Girosi, 1990, Gustafson, et al., 1992].

### **3.2 Far Field Beam Steering**

Figure 3.1 displays computer simulations in one dimension of the far field irradiance reflected from a piston-type micromirror array illuminated with collimated coherent light. This irradiance pattern may be observed, for example, by a receiver located at a sufficiently large distance from a transmitter in a laser communication system if the transmitter employs a micromirror array for beam steering, shaping, or aberration correction.

Since the array consists of a regularly-spaced finite group of small objects, the far field irradiance, which is proportional to the squared magnitude of the Fourier transform of the array, is an array of narrow functions (of width inversely proportional to the size of the array) multiplied by a wide envelope function (of width inversely proportional to the size of the mirrors). Here the array of narrow functions identifies diffraction orders (a zero order beam, a pair of first order beams, etc.). Each narrow function is the Fourier transform of the array pattern, and the wide envelope function is the Fourier transform of an individual mirror.

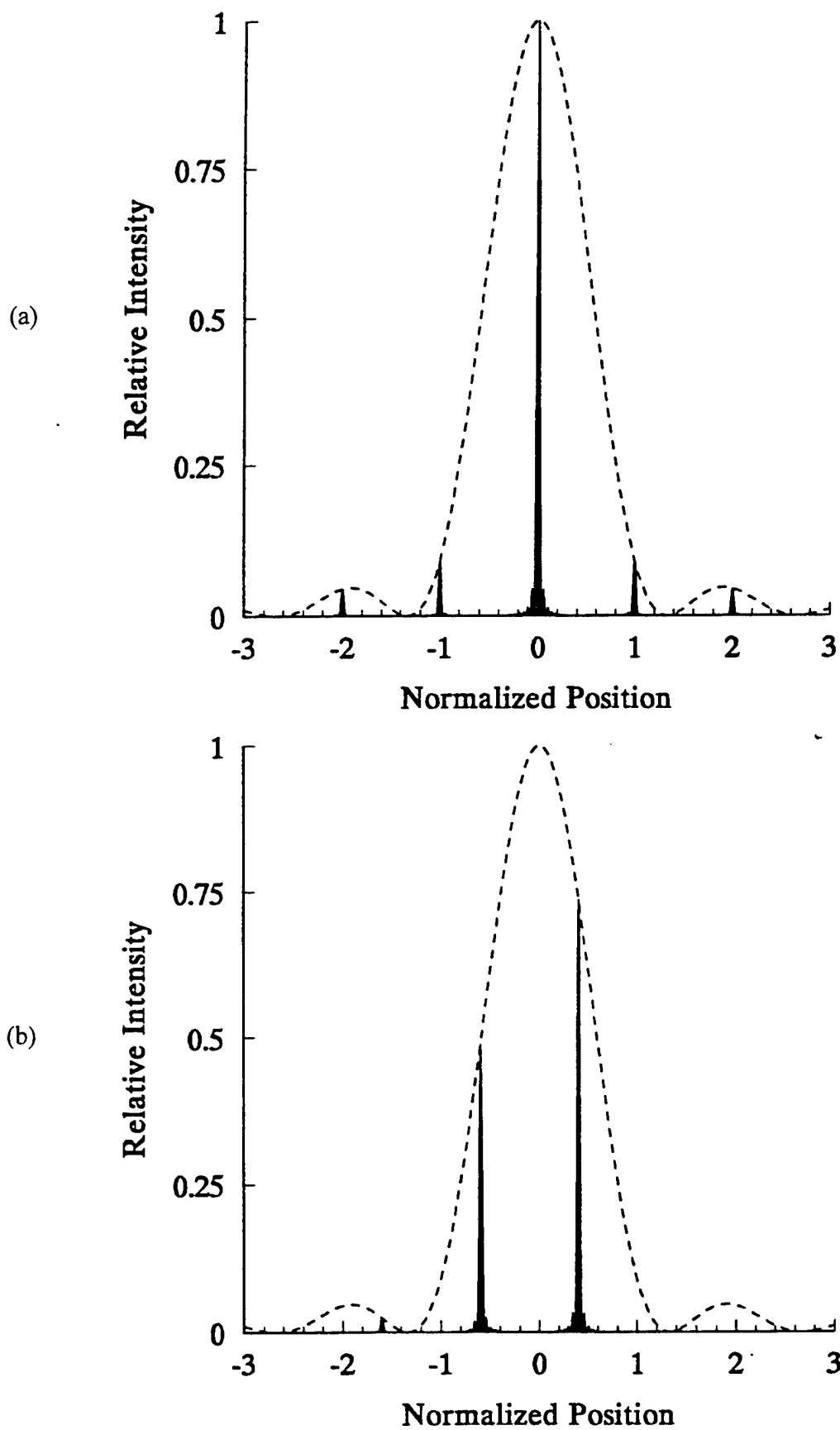


Figure 3.1. (a) Far field irradiance showing diffraction orders due to an array of micromirrors with constant piston positions, (b) this irradiance for piston positions with a linear ramp, showing beam steering [after Rhoadarmer, 1994].



In Figure 3.1(a) each micromirror has the same position (or control voltage), whereas in Figure 3.1(b) the element positions have a linear ramp so that there is a constant phase shift between adjacent elements. The result of this linear phase ramp is that the diffraction orders are displaced or “steered” within the wide envelope such that the steering angle is a continuous linear function of the slope of the ramp. Efficiency may be improved by increasing the irradiance in some diffraction orders (at the expense of others) using control voltages that perturb the ramp. This technique is analogous to the blazing methods used to improve the efficiency of diffraction gratings[e.g., McManamon, et al., 1996]. However, the maximum angular range over which any diffraction order may be steered is approximately the ratio of the wavelength to the separation of adjacent mirrors, and if this separation is 50 microns and the wavelength is 0.5 microns, then the maximum steering range is 10 milliradians or about one-half degree.

### **3.2 Far Field Beam Shaping In One Dimension**

Figure 3.2(a) shows a desired uniform beam shape (one of many possible or desired shapes) in the far field, where the irradiance is sampled at 64 points. The square root of the irradiance of the sample points is taken to obtain real amplitudes at these points, and these amplitudes are Fourier transformed to obtain the desired amplitude and phase at each micromirror array element. Each array element has a single control voltage, and thus the amplitude and phase at each element cannot be precisely the desired values. Since phase generally has more significant effects than amplitude [Oppenheim and Lim, 1981] because phase appears in the exponent of a complex-valued wavefront representation, the control voltages are initially adjusted to yield the correct phase at each element. Figure 3.2(b), which is the squared magnitude of the Fourier transform after this initial adjustment and is thus proportional to the observed far field irradiance, is not close to the desired uniform beam shape.

The control voltages must be therefore further adjusted, which may be accomplished using the same gradient descent optimization technique used in the standard training procedure for backpropagation neural networks [e.g., Wasserman,

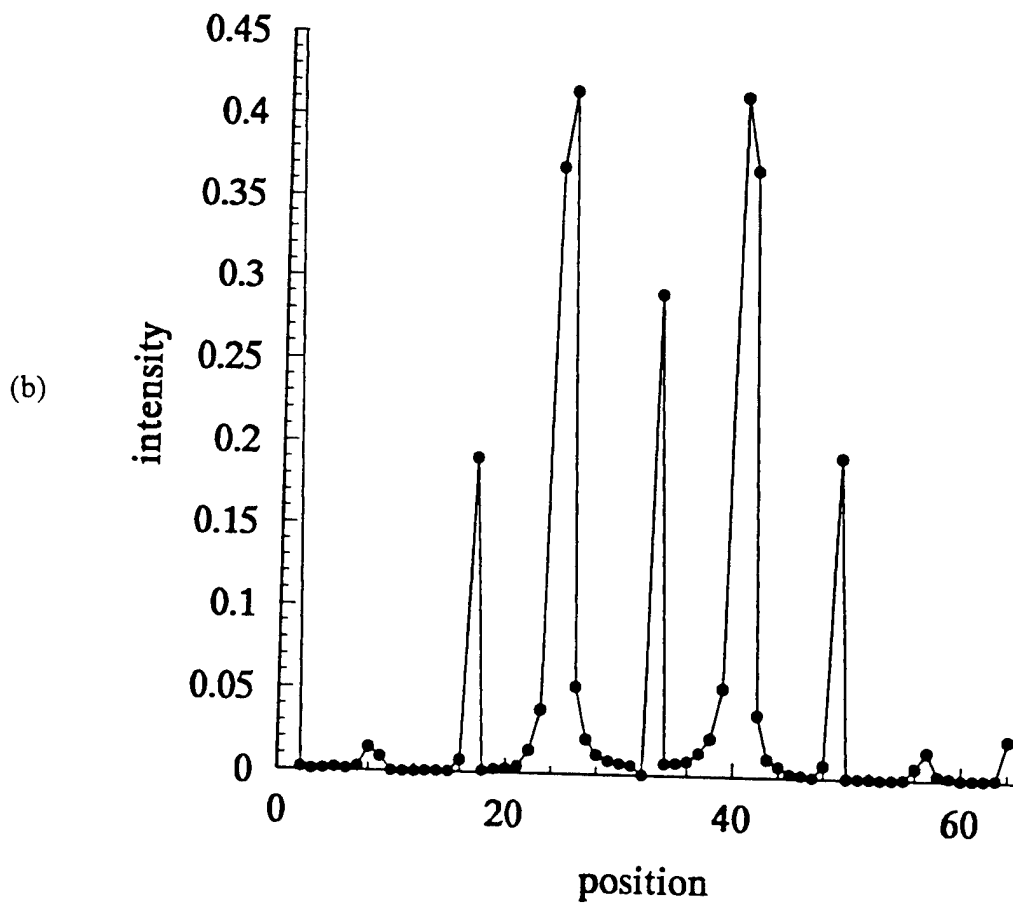
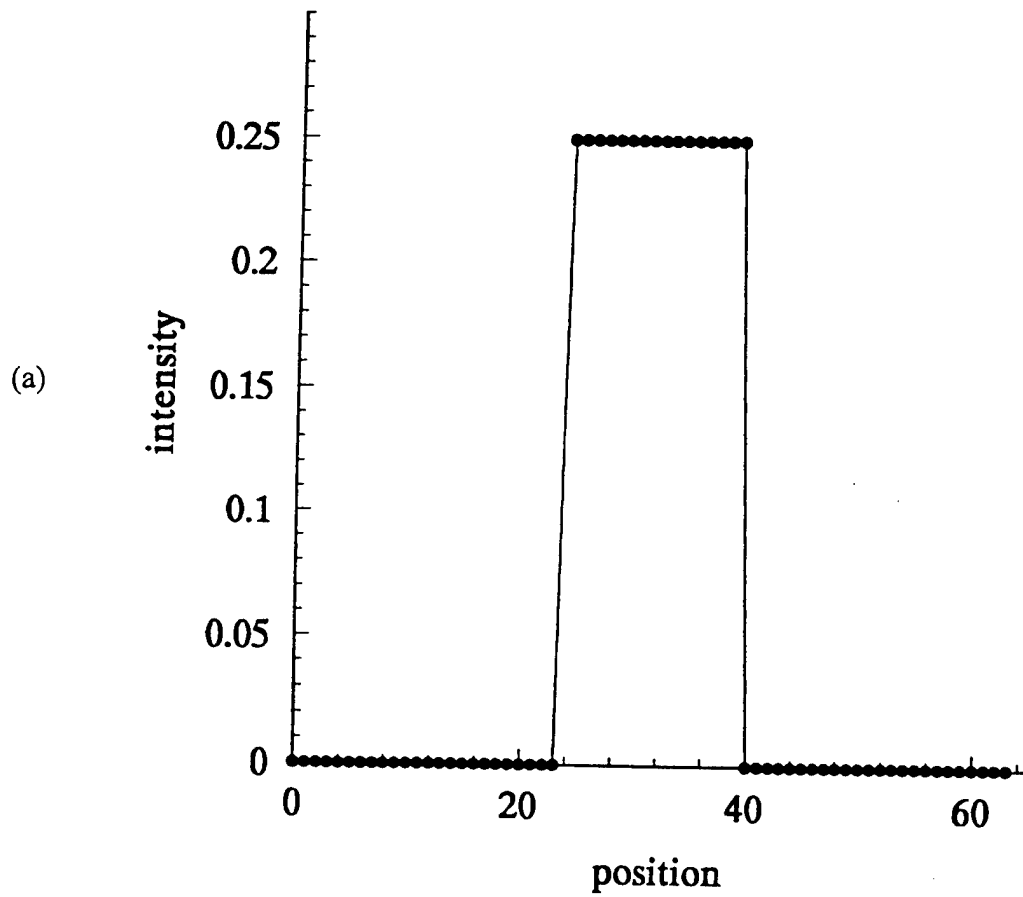


Figure 3.2. (a) Desired uniform beam shape, (b) beam shape obtained after adjusting micromirror piston positions to the correct phase [after Rhoadarmer, et al., 1994].

1989]. The optimization is performed so as to minimize the rms error (the square root of the mean of the sum of the squares of the differences) between the actual and desired beam shape at the 64 irradiance sample points. Figure 3.3(a), which is the squared magnitude of the Fourier transform after the final gradient descent adjustment, is roughly the desired beam shape, although the histogram of Figure 3.3(b) shows that many trials may be needed to achieve this result. Other optimization techniques may be used; Figure 3.4(a) shows the improved beam shape that results from a more exhaustive grid optimization, and the histogram of Figure 3.4(b) indicates that many trials may also be needed to achieve this result.

Among the most robust optimization techniques is simulated annealing [Press, et al., 1992], for which a diagram is shown in Figure 3.5. Here one micromirror element is randomly selected and its control voltage is changed. The change is adapted with probability  $1/(1 + \exp(C/T))$ , where  $C$  is the change in rms error and  $T$  is a parameter called temperature. This process is repeated for all micromirrors and for small decreases in  $T$  until the rms error is acceptable; if the decreases in  $T$  are sufficiently small, a globally optimal result is guaranteed at  $T = 0$ . Figure 3.6 shows that simulated annealing yields the beam shape with the smallest rms error relative to the desired uniform beam shape.

Figure 3.7 shows an improved simulated annealing result for a near-uniform beam shape (i.e., the rms error relative to the desired uniform shape is 0.0029 rather than 0.0057 as in Figure 3.6), and it also shows that the micromirror voltages that produce this result do not form a smooth pattern. Figure 3.8 shows a simulated annealing result for a near-parabolic beam shape: the desired shape is a parabola with a maximum equidistant from the same zeros used for the uniform beam shape and with the same area as this shape. Figure 3.9 is similar to Figure 3.8 except that the desired shape is a parabola with a minimum. For both parabolic shapes the Figures show that the micromirror voltages again do not form a smooth pattern.

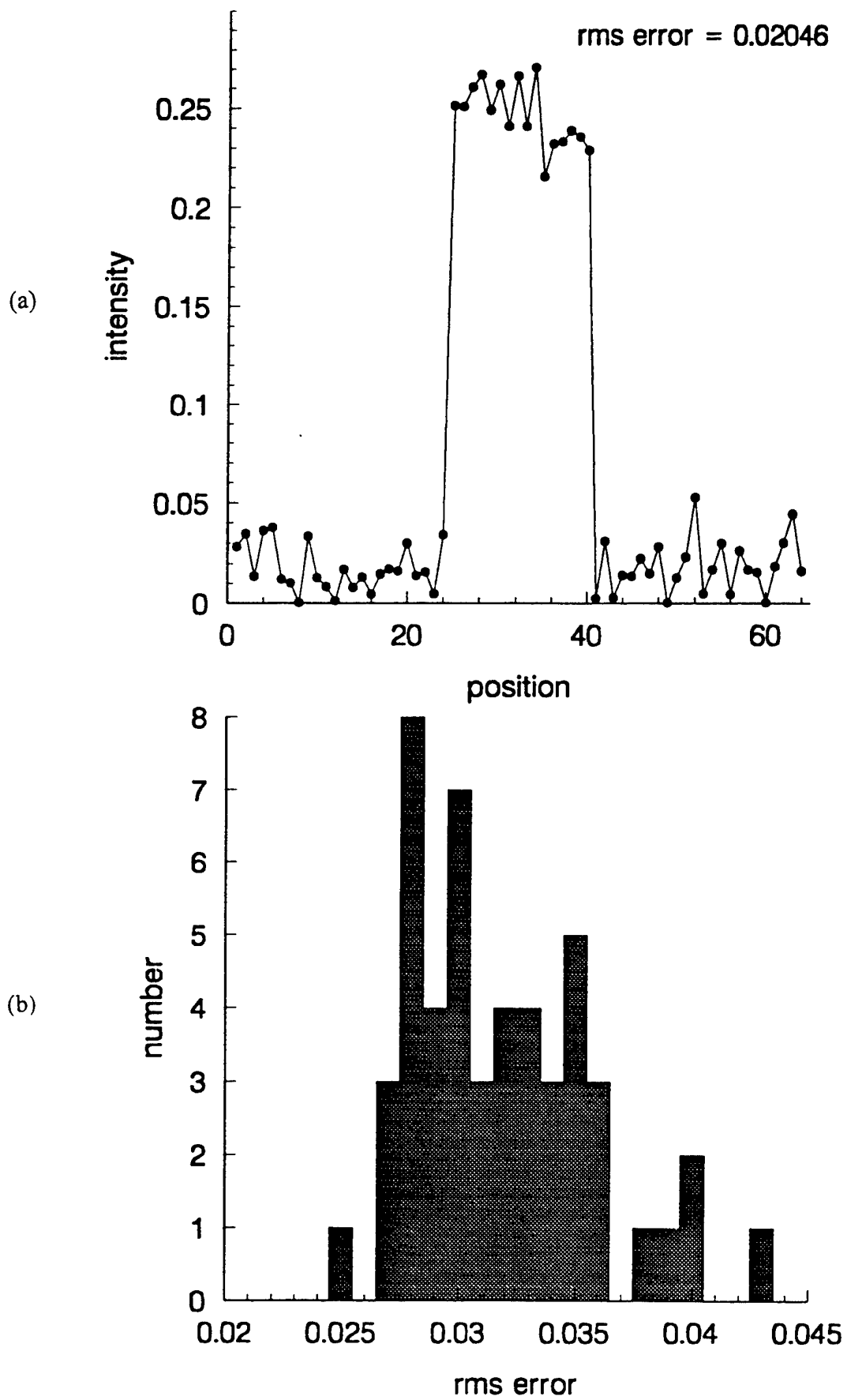


Figure 3.3. (a) Roughly uniform beam shape obtained using a backpropagation neural network. (b) histogram of rms error obtained for many neural network trials [after Rhoadarmer, 1994].

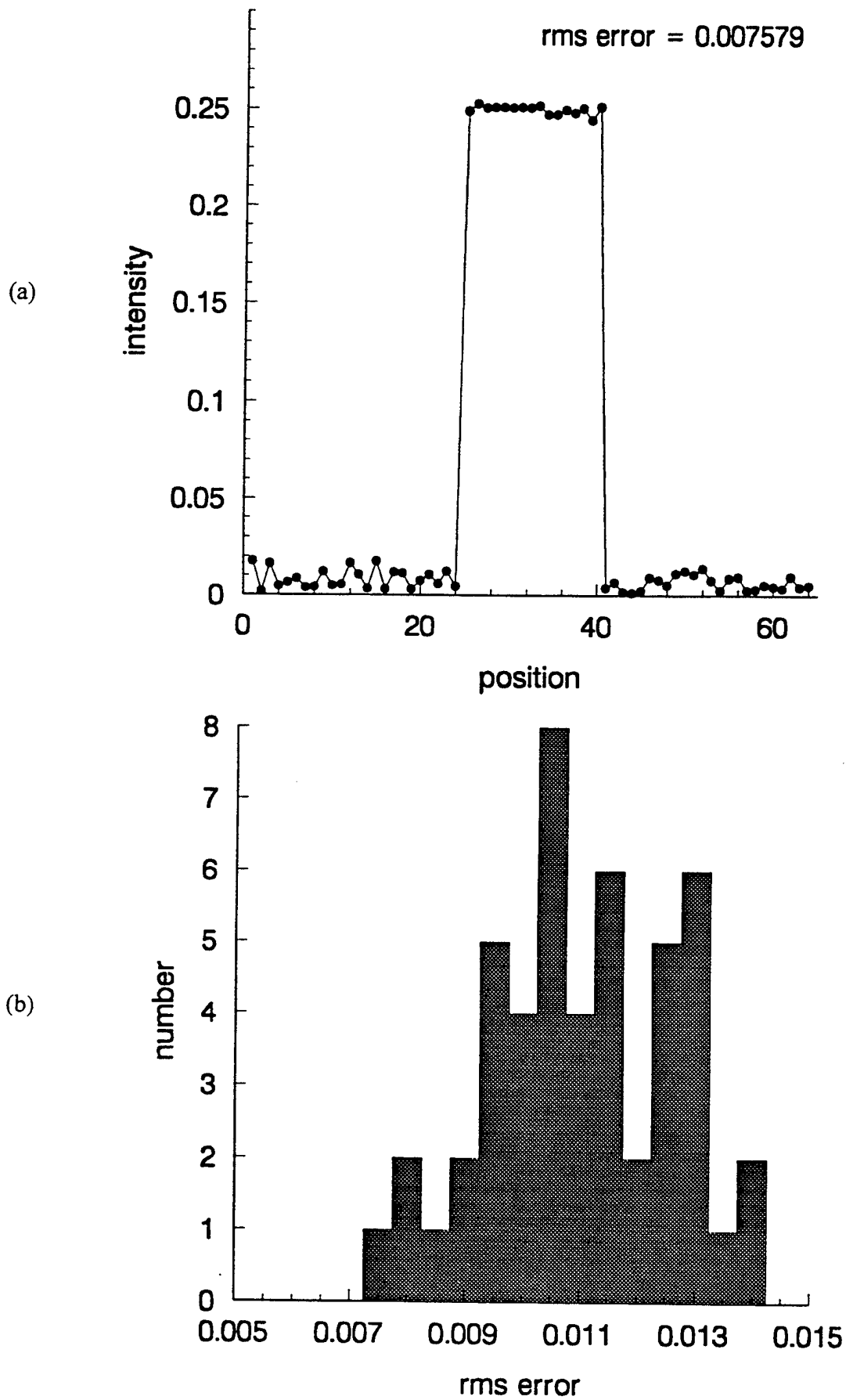


Figure 3.4. (a) Nearly uniform beam shape obtained using grid optimization, (b) histogram of rms error obtained for many trials [after Rhoadarmer 1994].

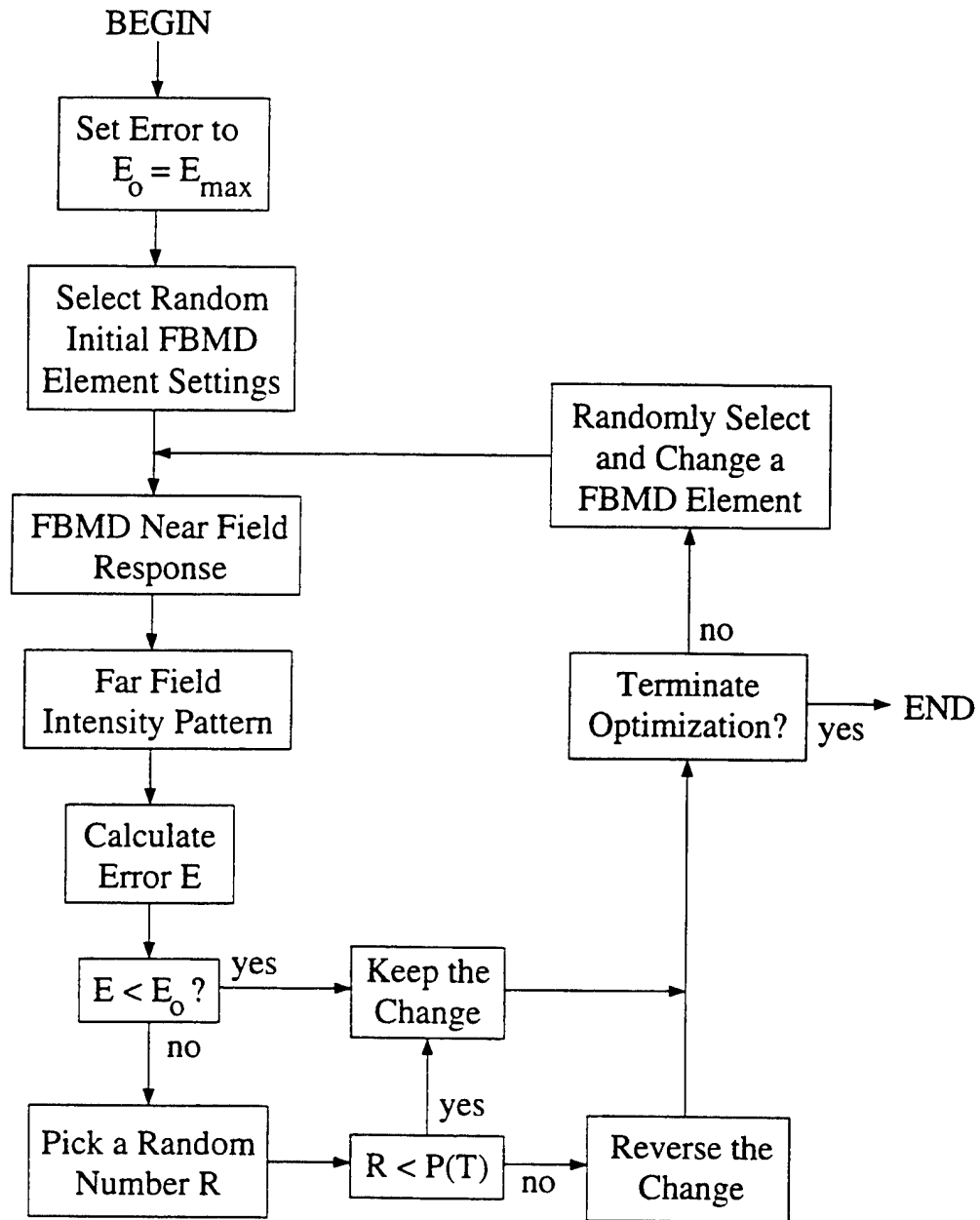
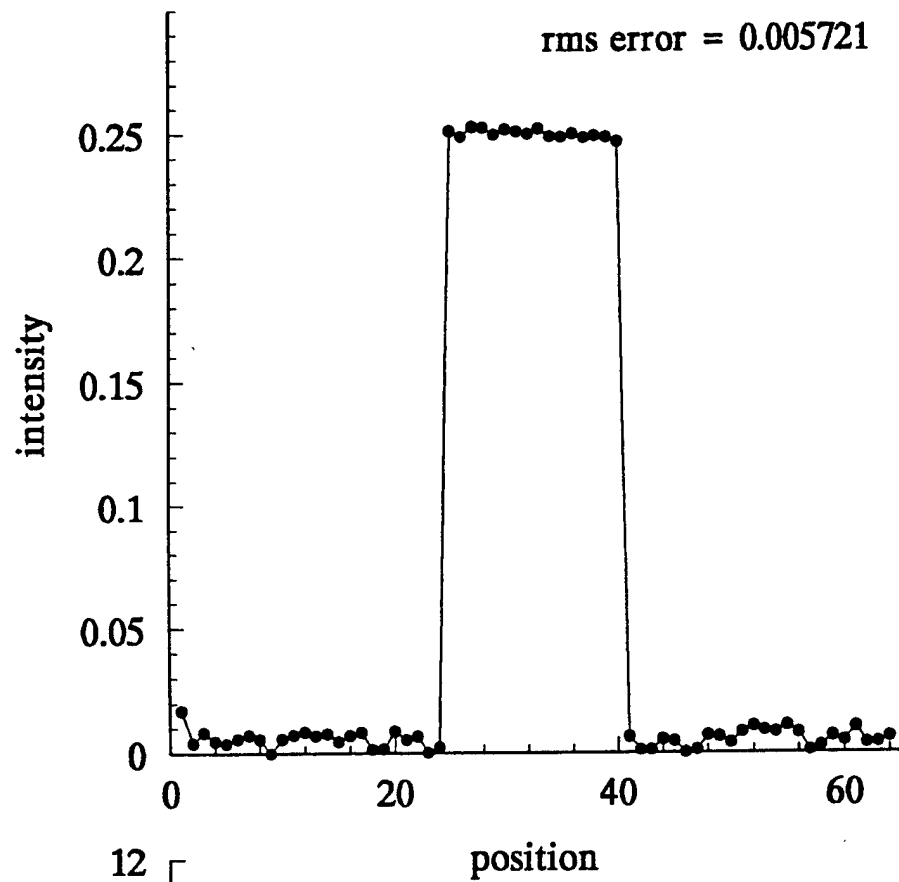


Figure 3.5. Diagram of simulated annealing optimization [after Rhoadarmer, 1994].

(a)



(b)

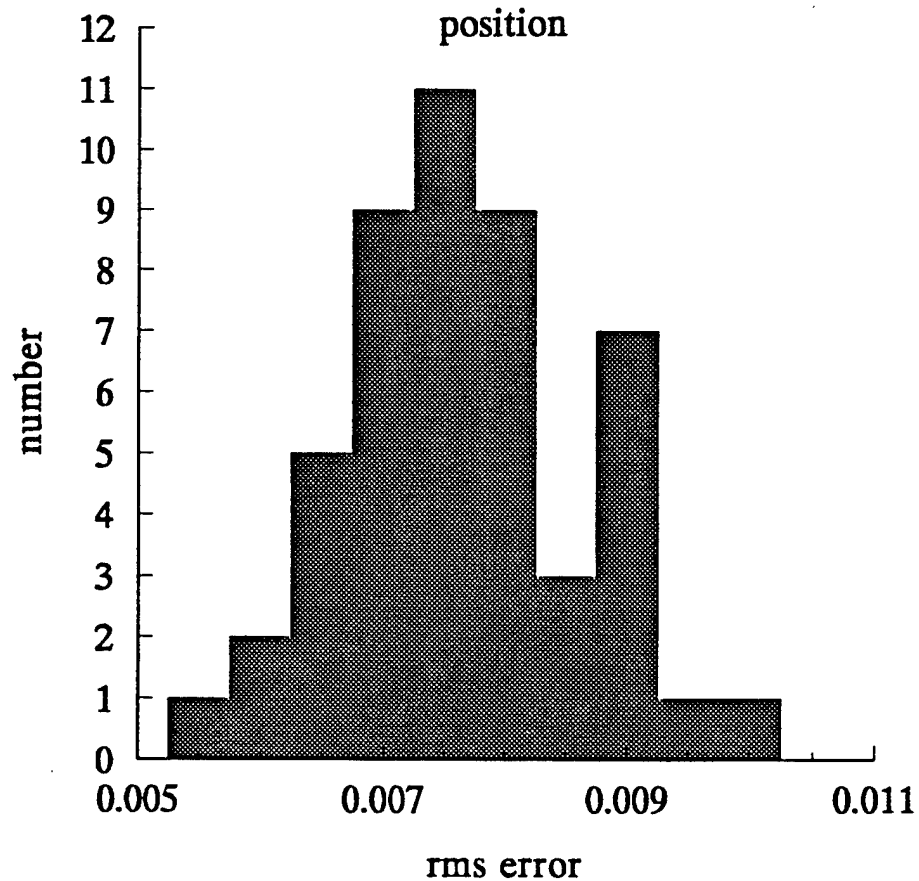
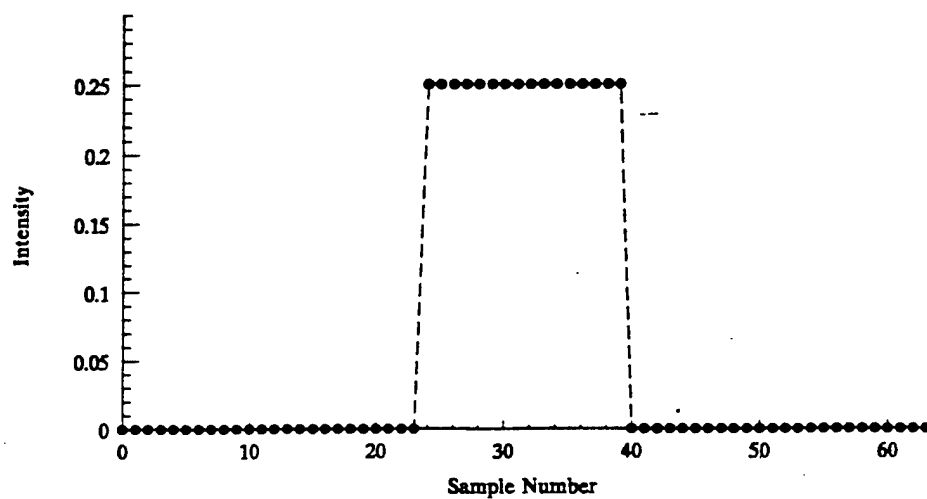
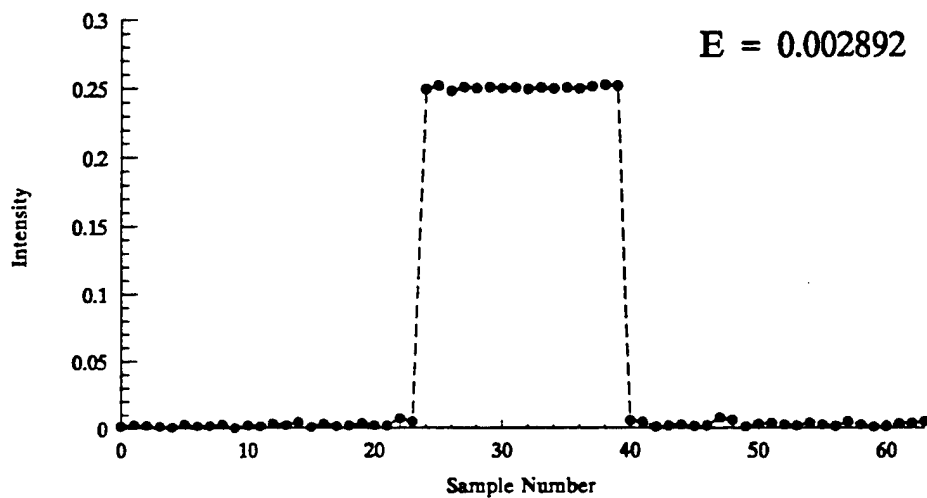


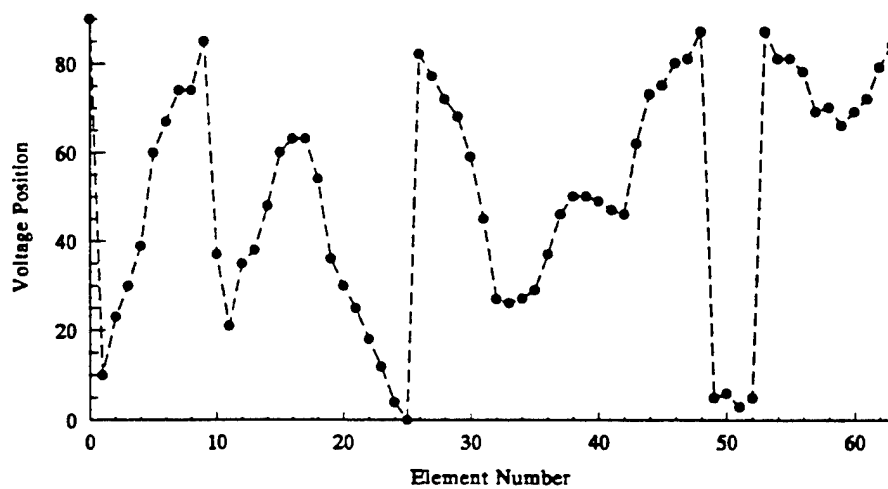
Figure 3.6. (a) Nearly uniform beam shape obtained using simulated annealing optimization. (b) histogram of rms error obtained for many trials [after Rhoadarmer, 1994].



(a)



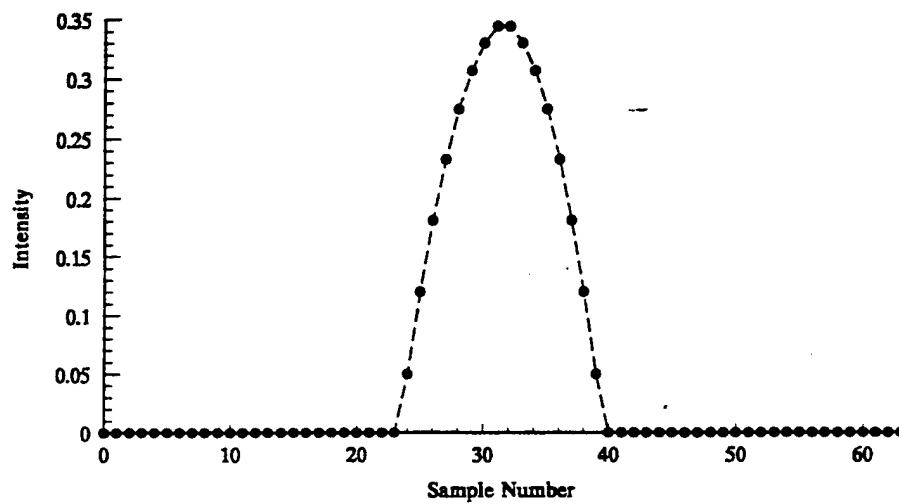
(b)



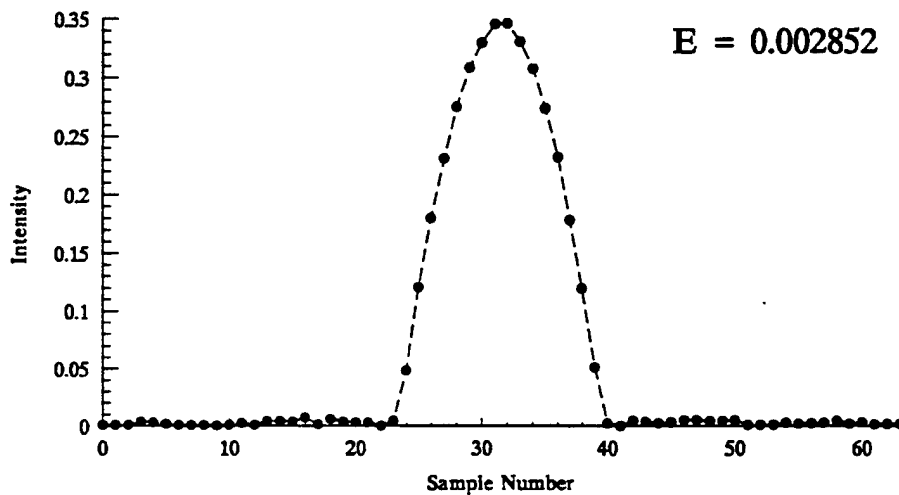
(c)

Figure 3.7. (a) Desired uniform beam shape, (b) improved simulated annealing result with rms error 0.029. (c) micromirror voltages that produce this result [after Rhoadarmer, 1994].

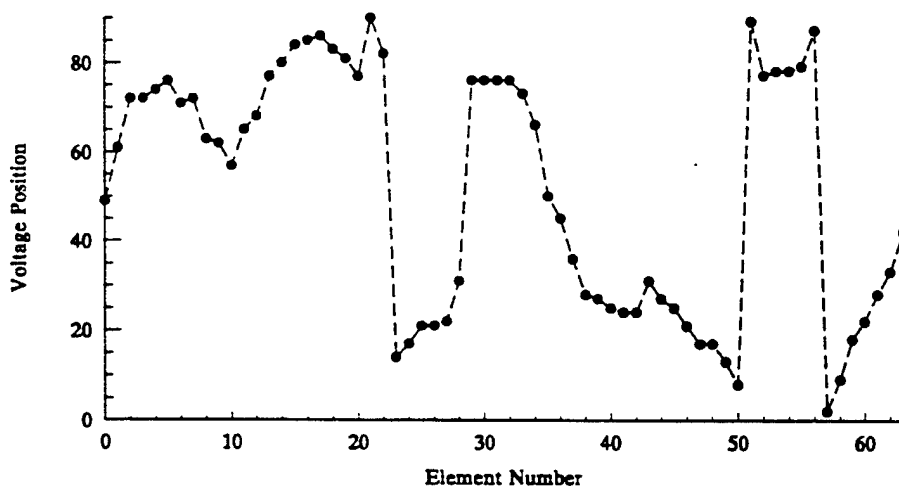




(a)

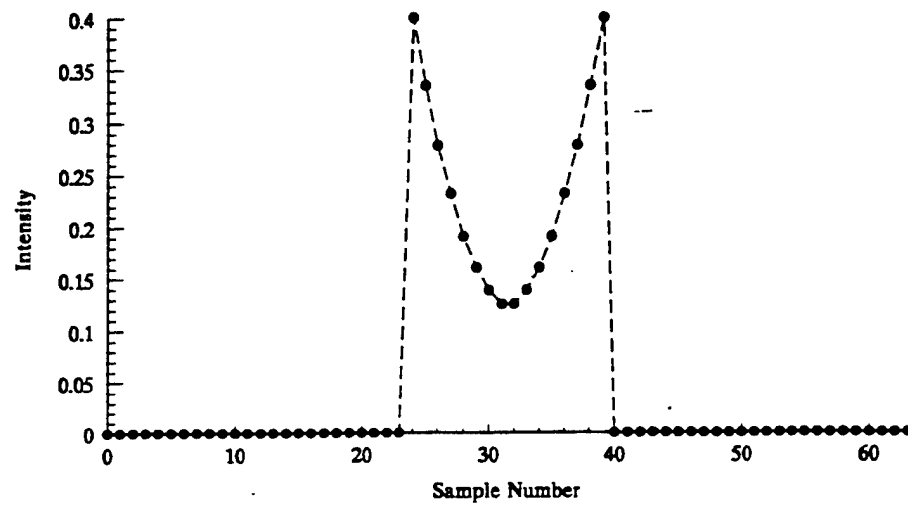


(b)

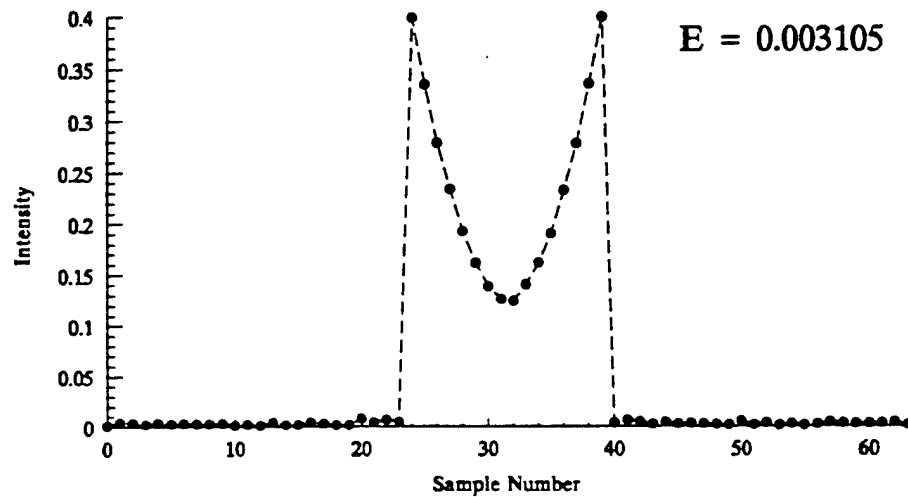


(c)

Figure 3.8. (a) Desired parabolic beam shape with maximum, (b) simulated annealing result with rms error 0.0029, (c) micromirror voltages that produce this result [after Rhoadarmer, 1994].

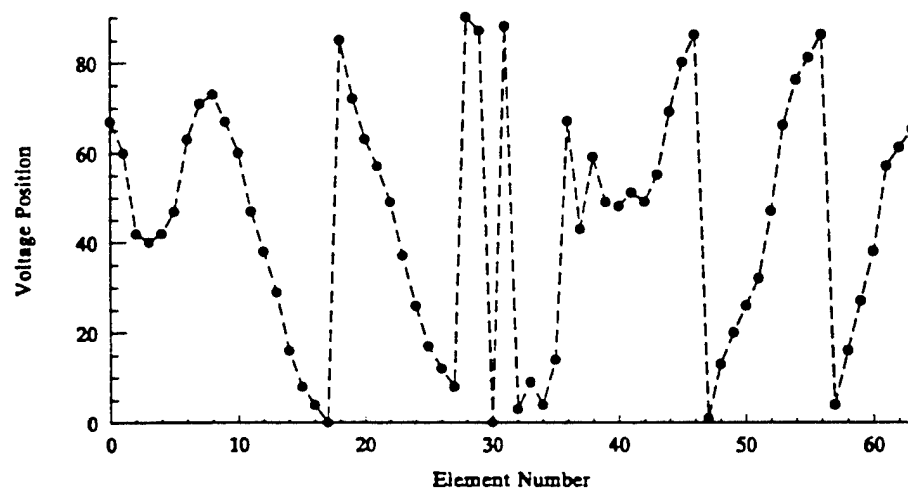


(a)



$E = 0.003105$

(b)



(c)

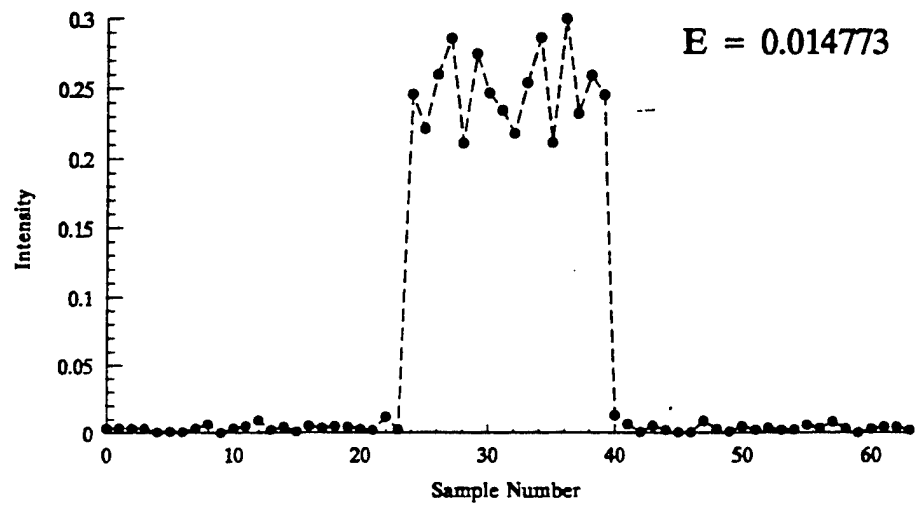
Figure 3.9. (a) Desired parabolic beam shape with minimum, (b) simulated annealing result with rms error 0.0031, (c) micromirror voltages that produce this result [after Rhoadarmer, 1994].

Since in the above simulations the micromirror voltages do not form smooth patterns, a concern is that the beam shape results could be excessively sensitive to small changes in micromirror voltages. Figure 3.10 shows the results of adding Gaussian phase noise to the micromirrors: the phase of each micromirror, adjusted as in Figure 3.7 to produce a near-uniform beam shape, is independently perturbed by adding a phase selected at random from a zero mean normal distribution of standard deviation 10, 20, or 40 degrees. These results and additional simulations for a range of standard deviations are summarized in Figure 3.11, which plots rms error relative to the desired uniform beam shape versus the standard deviation of the added Gaussian phase noise. A conclusion is that for beam shaping in one dimension phase noise with a standard deviation of a few degrees is not expected to significantly affect the ability of micromirror arrays to produce desired beam shapes.

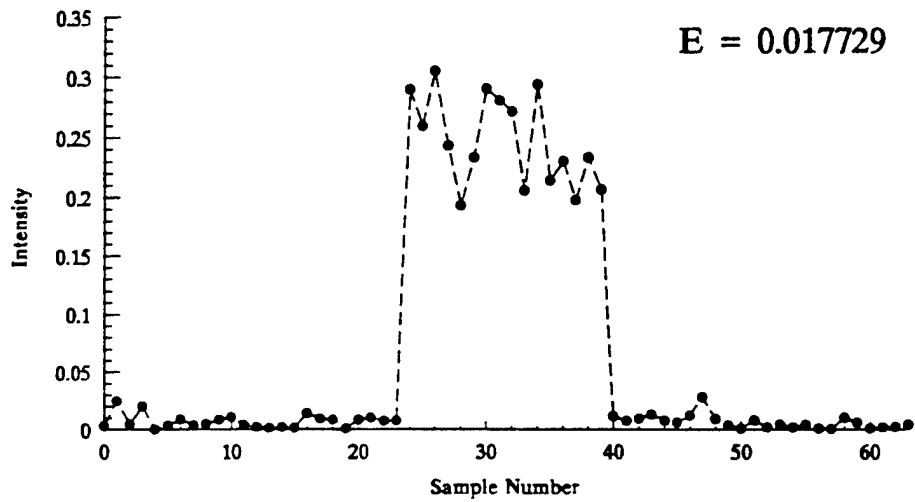
### 3.4 Far Field beam Shaping in Two Dimensions

Figure 3.12 shows simulated annealing results for achieving a near-uniform beam shape in two dimensions. A 12 by 12 array of micromirrors was pistoned to obtain a 4 by 4 pixel near-uniform beam irradiance in the far field with an rms error (over a 12 by 12 pixel field) of 0.0036, as shown in Figure 3.12(a). In (b) and (c) the consequences of adding zero-mean Gaussian noise with standard deviations of 5 and 10 degrees, respectively, to each micromirror are shown. A conclusion (consistent with the results for beam shaping in one dimension) is that phase noise of a few degrees is not problematic.

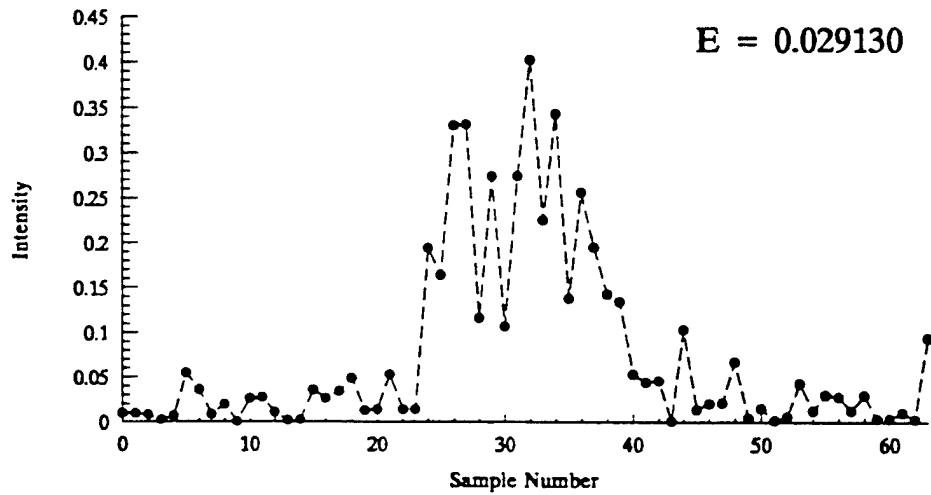
An additional practical concern is that although simulated annealing optimization yields excellent results, it is not real time: the results shown in Figure 3.12(a), for example, typically required many hours of execution time on a workstation-class computer. An approach that permits real-time application stores address voltages determined off-line by simulated annealing that produce key desired far field beam shapes. These stored results are then used as training data for Gaussian radial basis function neural networks [e.g., Poggio and Girosi, 1990; Gustafson et al. 1992] that



(a)



(b)



(c)

Figure 3.10. Beam shape obtained by adding zero-mean Gaussian noise of standard deviation (a) 10 degrees, (b) 20 degrees, and (c) 40 degrees to the phases that yield the near-uniform beam shape of Figure 3.7 [after Rhoadarmer, 1994].

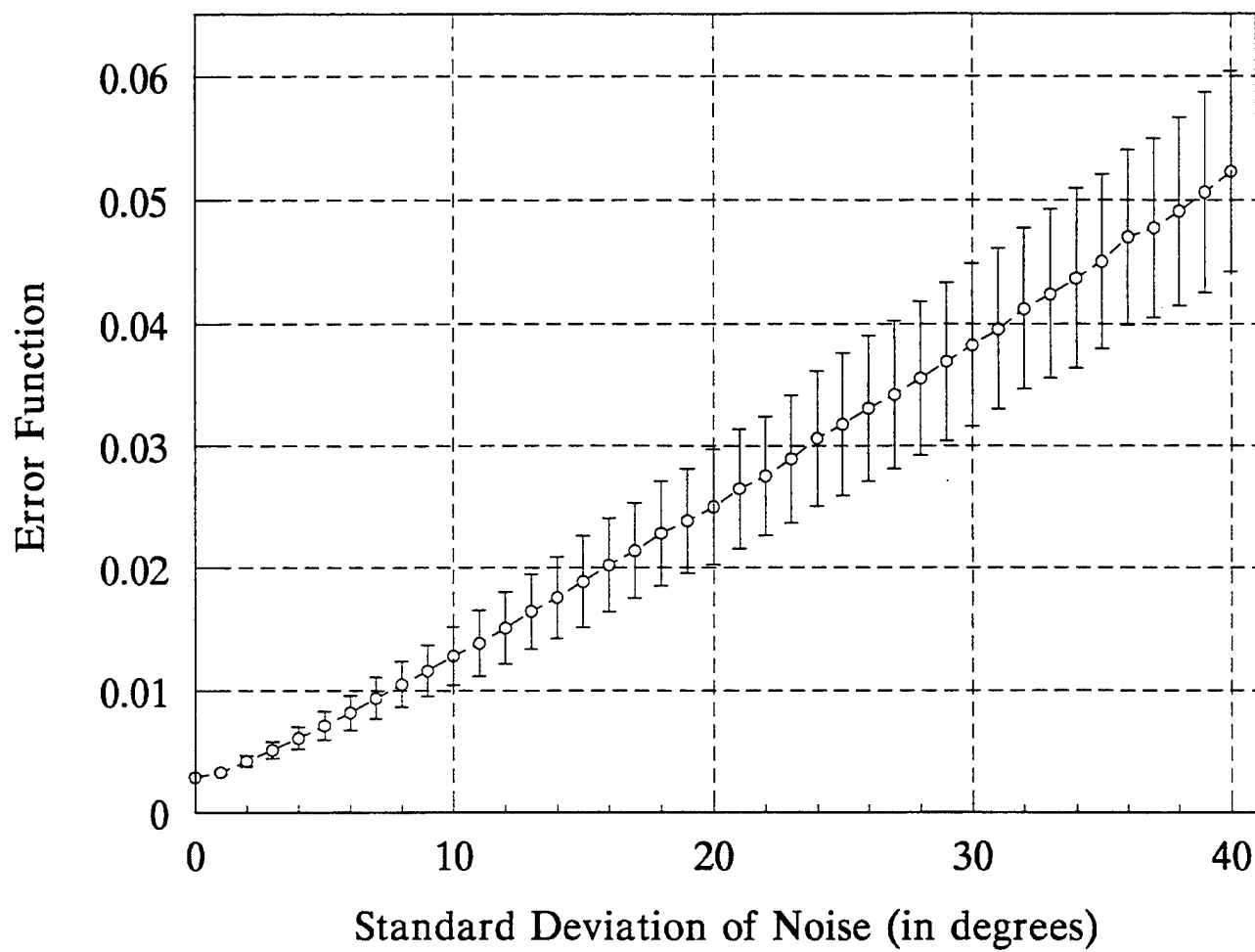
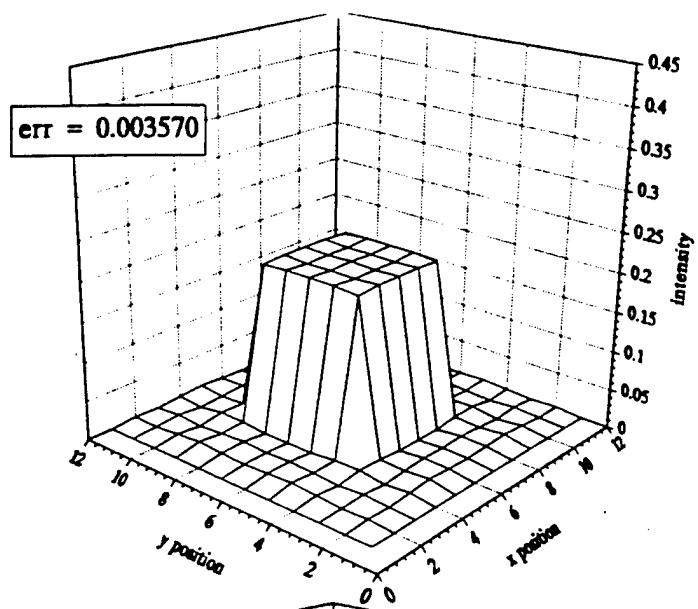
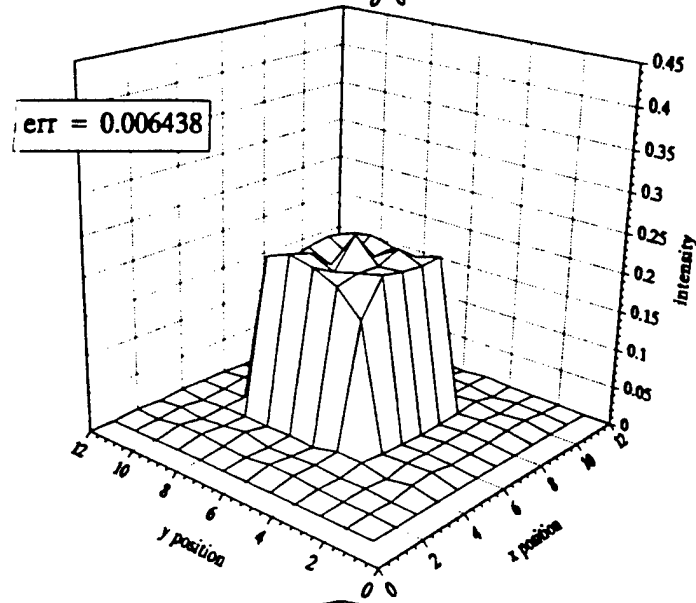


Figure 3.11. Rms error relative to the desired uniform beam shape versus the standard deviation of added Gaussian phase noise [after Rhoadarmer, 1994].

(a)



(b)



(c)

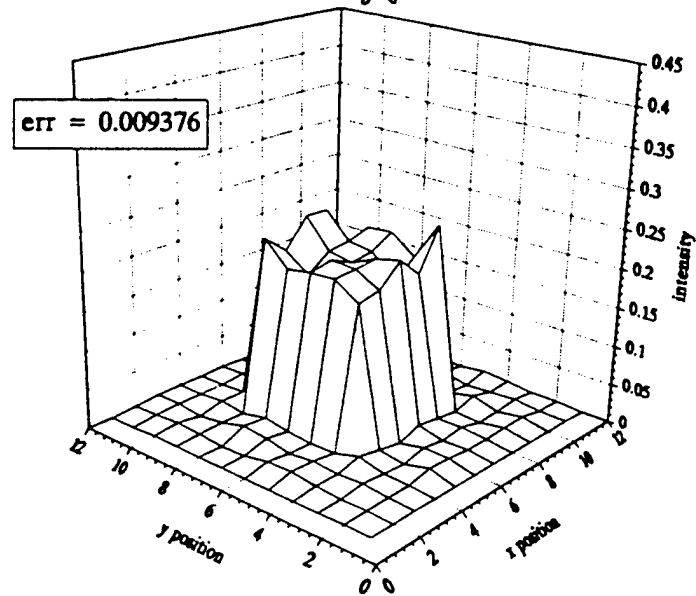


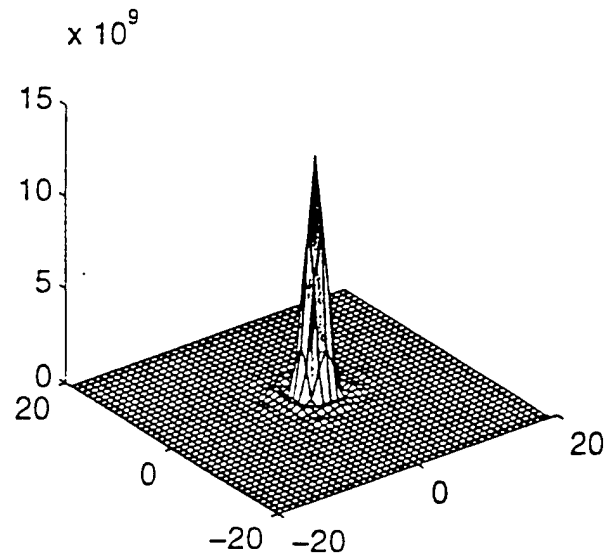
Figure 3.12. Simulated annealing results for achieving a near-uniform beam shape in two dimensions, where the standard deviation of zero-mean Gaussian noise added to each micromirror is (a) 0 degrees, (b) 5 degrees, and (c) 10 degrees [after Rhoadarmer, 1994].

interpolate in real time [e.g., Sandler, et al., 1991] between the training cases. The interpolated annealing micromirror control procedure is as follows:

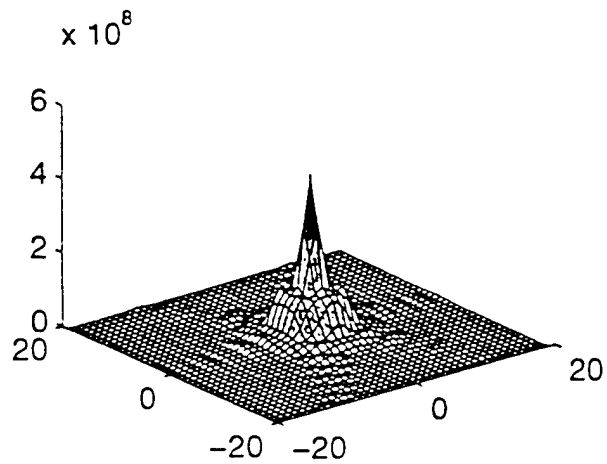
1. Select the training beam shapes.
2. Find (off line) and store the control voltages that produce these shapes with acceptable rms error using micromirror phase and amplitude versus address voltage data and simulated annealing optimization.
3. Find and store Gaussian radial basis function interpolation surfaces that have address voltages as the dependent variables and training beam shape samples as the independent variables.
4. Use the stored interpolation surfaces to find (in real time) the control voltages that produce desired beam shapes within the range of the training beam shapes.

This procedure is computationally intensive in training, particularly if the training beam shapes lack symmetry so that their two dimensional cross sections cannot be analyzed in terms of one-dimensional projections. However, execution is not computationally intensive and is suitable for real time application.

Straightforward two-dimensional numerical simulations were used to model a 127-element hexagonal array of hexagonal micromirrors, similar to the array shown in Figures 2.7 and 2.8. The elements had a nearest neighbor center-to-center spacing of 1.5 times their corner-to-corner maximum extent, were perfectly reflecting and flat, and had perfectly absorbing inter-mirror space. The array was quantized onto a 1024 by 102 grid so that a two-dimensional discrete Fourier transform could be performed with the array area less than 10 percent of the grid area to avoid aliasing. Figure 3.13(a) shows a plot (obtained from the squared absolute value of the discrete Fourier transform of the grid) that is proportional to the central portion of the reflected far field irradiance when the array is illuminated with collimated coherent light and all micromirrors are in the array plane (i.e., no micromirror displacement). Figure 3.13(b) shows a similar plot when the



(a)



(b)

Figure 3.13 (a) Plot proportional to the central portion of the far field irradiance reflected from an array of 127 hexagonal micromirrors for zero micromirror displacement. (b) similar plot for parabolic micromirror displacement [after Gustafson, et al., January 1996]

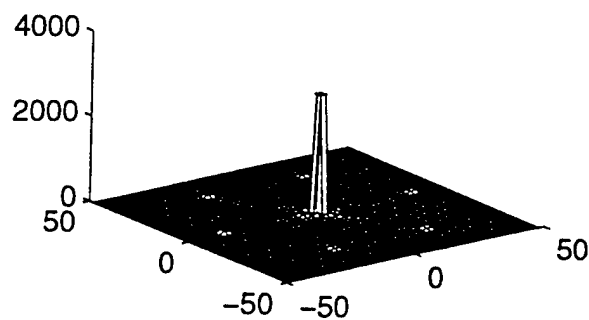


micromirrors are displaced normal to the initial array plane in a parabolic profile. For this profile all micromirrors in hexagonal rings of 1, 6, 12, 18, 24, 30, and 36 elements have the same displacement, where the displacements are such that their phases in units of  $\pi$  are 0,  $1/36$ ,  $4/36$ ,  $9/36$ ,  $16/36$ ,  $25/36$ , and 1, respectively. Note the considerable change in the center portion of the far field irradiance profile from uniform micromirror displacement to parabolic micromirror displacement.

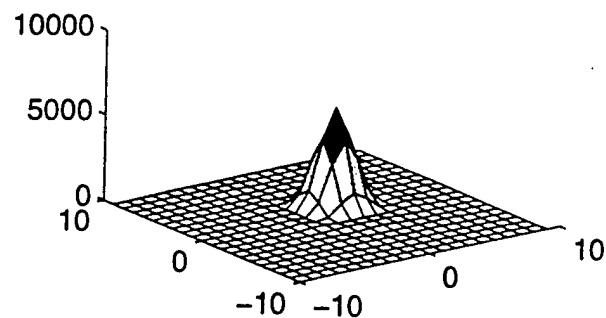
Figure 3.14 displays plots proportional to far field irradiance for the array of 127 hexagonal micromirrors with the same conditions used to obtain the results shown in Figure 3.13 except that the amplitude reflectivity of the inter-mirror space is 0.5. In Figure 3.14(a) and (b) there is no micromirror displacement; (a) shows six secondary maxima and (b) shows the central lobe in more detail. In (c) and (d) the displacements of the seven hexagonal rings of elements are optimized using simulated annealing to yield as-constant-as-possible irradiance over a circular central region that includes only the central and first side lobes. This beam shaping operation is accomplished by minimizing  $I$ , the integrated squared difference between actual and constant irradiance over the circular central region. Note that more constant irradiance at a greatly reduced irradiance level is obtained in the circular central region at the expense of a large increase in the irradiance of the six secondary maxima.

The phase values for the displacements of the seven hexagonal rings of elements that implemented the beam shaping operation shown in Figure 3.14(d) were 0.2690, 0.1464, 0.1330, 0.2662, 0.2712, 0.2506, and 0.2512 in units of  $\pi$  for increasing ring size. Figure 3.15 plots the minimized quantity  $I$  versus percent change in these phase values above (a) and below (b) the optimal values. These plots indicate that beam shaping is not critically sensitive (i.e., unstable) relative to small changes in the optimal phase values.

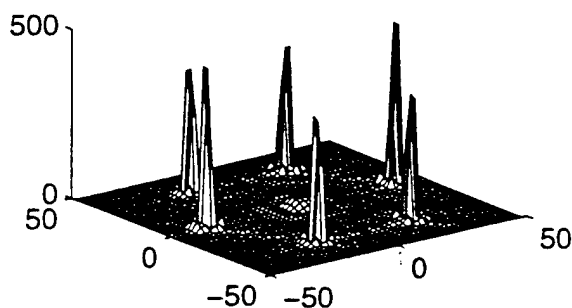
Although the simulations considered here have focused on achieving uniform beam shapes in the far field of a uniformly illuminated micromirror array, other desired beam shapes, e.g., Gaussian shapes or shapes that perform aberration correction, could be produced with the same ease (or lack thereof). For example, advanced simulations using



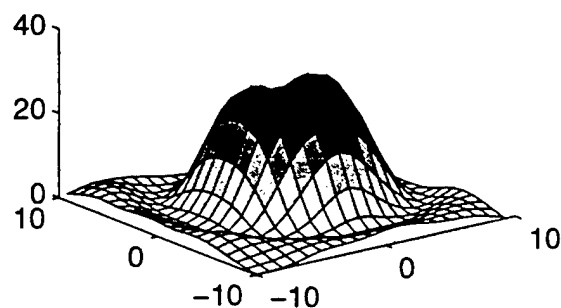
(a)



(b)



(c)



(d)

Figure 3.14 (a) Plot proportional to the far field irradiance reflected from the array of 127 hexagonal micromirrors with zero micromirror displacement, (b) central region of (a). (c) plot proportional to reflected far field irradiance with micromirror displacements optimized to yield as-constant-as-possible irradiance over a circular central region that includes only the central and first side lobes. (d) central region of (c) [after Gustafson, et al., January 1996].

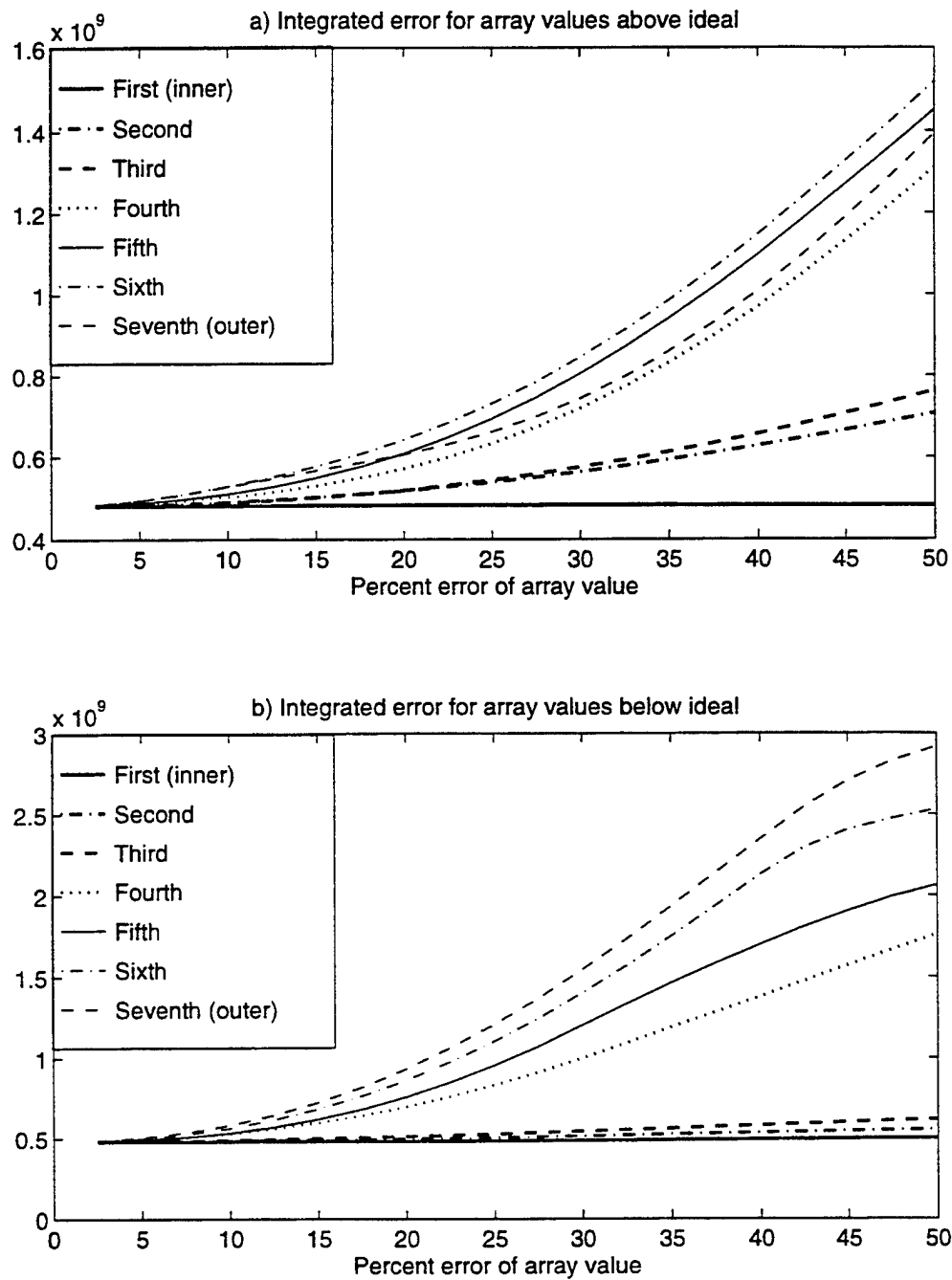


Figure 3.15 (a) Plot of the minimized quantity  $I$  versus percent change above the optimal phase values for the seven hexagonal rings of micromirrors, (b) as in (a) but for percent change below the optimal phase values [after Gustafson, et al., January 1996]

hexagonal micromirror arrays have been performed as indicated in Figure 3.16, which shows normalized and radially averaged far field beam shapes in the form of the point spread functions for cases where (a) a plane wave is reflected from micromirrors with the same piston displacements, (b) a quadratically aberrated wave is reflected from these micromirrors, and (c) the micromirror piston displacements are adjusted to compensate for the quadratic aberration. The peak intensities for cases (b) and (c) are, respectively, -2.63 dB and -1.00 dB of the peak intensity for (a), so that an aberration correction or Strehl ratio improvement of 1.63 dB or 45.7% is realized.

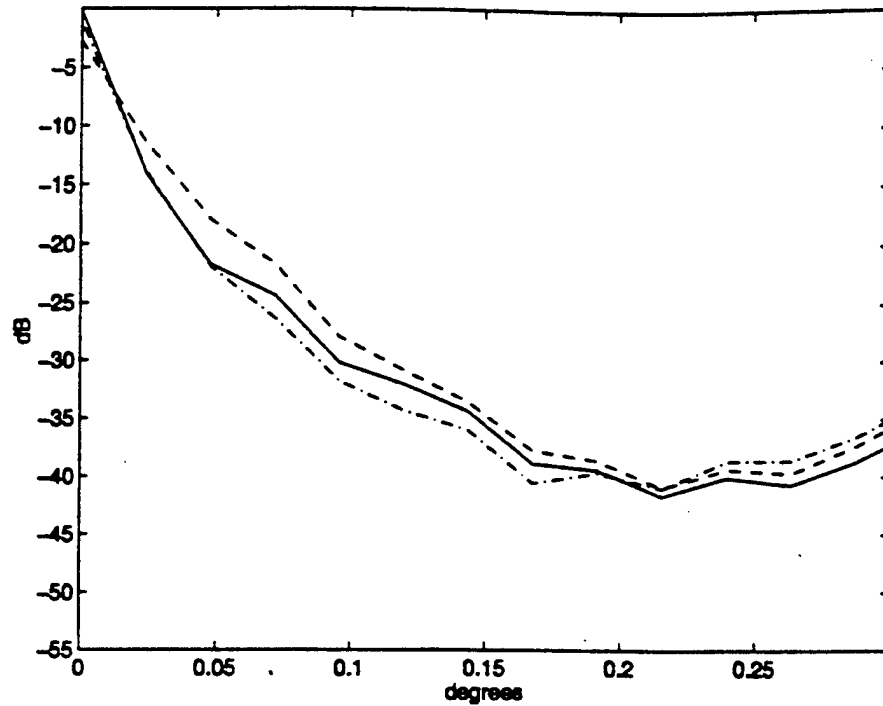


Figure 3.16 Normalized and radially averaged point spread functions for reflection from a hexagonal micromirror array for (a) solid line: a plane wave reflected from micromirrors with the same piston displacements, (b) dashed line: a quadratically aberrated wave reflected from these micromirrors, and (c) dash-dot line: micromirror piston displacements adjusted to compensate for the quadratic aberration. The peak intensities for (b) and (c) relative to (a) are -2.63 dB and -1.00 dB, respectively [after Roggemann, et al., 1997].

## **4. MICROMIRROR EXPERIMENTS**

This section considers micromirror experiments that have potential relevance for communications applications. In particular, interference microscopy experiments on micromirror characterization and experiments on beam steering and shaping are reviewed.

### **4.1 Experiments on Micromirror Characterization**

Figure 4.1 shows an interference microscope system designed for micromirror characterization. It employs standard reference-and-object beam techniques and uses a Helium-Neon laser of 632 nm wavelength to produce an array of interference fringes on microscopic images of individual micromirrors (or a small group of micromirrors). The fringes permit the determination of relative vertical displacements across the micromirrors as a function of control voltage.

Figure 4.2 shows sample results obtained using this system for an element of the micromirror array of Figure 2.3. Note that the element tilts as well as pistons as the control voltage increases. This effect is more apparent in the corresponding central cross sections shown in Figure 4.3. Figure 4.4(a) shows deflection (one radian is 1.01 micron) versus control (or address) voltage at the center of one element. As the control voltage is increased and decreased, the results indicate that the deflection at a central position on a single element is highly reproducible. Figure 4.4(b) shows deflection (one lambda is 632 nm) versus control voltage for many positions; the results indicate that deflection varies significantly with position.

Figure 4.5 shows an improved interference microscope system, and Figure 4.6 shows sample results obtained using this system for square and hexagonal micromirrors of the sort indicated in Figure 2.6. Note that the experimental and theoretical behavior are in close agreement but that individual micromirrors can vary significantly in deflection at a given voltage (by more than 50 nm for a half-wavelength deflection of 316 nm).

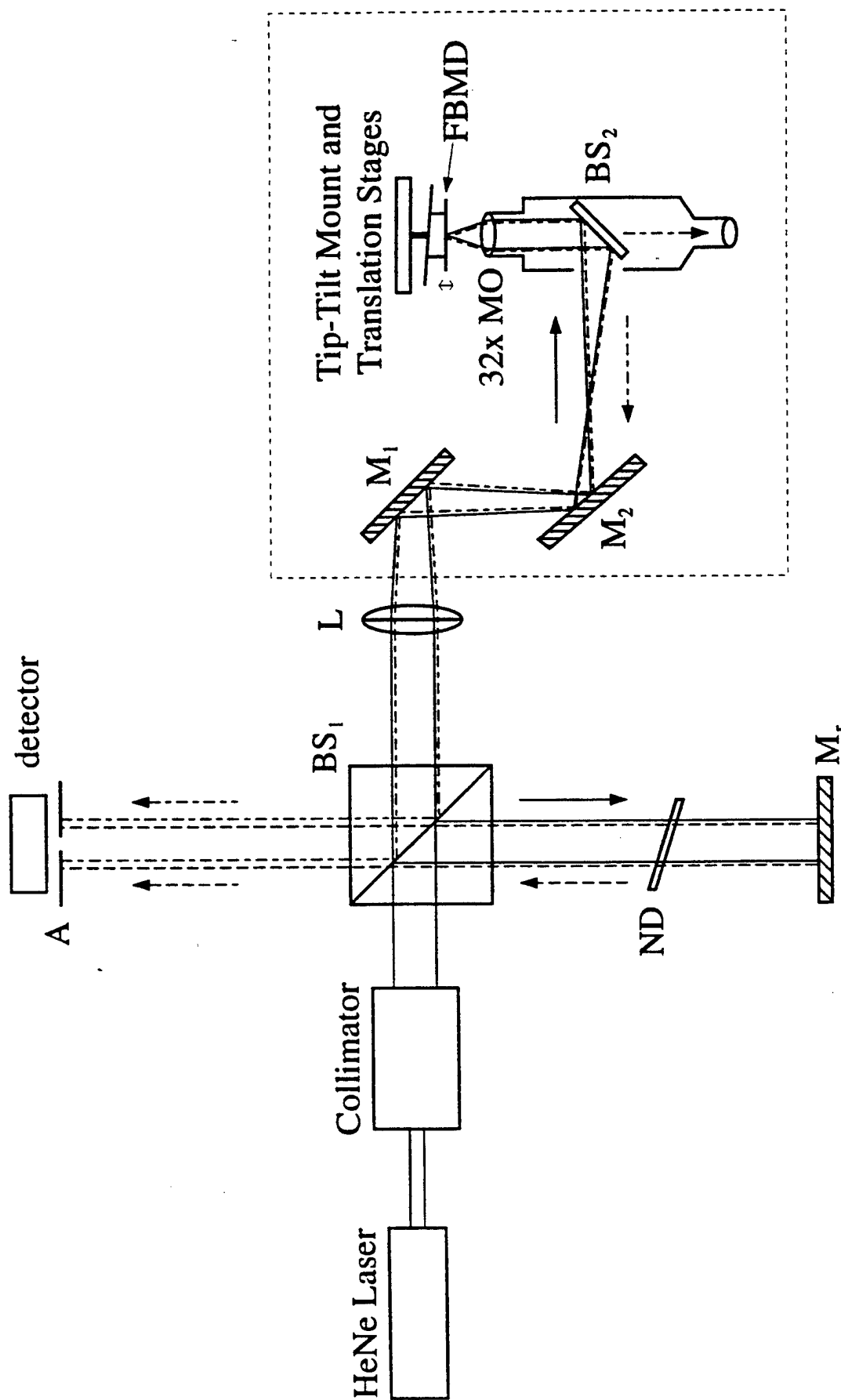


Figure 4.1. Interferometric microscope system for micromirror characterization: the dash-dash line is the return reference beam, the dash-dot line is the return object beam, and the objects in the dotted box are perpendicular to the rest of the setup [after Rhoadarmer, et al., 1994].

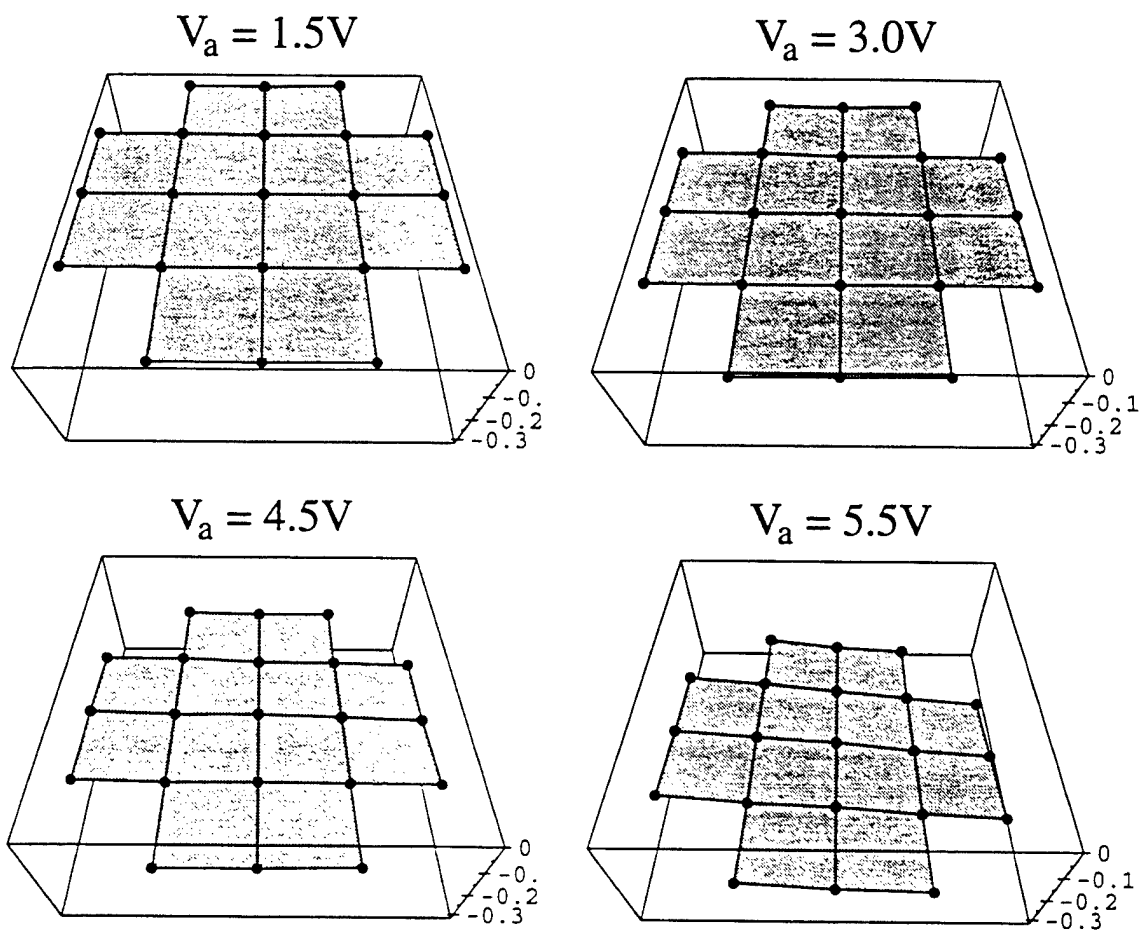
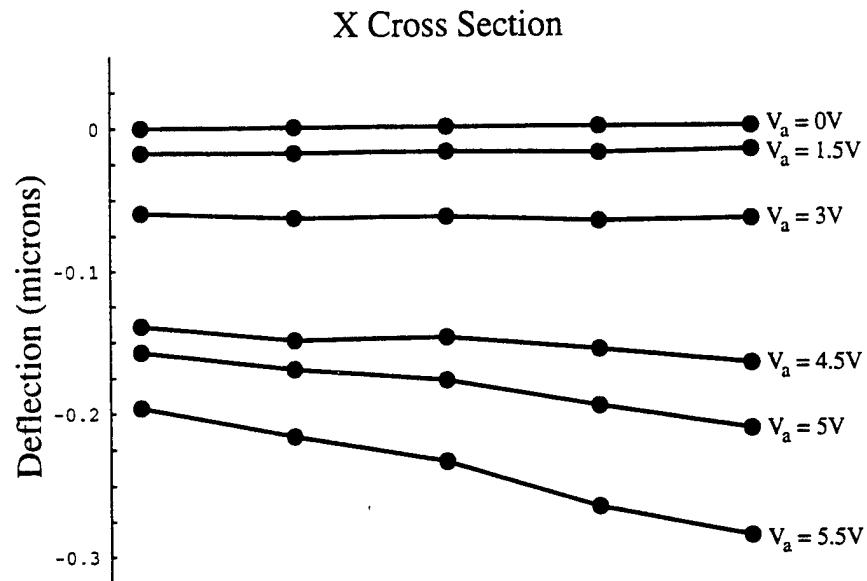
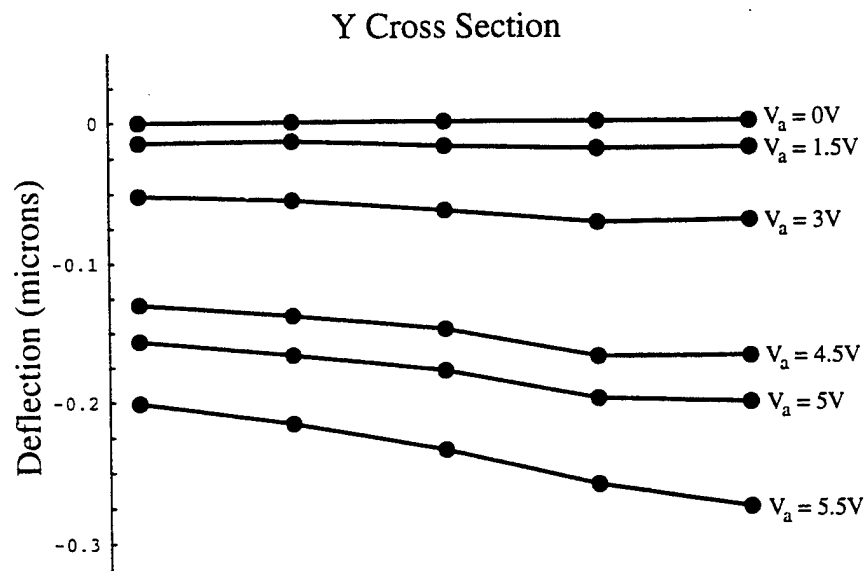


Figure 4.2. Deflection in microns versus control voltage  $V_a$  using the system of Figure 4.1 for 21 sample positions on an element of the micromirror array of Figure 2.3 [after Rhoadarmer, 1994].





(a)



(b)

Figure 4.3. Central cross sections of deflection versus control voltage for Figure 4.2, (a) perpendicular to addressing pad of Figure 2.3, (b) parallel to this pad [after Rhoadarmer, 1994].

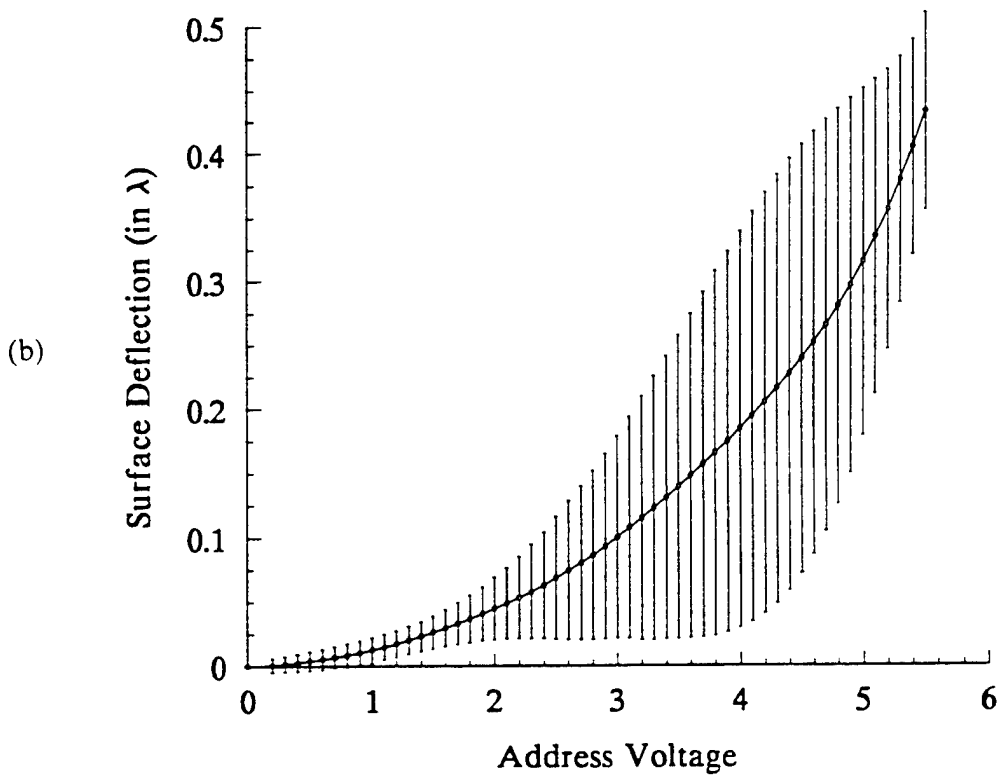
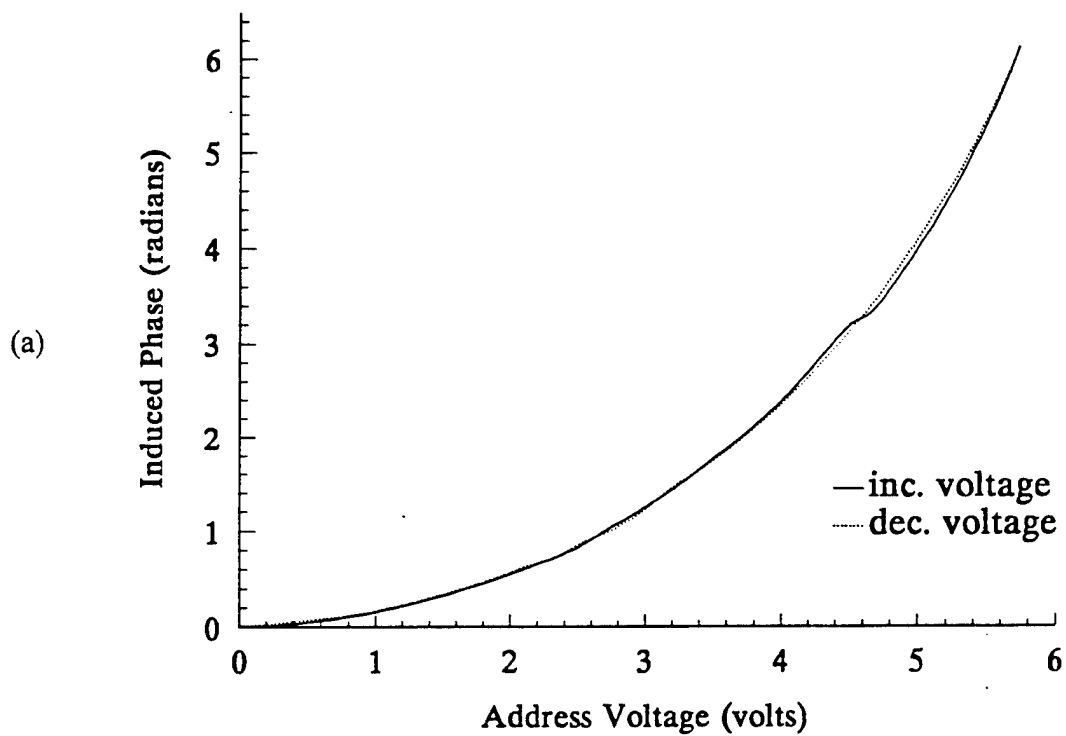


Figure 4.4. (a) Deflection (one radian is 1.01 micron) versus control (or address) voltage at the center of one element of Figure 2.3 as the voltage is increased and decreased. (b) deflection (one lambda is 632 nm) versus control voltage at many positions: the solid curve is mean deflection [after Rhoadarmer, 1994].

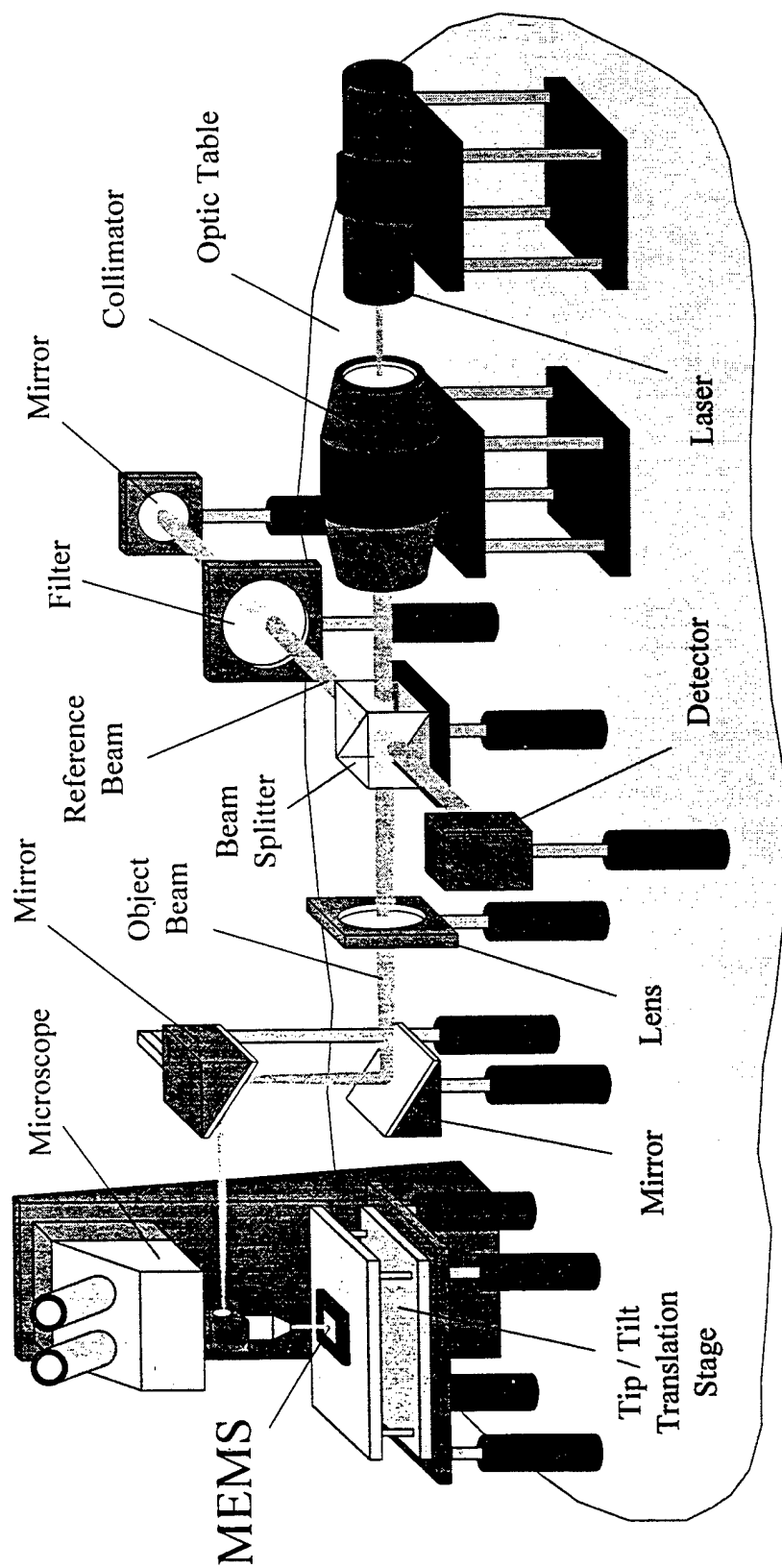
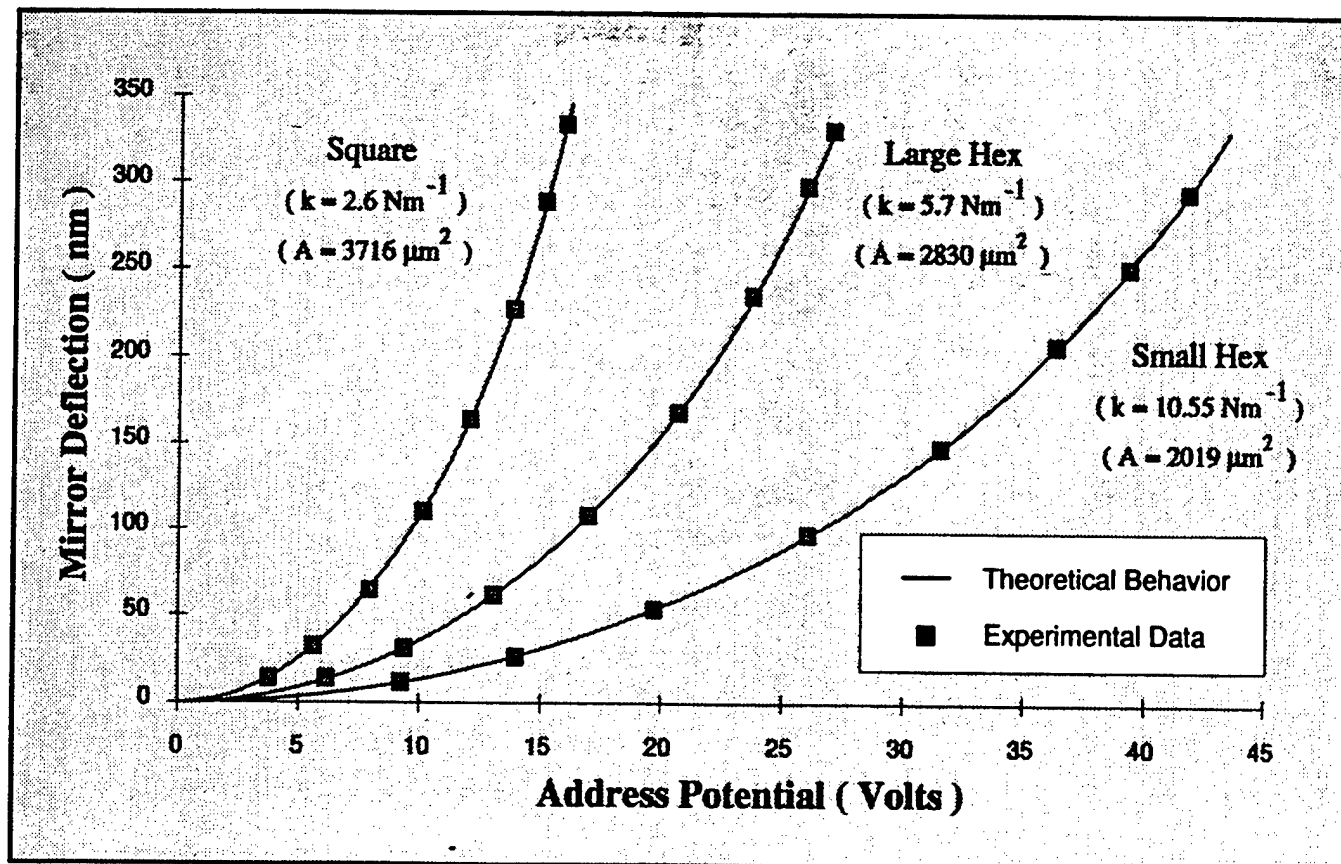


Figure 4.5. Improved interference microscope system for micromirror characterization [after Michalick, et al., 1995].

(a)



(b)

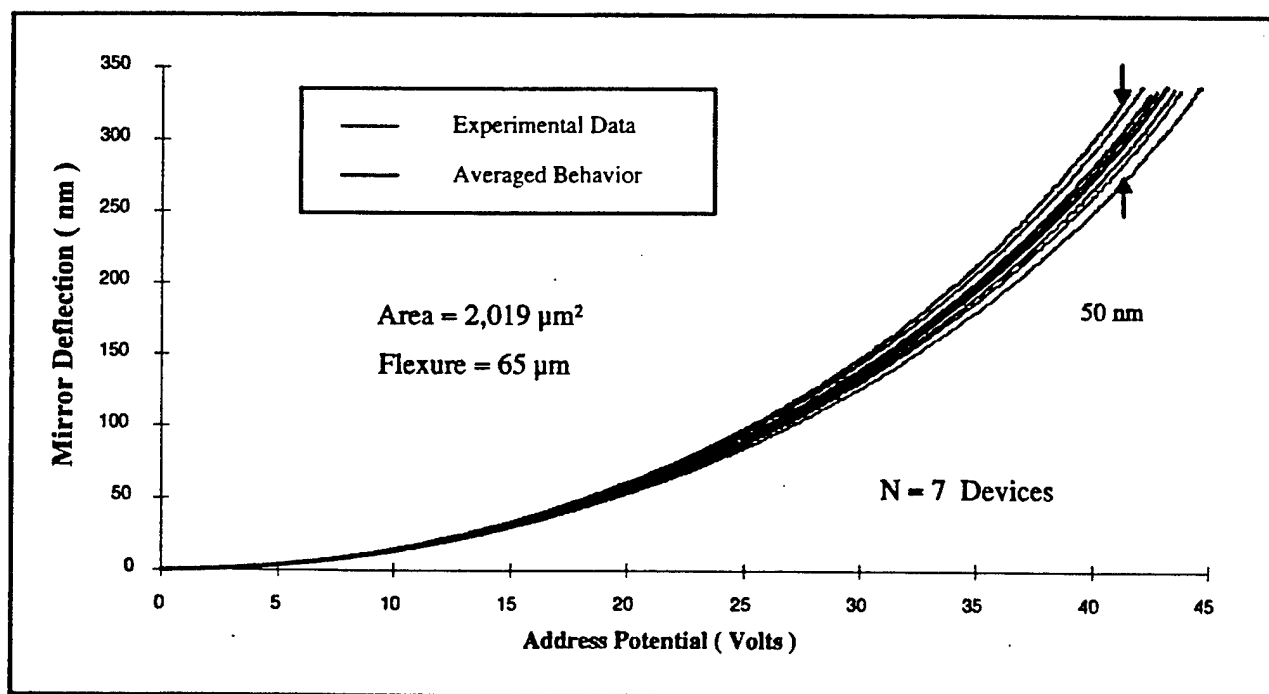


Figure 4.6. (a) Center deflection versus voltage for square and hexagonal micromirrors of the sort shown in Figure 2.6; the area  $A$  and spring constant  $k$  for each micromirror is indicated. (b) center deflection versus voltage for seven nominally identical hexagonal micromirrors [after Michalick, et al., 1995].

## 4.2 Experiments on Micromirror Beam Steering and Shaping

Figure 4.7(a) shows an optical system design for micromirror array interfacing. This system uses standard polarizing beam splitters (PBS) and half and quarter wave plates (HWP and QWP) to input a beam to the array and to output both an unfiltered near field beam reflected from the array and a spatially filtered near field beam. Figure 4.7(b) shows an experimental arrangement used to investigate micromirror array beam steering and phase control for beam shaping or aberration correction. The expanded laser beam illuminates a hexagonal mask that is imaged, after possible aberration insertion, onto the micromirror array. A polarizing beam splitting cube directs the reflected light (after sampling by another beam splitting cube and a near-field video camera) through Fourier transform optics, after which a video camera records the far-field intensity. The micromirror array is provided with 64 control voltages for its 127 micromirrors according to an addressing scheme which permits linear ramp and hexagonal ring voltage patterns and enables the correction of spherical, coma, and astigmatism aberrations. The control voltages (limited to 10 volt ranges) are programmed from a PC through a digital-to-analog converter board, and provision is made for applying bias voltages.

Figure 4.8 shows far field intensity reflected from a hexagonal array of 127 micromirrors as in Figure 2.8 as a function of bias voltage. Bias voltage is significant because, as indicated in Figure 4.6, the largest deflection change per volt is achieved at the highest voltage (approximately 45 volts), and biasing each micromirror to a relatively high voltage permits additional voltages of less than 10 volts (compatible with CMOS electronics) to deflect each micromirror at least one-half wavelength (as required for complete beam shaping and aberration correction capability). Note that the application of a bias voltage of up to 30 volts to all micromirrors causes a significant redistribution of intensity out of the central maximum of the array diffraction pattern and into six secondary maxima. This effect is due to the relatively intense and constant reflection from the largely reflective inter-micromirror regions. Both this effect and the relative width and spacing of the maxima are consistent with the simulations discussed in Section 3.

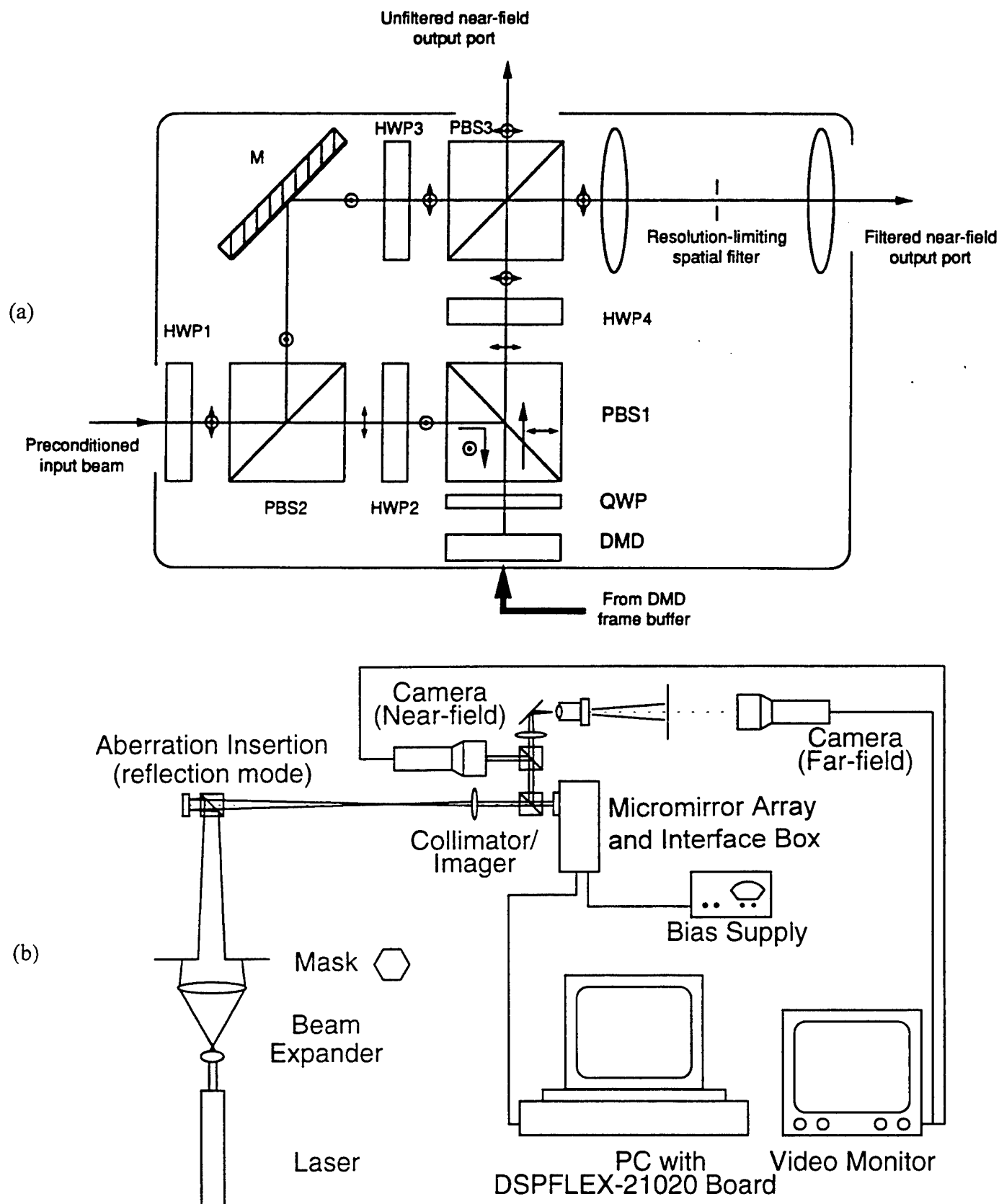


Figure 4.7. (a) Optical system design for micromirror array (or DMD) interfacing [after Gustafson, et al., August 1993], (b) experimental arrangement used to investigate micromirror array beam steering and shaping [after Gustafson, et al., October 1996].

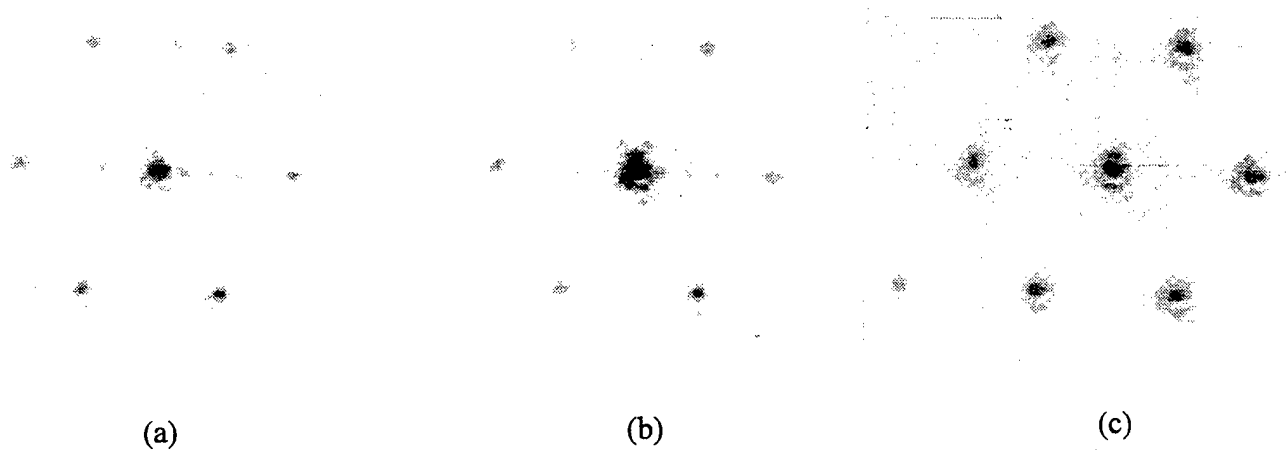


Figure 4.8 Effects of bias voltage on the far-field intensity for a hexagonal array of 127 micromirrors as in Figure 2.8; the potential applied to each micromirror is (a) 0 volts, (b) 20 volts, and (c) 30 volts [after Gustafson, et al., October 1996].

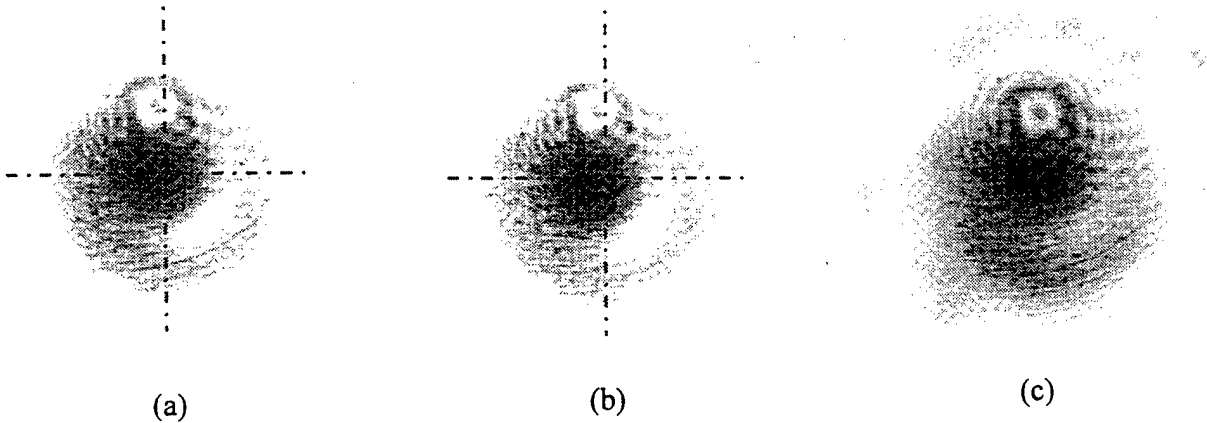


Figure 4.9. Central maximum beam steering and shaping for a hexagonal array of 127 micromirrors as in Figure 2.8; (a) all micromirrors at 24 volts, (b) beam steering due to a stepped linear ramp pattern from 20 to 29.6 volts, where the pattern steps 0.8 volts between each of the 13 array rows, (c) beam shaping due to a quadratic hexagonal ring pattern from 20 to 27.2 volts, where the pattern follows  $V(i) = 20 + (i-1)^2/5$ ,  $i = 1, 2, \dots, 7$ , for each of the seven array hexagonal rings with  $i = 1$  at the center [after Gustafson, et al., October 1996].

Figure 4.9 shows the far-field central maximum intensity for three control voltage patterns; the light spot above the dark central maximum is an artifact of the experimental system. In (a) all micromirrors are at 24 volts, which is near the mean of the voltages employed for the other two patterns. In (b) beam steering of approximately one-tenth of the central maximum width is implemented by a stepped linear ramp pattern from 20 to 29.6 volts, where the pattern steps 0.8 volts between each of the 13 array rows. In (c) beam shaping is implemented by a quadratic hexagonal ring pattern from 20 to 27.2 volts, where the pattern follows  $V(i) = 20 + (i-1)^2/5$ ,  $i = 1, 2, \dots, 7$ , for each of the seven array hexagonal rings with  $i = 1$  at the center. From Figure 4.6 it is apparent that the voltage range employed for beam steering yields a maximum micromirror displacement of about  $d = 80$  nm across the  $w = 790$  micron side-to-side width of the array, and thus the steering angle  $d/w$  is approximately 0.1 mrad or about 0.006 degrees. The angular width of the central maximum is approximately  $\lambda/w$  or 0.8 mrad for  $\lambda = 632$  nm. Thus the displacement of the central maximum due to steering should be approximately  $d/\lambda$  or 0.13 of the central maximum width, which is consistent with results shown in Figure 4.9(a) and (b). In (c) it is apparent that the quadratic pattern broadens the central maximum, which is consistent with the simulations considered in Section 3.

Figure 4.10(a) shows an improved experimental arrangement used to investigate micromirror array aberration correction. Here a long focal length lens may be inserted to introduce quadratic aberration in the laser beam, a Hartmann wave front sensor (WFS) is used to measure the aberration, MEM-DM is the micromirror array, and the large lens between beam splitter BS2 and the point spread function (PSF, proportional to far field intensity) camera is a Fourier transform lens. Figure 4.10(b) shows an example of results obtained using this improved arrangement. Here central-order radially averaged far field intensity is plotted versus distance from the central maximum for an uncorrected (aberrated) beam and for a normalized corrected beam reflected from a hexagonal micromirror array as in Figure 2.8, where voltages on the 127 elements are adjusted to maximize the central intensity. Note that the micromirror array increases the central intensity by about 43 percent and reduces off-axis intensities. Many additional



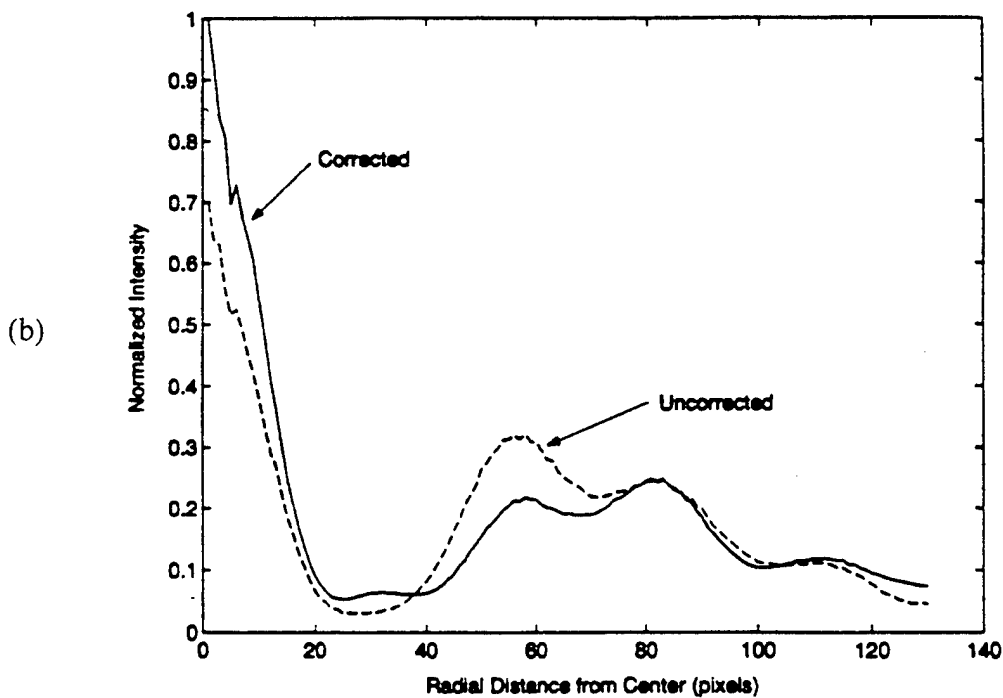
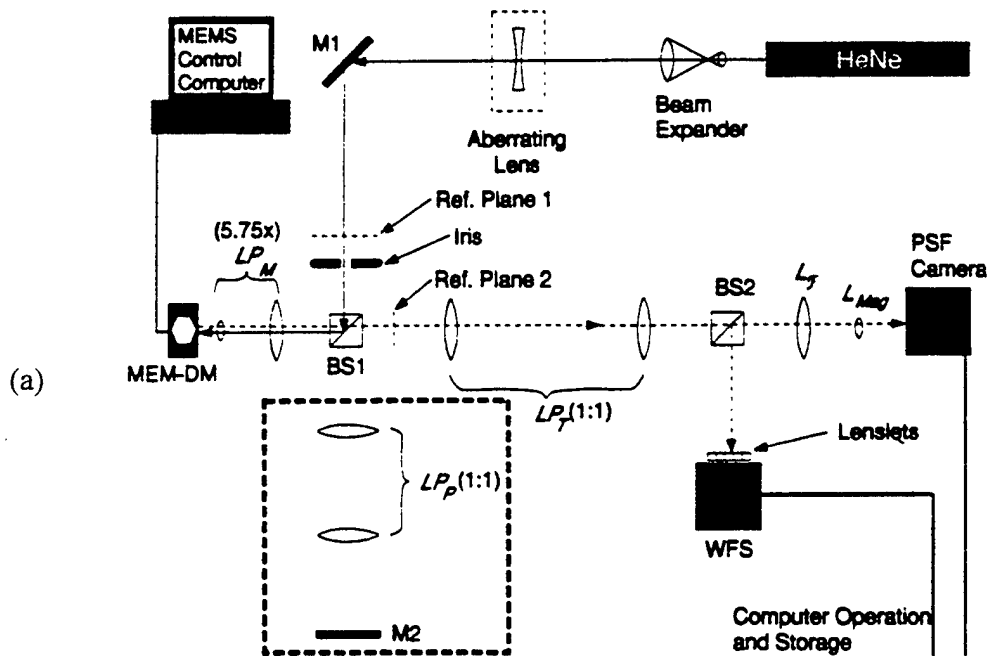


Figure 4.10. (a) Improved experimental system used to investigate micromirror array aberration correction. (b) radially averaged far field intensity versus distance from the central maximum using this system for an uncorrected (aberrated) and a corrected beam reflected from a hexagonal micromirror array as in Figure 2.8 [after Roggemann, et al., 1997].

experiments, mostly in good agreement with simulations, have been reported with this arrangement [Roggemann, et al., 1997].

## 5. CONCLUSION

It is apparent from the computer simulations described in Section 3 and the experimental demonstrations described in Section 4 that, despite their potential advantages in terms of small size, high ruggedness, and low cost, micromirror arrays have serious potential limitations in terms of their small beam steering range and, in particular, their low optical efficiency due to inactive inter-micromirror space, lack of tilt control, and diffraction into undesired orders.

The problem of inactive micromirror space might be addressed using lenslet arrays that focus light only near the center of each micromirror, but this potential solution introduces new problems such as limited lenslet depth of focus and possibly damaging optical intensities at the focus of each lenslet [Gustafson, 1997]. Lack of tilt control might be addressed using variable-blaze micromirror arrays to implement larger beam steering ranges [Burns, et al., January 1997]; however, this potential solution permits only discrete angle steering into allowed diffraction orders. Diffraction into undesired orders is a fundamental optical efficiency problem for segmented micromirror arrays. This problem could in principle be addressed using large numbers of micromirrors with large piston ranges to implement blazing profiles that transfer optical intensity from undesired orders into a desired order [e.g., McManamon, et al., 1996].

However, a more practical solution is likely to involve mirror designs with continuous deformable membranes or facesheets and with electrostatic or thermal micro-actuators [Cowan, 1996; Bifano, et al., 1997; Vdorin, et al., 1997]. A key issue for these designs is maintaining optical quality, i.e., since the mirror is not rigid and since an array of many micro-actuators (each applying approximately a point force) is used to deform the mirror, obtaining a surface of specified shape accurate to at least one-tenth wavelength is problematic. In any case the micro-actuator displacement is typically less than 10 microns, and if for example the aperture size is 1 cm, the maximum steering angle is 1 mrad. However, continuous deformable membrane or facesheet mirrors with

underlying micro-actuators are compact and potentially rugged and low cost, and they could readily implement aberration correction as well as fine beam steering.

## 6. REFERENCES

### Pre-1990

A. R. Oppenheim and J. S. Lim, "The Importance of Phase in Signals," *Proc. IEEE*, Vol. 69, p. 529-541, May 1981.

T. G. Bifano, R. K. Mali, J. K. Dorton, J. Perreault, N. Vandelli, M. N. Horenstein, and D. K. Castanon, "Continuous-Membrane Surface-Micromachined Silicon Deformable Mirror," *Opt. Eng.*, Vol. 35, pp. 1354-1360, May 1987.

B. M. Welsh and C. S. Gardner, "Performance Analysis of Adaptive Optics Systems Using Slope Sensors," *J. Opt. Soc. Am.*, Vol. 6, pp. 1913-1923, 1989.

P. D. Wasserman, *Neural Computing*, VanNostrand Reinhold, 1989.

### 1990

J. M. Florence, T. H. Lin, W. R. Wu, and R. D. Juday, "Improved FBM Device Configurations for Image Correlation," *Proc. SPIE* Vol. 1296, pp. 101-109, Orlando, FL, April 1990.

T. Poggio and F. Girosi, "Neural Networks for Approximation and Learning," *Proc. IEEE*, Vol. 78, pp. 1481-1497, September 1990.

J. M. Florence, "Optical Characteristics of Deformable Mirror Spatial Light Modulators," *OSA Tech. Digest*, Vol. 14, pp. 166-169, 1990.

### 1991

D. L. Begley, ed., "Selected Papers on Free-Space Laser Communications," *Proc. SPIE*, Vol. MS30, March 1991.

D. G. Sandler, T. K. Barrett, D. A. Palamer, R. Q. Fugate, and W. S. Wild, "Use of a Neural Network to Control An Adaptive Optics System for an Astronomical Telescope," *Nature*, Vol. 351, pp. 300-302, 23 May 1991.

W. C. Brown, "Omi-directional Optical Antenna Element," *U.S. Patent* No. 5,033,833, July 1991.

J. Florence, "Phase Only DMDs," Memorandum to Univ. of Dayton, 9 September 1991.

A. H. Suzaki, "An Investigation of the Application of Artificial Neural Networks to Adaptive Optics Imaging Systems," M. S. Thesis, Air Force Institute of Technology, Dayton, OH, December 1991.

R. K. Tyson, *Principles of Adaptive Optics*, Academic Press, 1991.

## 1992

T. A. Rhoadarmer, "Survey of Deformable Mirror Devices," Report UDR-TR-92-63, Univ. of Dayton, April 1992.

S. C. Gustafson, G. R. Little, M. A. Manzardo, and T. S. Puterbaugh, "Stretch and Hammer Neural Networks," *Proc. SPIE*, Vol. 1210, pp. 43-52, April 1992.

R. W. Cohen, "Random Phase Errors and Pseudorandom Phase Modulation of Deformable Mirror Spatial Light Modulators," *Proc. IEEE*, Vol. 1772 No. 34, San Diego, CA, July 21, 1992.

J. L. Horner and P. D. Gianino, "Effects of Quadratic Phase Distortion on Correlator Performance," *Appl. Opt.* Vol. 31, pp. 3876-3878, July 1992.

T. A. Rhoadarmer and S. C. Gustafson, "Beam Shaping Using Segmented Deformable Mirror Devices. Technical Note, Univ. of Dayton, July 1992.

M. Meline and M. Applegate, "Hughes Beam Steering Mirror," Hughes Aircraft Co., Technical Note, Albuquerque, NM, 1992.

W. H. Press, B. P. Flannery, S. A. Teukolsky, and W. T. Vetterling, *Numerical Recipes in C*, Cambridge Univ. Press, 1992.

## 1993

S. C. Gustafson, "Communications Applications for Deformable Mirror Devices," Presentation to USAF Phillips Lab., Albuquerque, NM, 18 March 1993.

L. McMackin, J. D. Gonglewski, B. Venet, M. P. Selonek, J. M. Spinherhe, R. C. Dymalo, K. P. Bishop, and M. Oliker, "Phase-Only Correction of Scintillated Laser Beams: Downrange Experimental Results," *Proc. SPIE*, Vol. 1968, pp. 436-447, Orlando, FL, 14-15 April 1993.

S. C. Gustafson, G. R. Little, and T. H. Lin, "Preliminary Design Review Presentation on Communications Applications for Deformable Mirror Devices," Dayton, OH, 4 August 1993.

S. C. Gustafson, "Neural Networks for Adaptive Optics," Presentation to Special Interest Group on Artificial Intelligence, Dayton, OH, 12 August 1993.

N. Hubin and L. Noethe, "Active Optics, Adaptive Optics, and Laser Guide Stars," *Science*, Vol. 262, pp. 1390-1394, 26 November 1993.

## 1994

S. C. Gustafson, T. H. Lin, and B. Welsh, "Active Diffractive Optical System," presentation to AF Rome Laboratory, Griffiss AFB, 10 January 1994.

O. Band and N. B. Yosef, "Number of Correcting Mirrors Versus the Number of Measured Points in Adaptive Optics," *Opt. Eng.*, Vol. 33, pp. 466-472 February 1994.

N. Yoshikawa and T. Yatagai, "Phase Optimization of a Kinoform by Simulated Annealing," *Appl. Opt.*, Vol. 33, pp. 863-868, February 1994.

T. A. Rhoadarmer, S. C. Gustafson, G. R. Little, and T. H. Lin, "Flexure-Beam Micromirror Spatial Light Modulator Devices for Acquisition, Tracking, and Pointing," *Proc. SPIE*, Vol. 2221, No. 40, Orlando, FL, 7 April 1994.

S. C. Gustafson, G. R. Little, T. A. Tuthill, and T. H. Lin, "Pre-CDR Presentation on Communications Applications for Deformable Mirror Devices," Dayton, OH, 21 April 1994.

T. A. Rhoadarmer, "Characterization of a Flexure-Beam Micromirror Device for Laser Beam Steering and Shaping," M.S. Thesis, Univ. of Dayton, Dayton, OH, May 1994.

S. C. Gustafson, G. R. Little, T. A. Rhoadarmer, V. M. Bright, and J. H. Comtois, "Minimally Connected Piston Micromirror Light Modulator, Revision A," Invention Disclosure. Univ. of Dayton. Dayton, OH, 13 June 1994.

T. A. Rhoadarmer, V. M. Bright, B. M. Welsh, S. C. Gustafson, and T. H. Lin, "Interferometric Characterization of the Flexure Beam Micromirror Device," *Proc. SPIE*, Vol. 2291, pp. 13-23, San Diego, CA, 26-28 July 1994.

T. S. Lin, "Implementation and Characterization of a Flexure-Beam Micromechanical Spatial Light Modulator," *Opt. Eng.*, Vol. 33, pp. 3643-3648, November 1994.

## 1995

R. Clark, J. Karpinsky, G. Borek, and E. Johnson, "High Speed Interferometric Device for Real Time Correction of Aero-Optic Effects," *Proc. AIAA*, Vol. 95-1984, pp. 1-11, San Diego CA, 19-22 June 1995.

G. Vdovin and P. M. Sarro, "Flexible Mirror Micromachined in Silicon," *Appl. Opt.*, Vol. 34, pp. 2968-2972, June 1995.

S. C. Gustafson, G. R. Little, T. A. Tuthill, and T. H. Lin, "Critical Design Review Presentation on Communications Applications for Deformable Mirror Devices," Dayton, OH, 18 July 1995.

T. A. Tuthill, "Hexagonal Micromirror Array Simulations," Technical Report, Univ. of Dayton, 30 September 1995.

J. H. Comtois, V. M. Bright, S. C. Gustafson, and M. A. Michalick, "Implementaton of Hexagonal Micromirror Arrays as Phase-Mostly Spatial Light Modulators," *Proc. SPIE*, Vol. 2641, pp. 76-87, Austin, TX, 24 October 1995.

M. A. Michalick, V. M. Bright and J. H. Comtois, "Design, fabrication, modeling, and testing of a surface-micromachined micromirror device," *Proc. 1995 ASME Inter. Mechanical Eng. Congress*, San Francisco, CA, 12-17 November 1995.

## 1996

E. A. Watson and A. R. Miller, "Analysis of Beam Steering Using Phased Micromirror Arrays," *Proc. SPIE*, Vol. 2687, No. 08, San Jose, CA, 30 January 1996.

S. C. Gustafson, T. A. Tuthill, and E. A. Watson, "Micromirror Arrays for Active Optical Aberration Control," *Proc. SPIE*, Vol. 2687, No. 02 San Jose, CA, 30 January 1996.

P. F. McManamon, T. A. Dorschner, D. L. Corkum, L. J. Friedman, D. S. Hobbs, M. Holtz, S. Liberman, H. Q. Nguyen, D. P. Resler, R. C. Sharp, and E. A. Watson, "Optical Phased Array Technology," *Proc. SPIE*, Vol. 84, pp. 268-298, February 1996.

J. H. Comtois, "Structural Techniques for Implementing and Packaging Complex, Large Scale Microelectromechanical Systems Using Foundary Fabrication Processes," Ph.D. Dissertation, Air Force Institute of Technology, Wright-Patterson AFB, OH, March 1996.

D. P. Kesler, D. S. Hobbs, R. C. Sharp, L. J. Friedman, and T. A. Dorschner, "High-efficiency liquid-crystal optical phased-array beam steering," *Optics Lett.*, Vol. 21, pp. 689-691, 1 May 1996.

L. J. Hornbeck, "Digital Light Processing and MEMS: Reflecting the Digital Display Needs of the Networked Society," *Proc. SPIE/EOS Symp. on Lasers, Optics, and Vision for Productivity in Manufacturing I*, Besancon, France, 10-14 June 1996.

D. M. Burns, "Micromechanical Optical Beam Steering Systems Design and Performance," Ph.D. Dissertation Prospectus, Air Force Institute of Technology, Wright-Patterson AFB, OH, 29 August 1996.



Y. Danziger, E. Hosman, A. A. Friesem, A. W. Lohman, "Multilevel Diffractive Elements for Generalized Wavefront Shaping," *Opt. Eng.*, Vol. 35, pp. 2556-2565, September 1996

S. C. Gustafson, G. R. Little, V. M. Bright, J. H. Comtois, and E. A. Watson, "Micromirror Arrays for Coherent Beam Steering and Phase Control," *Proc. SPIE*, Vol. 2881, No. 05, Austin, TX, 14 October 1996.

W. D. Cowan, "Extension of Foundary Surface Micromachining Process for Fabrication of a Continuous Facesheet Deformable Mirror," Ph.D. Dissertation Prospectus, Air Force Institute of Technology, Wright-Patterson AFB, OH, 16 October 1996.

S. C. Gustafson, G. R. Little, W. A. Bernard, V. M. Bright, J. H. Comtois, and D. M. Burns, "Micromirrors for Multiplexing in Holographic Data Storage Systems," paper MI3, *Opt. Soc. Am.*, Rochester, NY, 21 October 1996.

K. W. Markus and D. A. Koester, "Multi-User MEMS Process (MUMPS), Introduction and Design Rules, Rev. 4", MCNC Technical Report, Research Triangle Park, NC, October 1996.

E. A. Watson, R. J. Feldmann, V. M. Bright, and M. C. Roggeman, "Optical MEMS for Achieving New Laser Radar and Laser Communication Capabilities," Presentation to DARPA, Washington, DC, 3 December 1996.

M. A. Ealey, "Deformable Mirrors Correct Wavefront Errors," *Laser Focus World*, pp. 93-97, December 1996.

M. C. Roggemann and B. M. Welch, *Imaging Through Turbulence*, CRC Press, 1996.

## 1997

D. M. Burns and V. M. Bright, "Micro-electro-mechanical Variable Blaze Gratings," *Proc. IEEE MEMS Workshop*, ISBN 0-7803-3744-1, Nagoya, Japan, 26-30 January 1997.

S. C. Gustafson, G. R. Little, D. M. burns, V. M. Bright, and E. A. Watson, "Microactuated mirrors for beam steering," *Proc. SPIE*, Vol. 7008, No. 10, San Jose, CA, 10 February 1997.

V. M. Bright, J. H. Comtois, J. R. Reid, and D. E. Sene, "Surface Micromachined Micro-Opto-Electro-Mechanical Systems," *IEICE Trans. Electron.*, Vol. E80-C, pp. 206-213, February 1997.

S. C. Gustafson, "Micromirrors for Beam Control," Final Report for AFOSR URRP/IPA, 28 February 1997.

S. C. Gustafson, G. R. Little, and S. R. LeClair, "Laser Beam Shaping Using Deformable Mirrors," *Proc. Int. Conf. On Rapid Prototyping*, San Francisco, CA, 2 April 1997.

R. J. Feldmann, "Concept for Pre-Correction of a Laser Beam projected Through a Turbulent Atmosphere," Thesis presentation, Univ. of Dayton, Dayton, OH, 22 April 1997.

M. C. Roggemann, B. M. Welsh, and R. Q. Fugate, "Improving the Resolution of Ground-Based Telescopes," *Rev. Mod. Phys.*, vol. 69, pp. 437-505, April 1997.

T. G. Bifano, R. K. Mali, J. K. Dorton, J. Pevrenult, N. Vandelli, M. N. Horenstein, and D. A. Castanon, "Continuous-membrane Surface-micromachined Silicon Deformable Mirror," *Opt. Eng.*, Vol. 36, pp. 1354-1360, May 1997.

M. C. Roggeman, V. M. Bright, B. M. Welsh, S. R. Hick, P. C. Roberts, W. D. Cowan, and J. H. Comtois, "Use of Micro-electro-mechanical Deformable Mirrors to Control Aberrations in Optical Systems: Theoretical and Experimental Results," *Opt. Eng.*, Vol. 35, pp. 1326-1338, May 1997.

G. Vdovin, S. Middelhock, P. M. Sarro, "Technology and Applications of Micromachined Silicon Adaptive Mirrors," *Opt. Eng.*, Vol 35, pp. 1382-1390, May 1997.

D. M. Burns, V. M. Bright, S. C. Gustafson, and E. A. Watson, "Optical Beam Steering Using Surface Micromachined Gratings and Optical Phased Arrays," to be published, *Proc. SPIE*, Vol. 3131, San Diego, CA, 30 July 1997.

## APPENDIX

Attached are six articles published in proceedings of professional meetings that directly resulted from the technical effort reviewed in this report:

T. A. Rhoadarmer, S. C. Gustafson, G. R. Little, and T. H. Lin, "Flexure-Beam Micromirror Spatial Light Modulator Devices for Acquisition, Tracking, and Pointing," *Proc. SPIE*, Vol. 2221, No. 40, Orlando, FL, 7 April 1994.

T. A. Rhoadarmer, V. M. Bright, B. M. Welsh, S. C. Gustafson, and T. H. Lin, "Interferometric Characterization of the Flexure Beam Micromirror Device," *Proc. SPIE*, Vol. 2291, pp. 13-23, San Diego, CA, 26-28 July 1994.

J. H. Comtois, V. M. Bright, S. C. Gustafson, and M. A. Michalick, "Implementation of Hexagonal Micromirror Arrays as Phase-Mostly Spatial Light Modulators," *Proc. SPIE*, Vol. 2641, pp. 76-87, Austin, TX, 24 October 1995.

S. C. Gustafson, T. A. Tuthill, and E. A. Watson, "Micromirror Arrays for Active Optical Aberration Control," *Proc. SPIE*, Vol. 2687, No. 02, San Jose, CA, 30 January 1996.

S. C. Gustafson, G. R. Little, V. M. Bright, J. H. Comtois, and E. A. Watson, "Micromirror Arrays for Coherent Beam Steering and Phase Control," *Proc. SPIE*, Vol. 2881, No. 05, Austin, TX, 14 October 1996.

S. C. Gustafson, G. R. Little, and S. R. LeClair, "Laser Beam Shaping Using Deformable Mirrors," *Proc. Int. Conf. On Rapid Prototyping*, San Francisco, CA, 2 April 1997.

Not attached but also directly resulting from the technical effort:

T. A. Rhoadarmer, "Characterization of a Flexure-Beam Micromirror Device for Laser Beam Steering and Shaping," M.S. Thesis, Univ. of Dayton, Dayton, OH, May 1994.

S. C. Gustafson, G. R. Little, T. A. Rhoadarmer, V. M. Bright, and J. H. Comtois, "Minimally Connected Piston Micromirror Light Modulator, Revision A," Invention Disclosure, Univ. of Dayton, Dayton, OH, 13 June 1994.

# **FLEXURE-BEAM MICROMIRROR SPATIAL LIGHT MODULATOR DEVICES FOR ACQUISITION, TRACKING, AND POINTING**

**Troy A. Rhoadarmer, Steven C. Gustafson, and Gordon R. Little**

**Research Institute, University of Dayton**

**300 College Park**

**Dayton, OH 45469-0140**

**and**

**Tsen-Hwang Lin**

**Texas Instruments, Inc.**

**13588 N. Central Expressway**

**Dallas, TX 75265**

**[SPIE Proc. 2221, no. 40, Orlando, FL, 7 April 1994]**

## **ABSTRACT**

The new flexure-beam micromirror (FBM) spatial light modulator (SLM) devices developed by Texas Instruments Inc. have characteristics that enable superior acquisition, tracking, and pointing in communications and other applications. FBM devices can have tens of thousands of square micromirror elements, each as small as 20 microns on a side, each spaced relative to neighbors so that optical efficiency exceeds 90 percent, and each individually controlled with response times as small as 10 microseconds for piston-like motions that cover more than one-half optical wavelength. These devices may enable order-of-magnitude improvements in space-bandwidth product, efficiency, and speed relative to other spatial light modulator devices that could be used to generate arbitrary coherent light patterns in real time. However, the amplitude and phase of each mirror element cannot be specified separately because there is only one control voltage for each element. This issue can be addressed by adjusting the control voltages so that constructive and destructive interference in the coherent light reflected from many elements produces the desired far field coherent light pattern. Appropriate control voltages are best determined using a robust software optimization procedure such as simulated annealing. Simulated annealing yields excellent results, but it is not real time (it may require hours of execution time on workstation-class computers). An approach that permits real-time applications stores control voltages determined off-line by simulated annealing that produce key desired far field coherent light beam shapes. These stored results are then used as training data for radial basis function neural networks that interpolate in real time between the training cases.

## **1. FBM DEVICES**

Figure 1 sketches components typical of the new flexure-beam micromirror (FBM) spatial light modulator (SLM) device developed by Texas Instruments, Inc. This device<sup>1</sup> can have an array of tens of thousands of square micromirror elements, each as small as 20 microns on a side, each spaced relative to neighbors so that optical efficiency exceeds 90 percent, and each individually controlled (using electrostatic attraction) to move in a continuous piston-like

fashion. Each element can be independently positioned within a range of more than one-half micron to within 1 percent precision. The element response time can be as small as 10 microseconds, and the frame rate may range from approximately 100 kHz for small (e.g., 16 by 16) direct-addressed arrays to approximately 4 kHz for larger (e.g., 256 by 256) arrays that employ approximately 10 volt random-access CMOS addressing.

## **2. ACTIVE DIFFRACTIVE OPTICS**

The FBM device may enable order of magnitude improvements in space-bandwidth product, efficiency, and speed relative to other spatial light modulator devices that could be used to generate arbitrary coherent light patterns in real time. Figure 2(a) shows a general active diffractive optical subsystem for beam shaping, aberration control, and optical interconnection that uses two lenses, a polarizing beam splitting cube, and a quarter-wave plate to ensure that the FBM device is efficiently coupled to the Fourier transform plane of the subsystem input and output planes. Figure 2(b) shows an example application in which this subsystem is employed to correct aberrations in a laser beam reflected from an aspheric optical antenna element.<sup>2</sup> In general, the output must be in the far-field or Fourier transform plane of the FBM device so that the FBM device elements (which are large compared to optical wavelengths) function as diffractive structures. The far-field consists of a regular array of diffraction orders with both the envelope shape and the shape of each diffraction order determined by the pattern of address voltages applied to the FBM device elements. The pattern of address voltages can be adjusted to obtain desired far-field beam shapes and also to simulate blazing effects, i.e., the transfer of power into selected diffraction orders.

## **3. FBM ELEMENT RESPONSE**

Although each FBM device element has continuous piston-like motion, the element surface is not flat but has a deformation that is a function of the address (or control) voltage. Figure 3, which is based on data from ref. 3 and which shows phase and amplitude obtained from the Fourier transform of the surface deformation as a function of address voltage, indicates that the FBM device is a phase-mostly device but with significant amplitude variation. Thus measurement (as a function of address voltage) of element deformation, which varies with FBM device design features such as element size and flexure hinge length and thickness, is required for estimating FBM device performance.

## **4. FBM DEVICE CONTROL ISSUES**

Since there is only one control voltage for each FBM device element, phase and amplitude cannot be specified separately. This situation contrasts with that of conventional segmented-mirror adaptive optics,<sup>4</sup> where a smaller number of larger mirrors can each be independently controlled in both phase (which is related to piston-like position) and amplitude (which is related to tilt in two orthogonal directions). The lack of separate FBM device element amplitude and phase control can be compensated for by adjusting the control voltages so that constructive and destructive interference in coherent light reflected from many elements produces the desired far field coherent light pattern. In effect, some fraction of the large number

of FBM device elements available is sacrificed (thus reducing the space-bandwidth product) to realize full adaptive optical capabilities.

## 5. SUPERPIXEL FBM DEVICE CONTROL

Figure 4 shows typical permitted far-field FBM device element responses using data from ref. 3 for one element and for two elements. For a single element the permitted response is phase-mostly as indicated by the near-circular graph (a phase-only response would consist of an origin-centered unit circle graph). For two elements the figure shows that the address voltages may be selected to obtain any complex value within a near-circular graph twice as large as for a single element. This result motivates a superpixel FBM device control algorithm that is capable of generating any desired far-field beam shape:

1. Use a low-pass spatial filter on the FBM device output to define an array of resolvable areas on the FBM device such that each area includes more than one FBM device element.
2. Adjust the address voltages on the FBM device elements within each resolvable area so that the total amplitude and phase is as required and so that the power in unused diffraction orders is minimized.

This procedure is feasible for any desired beam shape, but it is suboptimal because of the required low-pass spatial filtering.

## 6. SIMULATED ANNEALING FBM DEVICE CONTROL

Determining the address voltages that lead to constructive and destructive interference in coherent light reflected from many FBM device elements so as to produce a desired far field beam shape (without low-pass spatial filtering) can be a substantial task. Related tasks have received considerable attention in the literature.<sup>5-10</sup> Figure 5 shows, for a one-dimensional simulation, a desired uniform far field beam shape and the beam shape achieved using address voltages determined from the characteristics shown in Figure 3 such that the phase at each FBM device element matches the phase obtained from the Fourier transform of the desired beam shape. Although correct phase is generally more important than correct amplitude, the result is completely unsatisfactory. Appropriate address voltages are thus best determined using a robust software optimization procedure such as simulated annealing.<sup>11</sup> Figure 6(a) shows a far-field beam shape obtained using simulated annealing optimization when the same uniform beam shape is desired, and Figure 6(b) shows a histogram of root-mean-squared error between the desired and achieved beam shapes for many optimization trials. The results are excellent, and Figure 7 shows that excellent results can also be obtained using simulated annealing optimization for other desired beam shapes. Scheduled annealing applied to the determinization of FBM device address voltages proceeds as follows.

1. Randomly assign address voltages and find the root mean squared (rms) error between the desired and achieved beam shape.

2. Randomly adjust one address voltage and determine the change in rms error due to the adjustment.
3. Accept the adjustment with a probability governed by the reciprocal of one plus a Boltzmann distribution, where the exponential factor in the distribution is the change in rms error divided by a temperature parameter.
4. Repeat steps 2 and 3 while slowly decreasing the temperature parameter until the rms error is acceptable.

If the temperature parameter decrease is sufficiently slow the achieved beam shape approaches a globally optimal result.

## 7. INTERPOLATED ANNEALING FBM DEVICE CONTROL

Although simulated annealing optimization yields excellent results, it is not real time: the results shown in Figure 6 and 7 typically required many hours of execution time on workstation-class computers. An approach that permits real-time applications stores address voltages determined off-line by simulated annealing that produce key desired far field beam shapes. These stored results are then used as training data for Gaussian radial basis function neural networks<sup>12,13</sup> that interpolate in real time<sup>14</sup> between the training cases. The interpolated annealing FBM device control procedure is as follows.

1. Select the training beam shapes.
2. Find (off line) and store the address voltages that produce these shapes with acceptable rms error using FBM device element phase and amplitude versus address voltage data and simulated annealing optimization.
3. Find and store Gaussian radial basis function interpolation surfaces that have one address voltage as the dependent variable and training beam shape samples as the independent variables.
4. Use the stored interpolation surfaces to find (in real time) the address voltages that produce desired beam shapes within the range of the training beam shapes.

This procedure is computationally intensive in training, particularly if the training beam shapes lack symmetry so that their two dimensional cross sections can not be analyzed in terms of one-dimensional projections. However, execution is not computationally intensive and is suitable for real time application.

## 8. APPLICATION POTENTIAL

Arbitrary far field beam shapes can be produced in real time using interpolated annealing FBM device control with no in-principal performance limitations other than those due to the finite number of FBM device elements (which limits the extent to which the rms error between

the desired and achieved beam shapes can be reduced) and the response time of the FBM device (which limits the rate at which the beam shape can be changed). FBM device technology thus enables active diffractive optical devices with potentially widespread and economically important applications in acquisition, tracking, and pointing and more generally in optical communications and processing.

## 9. ACKNOWLEDGMENTS

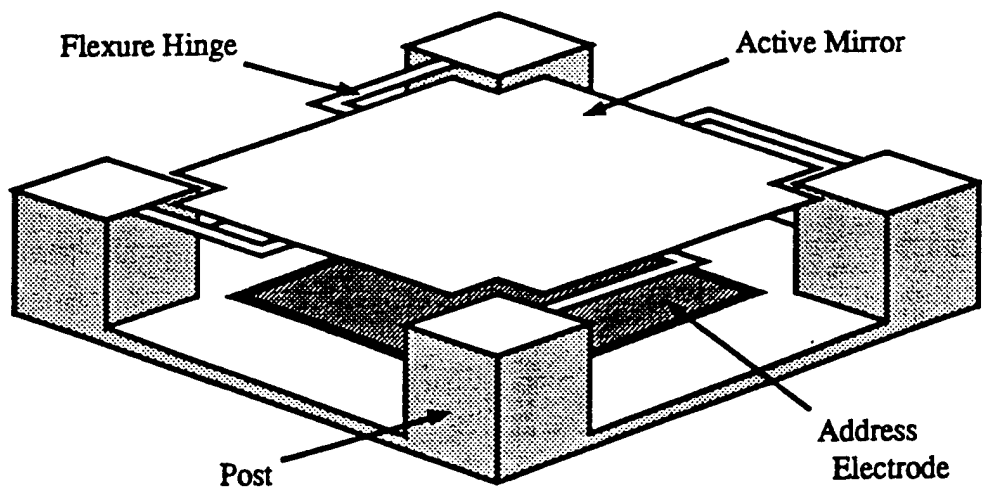
This work was performed on US Air Force Contract No. F33615-92-C-1120 through the Air Force Wright Laboratory (WL/AAAI). Enabling efforts for this work by Dr. Joseph Horner of the Air Force Rome Laboratory, Dr. Douglas Brown of Ft. Mead, MD and Dr. Byron Welsh of the Air Force Institute of Technology are gratefully acknowledged.

## 10. REFERENCES

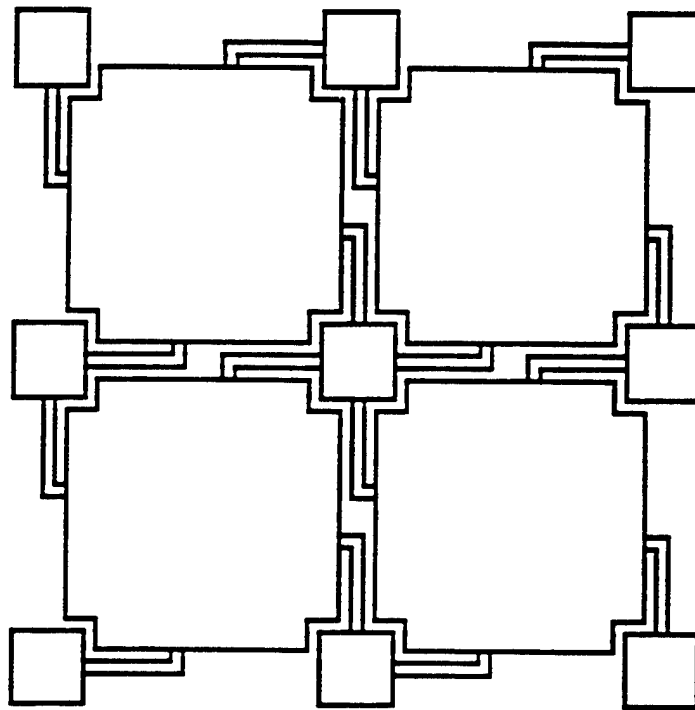
1. J. M. Florence, "Optical Characteristics of Deformable Mirror Spatial Light Modulators," in *Spatial Light Modulators and Applications*, *OSA Tech. Digest* Vol. 14, pp. 166-169, 1990.
2. W. C. Brown, "Omi-directional Optical Antenna Element," *U.S. patent* No. 5,033,833, Jul. 1991.
3. J. M. Florence, *private communication*, Sep. 1991.
4. R. K. Tyson, *Principles of Adaptive Optics*, Academic Press, 1991.
5. J. L. Horner and P. D. Gianino, "Effects of Quadratic Phase Distortion on Correlator Performance," *Appl. Optics* Vol. 31, pp. 2876-2878, 10 Jul. 1992.
6. M. D. Levenson, "Wavefront Engineering for Photolithography," *Physics Today* Vol. 46, pp. 28-30, Jul. 1993.
7. R. D. Juday, "Optimal Realizable Filters and the Minimum Euclidean Distance Principle," *Appl. Optics* Vol. 32, pp. 5100-5111, 10 Sep. 1993.
8. M. P. Dames, R. J. Dowling, P. McKee, and D. Wood, "Efficient Optical Elements to Generate Intensity Weighted Spot Arrays: Design and Fabrication," *Appl. Optics* Vol. 30, pp. 2685-2691, 1 July 1991.
9. R. W. Cohen, "Random Phase Errors and Pseudorandom Phase Modulation of Deformable Mirror Spatial Light Modulators," *Proc. IEEE*, Vol. 1772 no. 34, San Diego, CA, Jul. 1992.



10. J. M. Florence, T. H. Lin, W. R. Wu, and R. D. Juday, "Improved FBM Device Configurations for Image Correlation, *Proc. SPIE* Vol. 1296, pp. 101-109, Orlando, FL; Apr. 1990.
11. W. H. Press, B. P. Flannery, S. A. Tenkolsky, and W. T. Vetterling, *Numerical Recipes in C*, Cambridge Univ. Press, 1988.
12. T. Poggio and F. Girosi, "Neural Networks for Approximation and Learning," *Proc. IEEE* Vol. 78, pp. 1481-1497, Sep. 1990.
13. S. C. Gustafson, G. R. Little, M. A. Manzardo, and T. S. Puterbaugh, "Stretch and Hammer Neural Networks," *Proc. SPIE* Vol. 1210, pp. 43-52, Apr. 1992.
14. D. G. Sandler, T. K. Barrett, D. A. Palmer, R. W. Fugate, and W. J. Wild, "Use of a Neural Network to Control an Adaptive Optics System for an Astronomical Telescope," *Nature* Vol. 351, pp. 300-302, May 1991.



(a)



(b)

Figure 1. Typical flexure-beam micromirror (FBM) device. (a) Single element. (b) Element array.

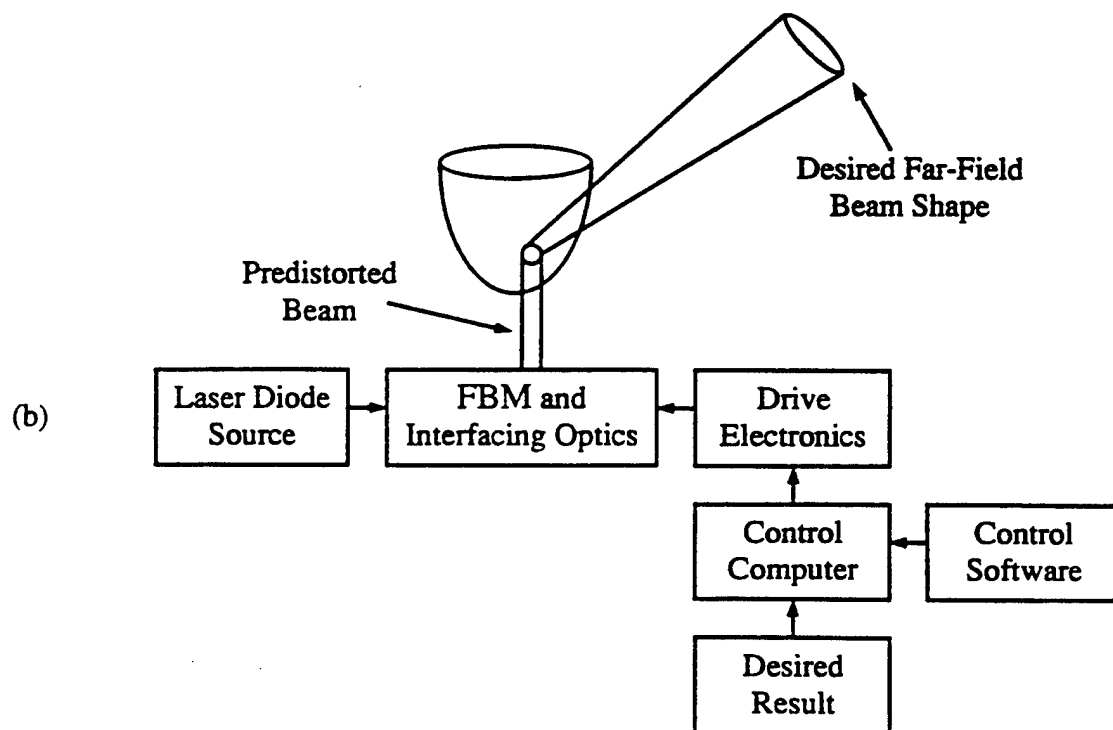
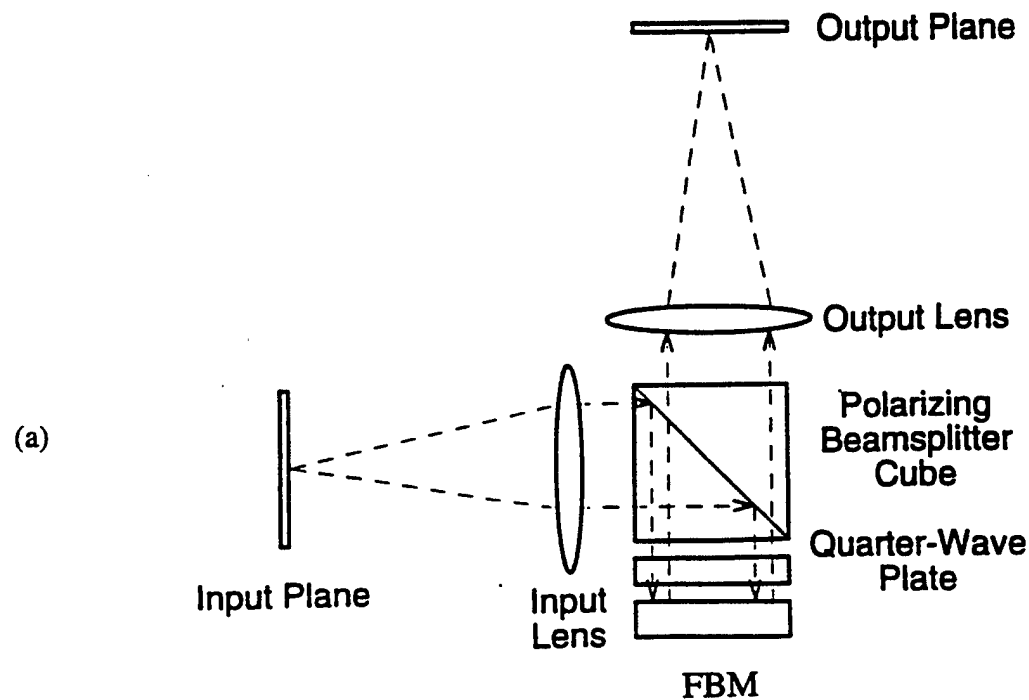


Figure 2. Active diffractive optics. (a) General subsystem for beam shaping, aberration control, and optical interconnection. (b) Example system for optical antenna aberration correction.

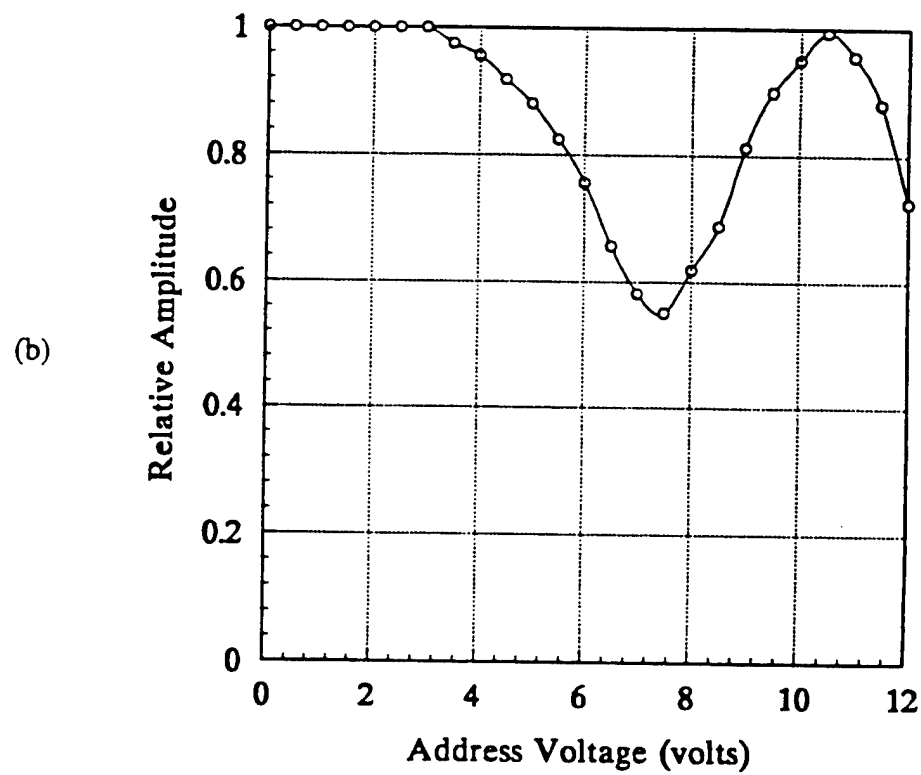
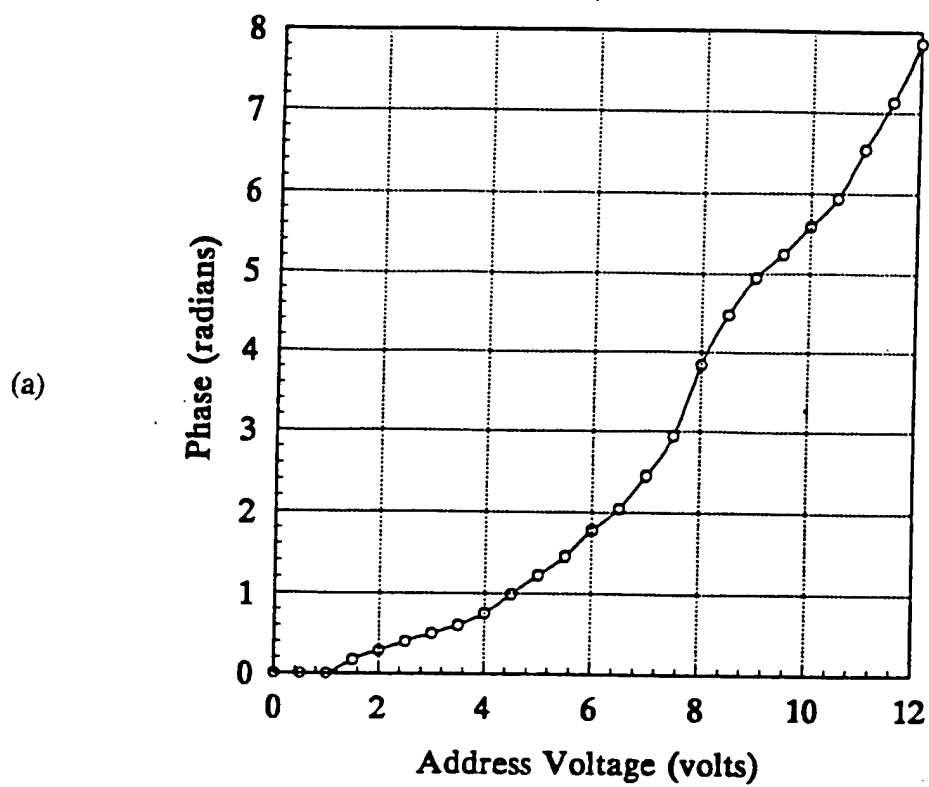


Figure 3. Typical FBM device element response (data from ref. 3). (a) Phase versus voltage. (b) Amplitude versus voltage.

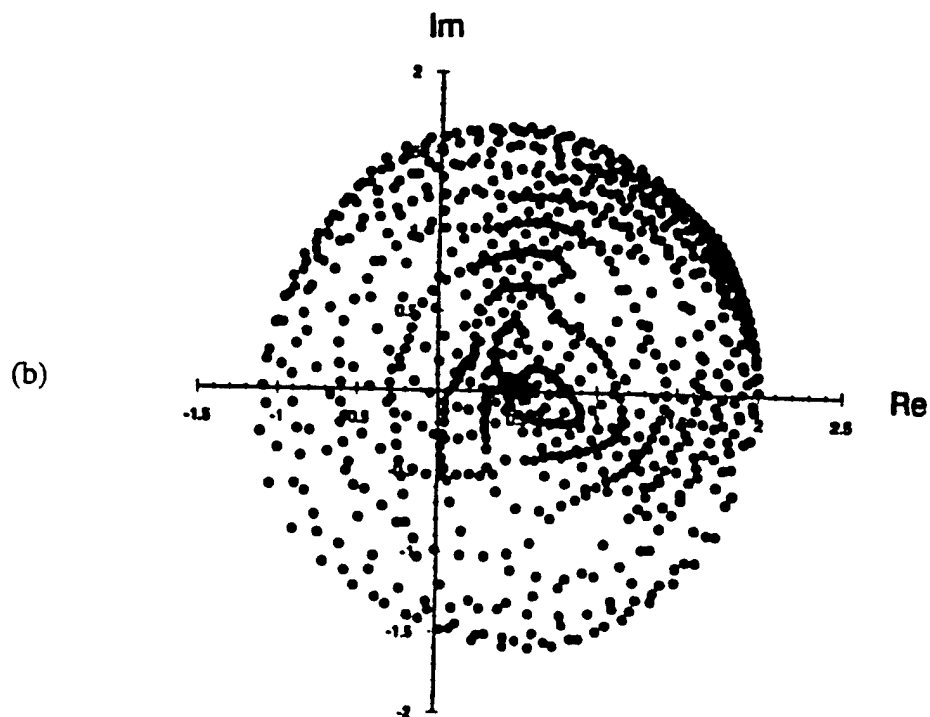
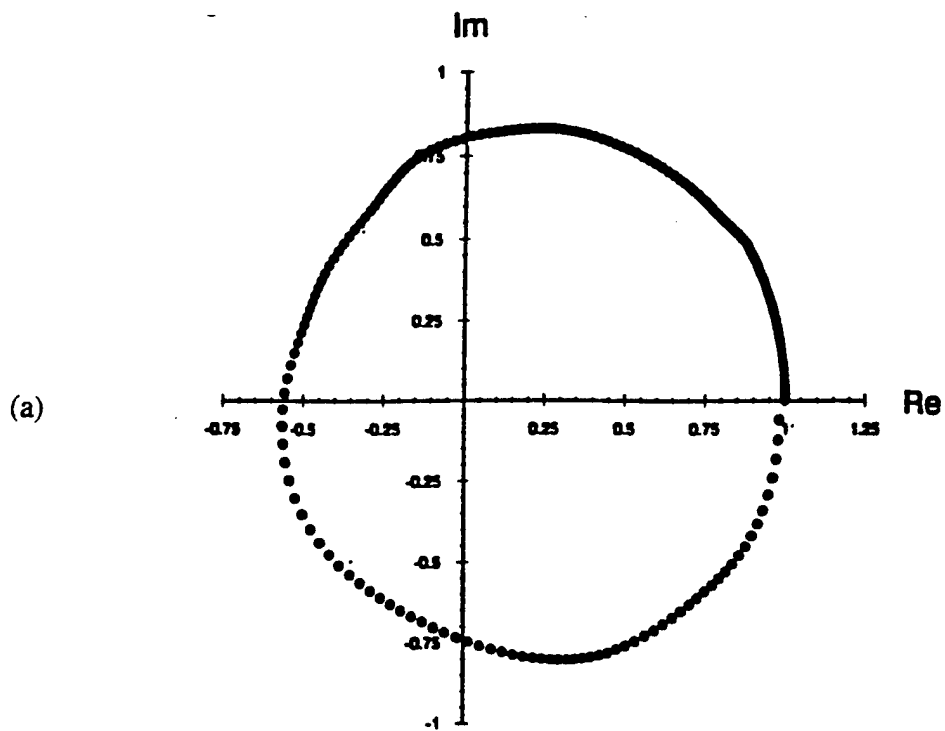


Figure 4. Typical permitted FBM device element complex-value responses. (a) One element.  
(b) Two elements.

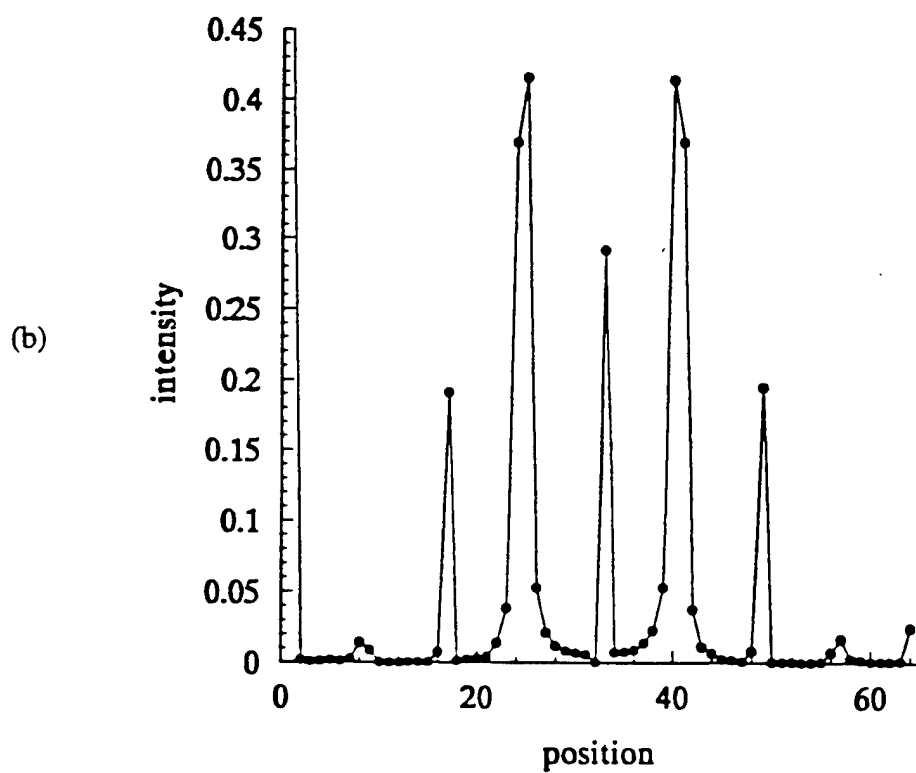
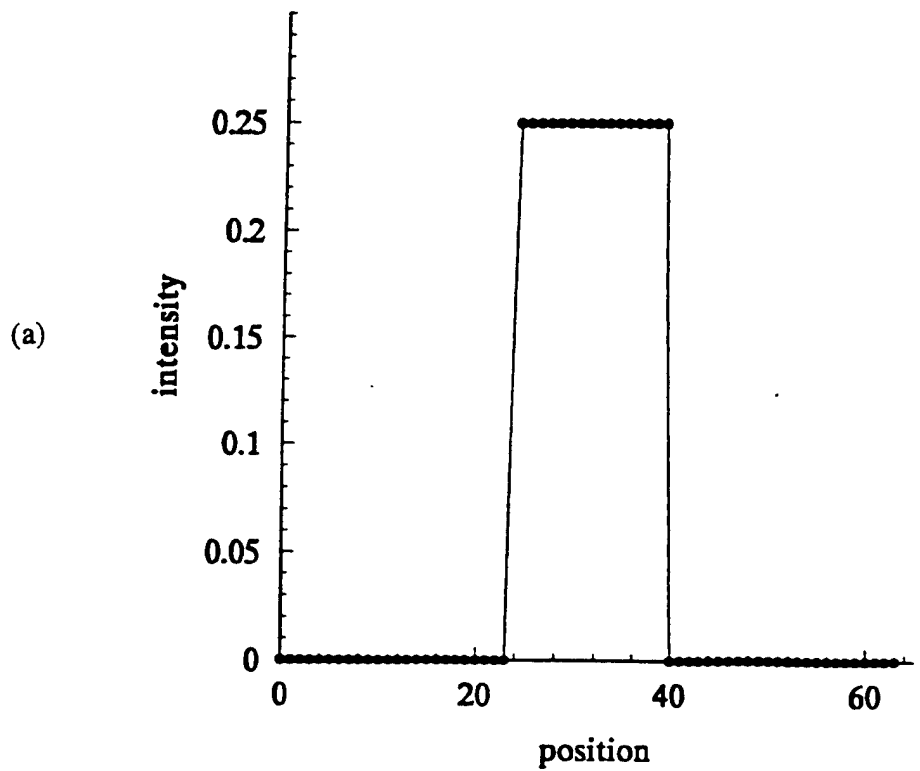


Figure 5. Example far-field beam shaping using address voltages determined by phase matching. (a) Desired beam shape. (b) Achieved beam shape.

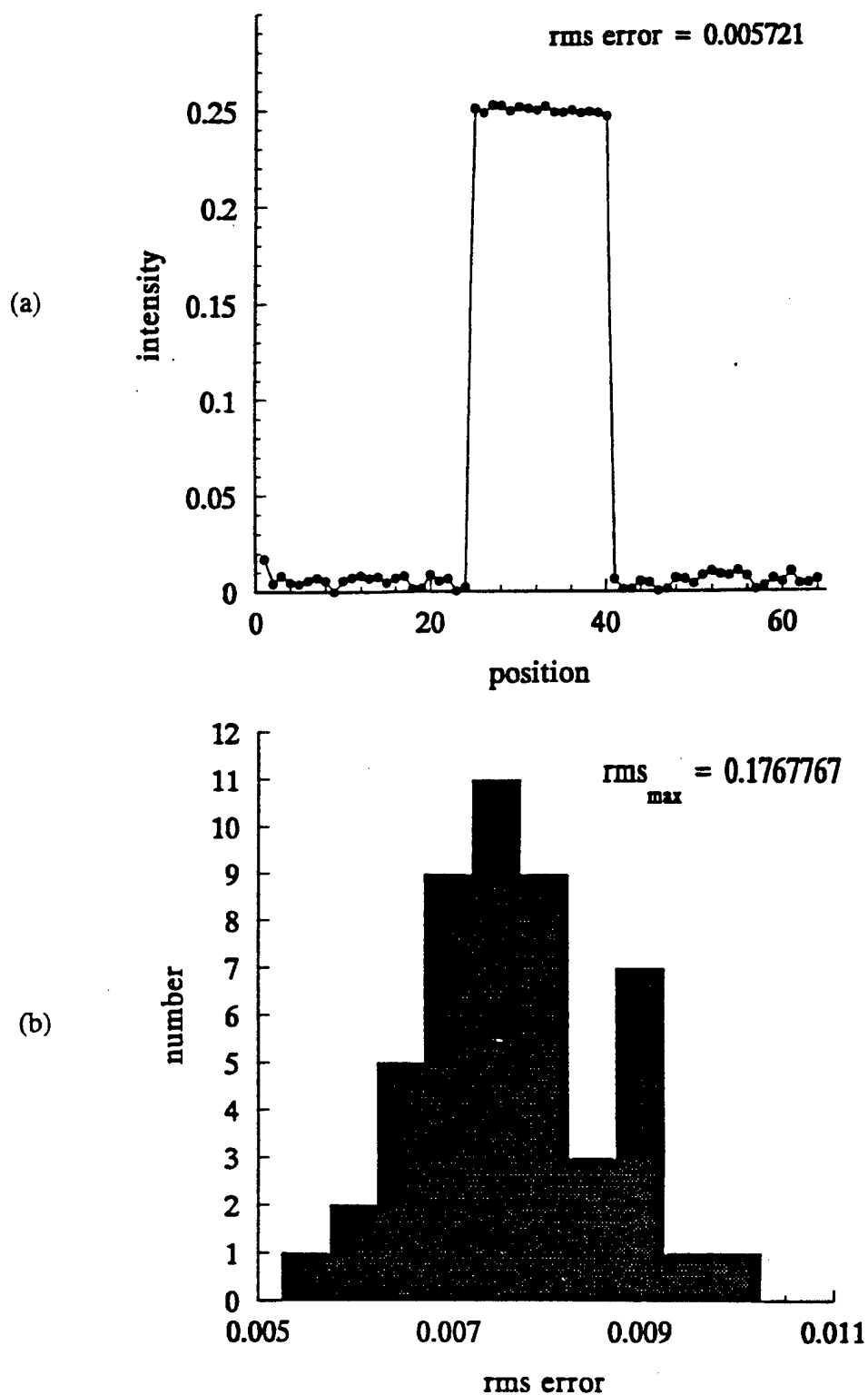


Figure 6. Example far-field beam shaping using address voltages determined by simulated annealing. (a) Achieved beam shape. (b) Histogram of rms error between desired and achieved beam shapes.

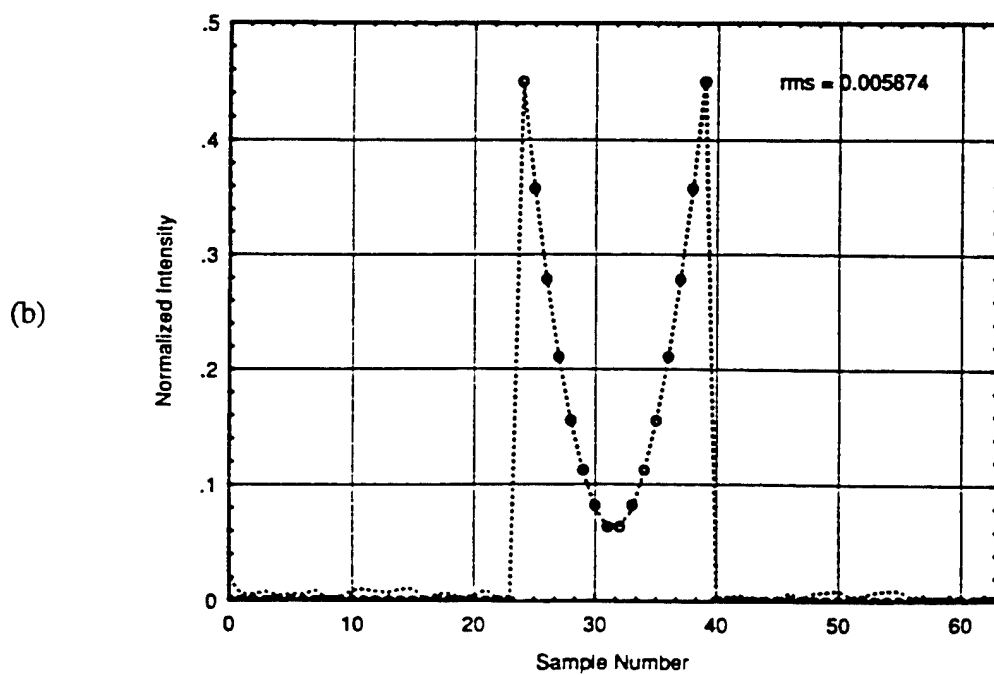
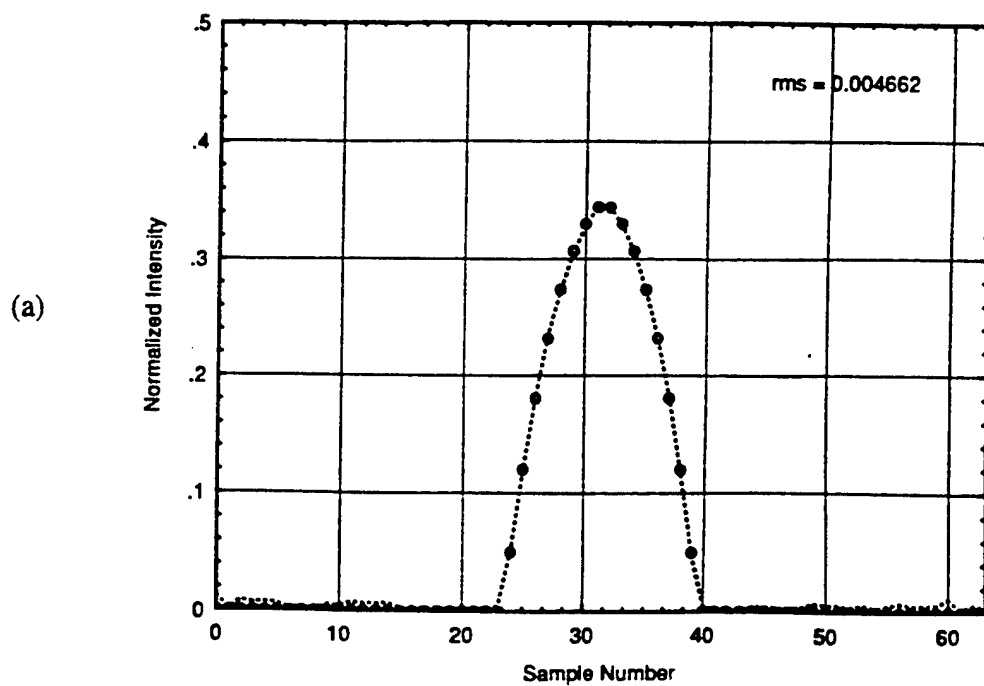


Figure 7. Example far field beam shaping using address voltages determined by simulated annealing: circles indicate desired beam shape; dots indicate achieved beamshape. (a) Negative quadratic beam shape. (b) Positive quadratic beam shape.



## Interferometric characterization of the flexure-beam micromirror device

Troy A. Rhoadarmer\*, Victor M. Bright, Byron M. Welsh, Steven C. Gustafson†, and Tsen-Hwang Lin‡

Air Force Institute of Technology  
Department of Electrical and Computer Engineering  
Wright-Patterson AFB, OH 45433-7765

†Research Institute, University of Dayton  
300 College Park  
Dayton, OH 45469-0140

‡Texas Instruments, Inc.  
13588 N. Central Expressway  
Dallas, TX 75265

### ABSTRACT

The flexure-beam micromirror device (FBMD) developed by Texas Instruments, Inc., is presently being considered for use in communication and imaging systems. This device consists of thousands of individually addressable micromirror elements with phase-mostly responses, greater than 70% active area, and response times of 10 microseconds. Accurate determination of individual mirror element amplitude and phase responses versus address voltage is important for understanding the effect this device will have in the various applications. An experimental setup based on a laser microscopic interferometric technique was used to precisely map the surface displacement of individual mirror elements as a function of address voltage. The test structure consisted of an  $8 \times 8$  array of  $25 \times 25 \mu\text{m}$  square flexure-beam elements. A phase response of greater than  $2\pi$  radians at a wavelength of 632.8 nm was observed for address voltages ranging from 0 to 5.8 V. The phase versus voltage relationship is shown to be nonlinear.

**Keywords:** micromirrors, spatial light modulators, interferometry, adaptive optics

### 1. INTRODUCTION

With spatial light modulators (SLMs) becoming more and more important in optical systems, the need for fast, compact, rugged, and low cost SLMs is increasing. In the last few years Texas Instruments, Inc., has been developing a new phase-mostly SLM, a flexure-beam micromirror device (FBMD), which has these attributes.<sup>1,2</sup> This device, diagrammed in Fig. 1, consists of a two-dimensional segmented array of aluminum microscopic mirror elements fabricated on a silicon substrate using standard CMOS processing and photolithography. The FBMD structure will ultimately consist of a  $256 \times 256$  array of  $37.5 \times 37.5 \mu\text{m}$  elements which can be electrostatically deflected in a piston-like motion using an underlying array of address electrodes. Preliminary FBMD designs have exhibited a continuous phase modulation of greater than  $2\pi$  radians coupled with some degree of amplitude modulation. Individual mirror elements have a response time on the order of 10  $\mu\text{s}$  and frame rates of 4 kHz have been achieved.

The list of potential applications for this device includes laser communications, active adaptive optics, optical correlation, spectrum analysis, optical switching, frequency excision, and optical neural networks.<sup>1-8</sup> Accurate determination of the effect individual elements have on incident wavefronts is important for understanding how this device

\*When this work was performed T.A. Rhoadarmer was a graduate student in the Electro-Optics program at the University of Dayton, Dayton, OH. He is now with the Starfire Optical Range, U.S. Air Force Phillips Laboratory, Kirtland Air Force Base, NM 87117.

will perform in the various applications. In this paper an experimental method of measuring the optical response of individual FBMD elements is discussed and demonstrated.

## 2. FLEXURE-BEAM MICROMIRROR DEVICE TEST STRUCTURE

The FBMD structure used in the experiments, shown in Fig. 2, consisted of an  $8 \times 8$  array of square micromirror elements  $25 \mu\text{m}$  on a side. Fabrication of the device was done using one-micron design rules so the smallest features, the gaps and hinge widths, were  $1 \mu\text{m}$ . The posts had a  $6 \times 6 \mu\text{m}$  cross section and the hinges were  $7.5 \mu\text{m}$  long and  $0.06 \mu\text{m}$  thick. For these hinges the address voltage had to be kept below  $6.0 \text{ V}$  to ensure the mirrors did not collapse. The separation between each active mirror and its electrode was  $2 \mu\text{m}$ . The 64 mirrors of the test structure were connected to a positive potential and suspended above a common addressing electrode that was attached to ground. Although individual addressing of the active mirrors was not possible, this design allowed easy direct addressing of the electrodes and mirrors.

## 3. MICROSCOPIC INTERFEROMETER

The microscopic interferometer shown in Fig. 3 was constructed to accomplish the task of mapping the surface displacement of individual mirror elements. This setup is similar to a Michelson interferometer.<sup>9</sup> A  $2 \text{ mW}$  helium-neon laser is used as the light source. The laser beam passes through a collimator to expand and filter the beam. The cube beamsplitter  $BS_1$  divides this beam into two equal intensity beams: the reference beam is reflected toward the reference mirror  $M_r$ , and the object beam proceeds to the FBMD surface. The object beam passes through a positive achromat lens  $L$ , and its height is adjusted by mirrors  $M_1$  and  $M_2$  so that it enters the vertical standing microscope just above the  $32\times$  microscope objective  $MO$  via the beamsplitter  $BS_2$ . The achromat works in conjunction with the microscope objective to focus the beam to a small spot on the FBMD surface in the image plane of the microscope. By using the achromat a plane wave is returned to the detector from the FBMD and the placement and focusing of the laser spot on the FBMD surface can be monitored through the microscope.

The reference beam and object beam are reflected back upon themselves by their respective mirrors,  $M_r$  and the FBMD surface, and after traveling approximately equal optical path lengths they are recombined at the detector surface, where they interfere. The intensity of the interference is measured by the detector and is dependent on the intensities and relative phases of the two beams. When the portion of the FBMD element where the object beam is focused deflects in response to an address voltage, the phase relationship between the reference and object beams changes and alters the intensity of the interference. The amount of FBMD element displacement can be determined by measuring this change in intensity.

The aperture  $A$  allows only the center section of the interference pattern to pass onto the detector, blocking the outlying edges of the interference pattern and all background light. Since the object beam is split twice more than the reference beam by  $BS_2$ , a neutral density filter  $ND$  is placed in the reference beam so that the intensity of the reference beam is only slightly larger than the intensity of the object beam, which increases the visibility of the intensity modulation and provides more accurate results. The tip-tilt mount under the FBMD is used to adjust the device in the image plane of the microscope, ensuring that the object beam is reflected directly back upon itself. The XY translation stages can move in  $0.1 \mu\text{m}$  increments and are used to position the device under the laser spot. A laser spot diameter of  $4\text{--}5 \mu\text{m}$  has been achieved on the FBMD surface with this setup, allowing small sections of the  $25 \times 25 \mu\text{m}$  mirror elements to be probed. By positioning the spot at several locations on the FBMD element, as shown in Fig. 4, and determining the displacement versus voltage response at each location, the deformation of the entire pixel as a function of address voltage can be mapped.

A signal generator was used to drive a  $40$  to  $50 \text{ Hz}$  sinusoidal voltage signal across the FBMD active mirror and its underlying address electrode. This signal caused the mirror element to deflect, lengthening the optical path traveled by the object beam and modulating the intensity of the light incident on the detector. The detector output current, which is proportional to the intensity of light incident on the detector surface, is sent through a current to voltage transducer to amplify the signal while ensuring linear operation of the detector. The amplified detector signal and the drive signal are input to a LeCroy 7200 Digital Storage Oscilloscope for data acquisition. A typical scan of the

detector output is shown in Fig. 5 with its corresponding drive signal. Each scan collects 4000 data points over 0.2 seconds. The detector signal is negative because an inverting amplifier is used. From this set of data the deflection versus address voltage of the point on the FBMD surface where the object beam is focused is determined.

#### 4. ANALYSIS OF THE DATA

Phasor representation of the reference and object beams was used to analyze the detector output. This model is shown schematically in Fig. 6, where  $R$  is the reference phasor incident on the detector,  $D$  is the object phasor incident on the detector,  $\theta$  is the relative phase angle between the two beams, and  $S$  is the sum of the two beams. The angle  $\theta$  is proportional to the deflection of the FBMD. The phasor  $R$  represents light from the reference leg of the interferometer and light reflected from the surfaces of optical components in the system. The phasor  $D$  represents only the light reflected from the FBMD. Both beams are planar across the aperture  $A$  and are therefore planar at the detector. The light intensity at the detector surface is given by

$$I = |S|^2 = |R + D|^2 \quad (1)$$

Choosing  $R$  to point along the  $x$ -axis and  $D$  to point in the  $\theta$ -direction as shown in Fig. 6 permits the definitions

$$R = \hat{x}R \quad (2)$$

$$D = \hat{x}D \cos \theta + \hat{y}D \sin \theta \quad (3)$$

Substituting Eq. (2) into Eq. (1) yields

$$\begin{aligned} I &= |\hat{x}(R + D \cos \theta) + \hat{y}D \sin \theta|^2 \\ &= (R + D \cos \theta)^2 + (D \sin \theta)^2 \\ &= R^2 + 2RD \cos \theta + D^2 \end{aligned}$$

The values of  $R$  and  $D$  can be determined by first blocking the reference beam and then the object beam and measuring the detector signal in each case. However, reflections from optical surfaces (i.e., beamsplitters, lenses, and filters) complicate this method. It is easier to obtain the minimum and maximum values of the intensity,  $I_{min}$  and  $I_{max}$ , directly from the detector output signal. From Fig. 6, these values are

$$\sqrt{I_{max}} = R + D \quad (4)$$

$$\sqrt{I_{min}} = R - D$$

Combining these relationships with Eq. (3) yields

$$\theta = \arccos \left( \frac{2I - I_{max} - I_{min}}{I_{max} - I_{min}} \right) \quad (5)$$

A drawback of this approach is that values of  $I_{max}$  and  $I_{min}$  must be found from the detector output, which is possible as long as  $\theta$  sweeps past 0 and  $\pi$  radians during a cycle of the drive signal. If  $\theta$  experiences full  $2\pi$  modulation, this condition is guaranteed. However, it was found that for laser wavelengths of 632.8 nm,  $2\pi$  modulation does not always occur for address voltages under 6 V, the safety limit for the device used in the experiments. This problem was circumvented by the fact that the setup was not isolated. Air currents along the beam paths caused the detector output to 'float' by altering the zero-voltage phase relationship between R and D. This effect was slow compared to the frequency of the driving signal and can be considered constant over the 0.2 second scan time. When collecting data, detector signals which clearly contained  $I_{max}$  and  $I_{min}$ , such as the data shown in Fig. 5, were acquired. When the detector signals did not contain both  $I_{max}$  and  $I_{min}$  these values were determined at the time of acquisition by observing the signal over a few minutes and recording the maximum and minimum detector output. By overcoming the problem in this manner, the relative zero-voltage phase at the sample points on the FBMD mirror cannot be determined accurately. Presently it is assumed that the mirror surface is flat so that all zero-voltage phases are equal. This assumption is not ideal and further work must be done to make it unnecessary.

Data analysis was done with Mathematica on a Sparc IPX workstation. Once the raw data of Fig. 5 was acquired, some pre-processing was performed before  $\theta$  was calculated. First average cycles of the drive and detector signals were computed and then the detector signal was shifted to align with the drive signal. This shift was necessary because apparently either capacitance in the connection between the signal generator and the device delayed the action of the drive signal on the FBMD or the response time of the detector circuit delayed the output of the signal to the oscilloscope. This delay must be accounted for to obtain the correct phase-voltage relationship. The shift was small (about 0.1 ms) and was performed by aligning the maximum point of the drive signal with the next local maximum or minimum of the detector signal. These maxima and minima were found using a Fourier transform smoothing routine that filters out frequencies in the signals which were not harmonics of the fundamental frequency. The averaged and shifted signals are shown in Fig. 7. Finally, the phase angle  $\theta$  was calculated from this data using Eq. (5). This equation outputs phase in the range 0 to  $\pi$  as shown in Fig. 8a. The graph of phase must be smooth since the drive signal is smooth. Therefore, the output from Eq. (5) must be pieced together to create a smooth graph of phase. The result of this process is shown in Fig. 8b. Finally, phase can be plotted against the address voltage as shown in Fig. 9.

After the data for all the sample points on a single micromirror element have been analyzed, the results can be combined as in Fig. 10 to show how the entire active mirror surface responds to address voltage  $V_a$ . For  $V_a = 0$  V all points are assumed to be in the same plane. Data was collected from nine of the 64 elements of the test structure (Fig. 2). A comparison of the nine tested elements revealed that the deflections at 5.5 V ranged from 0.153  $\mu\text{m}$  to 0.294  $\mu\text{m}$  with the average tending toward the higher end of that range.

## 5. SUMMARY

This paper presents an experimental method of measuring the optical response of individual FBMD elements. The analyzed data showed a wide range of responses from the nine tested elements with mirror deflections ranging from 0.153  $\mu\text{m}$  to 0.294  $\mu\text{m}$  for a 5.5 V address voltage. The device tested was one of many designs fabricated up to this time. Also this device was constantly pushed near its voltage limit to obtain as near a  $2\pi$  phase shift as possible and the strain induced by operating it in this manner may have weakened or damaged the flexure hinges. It is anticipated that future designs and materials will produce more favorable results. The data presented does demonstrate an encouraging result – a  $2\pi$  phase shift at the helium-neon wavelength (632.8 nm) is possible with low voltage CMOS electronics.

## 6. ACKNOWLEDGMENTS

This work was performed on US Air Force Contract No. F33615-92-C-1120 through the Air Force Wright Laboratory (WL/AAAI). Enabling efforts for this work by Dr. Joseph Horner of the Air Force Rome Laboratory and Dr. Douglas Brown of Ft. Mead, MD are gratefully acknowledged.

## 7. REFERENCES

1. J.M. Florence, J.B. Sampsel, L.J. Hornbeck, W.R. Wu, and R.O. Gale, "A new deformable mirror spatial light modulator for phase modulation applications", *Proc. 1988 Conference on Pattern Recognition for Advanced Missile Systems*, GACIAC PR88-04, pp. 379-386, Huntsville, AL, 1988.
2. R.M. Boysel, J.M. Florence, and W.R. Wu, "Deformable mirror light modulators for image processing", *Proc. SPIE*, Vol. 1151, pp. 183-194, 1989.
3. R.M. Boysel, "A  $128 \times 128$  frame-addressed deformable mirror spatial light modulator", *Optical Eng.*, Vol. 30, pp. 1422-1427, Sept. 1991.
4. D.A. Gregory, R.D. Juday, J. Sampsel, R. Gale, R.W. Cohn, and S.E. Monroe, Jr., "Optical characteristics of a deformable-mirror spatial light modulator", *Optics Lett.*, Vol. 13, pp. 10-12, Jan. 1988.
5. L.J. Hornbeck, "Deformable-mirror spatial light modulators", *Proc. SPIE*, Vol. 1150, pp. 86-103, 1989.
6. L.J. Hornbeck, "Current status of the digital micromirror device (DMD) for projection television applications", presented at *International Electron Devices Meeting*, Washington, DC, Dec. 1993.
7. J.M. Younse, "Mirrors on a chip", *IEEE Spectrum*, pp. 27-31, Nov. 1993.
8. T.A. Rhoadarmer, "Survey of deformable mirror devices", *Report UDR-TR-92-63*, University of Dayton, Dayton, OH, Apr. 1992.
9. M. Born and E. Wolf, *Principles of Optics*, Pergamon Press, Oxford, 1980.

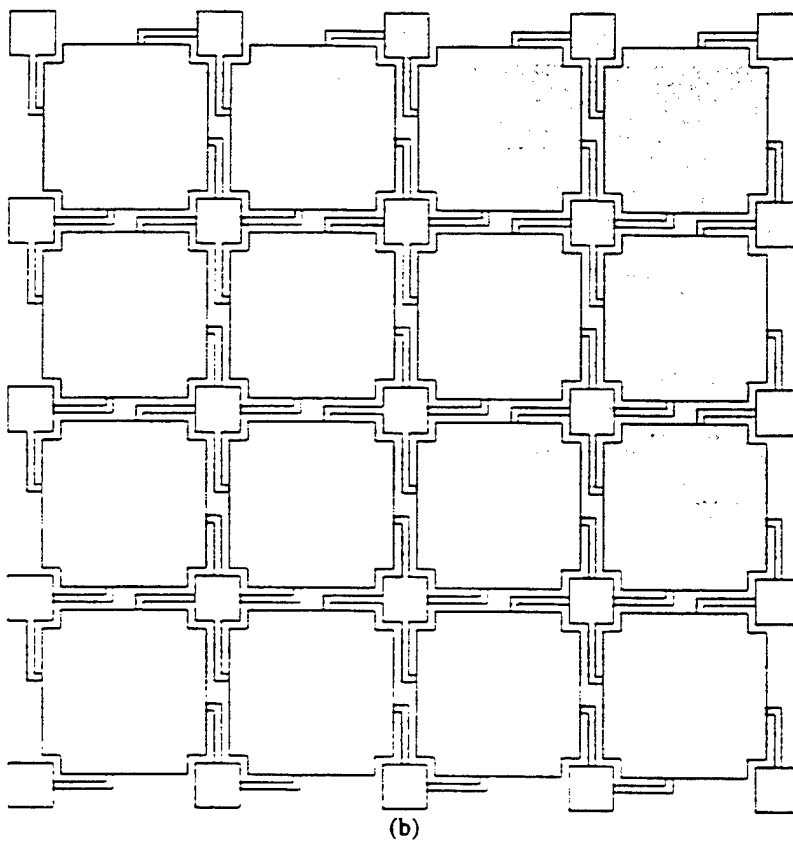
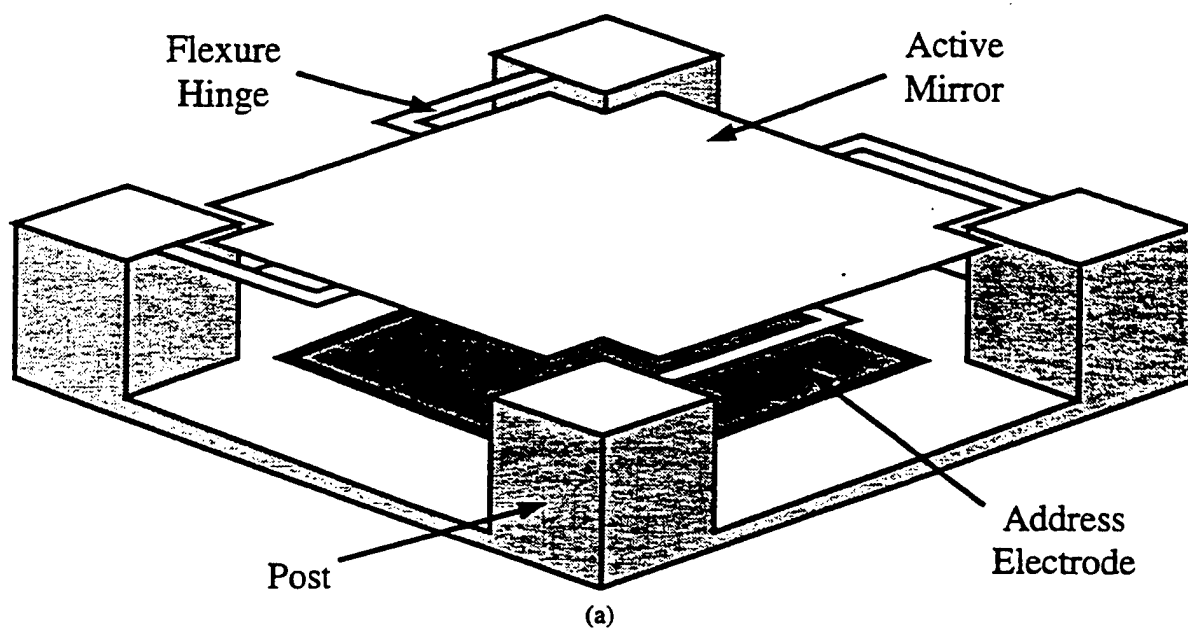


Figure 1. Flexure-beam micromirror device. (a) A single element and (b) orientation of elements in an array for high optical efficiency.

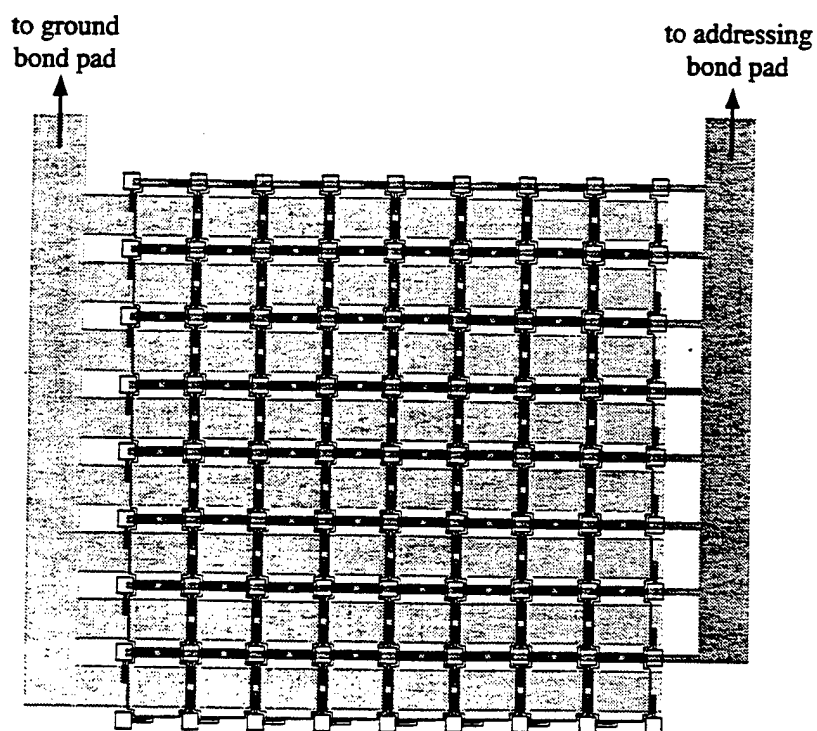


Figure 2. The FBMD structure tested in the experiments. The shaded regions show how the underlying addressing is accomplished.

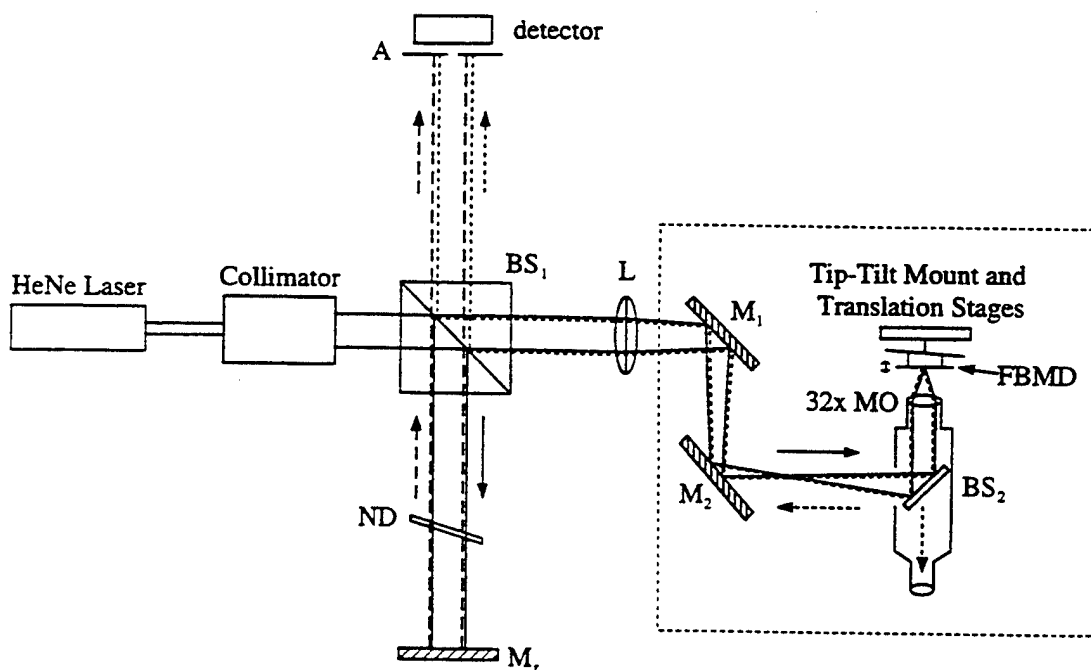


Figure 3. Diagram of the interferometric microscope experimental setup. The dashed line is the return reference beam and the dotted line is the return object beam. The objects in the dotted box are perpendicular to the rest of the setup.

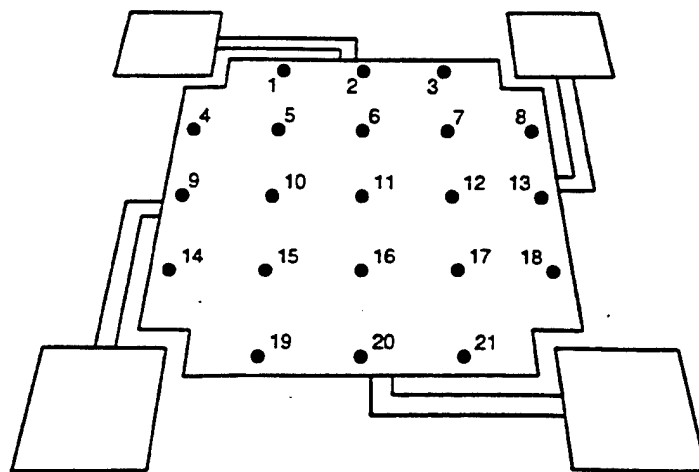


Figure 4. The locations of laser probe spots on a FBMD mirror element. Measurements were taken at these locations.

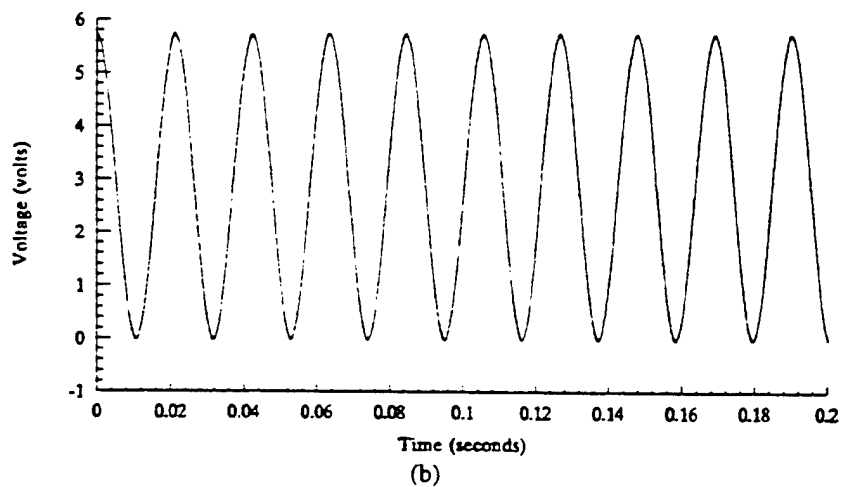
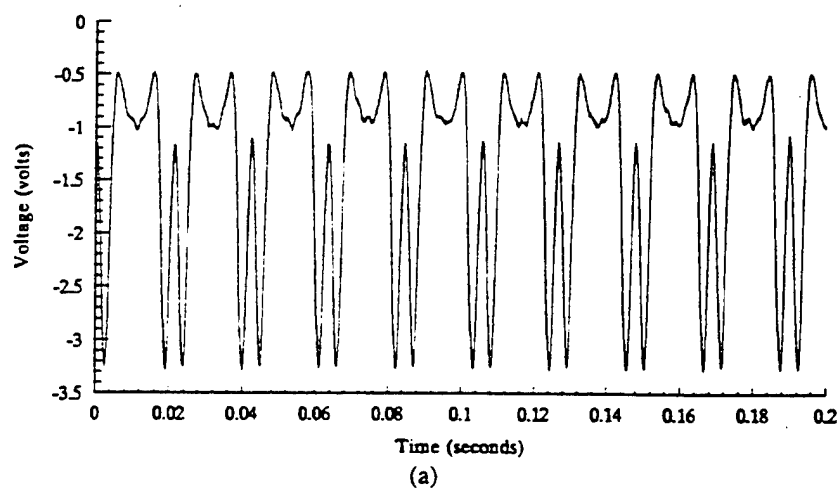


Figure 5. (a) The amplitude signal from the detector showing the modulation of light intensity and (b) the corresponding drive signal.



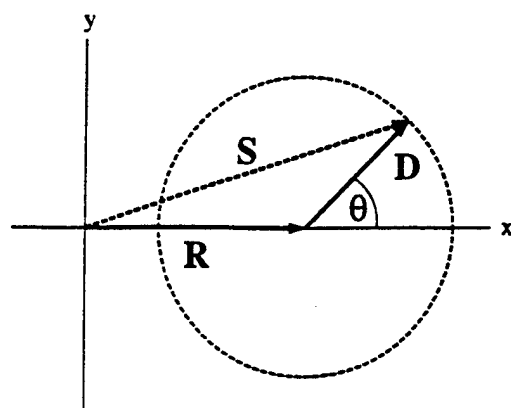
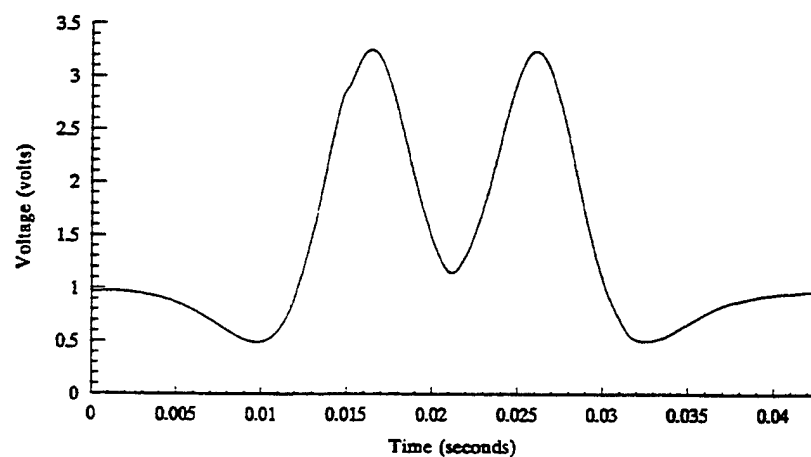
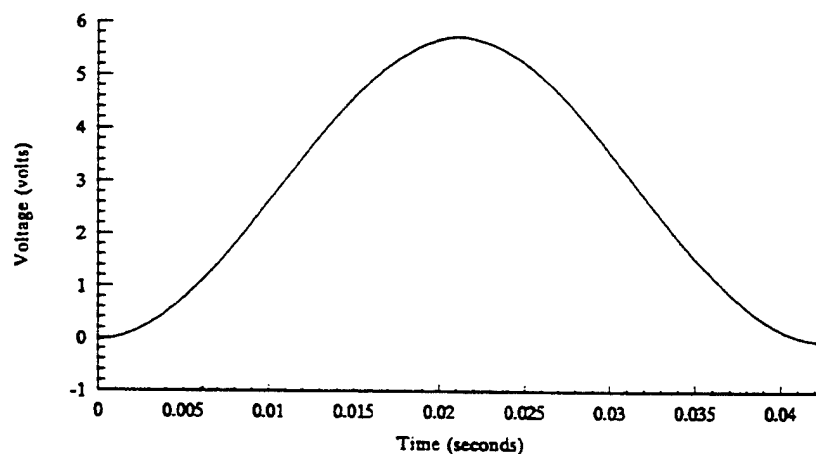


Figure 6. Phasor representation of the interference between the reference beam R and the object beam D.



(a)



(b)

Figure 7. After processing, the averaged, smoothed, and shifted (a) detector output and (b) corresponding drive signal.

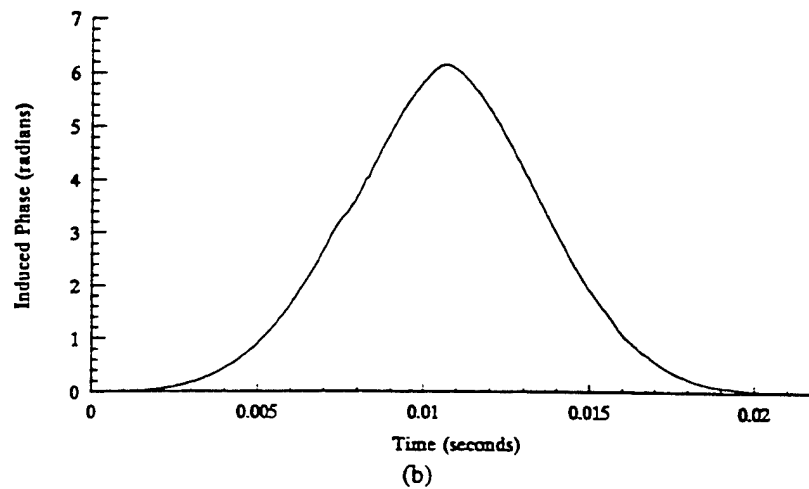
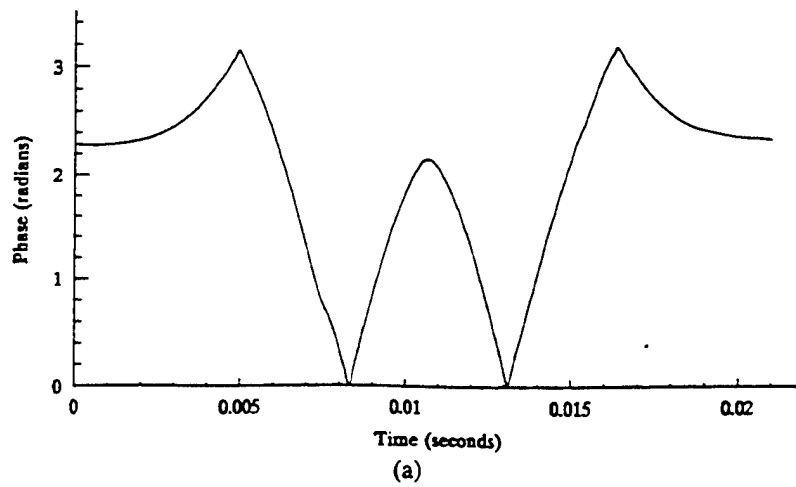


Figure 8. Processed phase output (a) with  $\pi$  ambiguity present, and (b) after accounting for the  $\pi$  ambiguity. The phase at the beginning of the drive cycle is set to zero.

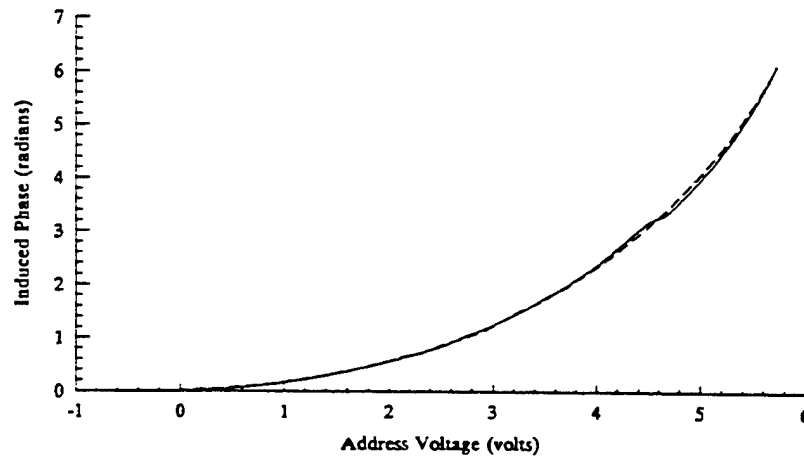


Figure 9. Phase vs. address voltage. The solid line corresponds to phase as a function of increasing address voltage and the dashed line corresponds to phase as a function of decreasing address voltage.

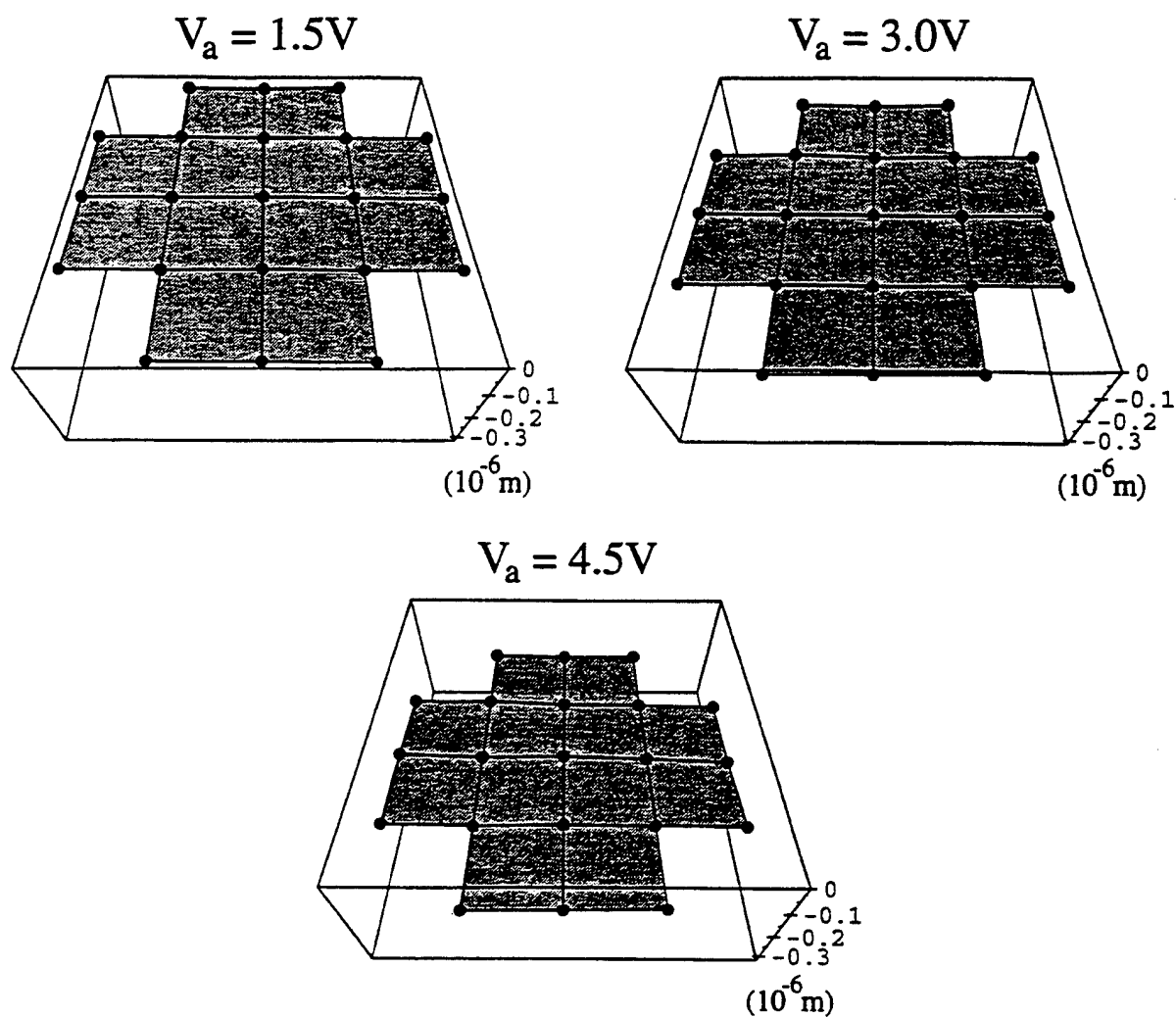


Figure 10. Combined results of deflection vs. address voltage  $V_a$ , for all 21 sample positions. Deflection is measured in micrometers, and for  $V_a = 0V$  all positions are set to zero.

# Implementation of hexagonal micromirror arrays as phase-mostly spatial light modulators

John H. Comtois, Victor M. Bright, Steven C. Gustafson, and M. Adrian Michalick

Air Force Institute of Technology  
Department of Electrical and Computer Engineering  
Wright-Patterson AFB, OH 45433-7765

University of Dayton Research Institute  
Dayton, OH 45469-0150

## ABSTRACT

Hexagonal micromirror arrays and associated test structures have been fabricated using a commercial surface-micromachining process. The hexagonal micromirrors are 50  $\mu\text{m}$  across and are arranged in a hexagonal array of 127 mirrors with 75  $\mu\text{m}$  center-to-center spacing between nearest micromirrors. Each micromirror is supported by three flexure hinges, each of which surrounds one third of the micromirror perimeter. Each micromirror in the array can be displaced independently through a vertical distance of over 1  $\mu\text{m}$  by a voltage applied to an underlying address electrode. The flexures and other highly diffracting or poorly reflecting areas can be covered by a stationary reflecting plate with holes that expose the moving micromirrors. These micromirror arrays thus function as efficient phase-mostly spatial light modulators. Applications for these micro-opto-electro-mechanical systems include optical processing, coherent beam shaping, and adaptive optics. This design has several important advantages. First, the hexagonal micromirror and array geometries maximize the active surface area of the array. Second, the use of three flexures instead of four, as is typical for square phase-mostly micromirrors, lowers the required drive voltage. Third, the reflecting cover plate ensures that light efficiency is maximized and that a substantial stationary coherent reference plane is provided. Design considerations for fabricating the arrays in commercial surface micromachining processes are discussed. The deflection versus voltage behavior of the hexagonal micromirror is determined analytically and experimentally. Test results are used to design the next generation array.

**Keywords:** micromirror, micromachining, spatial light modulator

## 1. INTRODUCTION

Piston-style micromirrors are finding increasing application as components of micro-opto-electro-mechanical systems (MOEMS), and are being fabricated in a variety of processes. This paper presents the design, fabrication, modeling, and testing of the micromirror array shown in Fig. 1. The array was fabricated through a commercial polycrystalline silicon (polysilicon) micro-electro-mechanical systems (MEMS) foundry process. This foundry is intended for prototyping MEMS designs, not for production of final systems. The advantages of using a prototyping foundry are the extremely low cost and reasonable turn-around time. This allows a design to go through several generations and a large number of variations in a short time. The details of the fabrication process are presented to illustrate their impact on the hexagonal micromirror array design. A disadvantage of this approach is that the operational characteristics of many MEMS devices are process dependent, so devices may have to be re-designed for the final production process and have to go through additional testing and adjusting. Also, users of a foundry have little control over important design parameters such as layer thicknesses and choice of materials, so their designs are constrained by more than just the design rules. An analytical model is used to describe the displacement versus address voltage for a micromirror, and its predictions are compared to experimental results measured with a microscope-based laser interferometer. The results of this testing are used to explain the changes made to the micromirror array for the second generation.

## 2. MICROMIRROR APPLICATIONS

Applications of micromirror arrays include active aberration correction for a variety of optical devices such as free space optical communication systems and optical correlation [1]. The micromirror array presented in this paper is designed as a Spatial Light Modulator (SLM) [2]. Spatial Light Modulator-based optical processing can be used in systems for non-cooperative target recognition or target acquisition, tracking and pointing.

Potential applications for SLMs are best assessed in terms of performance simulations of far-field irradiance patterns. As a simple example, consider a hexagonal array of 127 hexagonal micromirrors where the center-to-center spacing of nearest

neighbor hexagons is 1.5 times the corner-to-corner width of the hexagons. Figure 1 shows an example of such an array. The mirrors are individually addressable; and in this example they are connected to operate as concentric rings. The center and surrounding rings of 6, 12, 18, 24, 30, and 36 hexagonal mirrors are assigned phase angles of  $2\pi y_1, 2\pi y_2, \dots, 2\pi y_7$ , respectively; and the non-moving space between the mirrors is assigned an amplitude  $V$ . Figure 2 shows the far field irradiance for an array illuminated by a constant, coherent, collimated beam at normal incidence, plotted as a function of  $y_1, y_2, \dots, y_7$ , for various deflections of the mirrors. As this example shows, such an array can have a significant, controllable effect on the far field irradiance. Each mirror in the array is individually addressable, so more complex control over the far field irradiance is possible, and the small size of each mirror means they can be moved rapidly into position for accurate real-time control of the phase front.

### 3. MICROMIRROR ARRAY DESIGN AND FABRICATION

The design of the 127-mirror hexagonal array involved balancing the constraints of the fabrication process and the limitations of the materials used in that process, with the requirements for an efficient, flexible mirror array architecture. Ideally, each micromirror would have a perfectly flat surface with 100% reflectivity, and have identical, low stiffness flexures for zero-tilt vertical motion at low address voltages. The mirrors would completely cover the array surface with no gaps between them, and would have address wiring that could be extended to any depth and which would not affect micromirror properties. Also, the mirror addressing and drive circuitry would be integrated on-chip, simplifying the electrical and physical connection to the rest of the system. The realities of a surface-micromachining process force the designer to make tradeoffs to achieve a system that can be fabricated and also have reasonable performance characteristics.

#### 3.1. Fabrication process

The design of the individual micromirrors is constrained by the limitations of the fabrication process; so an overview of that process is necessary to explain some of the design choices. The mirrors presented in this paper were fabricated through the ARPA-sponsored Multi-User MEMS Process (MUMPS) fabrication service [3]. This is a three-layer surface-micromachining polysilicon process. The lowest polysilicon layer, poly0, is non-releasable and is used for address electrodes and local wiring. The upper two polysilicon layers, poly1 and poly2, can be released to form mechanical devices. The release of the upper two polysilicon layers is achieved by etching away the two layers of phosphosilicate glass (referred to as 'oxide' layers) that are deposited between the polysilicon layers. The MUMPS process allows gold to be deposited on top of the poly2 layer to form reflective surfaces, low resistance wiring, and bond pads.

The polysilicon and oxide layers are individually patterned, and unwanted material from each layer is removed by reactive ion etching before the next layer is added. The polysilicon layers are annealed at 1100°C to relieve stress and to diffuse phosphorus in from the surrounding oxide layers to make the polysilicon conductive. The polysilicon layers conform closely to the topology of the previously deposited and patterned layers. The induced topology can have detrimental effects on the uniformity of the reflective surfaces and mirror flexures.

The polysilicon and oxide layers are built up over a silicon nitride layer which insulates them from the conductive, n-doped silicon substrate. The MUMPS layers are illustrated in Fig. 3, using a simple device consisting of a metallized mirror with one flexure, anchored to one support post. Note that this design does not use the poly1 layer, which would be located between the two oxide layers. Figure 3(a) shows a cross-section of the device prior to metallization. After fabrication, the sacrificial oxide layers are etched away to release the mechanical polysilicon layers. Figure 3(b) shows the final structure after the sacrificial material has been removed. Not shown is a 0.02  $\mu\text{m}$  thick chromium adhesion layer under the gold. Table 1 lists the properties of the materials used in the sixth MUMPS run, in which the hexagonal array of Fig. 1 was fabricated.

#### 3.2. Hexagonal micromirror design

A hexagonal design was chosen for polysilicon micromirrors because it allows the minimum number of flexures for a purely vertical piston-like motion. Hexagons also pack efficiently, maximizing the active surface area of the array. Other versions of piston micromirrors use aluminum for the flexures [4], and so flexure stiffness is not a problem. However, the polysilicon layers used in the MUMPS process are much thicker than the aluminum design; so to get a reasonable drive voltage, every opportunity had to be used to reduce the overall mechanical spring constant of the device.

Based on results of earlier, square polysilicon piston mirrors, it was determined that just going to three flexures would not lower the drive voltage sufficiently. The flexures would also have to be as long as possible, and they would have to be made of the thinnest available polysilicon layer, since the stiffness of the flexure has a cubic relationship to thickness. This led to the first design tradeoff: the thinnest MUMPS layer, and therefore the one that would make the most pliable flexures, was poly2, which was also the only layer that could be reliably metallized. So both the flexures and the mirror would have to be designed

in the same layer. This meant that any area taken up by the flexures would directly reduce the area of the array covered by movable mirror surfaces.

The final design, shown in Fig. 4, has each of the three flexures running along two sides of the hexagonal micromirror, which gives the greatest length possible for each flexure without overlapping them laterally. Longer flexures can be made by going around more sides or by folding the flexure back along the same two sides, but these approaches add the width of extra flexures and gaps to the area between neighboring mirrors, subtracting from the overall useful reflective surface of the array. The extra flexure length also adds more diffracting edges and poorly reflective surfaces to the design, thus increasing stray light generation.

The design rules for the MUMPS process set the minimum dimension for lines and gaps designed in poly2 at 2  $\mu\text{m}$ , so 2  $\mu\text{m}$  was chosen for the widths of the flexures and the gaps on either side of the flexures. Another design constraint was that etch holes had to be placed every 30  $\mu\text{m}$  to guarantee the full release of the poly2 structures. The desire to have a minimally distorted mirror surface meant the number of etch holes had to be held to a minimum. Therefore only a single 4  $\mu\text{m}$  wide etch hole was considered acceptable, and this set the maximum width of the mirror at a conservative 50  $\mu\text{m}$ . A further design limitation was the required 3  $\mu\text{m}$  gap between the edge of the metallization and the edge of the poly2. This also reduced the useable mirror surface area of the array, although this design rule was pushed to 2  $\mu\text{m}$ , since a decrease in the gap between these edges adds greatly to the area covered by metal, and previous experience with the MUMPS process showed that the 3  $\mu\text{m}$  design rule was overly conservative.

### 3.3. Micromirror array design

Available resources were major factors in the design of the micromirror array. The array had to be designed and packaged with parts on hand. The first constraint on the number of mirrors in the array was the size of the available chip packages. The largest package was a 145 pin grid array, which limited the maximum possible number of mirrors in the array to 144. A hexagonal array of 127 mirrors arranged in concentric circles was considered large enough to demonstrate the possibility of producing a useful micromirror array in polysilicon.

The next constraint was a tradeoff between active and static mirror areas: to make each mirror individually addressable, a poly0 wire would have to be run to each mirror. These poly0 wires would have to be run between the mirrors so the topology they induced in the overlying poly2 layer would not affect the flatness of the active mirror surfaces or the stiffness of the flexures. The design rules for poly0 meant that 4  $\mu\text{m}$  would have to be added to the space between the mirrors for each additional address line. A circular array of 127 mirrors needs at most three poly0 wires between mirrors to address every mirror in the array, including the center one. The final design of the support frame around the hexagonal mirrors allowed three wires between mirrors, for a mirror edge-to-edge spacing of 26  $\mu\text{m}$ , and a mirror center-to-center distance of 75  $\mu\text{m}$ . The support frame was also metallized with gold to provide an optical reference plane in case the cover plate idea described below failed.

Past the edge of the array, the poly0 address lines were extended as poly0/poly2/gold wires [5] to provide a low resistance path to the bondpads. The resulting 127 mirror array was small enough so that two arrays could be fit on the 1 cm square MUMPS die, with 131 bondpads around each array, including substrate contacts [5], as shown in Fig. 5. Each array could be pre-tested on a micromanipulator probe station, the best one wire-bonded out, and the unused one covered over for the bond wires to pass across. There was also enough room around each array to place four copies of test cells, each containing 44 variations of the hexagonal micromirror. These were designed to test different sizes of mirrors and address electrodes, the need for the etch holes, and different arrangements of down-stops to prevent the mirror from touching the address electrode when fully deflected.

### 3.4. Cover plate

A cover plate was designed to be placed over the entire array to eliminate light scattering caused by the flexures, wire topology, and mirror anchors, and to improve the overall reflectance of the array by providing a stationary reference plane. The cover plate has hexagonal holes that expose only the metallized surface of the mirrors, so when it is in place the incident light sees a flat, reflective plane of which some portions can be moved vertically.

The cover plates were drawn in the thickest releasable layer (poly1) since that would best withstand rough handling. The chip layout had room for eight cover plates per array to compensate for losses during handling. The poly1 cover plates were fabricated on the same die as the micromirror arrays, and were drawn without anchors so they would be fully released from the die. The post-processing procedure for the cover plates was to have them wash off the die during the release etch so they could be sputtered with gold and then positioned over the mirror array and glued into place. The support frame around the perimeter of the mirror array was drawn with locating pins at the corners, corresponding to holes in the cover plate, as shown in Fig. 5.

The glue for the cover plate was placed by hand, which limited the accuracy of the gluing to  $\pm 25 \mu\text{m}$ . The glue used to date has been photoresist, a drop of which can be placed on the die, and a probe point can be used to drag the edge of the drop

over to the cover plate edge. As the photoresist air-hardens, it flows more slowly, so fairly precise control of the edge can be achieved with a little practice. Photoresist does not affect the address wiring. The support structure around the mirror array is drawn without etch access holes. The result of this design is that oxide remains under the poly2 structure all the way around the array. This not only anchors the support frame more securely, but it also forms a barrier which prevents the photoresist from creeping under the frame and over to the mirrors by capillary action.

### 3.5. Release and post processing

Unreleased die were delivered from the foundry with a protective photoresist layer on top, which was stripped off in a three minute acetone bath. The die were then rinsed in deionized water (DIW) for two minutes. The actual release etch was a two minute dip in concentrated (49%) hydrofluoric acid. The die were then rinsed for five minutes in gently stirred DIW. After the rinse, they were soaked for five minutes in 2-propanol, then baked dry in a 150°C oven for five minutes. The propanol displaces the water, and when it evaporates, its low surface tension prevents the pull-down and destruction of the released polysilicon structures.

Throughout the release etch and rinse process, cover plates would wash off the die. These were picked up with an eyedropper and placed in 2-propanol for cleaning. After the propanol rinse, they were air dried in a petri dish. Any released cover plates that did not come off the die during the release process were removed from the die using a vacuum pickup tool. None of the plates was stuck to the die too firmly to prevent their removal. The cover plates were then plated with a thin layer of sputtered gold to make them as reflective as the micromirrors.

## 4. MODELING

A detailed analytical model has been developed to compute the electrostatic force on an electrostatically actuated micromirror [6]. The model incorporates the effects of cross-talk from neighboring mirrors, ambient temperature, fringing electric fields around the edge of the mirror, and deformations of the mirror surface. However, the mirrors in this array have a large edge-to-edge separation of 26  $\mu\text{m}$ , and thus cross-talk is negligible. Ignoring thermal and fringing effects, which are minor, and ignoring deformation of the mirror surface due to gravitational or electrostatic forces, the address voltage versus displacement model simplifies to Eq. (1) [6].

$$V = (z_0 - d_f) \sqrt{\frac{2kd_f}{\epsilon_0 A}} \quad (1)$$

In Eq. (1),  $V$  is the positive address voltage,  $z_0$  is the resting separation between the bottom of the mirror and the addressing electrode,  $d_f$  is the desired downward mirror displacement from this resting position,  $\epsilon_0$  is the free space dielectric constant, and  $A$  is the micromirror area. The  $k$  term is a total spring constant which accounts for the number, geometry, and material of the mirror flexures [6]:

$$k = 3(k_{cs} + k_s) = 3 \left[ \frac{Ewt^3}{L^3} + \frac{\sigma(1-\nu)wt}{2L} \right] \quad (2)$$

In Eq. (2), '3' is the number of flexures, and  $k_{cs}$  is a cross-sectional spring constant where  $L$ ,  $w$ ,  $t$ , and  $E$  are the length, width, thickness, and modulus of elasticity for the flexure beam, respectively. Also included is a stress term,  $k_s$ , which accounts for the stress and Poisson ratio of the flexure material,  $\sigma$  and  $\nu$ , respectively. In Eq. (2), the flexure is modeled as a straight beam, which gives a good starting point for calculating a behavior curve from Eq. (1); however, the effective modulus of elasticity depends on the overall geometry of the beam, including any bends or topological features. Also, the modulus of elasticity of a thin film material depends on the fabrication process, and can vary significantly. Given this uncertainty in the value of the modulus of elasticity, the model will produce a representative behavior curve for the device. However, by altering only the modulus of elasticity,  $E$ , this representative behavior curve can be calibrated to the observed data.

## 5. MICROMIRROR TESTING

Two sizes of hexagonal micromirrors were fabricated, the 50  $\mu\text{m}$  wide mirrors in the hexagonal array of Fig. 1, and 75  $\mu\text{m}$  wide mirrors in the test arrays. The only difference between the two types of mirrors was the area of the mirror and the

corresponding change in the length of the flexures; all of the other flexure dimensions and layer thicknesses remained the same. Tests were performed on these mirrors to verify the model. The deflection versus voltage characteristics of the 50  $\mu\text{m}$  mirrors were also needed for designing the drive and control system for the 127 mirror hexagonal array. Prior to electrical testing, the arrays were carefully inspected under a microscope and in a scanning electron microscope (SEM), and they were probed to see that they were fully released.

Initial testing of individual micromirrors was performed on a micro-probe station using an electrometer and a digital multimeter. The electrometer output voltage was increased until the mirrors were observed to fully deflect. The voltage needed to fully deflect the mirrors sets a rough upper bound on the addressing voltage. The useful voltage is less than this rough maximum, since the mirrors only need to deflect far enough to introduce a  $2\pi$  phase change in the incident 632.8 nm wavelength light, a deflection which is much less than the full 2.5  $\mu\text{m}$  deflection possible with these mirrors. Also, the deflection of the mirrors is not controllable over the full 2.5  $\mu\text{m}$  deflection since the electrostatic force increases with increasing mirror displacement, and past  $d_f > \frac{1}{3} z_0$  the system becomes unstable and the mirror snaps all the way down [7].

A microscope-based laser interferometer, accurate to  $\pm 2$  nm, was used for vertical deflection measurements. The laser interferometer is shown schematically in Fig. 6. The interferometer modulates a fixed reference beam with a beam reflected from the device under test [8]. An incident 2 mW, 632.8 nm HeNe laser beam is expanded and split into reference and object beams. The reference beam is reflected back through the beam splitter to the aperture of the detector. The object beam is focused through the microscope objective down to a 4  $\mu\text{m}$  spot on the device under test. The reflected object beam returns to the beam splitter, where it is also reflected to the detector aperture, creating an interference pattern with the reference beam. The detector produces a current which is linearly related to the intensity of the interference pattern. The object beam's path length increases by twice the vertical displacement of the device under test, so a  $2\pi$  phase change in the interference pattern indicates a 316.4 nm deflection of the device. By using a periodic drive signal and knowing the exact wavelength of the incident laser beam, a continuous sample of the detector current yields an accurate measurement of the displacement of the micromirror surface. Comparison of this displacement with the input drive signal yields the deflection versus voltage characteristic of the device [8].

A translation table under the interferometer is used to move the device under test in the X and Y directions in 0.1  $\mu\text{m}$  increments, allowing measurements to be taken across the mirror surface. This allows characterization of an individual mirror's sag and tilt, and allows several mirrors in the hexagonal array to be compared to determine the uniformity of the fabrication process.

## 6. RESULTS

### 6.1 Deflection versus voltage and model verification

Figure 7 shows the deflection versus drive voltage for the two sizes of hexagonal mirrors. The 75  $\mu\text{m}$  wide mirrors were driven by a zero to 30 volt peak, 250 Hz sinusoidal signal; and the 50  $\mu\text{m}$  wide mirrors were driven with a similar signal of 45 volts peak. The laser spot was positioned at a corner of the mirror where a flexure attaches. The theoretical behaviors of the devices, as modeled by Eq. (1), are shown as solid lines in Fig. 7. Those curves are calculated using designed dimensions and a modulus of elasticity of 162.3 GPa, determined experimentally from separately fabricated cantilever-shaped test devices. The final calibrated values for the moduli of the 50  $\mu\text{m}$  and 75  $\mu\text{m}$  mirrors are  $E=152$  GPa and  $E=125$  GPa, respectively. As seen by the dashed lines in Fig. 7, these calibrated values bring the modeled responses in line with the measured responses, within the limitations of the measurement system. These results also show a significant decrease in the maximum drive voltage for the larger mirrors, indicating that even larger mirrors could lower the maximum drive voltage below 20 volts.

### 6.2 Mirror surface distortion

Tests of mirror sag and tilt were performed on a 62  $\mu\text{m}$  square mirror fabricated in the same process as the hexagonal mirrors. Measurements showed that at an address voltage which deflected the mirror to its full useful distance of 316.4 nm, the mirror sagged down in the center only 5 nm compared to measurements taken at the points on the mirror where the flexures attached. This very small sag is negligible both in the deflection versus voltage model and in the optical modeling.

The other source of mirror surface distortion, the etch access hole, turned out to be an unnecessary design feature. The test mirror array revealed that 75  $\mu\text{m}$  wide mirrors without etch access holes were fully released in the two minute release etch. This means that even larger mirrors could be released without requiring etch holes. Tests have shown that no damage occurs to die left in the release etch for up to five minutes, so even longer etch times would be practical for gold metallized mirrors.

### 6.3 Flexure distortion

Visual inspection revealed unevenness in the mirror flexures: the flexure sections that ran in directions parallel to the die edges were 1.65  $\mu\text{m}$  wide, while sections that ran at 60 degree angles to the die edges were 1.99  $\mu\text{m}$  wide. The design width of



the flexures was 2  $\mu\text{m}$ . Figure 8 is a close-up of a flexure corner showing this effect. This unevenness was probably caused by stair-stepping of the angled lines on the mask. Also, due to the orientation of each hexagonal mirror, two of its three flexures are half 1.65  $\mu\text{m}$  and half 1.99  $\mu\text{m}$  wide; while the third flexure, whose halves are both at 60 degree angles to the die edges, is 1.99  $\mu\text{m}$  wide along its entire length.

A related distortion occurred regularly across the array in every fifth row of mirrors; this was a narrowing of the gap between the flexure and the mirror. This indicated an interaction between the underlying step sizes of the design grid and the mask grid. It turned out that the masks were made on a 0.25  $\mu\text{m}$  grid instead of a 0.1  $\mu\text{m}$  grid; so as the mirror layouts stepped across the array, the flexure sections at 60 degree angles were stair-stepped differently. Another distortion that showed up on all the mirrors was a bump in one of the flexures where the poly0 wire goes under the flexure to the address electrode. This topological distortion was expected, however.

All of the mirrors therefore suffered distortions of their flexures; so they were all expected to tilt when they were fully deflected to 316.4 nm. Tilt measurements were taken of a fully deflected 50  $\mu\text{m}$  wide hexagonal mirror whose only flexure distortion was the difference in width due to angular orientation. Measurements taken at each corner where a flexure joined the mirror revealed a 7 nm difference in deflection between the flexure that was 1.99  $\mu\text{m}$  wide along its entire length and the flexures that were 1.99  $\mu\text{m}$  wide along only half their length. These distortions lead to the design of a second generation array.

#### 6.4. Cover plate attachment

Another feature of the first generation array that did not work out well was the cover plate. Washing the plates off the die during the release etch and gold sputtering them separately from the rest of the die worked out very well; but it was too difficult to align and hold the cover in place using microprobes. The guide pins fabricated into the mirror support frame were too short to hold the cover plate in place, so it could not be held steadily enough to be glued down precisely in position. The arrays that were bonded out for testing therefore did not include cover plates, but instead had to rely on the metallization of the support frame between the mirrors to provide the optical reference plane, which was the backup plan. A vacuum pickup tool was built to place and hold the cover plate, but an improved design for the second generation array eliminated the need for the cover plate to be loose.

#### 6.5. Micromirror and array improvements

The most important result of all the testing was a series of improvements incorporated into the next generation of the hexagonal micromirror and the 127 mirror array. These improvements are intended to overcome the problems with non-uniform flexure fabrication of each micromirror, to decrease the driving voltage requirements, and to make the cover plate easier to attach and adjust. Below is a summary of the improvements made and the reasons for them, based on the testing results reviewed above. Figure 9 shows the layout drawing of a single mirror, and Fig. 10 shows the layout drawing of the die.

- The new mirrors are 100  $\mu\text{m}$  across their widest dimension, with no etch holes. The results from the test arrays indicate that these mirrors are feasible. The main limitation on making mirrors larger than this would be the amount of sagging in the center when the mirror is fully deflected; such a distortion may become optically significant.
- Down-stops are placed at the mirror end of each flexure. Test mirrors indicate that this is the best location for these stops. The stops are fabricated by using the 'dimple' feature of the MUMPS process. Although the dimples are intended to be fabricated in poly1, the conformality of the thin films results in a useable dimple in poly2 also, even if the poly1 is completely removed.
- The mirrors and flexures were drawn such that there were no edges or lines parallel to the edges of the die. All the lines are at some multiple of 15 degrees, so they should all get stair-stepped similarly on the mask grid. With this angled layout approach all the flexures drawn the same width should be fabricated the same width. Also, all features are drawn to a 0.25  $\mu\text{m}$  grid to match the mask grid; this should eliminate the problem of matching features of different mirrors being fabricated with different widths across the array. Another change made to prevent flexure width variations was to widen the gap on either side of the flexures from the minimum 2  $\mu\text{m}$  to a more conservative 3.1  $\mu\text{m}$ .
- Poly0 address line stubs are placed under the corners of all three flexures. One stub is used for the actual address line and the other two stop short of connecting with the address lines under the support frame. This ensures that the flexures all get the same topology. The wider flexure gaps mean that these stubs can be drawn without having to increase the width of the support frame that runs between the mirrors.

- The new cover plate is attached to the substrate by a long hinge. The cover plate flips over into position on the array. Due to the compressive stress in the poly1 layer, the cover plate will tend to curl down at the edges; when it is flipped over its center should contact the array first, and the cover should flatten out as the edges are pressed down for gluing. The die will have to be masked when the back side of the cover plate is metallized, but the features to be masked are so large that the mask can be placed manually. The fabrication sequence is not a batch process, but the required manual processing is simple.
- The cover plate and mirror array support frame have cross-hair fiducials for fine alignment of the cover plate to the array. Holes are fabricated in the cover plate to allow better control of the plate by microprobes whose tips are inserted in the holes.
- A larger margin of the mirror support frame, without etch holes, is left around the array since the die may be in the etch longer, and residual glass is still needed under the frame to prevent the cover plate glue from creeping under the frame to the mirror array by capillary action. The gluing step can also be less precise with this larger margin.
- There is only one array per die. The larger mirrors and the hinged cover plate scheme leave room for only a single hexagonal array and a few test mirror arrays. A single row of large ( $350\text{ }\mu\text{m} \times 175\text{ }\mu\text{m}$ ) bondpads will simplify wire-bonding.

## 7. CONCLUSIONS

Factors beyond the design rules and material properties need to be considered when moving from single MOEM device designs to large arrays of devices. Specifically, the mask-making process, process uniformity, on-chip wiring, and packaging considerations become important as the designer moves to large arrays of devices. For example, in a surface-micromachining process such as MUMPS, considerable die space must be allowed for wiring large numbers of devices. Systems that require some manual assembly benefit from any steps taken to make the assembly process more precise. Very large released structures must take into account the bowing of the material due to the residual stress, even if the stress is extremely low. Polysilicon is a promising material for micromirror arrays, but annealed polysilicon fabrication processes must be able to provide sufficient wiring layers to individually address mirrors in large arrays without detracting from active mirror area.

## 8. REFERENCES

1. R.M. Boysel, J.M. Florence and W.-R. Wu, "Deformable mirror light modulators for image processing," *Proc. SPIE*, vol. 1151, 1989, pp. 183-194.
2. L.J. Hornbeck, "Deformable mirror spatial light modulators," *Proc. SPIE*, vol. 1150, 1990, pp. 86-102.
3. K. W. Markus and D. A. Koester, "Multi-User MEMS Process (MUMPS) introduction and design rules," MCNC Electronics Tech. Div., 3021 Cornwallis Road, Research Triangle Park, North Carolina, Oct. 1994.
4. T.H. Lin, "Implementation and characterization of a flexure-beam micromirror spatial light modulator," *Optical Engineering*, vol. 33, 1994, pp. 3643-3648.
5. J.H. Comtois and V.M. Bright, "Design techniques for surface-micromachining polysilicon processes," *to be published in the Proc. SPIE*, vol. 2639, 1995.
6. M.A. Michalick, V.M. Bright and J.H. Comtois, "Design, fabrication, modeling, and testing of a surface-micromachined micromirror device," *to be published in the Proceedings of the 1995 ASME International Mechanical Engineering Congress and Exposition, San Francisco, CA, 12-17 Nov. 1995.*
7. P.M. Osterberg, R.K. Gupta, J.R. Gilbert and S.D. Senturia, "Quantitative models for the measurement of residual stress, Poisson ratio, and Young's modulus using electrostatic pull-in of beams and diaphragms," *Technical Digest, Solid State Sensor and Actuator Workshop*, Hilton Head, SC, 1994, pp. 184-188.
8. T. A. Rhoadarmer, V. M. Bright, B. M. Welsh, S. C. Gustafson and T. H. Lin, "Interferometric characterization of the flexure beam micromirror device," *Proc. SPIE*, vol. 2291, pp. 13-23, Jul. 1994.

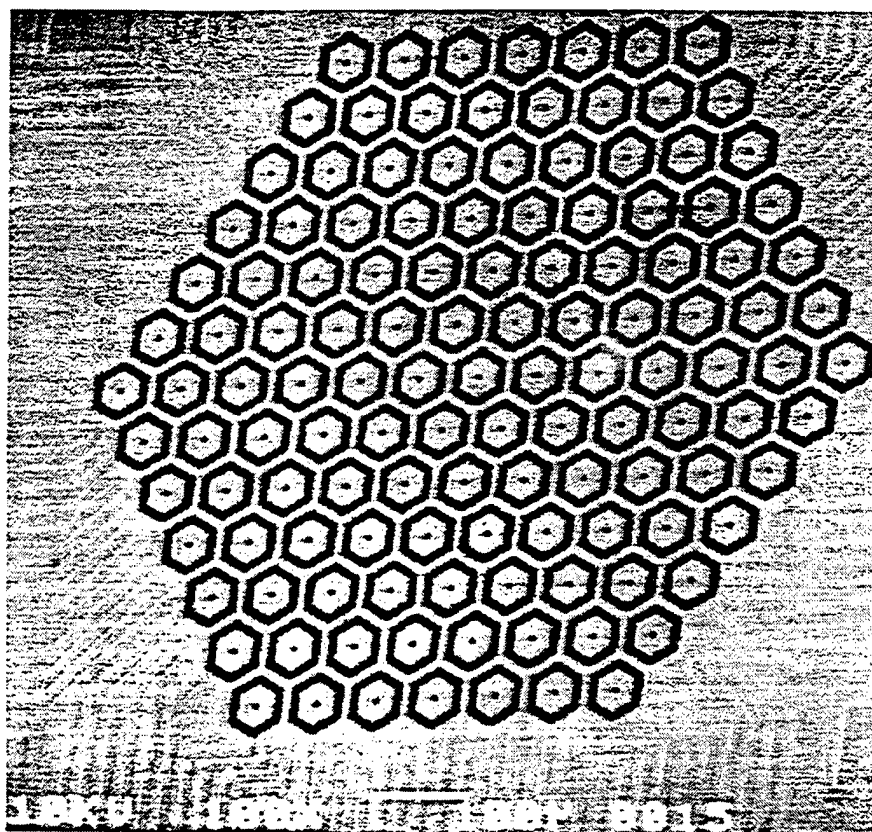


Figure 1. First generation hexagonal micromirror array consisting of 127 individually addressable mirrors. Each mirror is 50  $\mu\text{m}$  corner-to-corner across the center, and the distance between the centers of adjacent mirrors is 75  $\mu\text{m}$ . The mirrors are made of 1.5  $\mu\text{m}$  thick polysilicon, with 0.5  $\mu\text{m}$  thick gold metallization.

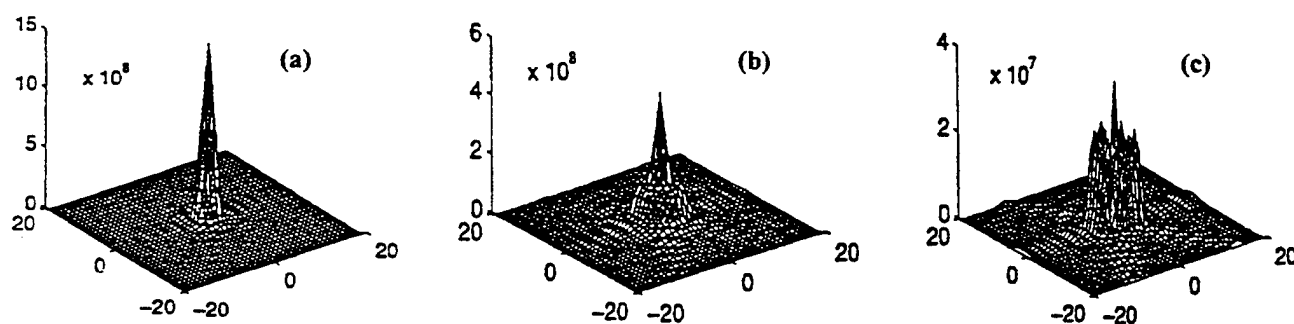


Figure 2. Far field irradiance pattern in arbitrary units for a 127-element hexagonal micromirror array illuminated by a constant, coherent, collimated beam at normal incidence. The mirrors are operated as concentric rings. The center and surrounding rings of 6, 12, 18, 24, 30, and 36 hexagonal mirrors are assigned phase angles of  $2\pi y_1, 2\pi y_2, \dots, 2\pi y_7$ , respectively. The non-moving space between the mirrors is assigned an amplitude  $V$ . The far-field irradiance is plotted as a function of the following values for  $y_1, y_2, \dots, y_7$ , and  $V$ : (a) undeflected mirrors:  $y_1, y_2, \dots, y_7, V=0$ ; (b) parabolic deflection profile:  $y_1, y_2, \dots, y_7 = 0.014, 0.056, 0.125, 0.222, 0.347, 0.500$ , and  $V=0$ ; (c) deflections optimized to yield, as close as possible, a flat-topped profile over the main and first side lobes:  $y_1, y_2, \dots, y_7 = 0.7251, 0.2239, 0.1683, 0.5734, 0.5709, 0.5275, 0.5169$ ,  $V=0.5$ .

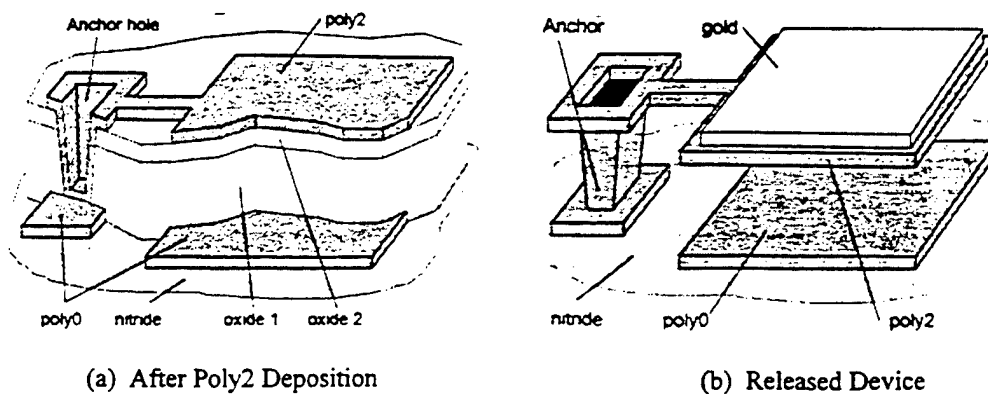


Figure 3. Graphical illustration of the MUMPS fabrication process using a simple cantilever micromirror device. Thicknesses of the layers are not shown to scale.

Table 1. Manufacturer's Reported Properties of Materials from the Sixth MUMPS Fabrication Run.

Material Layer	Thickness ( $\mu\text{m}$ )	Stress (MPa)	Resistivity ( $\Omega\text{-cm}$ )
poly0	0.52	19.7 compressive	$1.84 \times 10^{-3}$
poly1	2.0220	5.1 compressive	$2.58 \times 10^{-3}$
poly2	1.5650	5.1 compressive	$2.72 \times 10^{-3}$
metal (Cr/Au)	0.5540	$\sim 30$ tensile	$3.39 \times 10^{-6}$
silicon nitride	0.6213	19.2 compressive	-
oxide 1	2.0151	-	-
oxide 2	0.5230	-	-

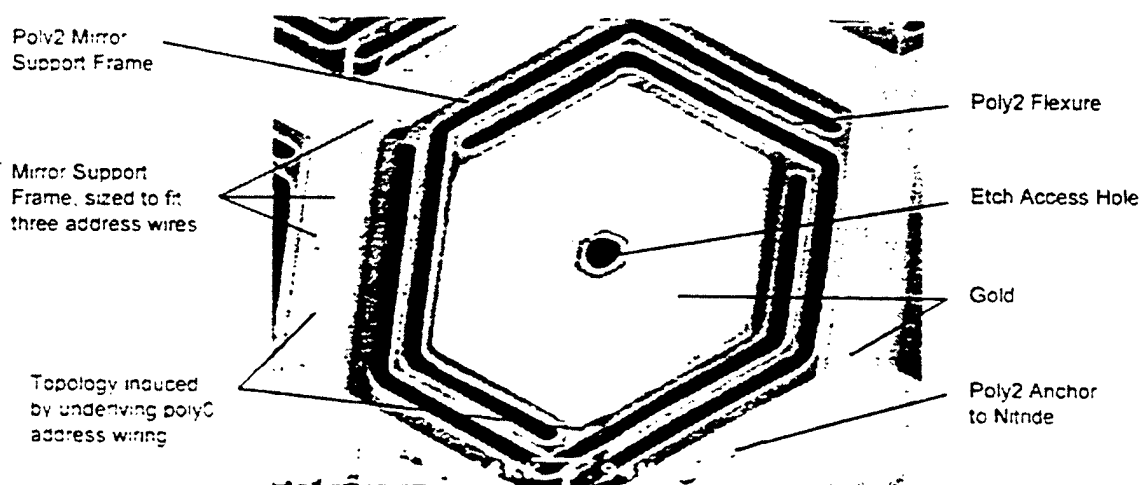


Figure 4. Scanning electron microscope micrograph of a 50  $\mu\text{m}$  wide hexagonal micromirror. The mirror is poly2 with gold metallization. The three flexures are designed to be 2  $\mu\text{m}$  wide with 2  $\mu\text{m}$  gaps. Three 2  $\mu\text{m}$ -wide wires with 2  $\mu\text{m}$  spacing can fit between the mirrors.

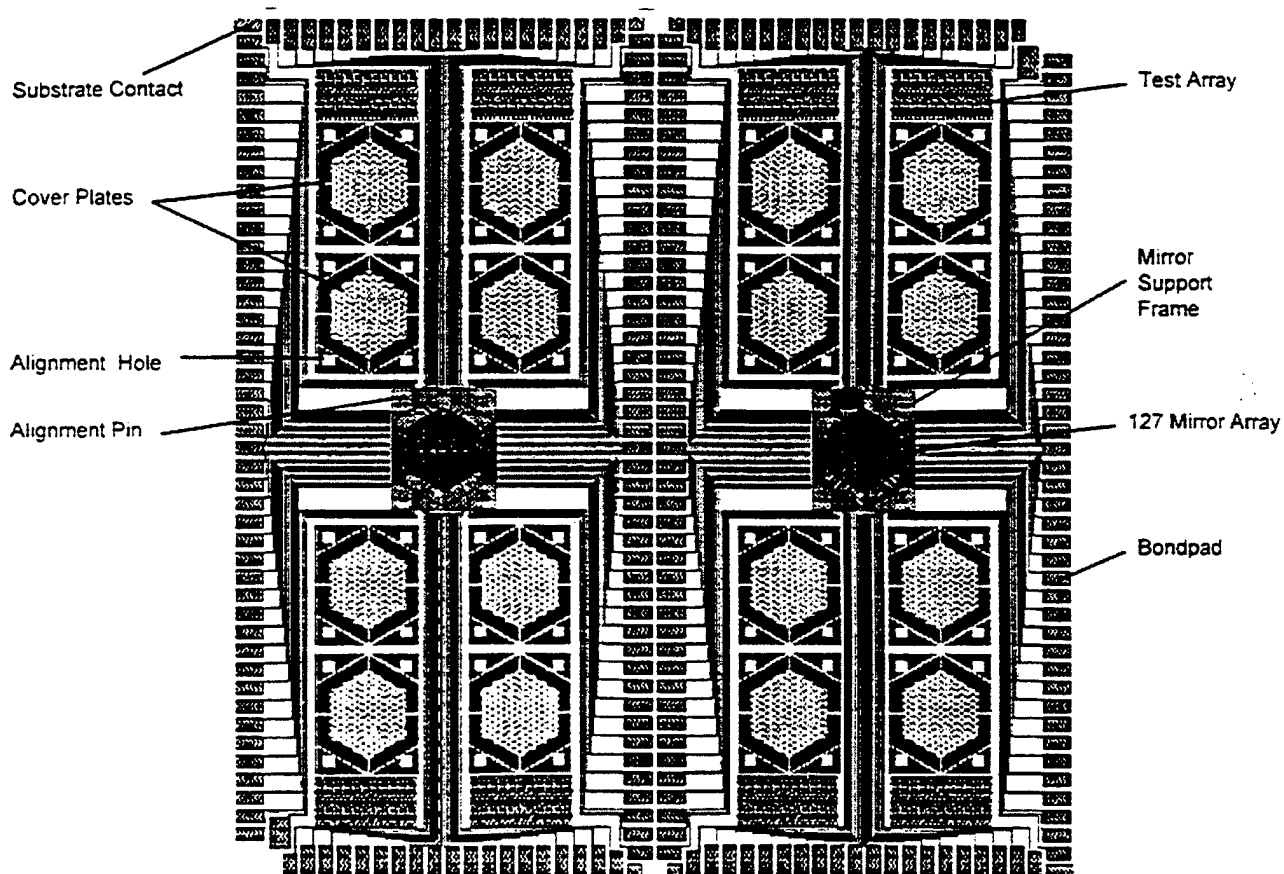


Figure 5. Layout of the first hexagonal micromirror array die. The one square centimeter die holds two independent arrays.

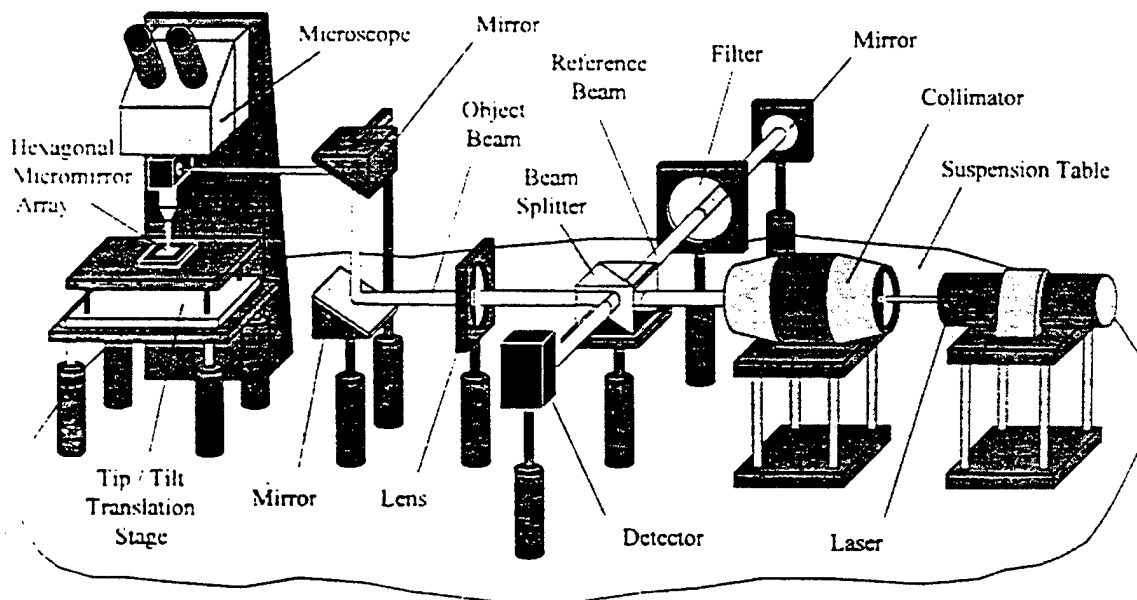


Figure 6. Microscope-based laser interferometer experimental setup [6].

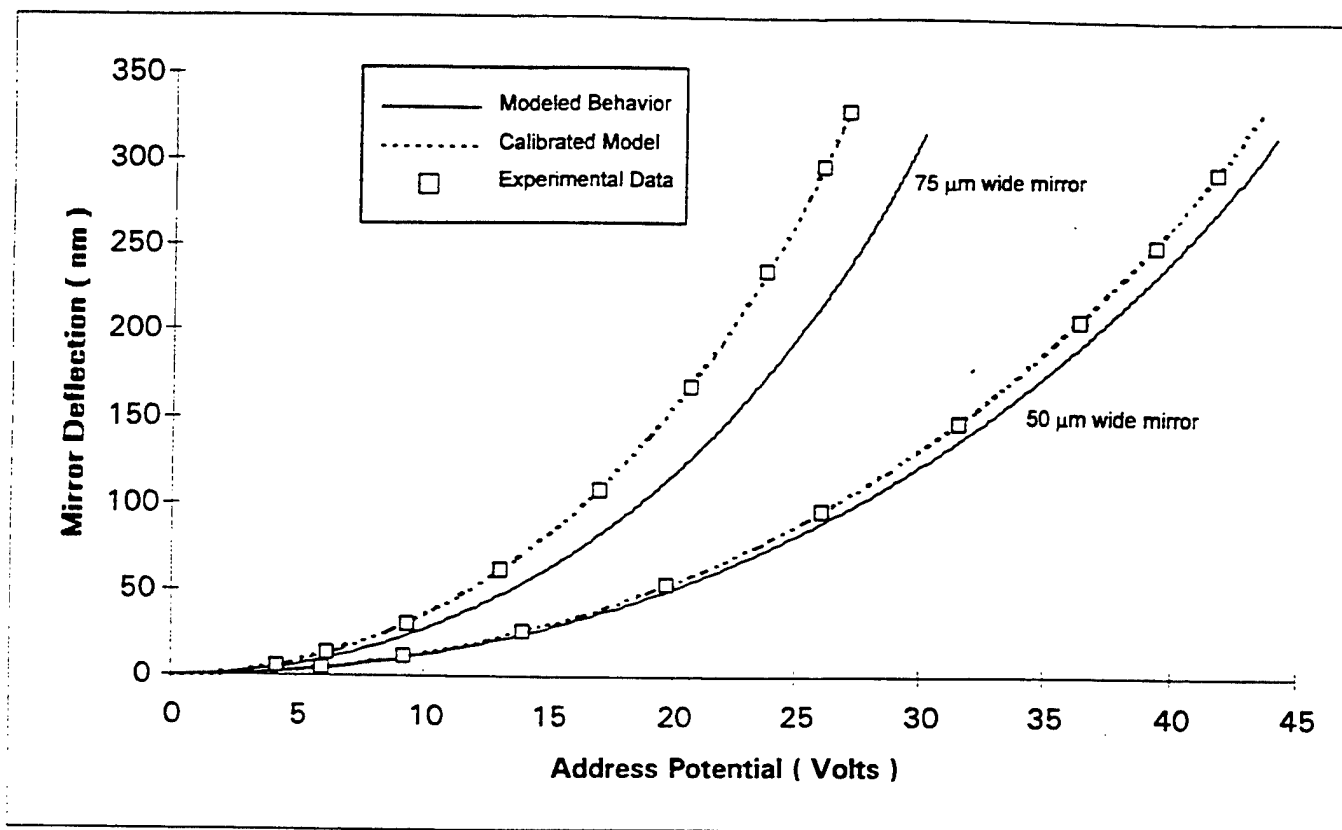


Figure 7. Comparison of theoretical and experimental behavior curves. Theoretical curves are plotted using the model with a Young's modulus of 162.3 GPa. The calibrated moduli for the 50  $\mu\text{m}$  and 75  $\mu\text{m}$  wide mirror curves are 152 GPa and 125 GPa, respectively.

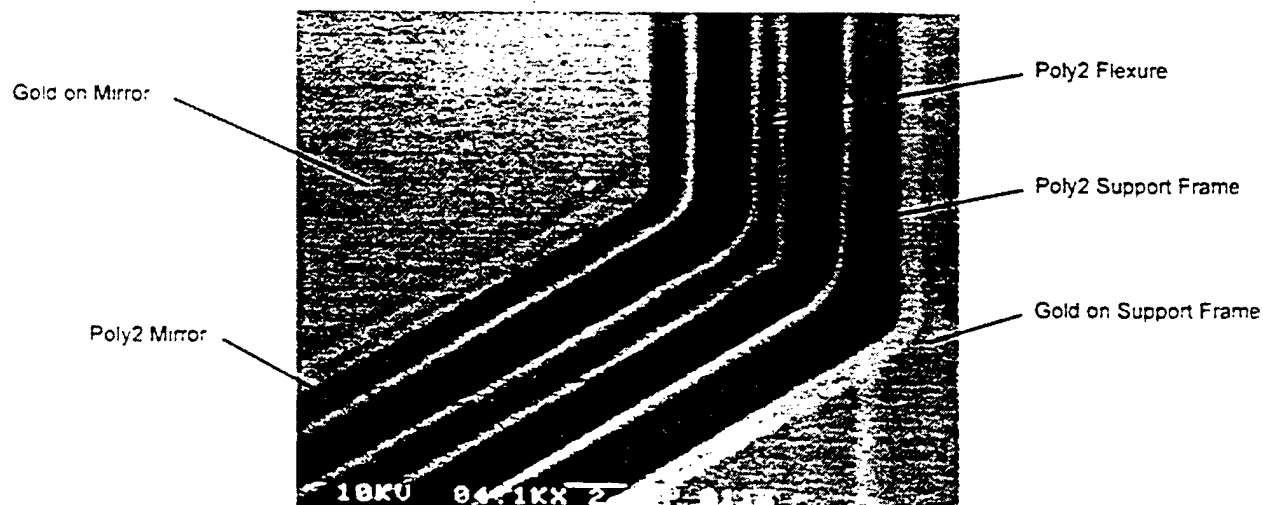


Figure 8. Uneven flexure widths, caused by stair-stepping of the angled line on the mask grid. The thinner vertical half of the flexure is 1.65  $\mu\text{m}$  wide, and the thicker angled half of the flexure is 1.99  $\mu\text{m}$  wide. The flexure design width was 2  $\mu\text{m}$ .

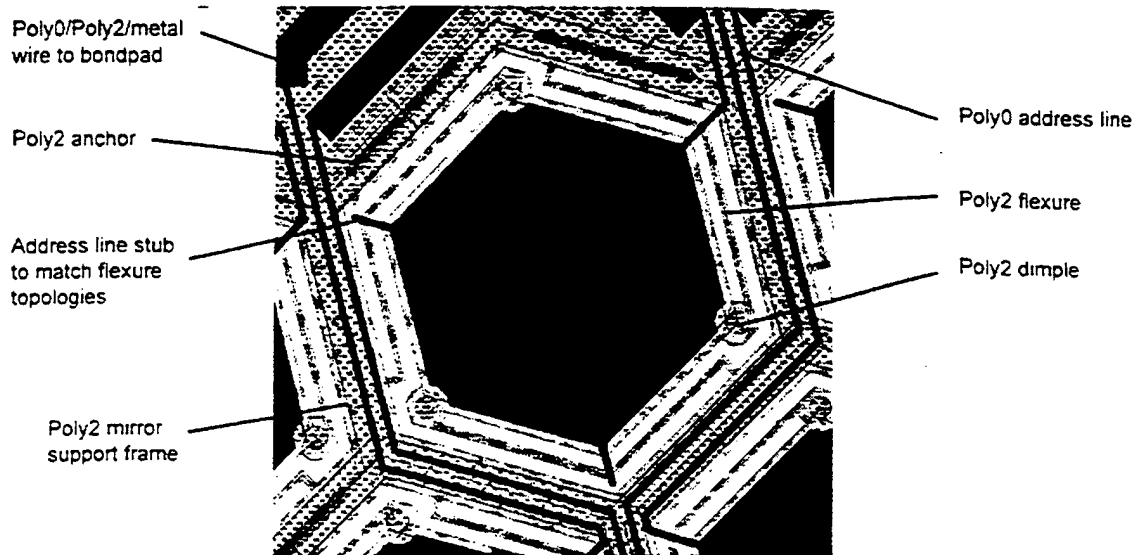


Figure 9. Layout drawing of the second generation hexagonal micromirror. The mirror is 100  $\mu\text{m}$  from corner to corner across the center of the mirror. The flexures are 2  $\mu\text{m}$  wide with 3.1  $\mu\text{m}$  gaps. Dimples are placed at the mirror end of each flexure to prevent the mirror from shorting to the address electrode when fully deflected.

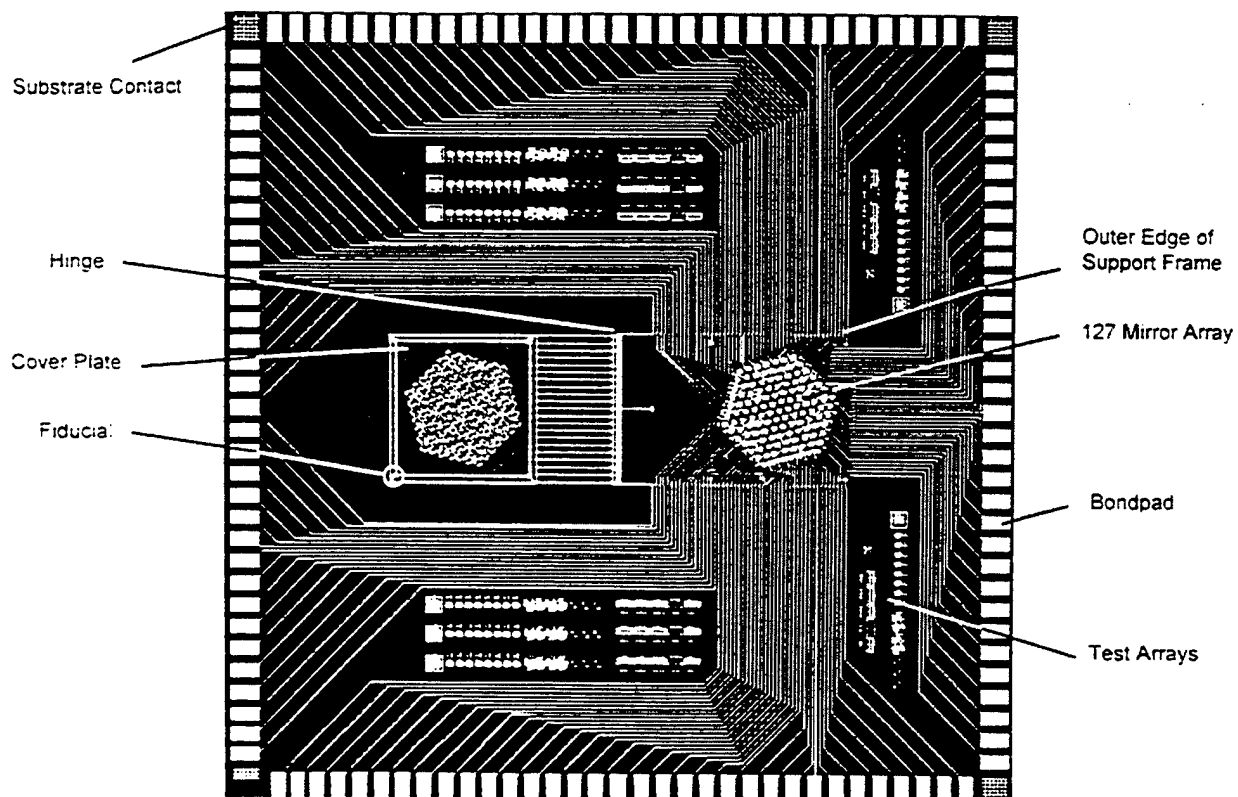


Figure 10. Layout drawing of the second generation hexagonal micromirror array chip. The die is one square centimeter.

# MICROMIRROR ARRAYS FOR ACTIVE OPTICAL ABERRATION CONTROL

Steven C. Gustafson and Theresa A. Tuthill  
University of Dayton, Dayton, Ohio 45469

and

Edward A. Watson  
Air Force Wright Laboratory, WL/AARI  
Wright-Patterson AFB, Ohio 45433

[SPIE Proc. 2687, No. 02, San Jose, CA, 30 January 1996]

## ABSTRACT

Micromirror arrays are being developed that can have up to tens of thousands of micromirror elements, each as small as 20 microns on a side, each spaced relative to neighbors so that optical efficiency exceeds 90 percent, and each individually controlled with response times as small as 10 microseconds for piston-like phase-mostly displacements that cover more than one-half optical wavelength. These arrays may be well suited for active aberration control of the focused coherent beams used in many applications, including optical disk storage, optical scanning, and laser radar systems. Active aberration control requires determination of the voltages supplied to the micromirror array elements so that constructive and destructive interference in light reflected from many elements yields the desired result. This paper discussed an approach in which the voltages are determined off-line by simulated annealing optimization and stored for real-time use.

**Keywords:** micromirror arrays, active aberration control.

## 1. PHASE-MOSTLY MICROMIRRORS AND ARRAYS

Figure 1 shows, schematically, a typical single micromirror element and a typical micromirror array<sup>1,2</sup>. Each micromirror can be as small as 20 microns on a side, although micromirrors up to 100 microns in width generally retain the micro-electro-opto-mechanical advantages of ruggedness, ease of integration with drive electronics, and potential low cost (due to the use of standard silicon integrated circuit fabrication technology). Each micromirror has hinges typically less than three microns wide that permit electrostatically-actuated piston-like displacement toward an underlying electrode. The mean displacement may be several tenths of a micron, generally with less displacement near the hinges, with more displacement near the micromirror center, and with a displacement time constant of less than 10 microseconds. Micromirror arrays, which may have up to tens of thousands of elements, can have an inactive area less than 10 percent of the total area so that the gross optical efficiency may exceed 90 percent.

Figure 2 shows a hexagonal micromirror element that has three hinges (each following two sides of the hexagon) and an array of 127 of these elements<sup>3</sup>. Hexagonal micromirrors can have larger piston-like displacement per unit actuation voltage because they may be supported by three relatively long hinges instead of four relatively short hinges as is typical for square micromirrors. Hexagonal micromirrors can also be packed so that the ratio of mirror to inter-mirror area is larger than for square micromirrors.

## 2. DETERMINATION OF CONTROL VOLTAGES

For applications such as active aberration control, the voltage supplied to each micromirror element must be determined so that constructive and destructive interference in light reflected from many elements yields the desired result.



This determination generally involves solving a nonlinear optimization problem in many variables. Such problems are encountered in designing classic diffractive optical elements such as Dammann gratings<sup>4</sup>, but for micromirror arrays the problem can involve many more variables and global optimization can be more difficult to achieve. In the optimized simulations discussed below simulated annealing<sup>5</sup> was employed to increase the likelihood of obtaining good solutions. Simulated annealing is not a real time technique, but the optimization results can be stored for real-time use.

### 3. ELEMENTARY SIMULATIONS

The simplest non-trivial phase-only micromirror array is a row of four micromirrors with symmetric displacements normal to the array plane, where each micromirror is perfectly reflecting and flat and all micromirrors are parallel. The micromirrors have unit separation and width  $w$ , and all inter-mirror space is perfectly absorbing. The central-most and outer-most pairs of micromirrors have the same displacement, and these displacements differ in phase by  $\theta$ . For collimated coherent light reflected from the array, the irradiance in the far field (parallel to the array) is proportional to the squared absolute value of the Fourier transform of the array:

$$y(x) = 4w^2 \text{sinc}^2(wx) [\cos^2(\pi x) + \cos^2(3\pi x) + 2 \cos(\pi x) \cos(3\pi x) \cos\theta]$$

This expression is plotted in Figure 3 for  $w = 1$  and (no inter-mirror space) and  $w = .5$  (equal mirror and inter-mirror space) and  $\theta/\pi = 0, 1/4, 1/2, 3/4, 1$ . Note that the size and position of the several maxima vary depending on the values of  $w$  and  $\theta$ .

A straightforward two-dimensional numerical simulation involves a 127-element hexagonal array of hexagonal micromirrors. The elements have a nearest-neighbor center-to-center spacing of 1.5 times their corner-to-corner maximum extent, are perfectly reflecting and flat, and have perfectly absorbing inter-mirror space. Figure 4 shows the quantization of this array onto a 1024 by 1024 grid so that a two-dimensional discrete Fourier transform can be performed, where the array area is less than 10 percent of the grid area to avoid aliasing. Figure 5a shows a plot (obtained from the squared absolute value of the discrete Fourier transform of the grid) that is proportional to the central portion of the reflected far field irradiance when the array is illuminated with collimated coherent light and all micromirrors are in the array plane (i.e., no micromirror displacement). Figure 5b shows a similar plot when the micromirrors are displaced normal to the initial array plane in a parabolic profile. For this profile all micromirrors in hexagonal rings of 1, 6, 12, 18, 24, 30, and 36 elements have the same displacement, where the displacements are such that their phases in units of  $\pi$  are 0, 1/36, 4/36, 9/36, 16/36, 25/36, and 1, respectively. Note the considerable change in the center portion of the far field irradiance profile from Figure 5a (no micromirror displacement) to Figure 5b (parabolic micromirror displacement).

### 4. OPTIMIZED SIMULATIONS

Figure 6 displays plots proportional to far field irradiance for the array shown in Figure 4 and with the same conditions used to obtain the results shown in Figure 5 except that the amplitude reflectivity of the inter-mirror space is .5. In Figure 6a and 6b there is no micromirror displacement; Figure 6a shows six secondary maxima and Figure 6b shows the central lobe in more detail. In Figure 6c and 6d the displacements of the seven hexagonal rings of elements are optimized using simulated annealing to yield as-constant-as-possible irradiance over a circular central region that includes only the central and first side lobes. This beam shaping operation is accomplished by minimizing  $I$ , the integrated squared difference between actual and constant irradiance over the circular central region. Note that more constant irradiance at a greatly reduced irradiance level is obtained in the circular central region (see Figure 6b) at the expense of a large increase in the irradiance of the six secondary maxima (see Figure 6a).

The phase values for the displacements of the seven hexagonal rings of elements that implemented the beam shaping operation shown in Figure 5d are .2690, .1464, .1330, .2662, .2712, .2506, and .2512 in units of  $\pi$  for increasing ring size. Figure 7 plots the minimized quantity  $I$  versus percent change in these phase values above (Figure 7a) and below (Figure 7b)

the optimal values. These plots indicate that beam shaping is not critically sensitive (i.e., unstable) relative to small changes in the optimal phase values.

## 5. APPLICATION TO ACTIVE ABERRATION CONTROL

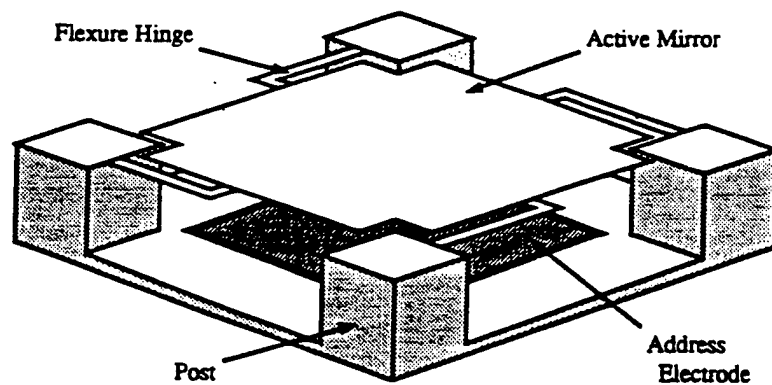
The above discussion and results indicate that micromirror arrays, because of their beam shaping capabilities, may be well suited for active aberration control<sup>5</sup> of the focused coherent beams used in many applications, including optical disk storage, optical scanning, and laser radar systems. A key concern is that although essentially arbitrary beam shaping may be achieved using arrays with large numbers of micromirror elements, this capability may be generally available only at the expense of reduced optical efficiency.

## 6. ACKNOWLEDGMENTS

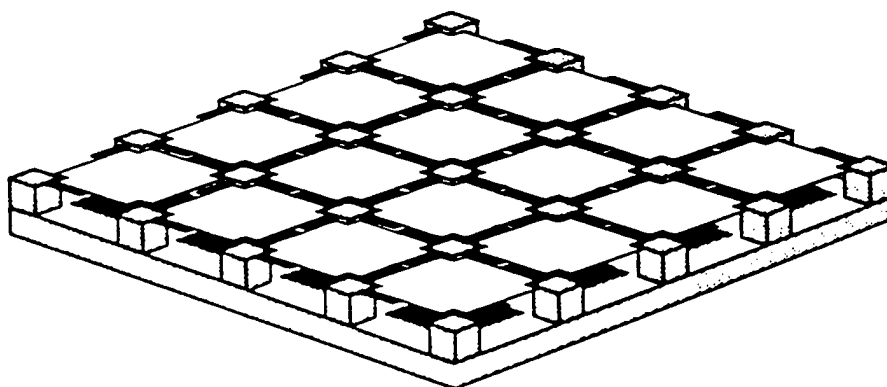
This work was performed in part on US Air Force Contract No. F33615-92-C-1120 through the Air Force Wright Laboratory. The hexagonal micromirror elements and array shown in Figure 2 were designed by John H. Comtois and Victor M. Bright of the Air Force Institute of Technology and were fabricated by the ARPA-supported MUMPS facility.

## 7. REFERENCES

1. T. A. Rhoadarmer, S. C. Gustafson, G. R. Little, and T. H. Lin, "Flexure-Beam Micromirror Spatial Light Modulator Devices for Acquisition, Tracking, and Pointing," *Proc SPIE* Vol. 2221, no. 40, Orlando, FL, April 1994.
2. T. A. Rhoadarmer, V. M. Bright, B. M. Welsh, S. C. Gustafson, and T. H. Lin, "Interferometric Characterization of the Flexure Beam Micromirror Device," *Proc SPIE*, Vol. 2291, pp. 13-23, San Diego, CA, July 1994.
3. J. H. Comtois, V. M. Bright, S. C. Gustafson, and M. A. Michalick, "Implementation of Hexagonal Micromirror Arrays as Phase-Mostly Spatial Light Modulators," *Proc SPIE*, Vol. 2641, pp. 76-87, Austin, TX, October 1995.
4. H. Dammann and K. Görtler, "High-efficiency In-line Multiple Imaging by Means of Multiple Phase Holograms," *Opt. Comm.*, Vol. 3, pp. 312-315, 1971.
5. W. H. Press, B. P. Flannery, S. A. Teukolsky, and W. T. Vetterling, *Numerical Recipes in C*, Cambridge Univ. Press, 1992.
6. R. K. Tyson, *Principles of Adaptive Optics*, Academic Press, 1991.

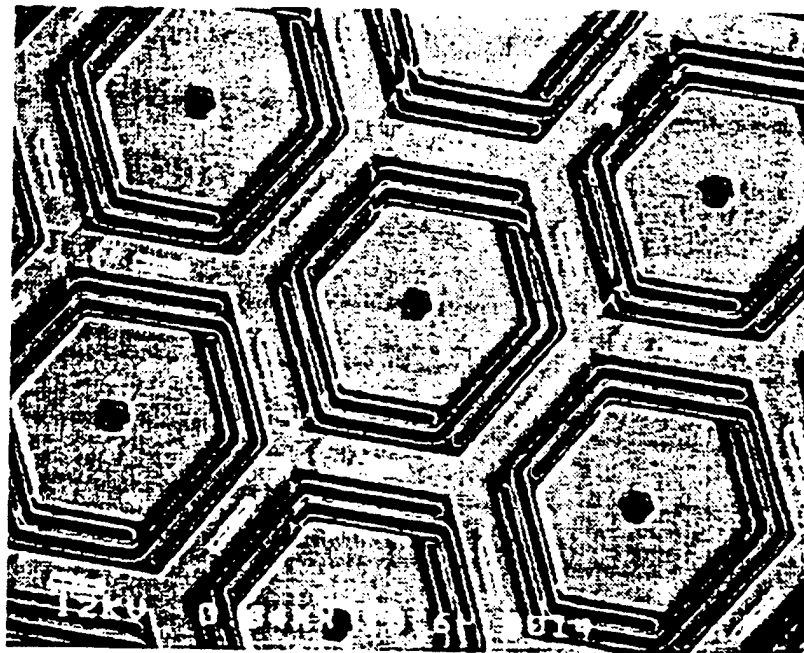


(a)

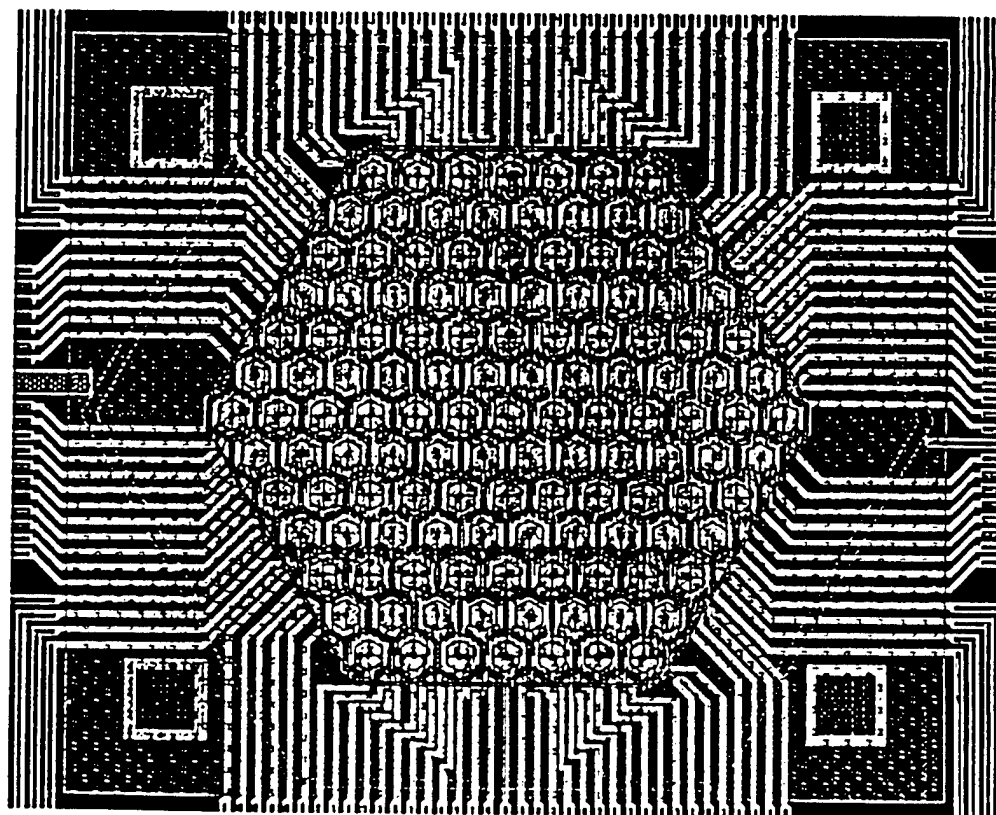


(b)

Figure 1. (a) Typical single micromirror element, (b) typical micromirror array.



(a)



(b)

Figure 2. (a) Hexagonal micromirror elements, (b) hexagonal array of 127 hexagonal elements.

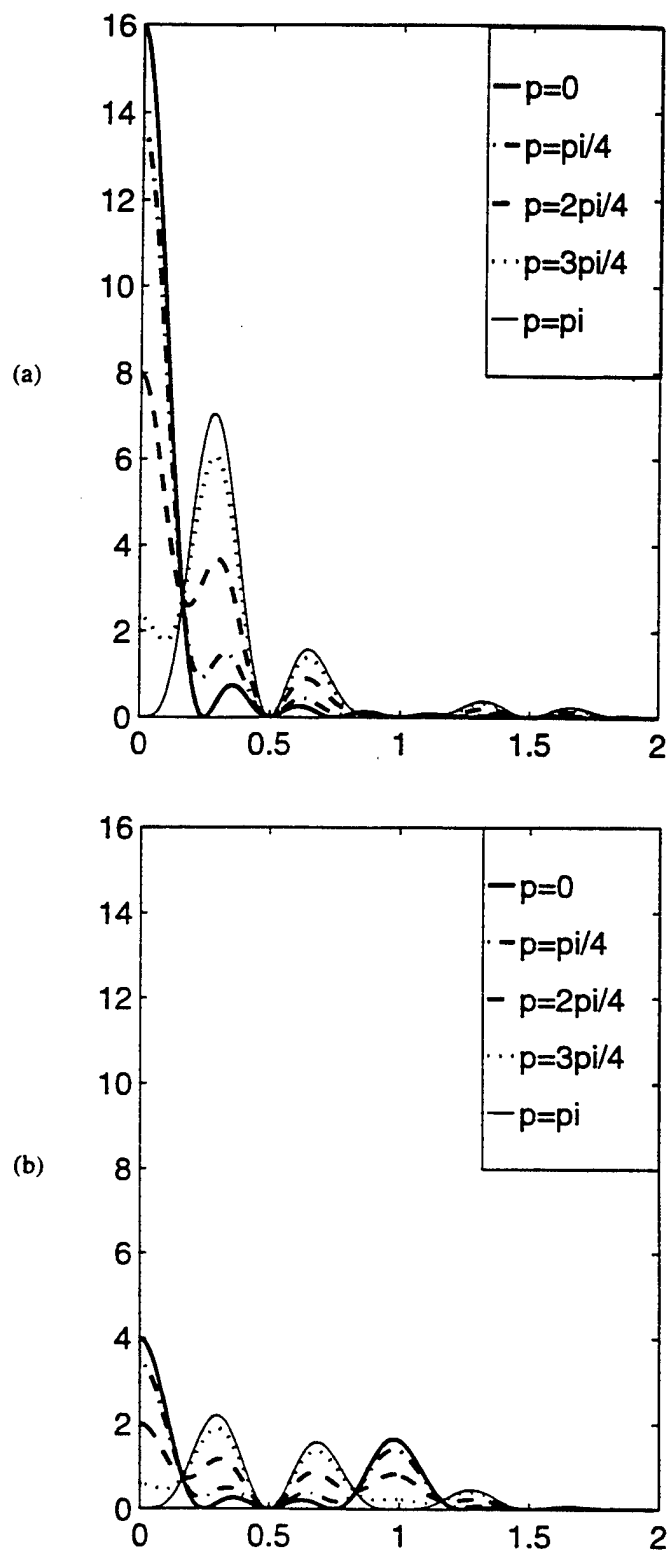
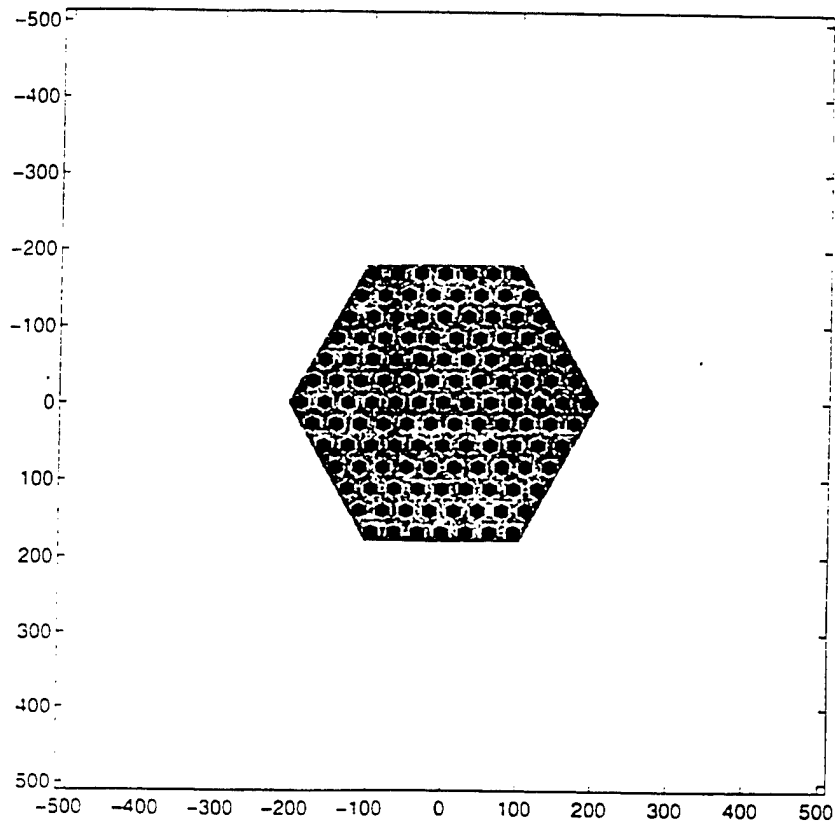
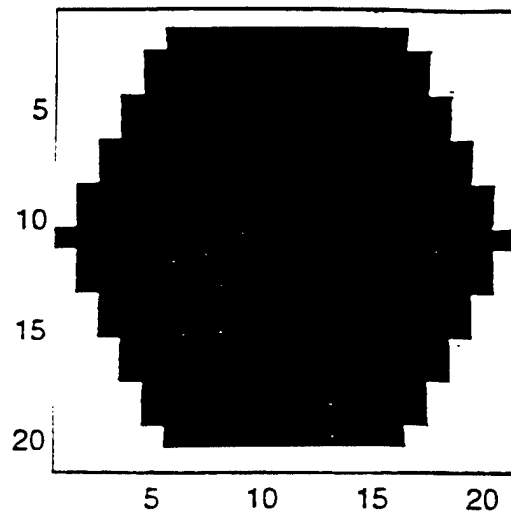


Figure 3. (a) Plot of  $y(x)$  for  $w = 1$  (no inter-mirror space), (b) plot of  $y(x)$  for  $w = .5$  (equal mirror and inter-mirror space).

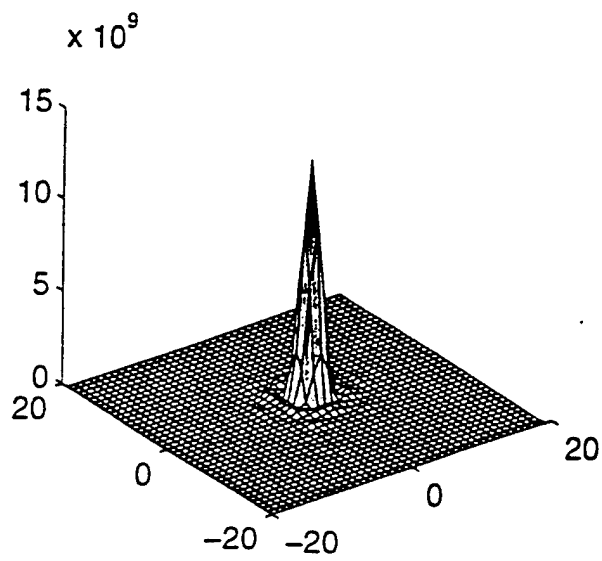


(a)

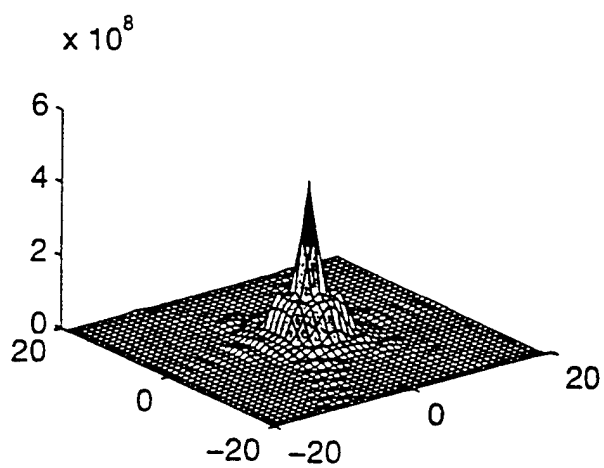


(b)

Figure 4. (a) Hexagonal array of hexagonal micromirror elements quantized on a 1024 by 1024 grid, (b) quantized single micromirror element.

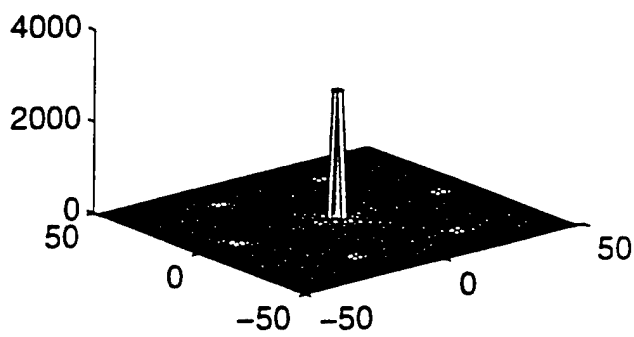


(a)

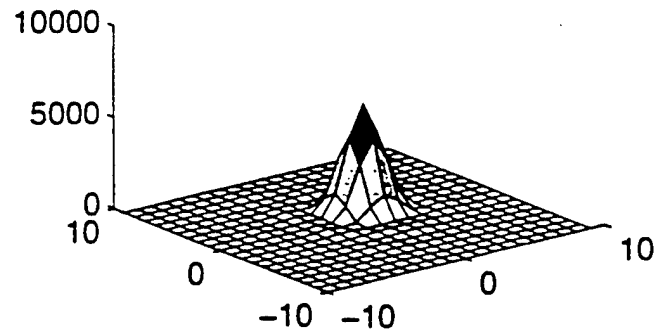


(b)

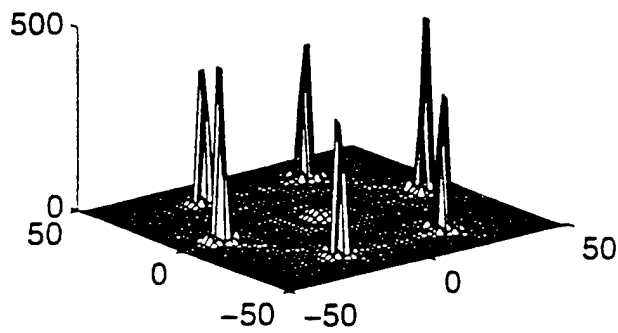
Figure 5. (a) Plot proportional to the central portion of the far field irradiance reflected from the array of Figure 4 for zero micromirror displacement, (b) similar plot for parabolic micromirror displacement.



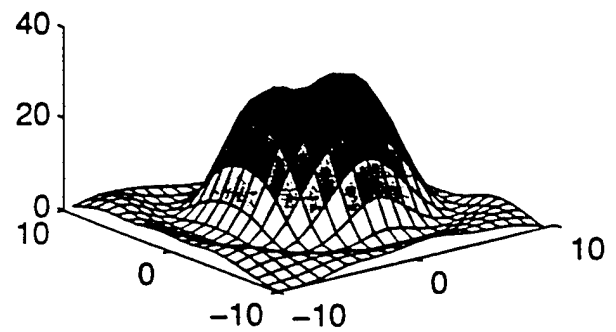
(a)



(b)



(c)



(d)

Figure 6. (a) Plot proportional to the far field irradiance reflected from the array of Figure 4 with zero micromirror displacement, (b) central region of (a), (c) plot proportional to the far field irradiance reflected from the array of Figure 4 with micromirror displacement optimized to yield as-constant-as-possible irradiance over a circular central region that includes only the central and first side lobes, (d) central region of (c).



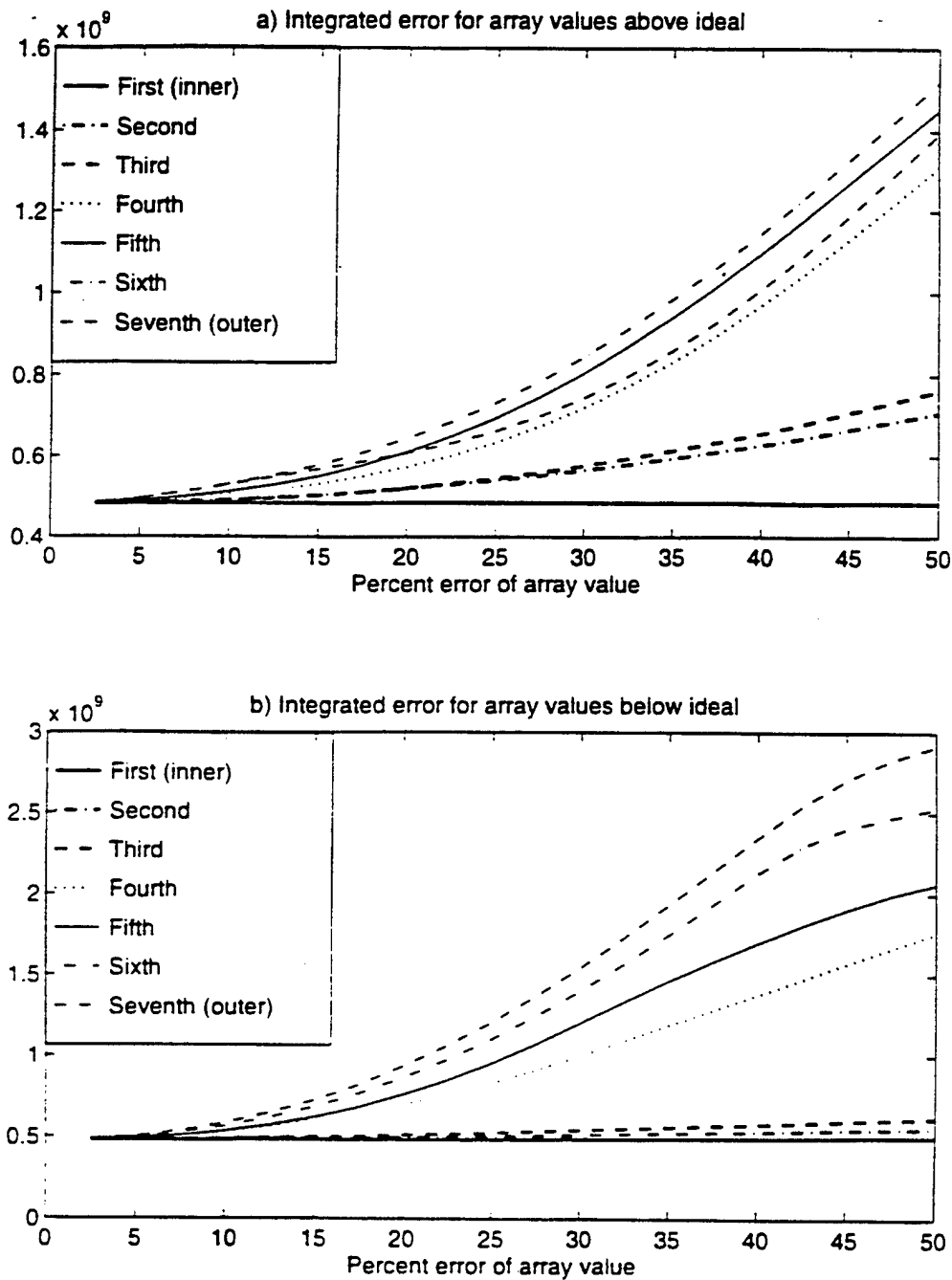


Figure 7. (a) Plot of the minimized quantity  $I$  versus percent change above the optimal phase values for the seven hexagonal rings of micromirrors, (b) as in (a) but for percent change below the optimal phase values.

# MICROMIRROR ARRAYS FOR COHERENT BEAM STEERING AND PHASE CONTROL

Steven C. Gustafson and Gordon R. Little,  
University of Dayton, Dayton, Ohio 45469;

Victor M. Bright and John H. Comtois,  
Air Force Institute of Technology, AFIT/ENG,  
Wright-Patterson AFB, Ohio 45433;

Edward S. Watson,  
Air Force Wright Laboratory, WL/AARI,  
Wright-Patterson AFB, Ohio 45433

[SPIE Proc. 2881, No. 05, Austin, TX, 14 October 1996]

## ABSTRACT

Micromirror arrays have been designed, fabricated, and tested that can steer coherent beams and that can simultaneously implement continuous phase control for beam shaping or aberration correction. A typical micromirror consists of a polysilicon plate (metalized for reflection) that is less than 100 microns in maximum dimension. Each micromirror is suspended a few microns above a polysilicon electrode by flexure hinges, and potentials of less than 50 volts applied to the electrodes displace the micromirrors over continuous ranges. Applications for arrays of these micromirrors include adaptive optics, active optical interconnections, and laser radar and communications.

**Keywords:** micromirror arrays, beam steering, beam shaping

## 1. MICROMIRRORS AND MICROMIRROR ARRAYS SUITABLE FOR COHERENT BEAM STEERING AND PHASE CONTROL

Many types of micromirrors and micromirror arrays have been designed and tested, notably at the Air Force Institute of Technology<sup>1</sup> (Dayton, Ohio), with fabrication mainly by the MUMPS facility of MCNC (Durham, North Carolina). Some of these designs may be suitable for coherent beam steering and phase control in applications such as active optical interconnections (including phase encoded reference beam multiplexing for holographic data storage), laser radar and communications, and adaptive optics.<sup>2</sup>

Figure 1 shows a micromirror design<sup>3</sup> of a kind that may be particularly appropriate for these applications. The micromirror consists of a 50 micron wide polysilicon plate (metalized for reflection) that is suspended a few microns above a polysilicon electrode by two micron wide flexure hinges. The polysilicon is conducting,

and potentials of less than 50 volts applied between the micromirror plate and the underlying electrode can displace the micromirror by more than 200 nm. The hexagonal structure permits close micromirror array spacing as shown in Figure 2 for an array of 127 micromirrors. This structure also permits support by three relatively long flexure hinges (instead of four relatively short hinges as is typical for square micromirrors), thus enabling larger micromirror displacement per unit voltage.

Some practical concerns include (1) the possible nonuniform behavior of the micromirrors as a function of control voltage over the array and over time, (2) the possible tilting and deviation from flatness of the micromirrors as a function of deflection toward the substrate<sup>4</sup>, and (3) light scattering from flexure hinges and other non-micromirror structures (such as the etch hole shown in Figure 1), including reflection from static inter-micromirror regions. The first and second concerns can presumably be addressed by careful design and fabrication. Both the second and third concerns may be addressed by using a lenslet array that focuses light only near the center of each micromirror. Possible problems with this approach include limited lenslet depth of focus and potentially damaging optical intensity at the focus of each lenslet.

The second and third concerns may also be addressed using a cover plate that masks inter-micromirror regions and structures as shown in Figure 3 (note also the absence of an etch hole, which has been found to be unnecessary for micromirrors less than about 100 microns wide<sup>3</sup>). The cover plate may be reflective and tilted relative to the micromirror array plane so that light incident on the plate is reflected out of the optical system. The array may also be in the focal plane of a Fourier transform lens with an f-number large enough to ensure that the width of its point spread function exceeds the width of each cover plate opening. In this case each micromirror approximates a point source and the effects of micromirror tilt and distortion may be greatly reduced.

## **2. ANALYSIS AND SIMULATION OF MICROMIRROR PHASED ARRAY BEAM STEERING AND SHAPING**

Optical phased array technology is well-understood in aspects analogous to microwave phased array technology, which has been much more extensively developed. In particular, a stair-step linear phase profile or blaze can be used to steer an optical beam into the first diffraction order with an efficiency of  $[\sin(\pi/n)/(\pi/n)]^2$ , where  $n$  is the number of steps in one blaze period with no inactive space between steps (i.e., the fill factor is unity).<sup>5</sup> Such steering has been investigated in simulations for square and rectangular micromirror arrays using realistic micromirror sizes and fill factors and including some effects of micromirror deformations (deviations from ideal piston deflection).<sup>6</sup> However, since (1) the size and thus the spacing  $d$  of the micromirrors is typically at least 50 microns, (2) at least eight micromirrors must be used in each blaze period to achieve 95 percent diffraction efficiency, and (3) the wavelength  $\lambda$  is typically

one micron or less, the maximum steering angle  $\lambda/(nd)$  is generally less than 2.5 mrad or 0.14 degree.

Beam shaping using phased array micromirrors has been investigated in simulations for the hexagonal array of 127 micromirrors shown in Figures 1 and 2.<sup>7</sup> In these simulations the phase or piston displacements of all micromirrors in each of the seven concentric hexagonal rings of 1, 6, 12, 18, 24, 30, and 36 micromirrors were the same. The simulations included a direct calculation of the far field intensity when the ring displacements had a parabolic profile (phases in units of  $\pi$  of 0, 1/36, 4/36, 9/36/16/36, 25/36, and 1 from the center to the outermost ring). The simulations also included a simulated annealing optimization of the phases for the seven rings that produced as-constant-as-possible (or flat-top) intensity over a circular central region. It was found that a flat-top-like central maximum beam shape could be achieved only if the first six secondary maxima, which formed a hexagonal pattern around the central maximum, had greatly increased intensity. However, this beam shape was found to be robust with respect to small phase variations.

If a cover plate (as in Figure 3) tilted to reflect non-micromirror light out of the system is used with a sufficiently high f-number Fourier transform lens, each micromirror functions as a point source with adjustable phase. In the far-field the result is a set of plane waves with uniform angular spacing of the propagation directions and with adjustable relative longitudinal phases. This case may be readily implemented both experimentally and in simulations to address a variety of beam steering, beam shaping, and aberration correction requirements.

### **3. TESTS OF MICROMIRROR PHASED ARRAY BEAM STEERING AND SHAPING**

Figure 4 shows the experimental arrangement used to investigate micromirror array beam steering and phase control for beam shaping or aberration correction. The expanded laser beam illuminates a hexagonal mask that is imaged, after possible aberration insertion, onto the micromirror array. A polarizing beam splitting cube directs the reflected light (after sampling by another beam splitting cube and a near-field video camera) through Fourier transform optics, after which a video camera records the far-field intensity. The micromirror array is provided with 64 control voltages for its 127 micromirrors according to the addressing scheme shown in Figure 5, which permits linear ramp and hexagonal ring voltage patterns and enables the correction of spherical, coma, and astigmatism aberrations. The control voltages (limited to 10 volt ranges) are programmed from a PC through a digital-to-analog converter board, and provision is made for applying bias voltages.

Figure 6 shows the typical micromirror deflection versus voltage characteristic for the tested arrays<sup>3</sup>; note that a bias of 40 volts is desirable to achieve a deflection range of at least 200 nm for a 10 volt control range. Figure 7 shows that the application of a bias

voltage of up to 30 volts to all micromirrors causes a significant redistribution of intensity out of the central maximum of the array diffraction pattern and into six secondary maxima. This effect is due to the relatively intense and constant reflection from the largely reflective inter-micromirror regions. Both this effect and the relative width and spacing of the maxima are consistent with simulations.<sup>7</sup>

Figure 8 shows the far-field central maximum intensity for three control voltage patterns; the light spot above the dark central maximum is an artifact of the experimental system. In (a) all micromirrors are at 24 volts, which is near the mean of the voltages employed for the other two patterns. In (b) beam steering of approximately one-tenth of the central maximum width is implemented by a stepped linear ramp pattern from 20 to 29.6 volts, where the pattern steps 0.8 volts between each of the 13 array rows. In (c) beam shaping is implemented by a quadratic hexagonal ring pattern from 20 to 27.2 volts, where the pattern follows  $V(i) = 20 + (i-1)^2/5$ ,  $i = 1, 2, \dots, 7$ , for each of the seven array hexagonal rings with  $i = 1$  at the center. From Figure 5 it is apparent that the voltage range employed for beam steering yields a maximum micromirror displacement of about  $d = 80$  nm across the  $w = 790$  micron side-to-side width of the array, and thus the steering angle  $d/w$  is approximately 0.1 mrad or about 0.006 degrees. The angular width of the central maximum is approximately  $\lambda/w$  or 0.8 mrad for  $\lambda = 633$  nm. Thus the displacement of the central maximum due to steering should be approximately  $d/\lambda$  or 0.13 of the central maximum width, which is consistent with results shown in Figure 8 (a) and (b). In (c) it is apparent that the quadratic pattern broadens the central maximum, which is consistent with simulations.<sup>7</sup>

#### 4. FUTURE PROSPECTS

The limitations of micromirror phased arrays for beam steering are primarily due to large micromirror sizes relative to optical wavelengths. As discussed above, efficient (e.g., greater than 95 percent diffraction efficiency) beam steering may be achieved for visible wavelengths and for tens-of-microns-wide micromirrors only over angular ranges of a few tenths of a degree. However, the ability to independently and continuously control the phase of each micromirror in a large array may enable important beam shaping, aberration correction, and other applications. In general, these applications will require (1) large numbers of micromirrors to achieve high diffraction efficiency, (2) elimination of light reflected from non-micromirror regions using, for example, lenslet arrays or tilted cover plates, and (3) accurate and reproducible phase control for each micromirror, which is an anticipated consequence of future advances in micromirror design and fabrication.

#### 5. ACKNOWLEDGMENTS

This work was performed in part on US Air Force Contract No. F33615-92-C-1120 through the Air Force Wright Laboratory. The hexagonal micromirror elements and array shown in Figures 1, 2, and 3 were designed by John H. Comtois and Victor M.

Bright of the Air Force Institute of Technology and were fabricated by the MUMPS facility at MCNC.

## 6. REFERENCES

1. J. H. Comtois, "Structural Techniques for Implementing and Packaging Complex, Large Scale Microelectromechanical Systems Using Foundry Fabrication Processes," *Ph.D. Dissertation*, Air Force Institute of Technology, Wright-Patterson AFB, OH, March 1996.
2. T. A. Rhoadarmer, S. C. Gustafson, G. R. Little, and T. H. Lin, "Flexure-Beam Micromirror Spatial Light Modulator Devices for Acquisition, Tracking, and Pointing," *Proc SPIE*, Vol. 2221, No. 40, Orlando, FL, April 1994.
3. J. H. Comtois, V. M. Bright, S. C. Gustafson, and M. A. Michalick, "Implementation of Hexagonal Micromirror Arrays as Phase-Mostly Spatial Light Modulators," *Proc SPIE*, Vol. 2641, pp. 76-87, Austin, TX, October 1995.
4. T. A. Rhoadarmer, V. M. Bright, B. M. Welsh, S.C. Gustafson, and T. H. Lin, "Interferometric Characterization of the Flexure Beam Micromirror Device," *Proc SPIE*, Vol. 2291, pp. 13-23, San Diego, CA, July 1994.
5. P. F. McManamon, T. A. Dorschner, D. L. Corkum, L. J. Friedman, D. S. Hobbs, M. Holtz, S. Liberman, H. Q. Nguyen, D. P. Resler, R. C. Sharp, and E. A. Watson, "Optical Phased Array Technology," *Proc. SPIE*, Vol. 84, pp. 268-298, February 1996.
6. E. A. Watson and A. R. Miller, "Analysis of Beam Steering Using Phased Micromirror Arrays," *Proc. SPIE*, Vol. 2687, No. 08, San Jose, CA, January 1996.
7. S. C. Gustafson, T. A. Tuthill, and E. A. Watson, "Micromirror Arrays for Active Optical Aberration Control," *Proc SPIE*, Vol. 2687, No. 02, San Jose, CA, January 1996.

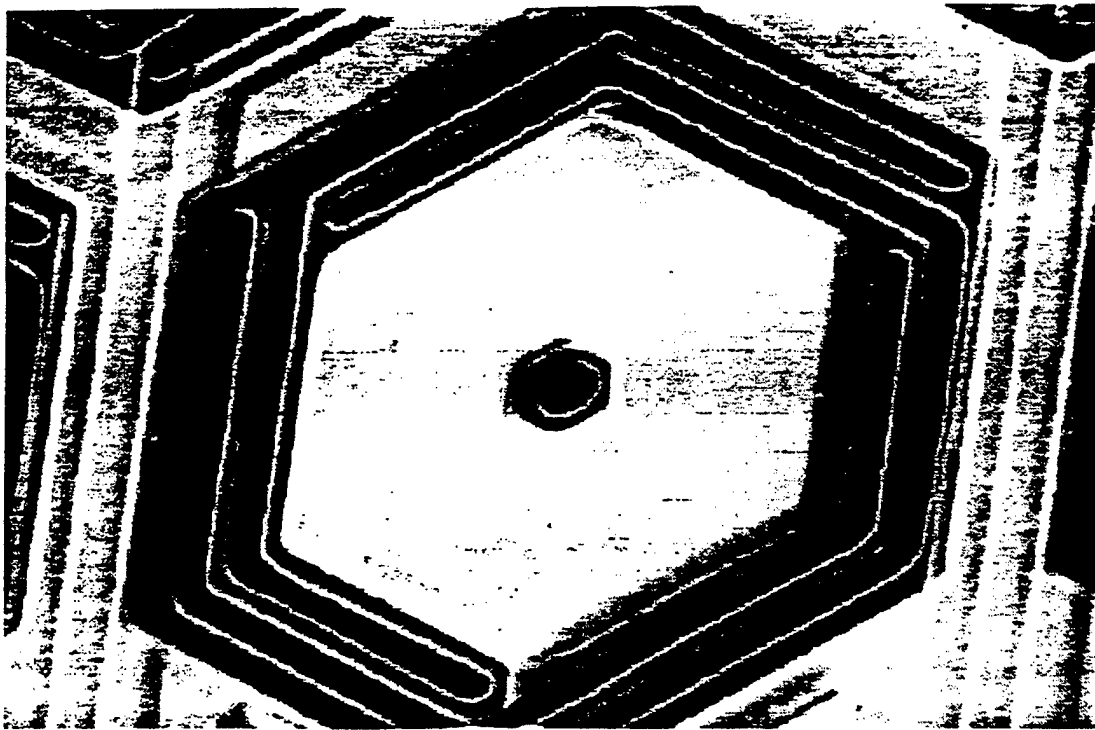


Figure 1. Micrograph of a 50 micron wide hexagonal micromirror with two micron wide flexure hinges.<sup>3</sup>

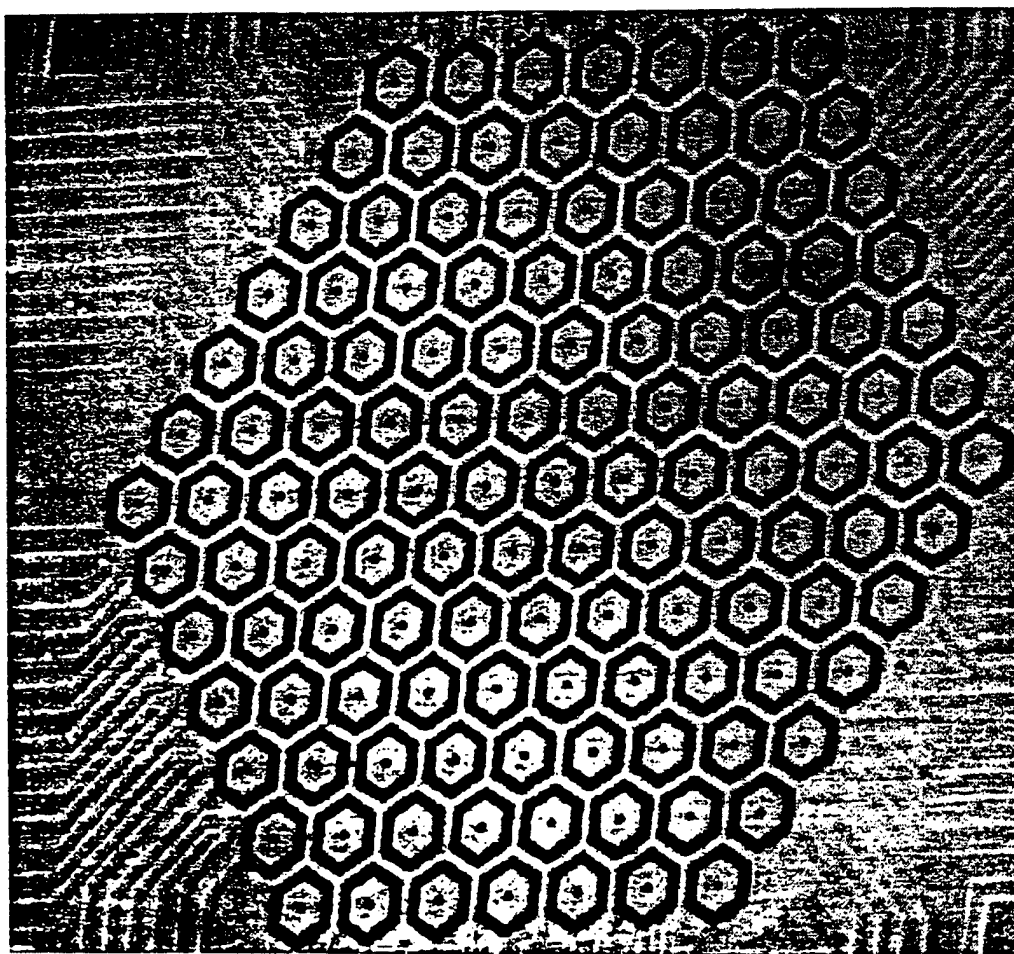


Figure 2. Micrograph of a hexagonal array of 127 micromirrors, each 50 microns wide; maximum extent of the array is 975 microns.<sup>3</sup>

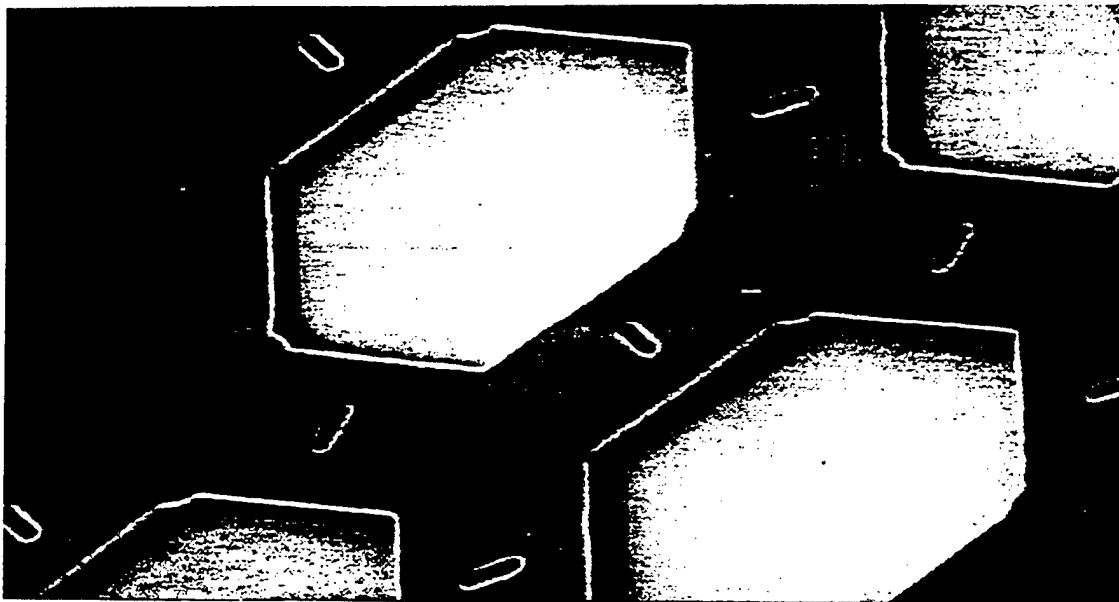


Figure 3. Micrograph of a 100 micron wide etch-hole-free hexagonal micromirrors with a hexagonal-hole cover plate that masks flexure hinges and other inter-mirror support structures.<sup>1</sup>

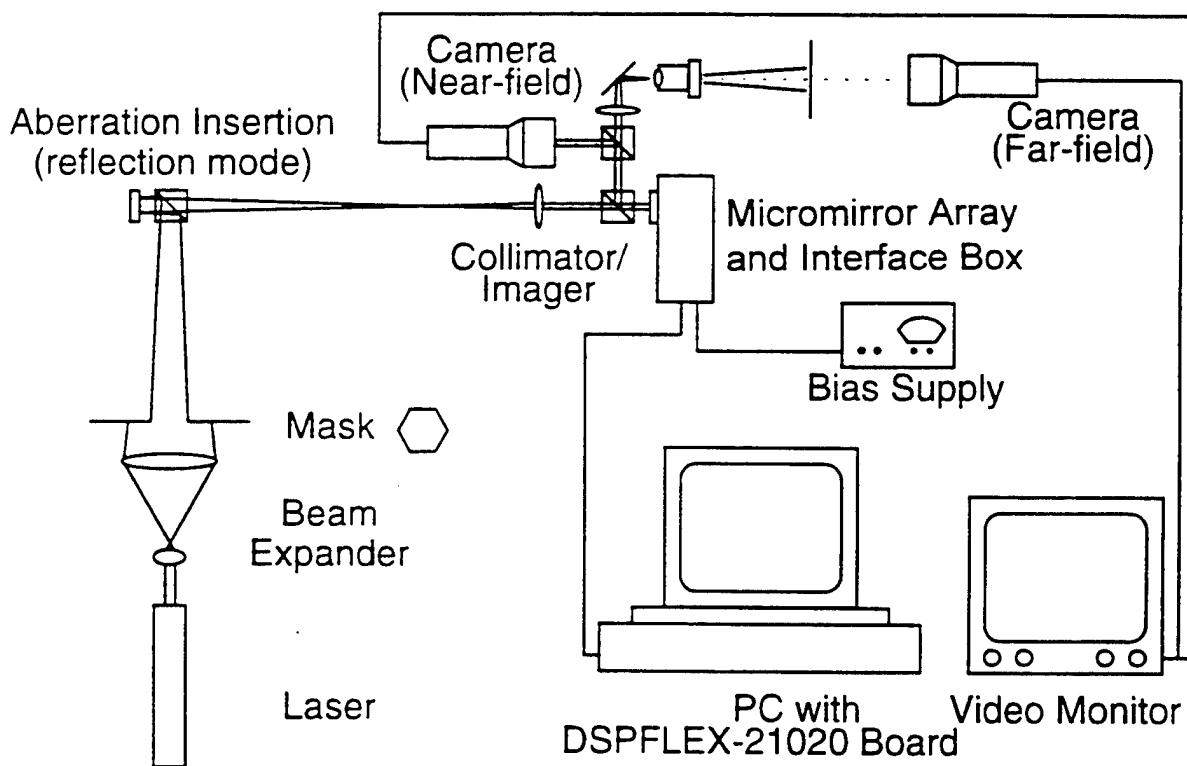


Figure 4. Experimental arrangement used to investigate micromirror array beam steering and phase control for beam shaping or aberration correction.



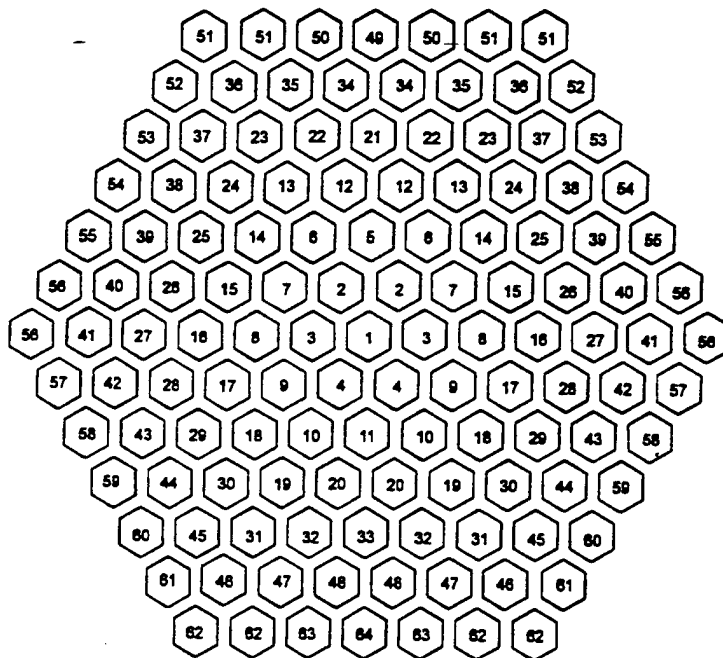


Figure 5. Addressing scheme with 64 control voltages for a hexagonal array of 127 micromirrors; this scheme permits linear ramp and hexagonal ring voltage patterns and enables the correction of spherical, coma, and astigmatism aberrations.

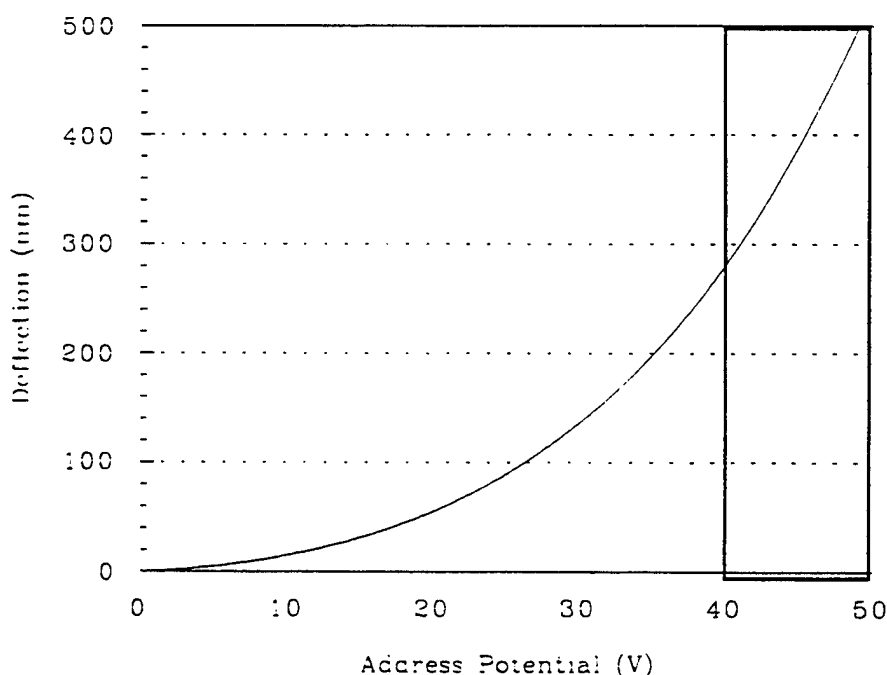


Figure 6. Typical micromirror deflection versus voltage characteristic<sup>3</sup> for micromirrors of the type shown in Figures 1 and 2; a bias of 40 volts is desirable to achieve a deflection range of at least 200 nm for a 10 volt control range (boxed region).

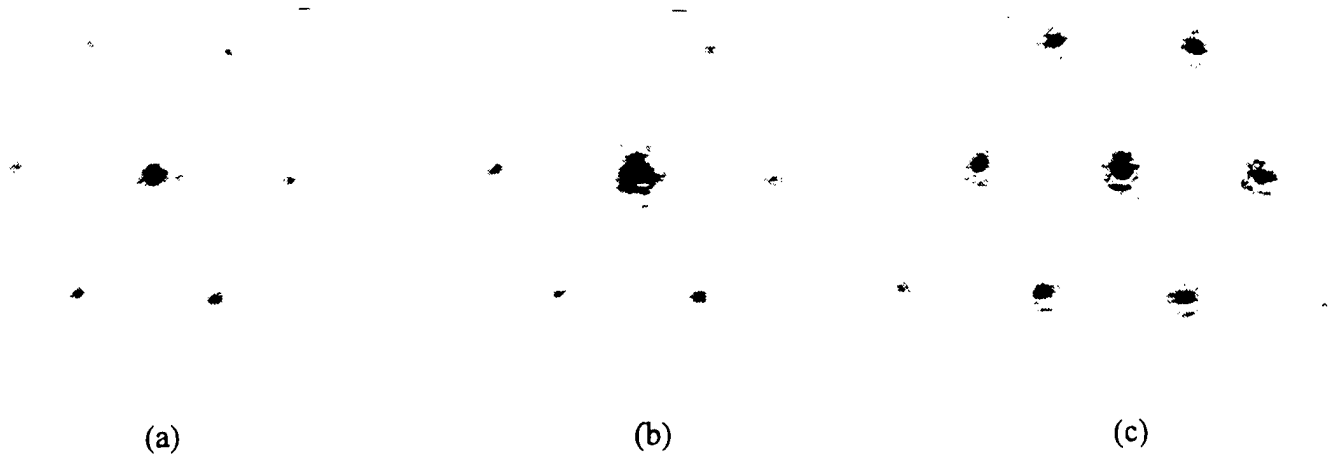


Figure 7. Effects of bias voltage on the far-field intensity for a hexagonal array of 127 micromirrors as in Figures 1 and 2; the potential applied to each micromirror is (a) 0 volts, (b) 20 volts, and (c) 30 volts.

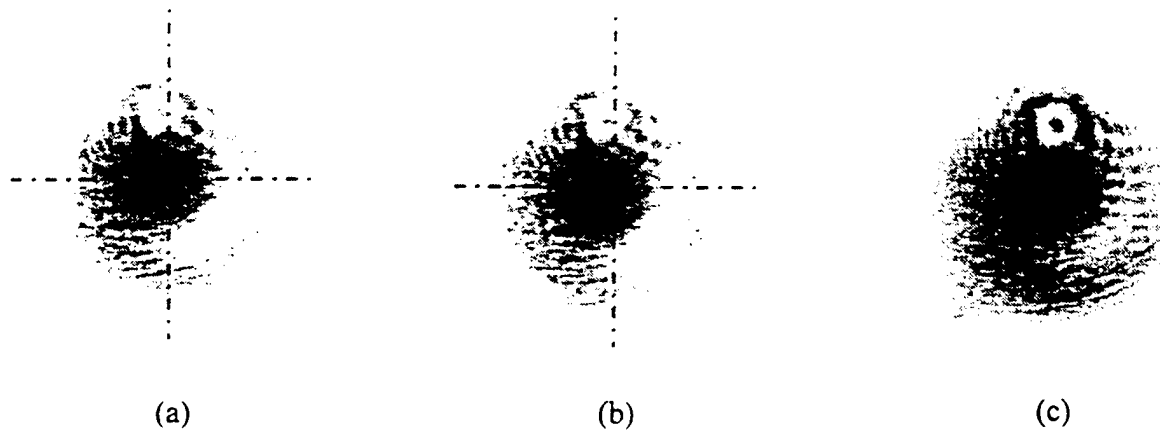


Figure 8. Central maximum beam steering and shaping for a hexagonal array of 127 micromirrors as in Figures 1 and 2; (a) all micromirrors at 24 volts, (b) beam steering due to a stepped linear ramp pattern from 20 to 29.6 volts, where the pattern steps 0.8 volts between each of the 13 array rows, (c) beam shaping due to a quadratic hexagonal ring pattern from 20 to 27.2 volts, where the pattern follows  $V(i) = 20 + (i-1)^2/5$ ,  $i = 1, 2, \dots, 7$ , for each of the seven array hexagonal rings with  $i = 1$  at the center.

# **LASER BEAM SHAPING USING DEFORMABLE MIRRORS**

**Steven C. Gustafson and Gordon R. Little**  
**University of Dayton, Dayton, Ohio 45469-0150**  
**Phone/fax 937-229-3978/3433, gustafson@udri.udayton.edu**

**and**

**Steven R. LeClair**  
**Air Force Wright Laboratory, Dayton, Ohio**

**Submitted to International Conference on Rapid Prototyping,**  
**San Francisco, California, 31 March - 3 April 1997**

## **Abstract**

Real-time shaping of the laser beams that determine material boundaries may dramatically improve the precision and resolution of rapid prototyping systems. Recent advances in deformable mirrors that implement dynamic optical phase profiling could enable the required real-time laser beam shaping using relatively small and low cost components. This paper reviews the deformable mirror technology appropriate for application to rapid prototyping.

## **Introduction**

Figure 1 illustrates some key features of laser beam shaping for rapid prototyping using a deformable mirror. The laser and beam transfer and focus optics are standard components and configurations found in typical rapid prototyping and laser material processing systems.<sup>1,2</sup> The deformable mirror may be one of at least two types<sup>3</sup>: (1) continuous, consisting of a thin plate or membrane with underlying actuators that deform the mirror surface, or (2) segmented, consisting of an array of small, closely spaced mirrors that may be independently moved through small angles or distances. The material being processed is either cured, cut, or sintered consistent with the type of rapid prototyping employed. In general, the laser beam is scanned or rastered in a focused or nearly focused form on the surface of the material. Light is scattered from the focus region into three or more photodetectors, and the intensity of this light is a real-time measure, quantifiable by calibration, of the focus beam shape. (The deformable mirror may also be used to modulate the laser beam to enable phase-lock detection of the scattered light and thus discriminate against noise.) A small computer inputs signals from the detectors and information on desired beam shape, processing rate, etc., and outputs feedback signals to the deformable mirror drive electronics. The end result is that the quality of curing, cutting, or sintering may be controlled as a function of material surface shape, processing rate, etc., so that rapid prototyping precision and resolution may be dramatically improved.

## Prospects for Continuous Deformable Mirrors

The key enabling component in laser beam shaping for rapid prototyping as depicted in Figure 1 is the deformable mirror. Three basic kinds of continuous deformable mirror designs could be employed.<sup>5</sup> The bimorph design uses a plate of piezoelectric material with an optically flat reflective and a conductive surface attached to one side and a segmented electrode array attached to the other side. The discrete actuator design uses stacks of piezoelectric elements in place of the single piezoelectric plate to achieve larger mirror deformations: force may be applied either perpendicular or parallel (i.e., on edge) to the reflective surface. Finally, the membrane design uses a flexible reflective and conductive membrane, often called a "rubber mirror", that is electrostatically attracted, generally through a damping fluid (but not through an intervening piezoelectric material), toward an electrode array.

Continuous deformable mirrors have advantages in terms of efficiency (e.g., light is not wasted by diffraction into unused orders) and ability to achieve, in principle, any desired wavefront correction or beam shape. However, determining the electrode voltages that produce desired beam shapes is complex because the mirror deformation caused by one electrode is not independent of the deformations caused by other electrodes. Also, continuous deformable mirrors are difficult to fabricate and are consequently expensive, typically costing several tens of thousands of dollars.

## Prospects for Segmented Deformable Mirrors

Segmented deformable mirrors have advantages in terms of ease of control (i.e., the mirror deformation caused by one electrode is independent of the deformations caused by other electrodes), relatively small size, and low cost.<sup>4,5</sup> However, significant light is generally lost through diffraction into unused orders,<sup>6,7</sup> and the wavefront corrections or beam shapes that may be achieved are not arbitrary but typically form a limited number of types.<sup>8,9</sup>

Figures 2 and 3 are micrographs of arrays of hexagonal micromirrors, each 50 microns wide.<sup>4</sup> These micromirrors were designed by Victor M. Bright and John H. Comtois at the Air Force Institute of Technology and were fabricated using the DARPA-supported MUMPS foundry. MUMPS refers to the Multi-User MEMS Process, and MEMS denotes micro-electro-mechanical-system. MUMPS uses standard silicon integrated circuit fabrication technology, i.e., multi-layer lithography and etching, to form polysilicon structures that move through electrostatic attraction in response to underlying applied voltages. The micromirrors shown in Figures 2 and 3 consist of hexagonal polysilicon plates suspended a few microns above a polysilicon electrode by two micron wide flexure hinges. The polysilicon is conducting, and potentials of less than 50 volts applied between the micromirror plate and the underlying electrode can displace the

micromirrors by more than 200 nm. The hexagonal design permits close micromirror array spacing as shown in Figure 3 for an array of 127 micromirrors.

Figure 4 shows three example beam shapes. These shapes are simulated far field central irradiance patterns that may be achieved using a 127-element hexagonal micromirror array,<sup>4</sup> and key features of these simulations have been verified experimentally.<sup>7,10</sup> As detailed in the Figure caption, the three beam shapes are due to undeflected mirrors, mirrors deflected in a parabolic profile, and mirrors deflected so that the beam shape approximates a flat top profile. Figure 5 also shows a beam shape due to undeflected mirrors and a beam shape that approximates a flat top profile,<sup>10</sup> but both the sidelobe patterns and the central irradiance patterns are shown, and it is clear for the flat top beam shape that significant light is lost through diffraction into sidelobes. However, Figure 6 indicates that beam shapes can be relatively insensitive to changes in control voltages,<sup>10</sup> which is a result of significant practical importance for the potential use of segmented deformable mirrors in rapid prototyping systems.

### **Issues that Must be Addressed for Implementation of Deformable Mirrors in Rapid Prototyping Systems**

For continuous deformable mirrors the key concerns are high cost and complex control. Advances in materials and fabrication technology could address the former concern, and appropriate software development could address the latter concern. For segmented deformable mirrors important issues include<sup>11</sup> (1) the possible nonuniform behavior of the micromirrors as a function of control voltage over the array and over time, (2) the possible tilting and deviation from flatness of the micromirrors as a function of deflection toward the substrate, and (3) light scattering from flexure hinges and other non-micromirror structures (such as the etch holes shown in Figures 2 and 3), including reflection from static inter-micromirror regions. Again, advances in materials and fabrication technology could address the first two concerns, and appropriately designed interfacing optics could address the last concern.

If the necessary advances in deformable mirror design and fabrication are executed and the potential for relatively small size and low cost components is realized, then it may be anticipated that laser beam shaping implemented as indicated in Figure 1 will enable many components produced by rapid prototyping to have dramatically improved dimensional accuracy and surface finish.

## REFERENCES

1. P. F. Jacobs. Rapid Prototyping and Manufacturing: Fundamentals of Stereolithography. Society of Manufacturing Engineers. 1992.
2. L. Migliore, ed., Laser Materials Processing. Marcel Dekker. 1996.
3. R. K. Tyson. Principles of Adaptive Optics. Academic Press. 1991.
4. J. H. Comtois, V. M. Bright, S. C. Gustafson, and M. A. Michalick, "Implementation of Hexagonal Micromirror Arrays as Phase-Mostly Spatial Light Modulators." Proc. SPIE Vol. 2641, pp. 76-87. Austin, TX. 24 Oct 1995.
5. T. G. Bifano and R. Krishnamoorthy, "Surface Micromachined Deformable Mirrors." Proc. 5<sup>th</sup> IEEE Conf. On Emerging Technologies and Factory Automation. Kauai, HI. 18-21 Nov 1996.
6. T. A. Rhoadarmer, S. G. Gustafson, G. R. Little, and T. H. Lin, "Flexure-Beam Micromirror Spatial Light Modulator Devices for Acquisition, Tracking, and Pointing." Proc. SPIE. Vol. 2221, No. 40. Orlando, FL. 7 Apr 1994.
7. M. C. Roggemann, V. M. Bright, B. M. Welsh, S. R. Hick, P. C. Roberts, W. D. Cowan, and J. H. Comtois, "Use of Micro-Electro-Mechanical Deformable Mirrors to Control Aberrations in Optical Systems: Theoretical and Experimental Results." accepted November 1996 for publication in Optical Engineering.
8. P. F. McManamon, T. A. Dorschner, D. L. Corkum, L. J. Friedman, D. S. Hobbs, M. Holz, S. Liberman, H. Q. Nguyen, D. P. Resler, R. C. Sharp, and E. A. Watson, "Optical Phased Array Technology." Proc. IEEE. Vol. 84, pp. 268-298, Feb 1996.
9. Y. Danziger, E. Hasman, A. A. Friesem, A. W. Lohmann, "Multilevel Diffractive Elements for Generalized Wavefront Shaping." Opt. Eng. Vol. 35, pp. 2556-2565, Sept 1996.
10. S. C. Gustafson, T. A. Tuthill, and E. A. Watson, "Micromirror Arrays for Active Optical Aberration Control." Proc. SPIE Vol. 2687, No. 2, San Jose, CA, 30 Jan 1996.
11. S. C. Gustafson, G. R. Little, V. M. Bright, J. H. Comtois, and E. A. Watson, "Micromirror Arrays for Coherent Beam Steering and Phase Control." Proc. SPIE Vol. 2881, No. 5, Austin, TX. 14 Oct 1996.

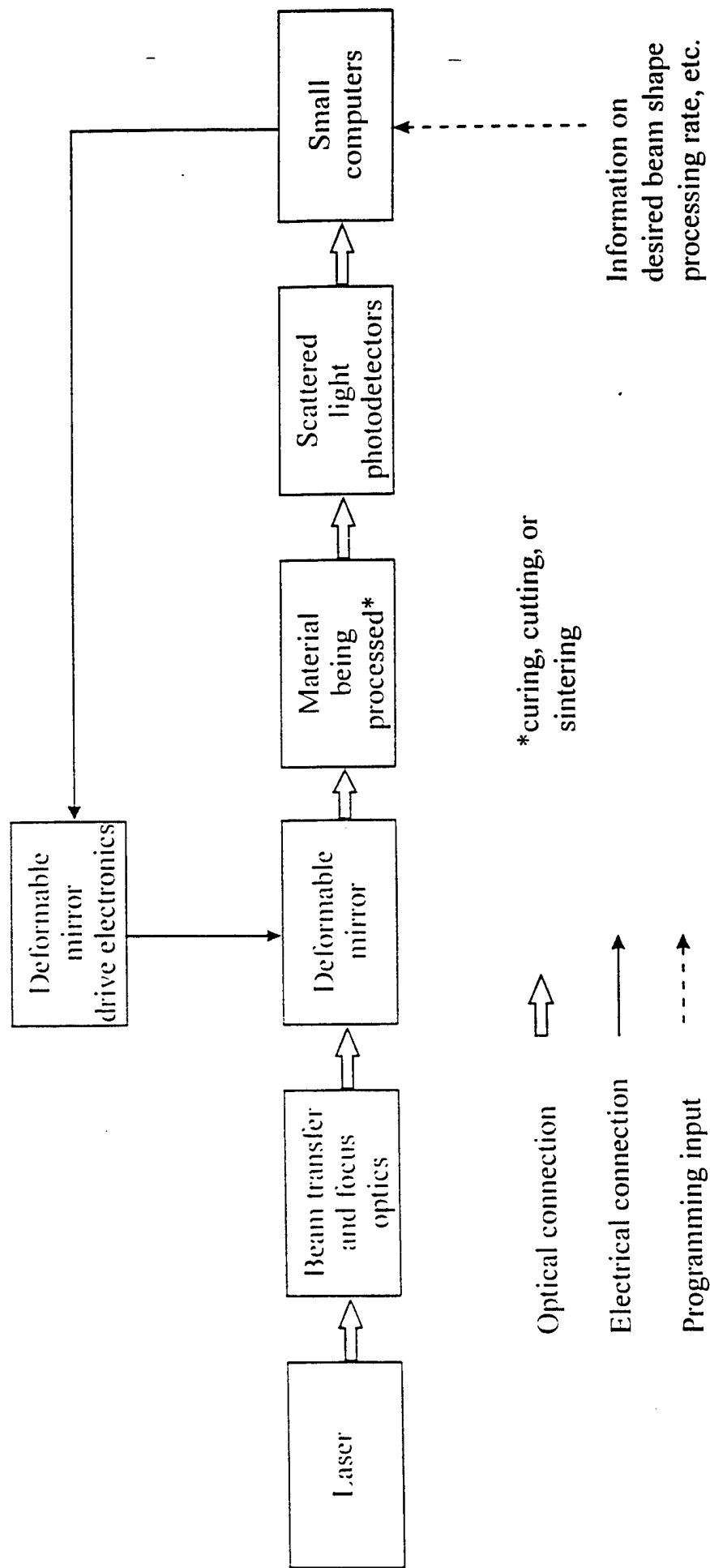


Figure 1. Laser beam shaping for rapid prototyping using a deformable mirror.

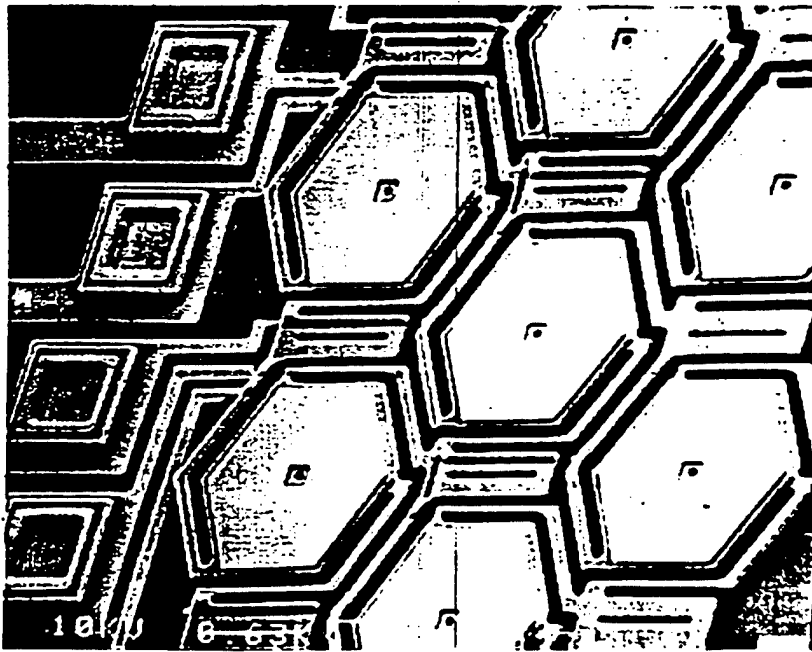


Figure 2. Micrograph of hexagonal micromirrors, each 50 microns wide with two micron wide flexure hinges.

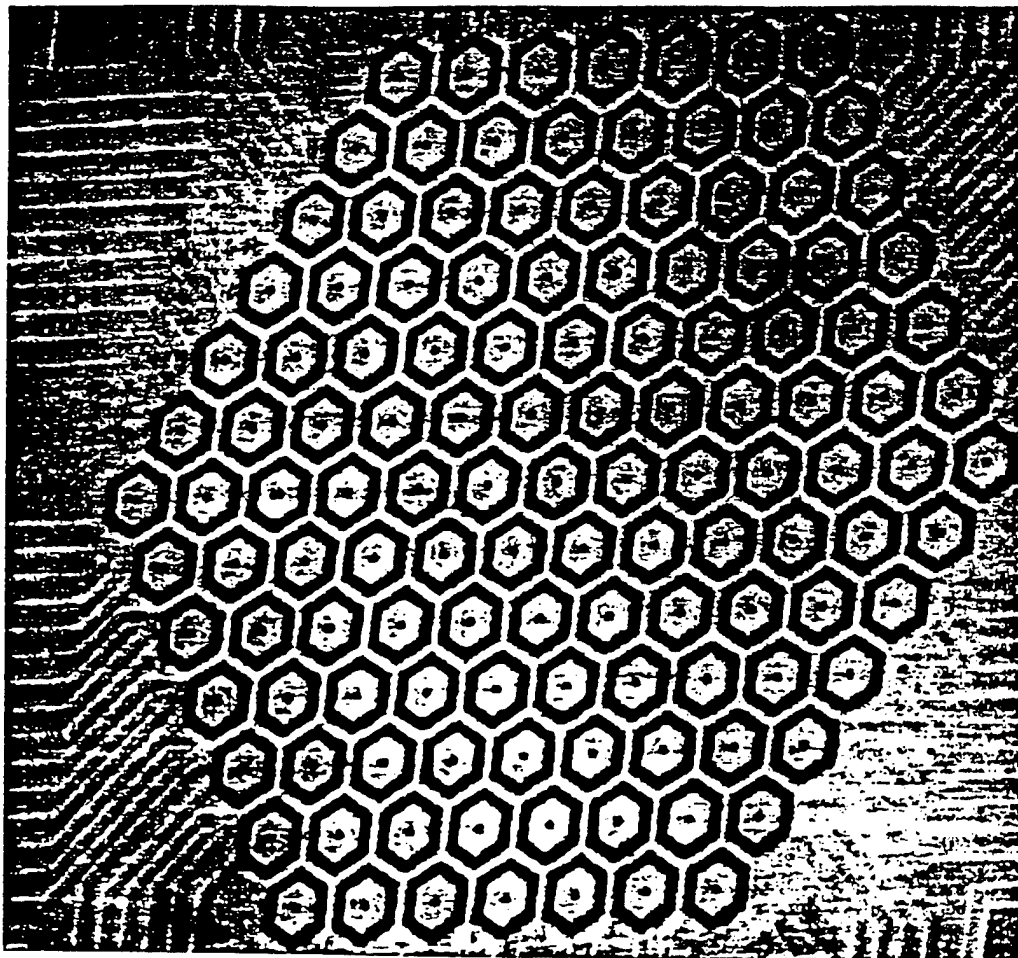


Figure 3. Micrograph of a hexagonal array of 127 micromirrors: maximum extent of the array is 975 microns.



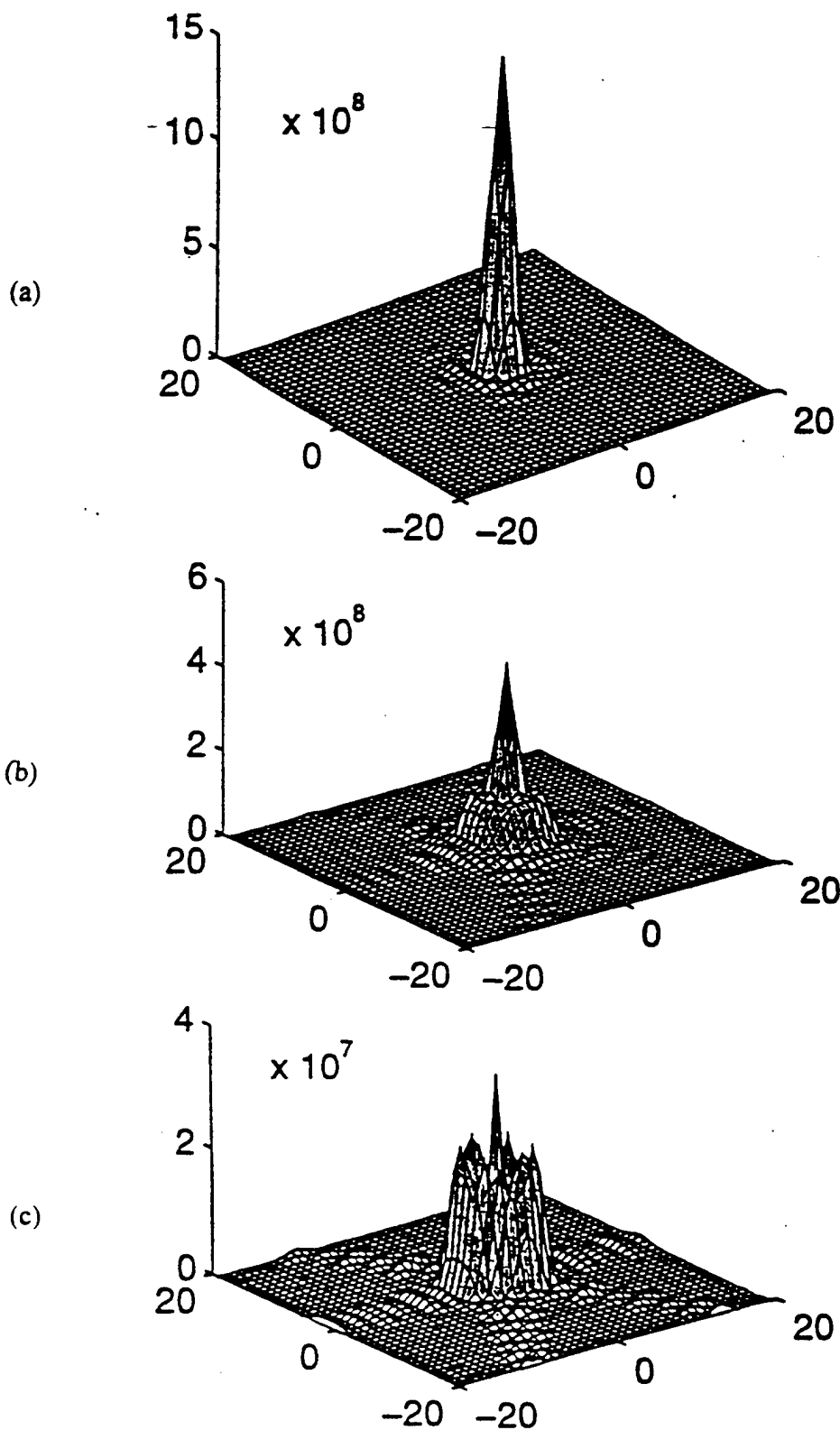
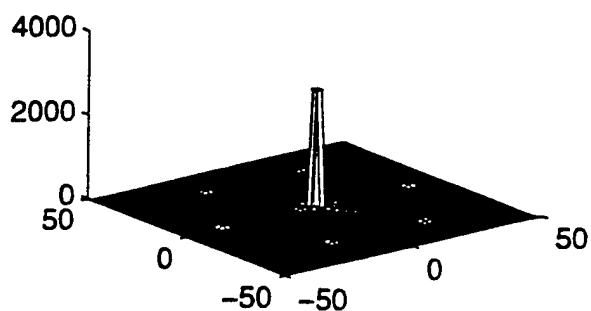
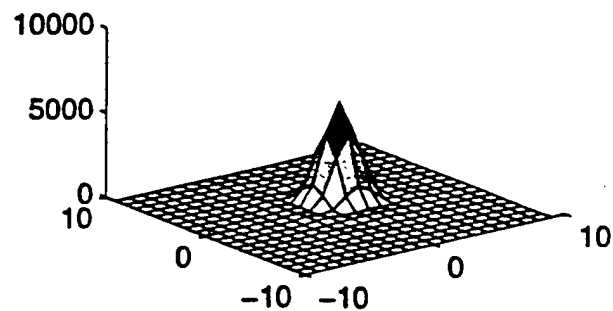


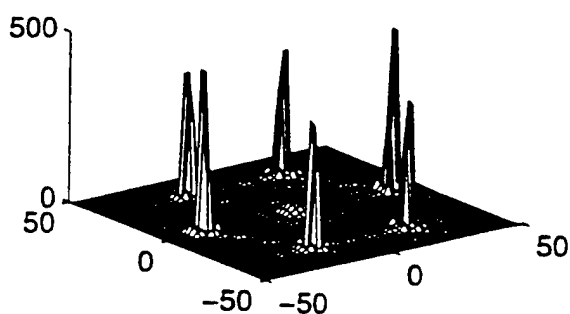
Figure 4. Simulated far field irradiance patterns in arbitrary units for the array of Figure 3 illuminated by a constant, coherent, collimated beam at normal incidence. The mirrors are operated as concentric rings. The center and surrounding rings of 6, 12, 18, 24, 30, and 36 hexagonal mirrors are assigned phase angles of  $2\pi y_1, 2\pi y_2, \dots, 2\pi y_7$ , respectively. The non-moving space between the mirrors is assigned an amplitude  $V$ . The far-field irradiance is plotted as a function of the following values for  $y_1, y_2, \dots, y_7$ , and  $V$ : (a) undeflected mirrors:  $y_1, y_2, \dots, y_7, V = 0$ ; (b) parabolic deflection profile:  $y_1, y_2, \dots, y_7 = 0.014, 0.056, 0.125, 0.222, 0.347, 0.500$ , and  $V = 0$ ; (c) deflections optimized to yield, as close as possible, a flat-topped profile over the main and first side lobes:  $y_1, y_2, \dots, y_7 = 0.7251, 0.2239, 0.1683, 0.5734, 0.5709, 0.5275, 0.5169, V = 0.5$ .



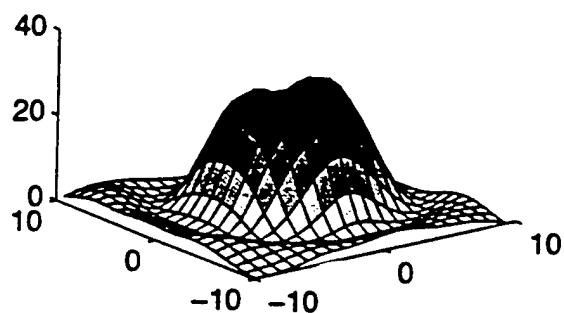
(a)



(b)



(c)



(d)

Figure 5. Simulated far field irradiance patterns reflected from the array of Figure 3: (a) zero micromirror displacement. (b) central region of (a). (c) micromirror displacement optimized to yield as-constant-as-possible irradiance over a circular central region that includes only the central and first side lobes. (d) central region of (c).

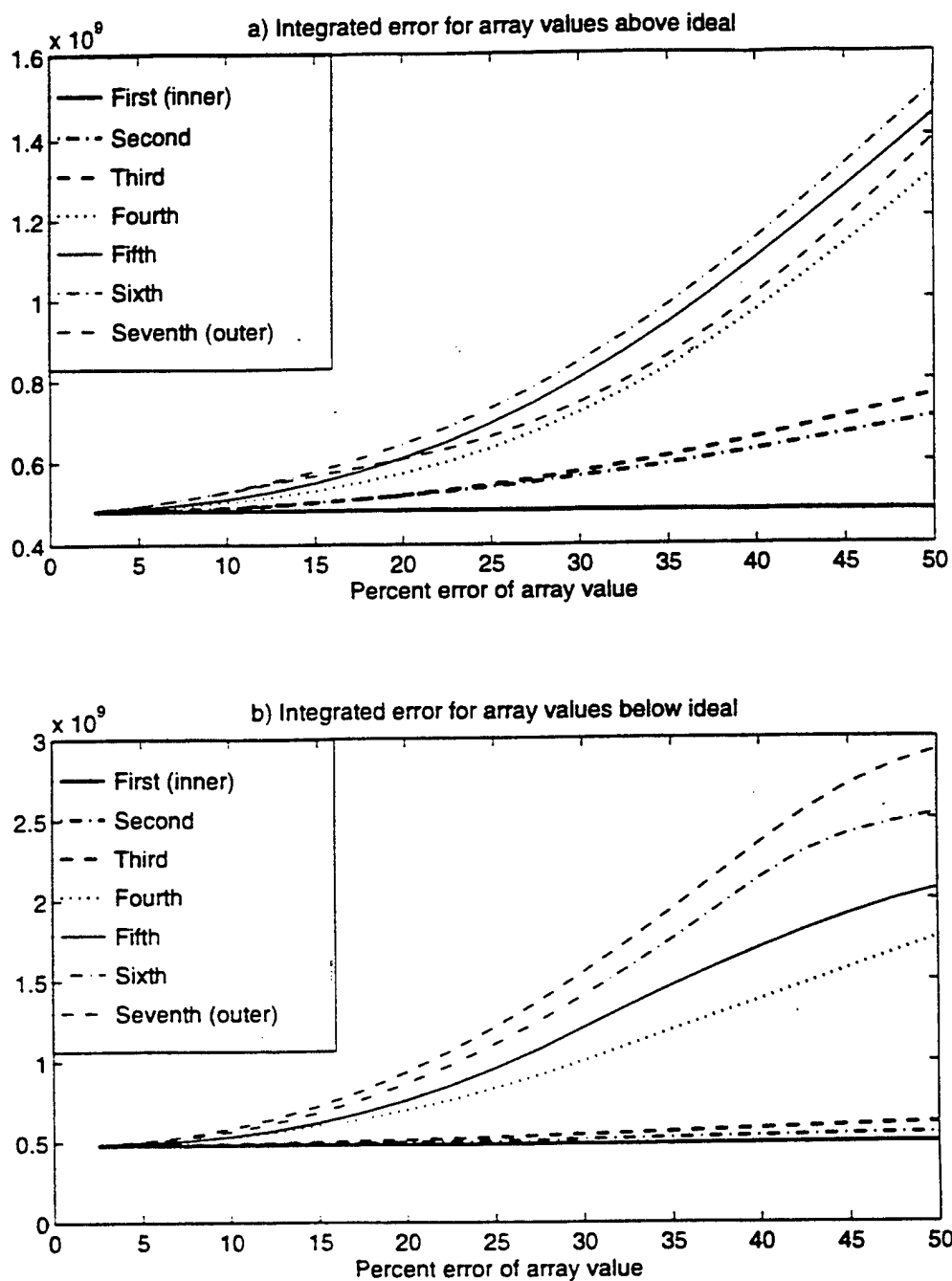


Figure 6. Simulated integrated squared difference between actual and desired beam shape irradiance from Figure 5d versus (a) percent change above the optimal phase values for the seven hexagonal rings of micromirrors, and (b) as in (a) but for percent change below the optimal phase values.